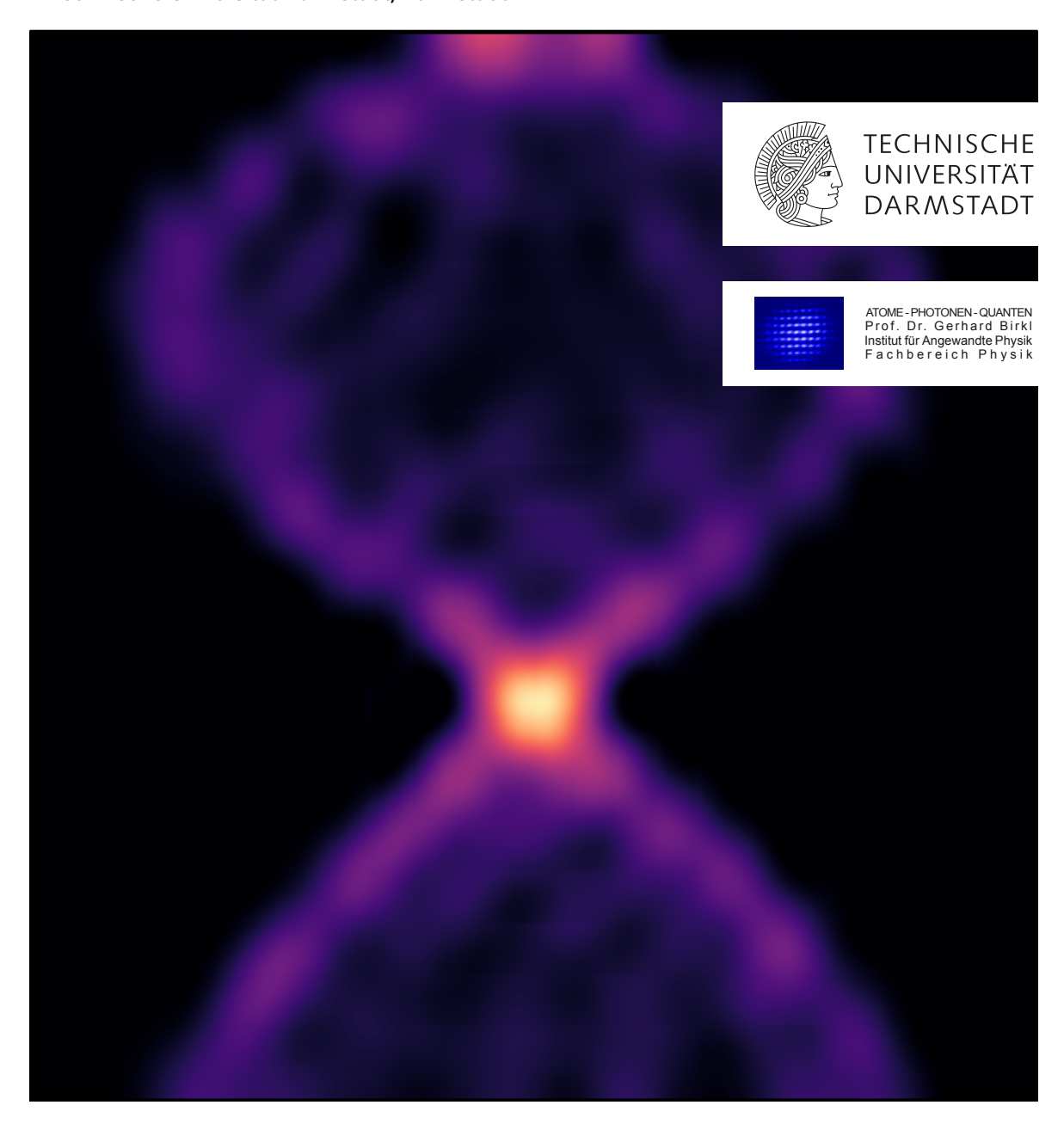
Novel Techniques for Atom Trapping and Large-Momentum-Transfer Atom Interferometry

Neuartige Techniken für Atomfallen und Atominterferometer mit hohem Impulsübertrag Vom Fachbereich Physik der Technischen Universität Darmstadt zur Erlangung des Grades eines Doktors der Naturwissenschaften (Dr. rer. nat.) genehmigte Dissertation von **Dominik Pfeiffer** Tag der Einreichung: 24.06.2025, Tag der Prüfung: 16.07.2025

Gutachten: Prof. Dr. Gerhard Birkl
 Gutachten: Prof. Dr. Enno Giese

Technische Universität Darmstadt, Darmstadt



Novel Techniques for Atom Trapping and Large-Momentum-Transfer Atom Interferometry Neuartige Techniken für Atomfallen und Atominterferometer mit hohem Impulsübertrag

Accepted doctoral thesis by Dominik Pfeiffer

1st reviewer: Prof. Dr. Gerhard Birkl 2nd reviewer: Prof. Dr. Enno Giese

Date of submission: 24.06.2025 Date of thesis defense: 16.07.2025

Technische Universität Darmstadt, Darmstadt

Bitte zitieren Sie dieses Dokument als: URN: urn:nbn:de:tuda-tuprints-311450

URL: https://tuprints.ulb.tu-darmstadt.de/31145 DOI: https://doi.org/10.26083/tuprints-00031145 Jahr der Veröffentlichung auf TUprints: 2025

Dieses Dokument wird bereitgestellt von tuprints, E-Publishing-Service der TU Darmstadt https://tuprints.ulb.tu-darmstadt.de tuprints@ulb.tu-darmstadt.de



Die Veröffentlichung steht unter folgender Creative Commons Lizenz: Namensnennung – Nicht kommerziell – Keine Bearbeitungen 4.0 International https://creativecommons.org/licenses/by-nc-nd/4.0/

This work is licensed under a Creative Commons License: Attribution–NonCommercial–NoDerivatives 4.0 International https://creativecommons.org/licenses/by-nc-nd/4.0/

Cover art: The front cover shows the collapse and revival of the interferometric visibility in a Mach–Zehnder type atom interferometer. Through an external acceleration, a time-dependent differential phase is applied to the magnetic sub-states of ⁸⁷Rb which leads to a beating of the interferometer signal resulting in this collapse and revival.

To my parents Claudia and Andreas, To my grandparents, To Thyrza

"Remember kids, the only difference between science and screwing around is writing it down."

— Adam Savage

Abstract

Matter-wave interferometry has emerged as a vital addition to high-precision measurements of fundamental constants like the gravitational constant G and the fine-structure constant G, while enabling stringent tests of foundational principles, such as the Einstein equivalence principle. Current efforts aim to extend these techniques toward inertial sensing, magnetometry and gradiometry, gravitational-wave detection and dark-matter searches through enhanced sensitivity.

This work advances these goals by experimentally implementing Bragg diffraction-based matterwave interferometers and introducing novel precision-enhancing methods, including correlated interferometer analysis techniques. The results are achieved at the ATOMICS experiment, which produces Bose–Einstein condensates (BEC) of 25000^{87} Rb atoms in an all-optical crossed dipole trap. With a $20\,\mathrm{s}$ experimental cycle and exceptional laboratory stability, the setup enables systematic exploration of various interferometric protocols and novel trapping geometries.

A key achievement is the first experimental realisation of a blue-detuned *bottle-beam* potential via conical refraction in biaxial crystals for ultracold atoms. This unique optical dipole trap confines ultracold ensembles in a three-dimensional dark focus surrounded by intensity maxima, minimising photon scattering. Numerical studies project this approach to scalable bottle-beam arrays using microlens technology, opening avenues for single-atom quantum computing architectures with extended coherence.

Central to this work is the implementation of free-space Mach–Zehnder interferometers using higher-order Bragg diffraction $n \leq 5$, combined with a novel analysis method for evaluating correlated interferometers from magnetic sublevel populations. The technique extracts differential phases induced by external magnetic field gradients through interferometric beat notes, validated against state-selective detection and ellipse-fitting methods. Complementing this, dichroic mirror pulses, a technique proposed to suppress parasitic momentum states, are experimentally demonstrated for n=3 and n=5 Bragg transitions, showcasing scalability for large momentum transfer interferometry.

Finally, a dual digital-micromirror-device system is integrated into the experiment, enabling fully configurable optical potentials. This system adiabatically generates up to four ultracold ensembles from a single thermal reservoir via dynamic dimple traps, exhibiting non-thermal expansion dynamics suggestive of incipient condensation. Future applications include high-repetition-rate BEC production for sequential interferometric measurements, bypassing the need for full experimental cycle repetition.

Collectively, these advancements expand the toolkit for quantum sensing, simulation, and metrology with ultracold atoms, while laying the groundwork for next-generation experiments in guided interferometry and atomtronic circuitry.

vii

Zusammenfassung

Materiewelleninterferometrie hat sich als wichtige Technik für Hochpräzisionsmessungen fundamentaler Konstanten wie der Gravitationskonstante G und der Feinstrukturkonstante α etabliert, während sie gleichzeitig rigorose Tests grundlegender Prinzipien wie des Einstein-Äquivalenzprinzips ermöglicht. Aktuelle Bestrebungen zielen darauf ab, diese Techniken auf Inertialsensoren, Magnetometrie und Gradiometrie, die Detektion von Gravitationswellen sowie die Suche nach Dunkler Materie durch gesteigerte Empfindlichkeit auszuweiten.

Diese Arbeit trägt zu diesen Zielen bei, indem sie experimentell Mach-Zehnder-Materiewelleninterferometer basierend auf Bragg-Beugung realisiert und neuartige Präzisionstechniken einführt, einschließlich korrelierter Interferometeranalysemethoden. Die Ergebnisse wurden mit dem ATOMICS-Experiment erzielt, das Bose-Einstein-Kondensate (BEC) aus $25000\,^{87}$ Rb-Atomen in einer rein optischen gekreuzten Dipolfalle erzeugt. Mit einem experimentellen Zyklus von $20\,\mathrm{s}$ und außergewöhnlicher Laborstabilität ermöglicht der Aufbau systematische Untersuchungen interferometrischer Protokolle und Fallengeometrien.

Ein zentrales Ergebnis ist die erstmalige experimentelle Realisierung eines blauverstimmten *Bottle-Beam*-Potentials mittels konischer Refraktion in biaxialen Kristallen. Diese einzigartige optische Dipolfalle begrenzt ultrakalte Ensembles in einem dreidimensionalen Dunkelfokus, umgeben von Intensitätsmaxima, und minimiert dabei die Photonenstreuung. Numerische Studien erweitern diesen Ansatz auf skalierbare Bottle-Beam-Arrays mittels Mikrolinsentechnologie, was Perspektiven für Einzelatom-Quantencomputing-Architekturen bei geringen Streuraten eröffnet.

Ein weiterer Kern dieser Arbeit ist die Implementierung freier Mach–Zehnder-Interferometer mit Bragg-Beugung höherer Ordnung $(n \leq 5)$, kombiniert mit einer neuartigen Analysemethode zur Entkopplung korrelierter Interferometer aus magnetischen Unterzuständen. Die Technik extrahiert durch interferometrische Schwebungen Differenzphasen, die durch externe Magnetfeldgradienten induziert werden, und validiert diese mittels zustandsselektiver Detektion und Ellipsenanpassungsmethoden. Ergänzend werden theoretisch vorgeschlagene dichroitische Spiegelpulse zur Unterdrückung parasitärer Impulszustände experimentell für n=3 und n=5 Bragg-Übergänge demonstriert, was die Skalierbarkeit für Interferometrie mit großem Impulstransfer belegt.

Abschließend wird ein zweikanaliges digitales Mikrospiegelsystem in den Aufbau integriert, das vollständig konfigurierbare optische Potentiale ermöglicht. Dieses System erzeugt adiabatisch bis zu vier ultrakalte Ensembles aus einem thermischen Reservoir via dynamischer Dimple-Fallen, wobei nicht thermische Ausdehnungsdynamiken auf beginnende Kondensation hindeuten. Zukünftige Anwendungen umfassen die Erzeugung von BECs mit hoher Wiederholrate für sequenzielle interferometrische Messungen, ohne jeweils den vollständigen experimentellen Zyklus wiederholen zu müssen.

Zusammengenommen erweitern diese Fortschritte den Werkzeugkasten für Quantensensorik, -simulation und -metrologie mit ultrakalten Atomen und legen die Grundlage für zukünftige Experimente in geführter Interferometrie und atomtronischer Schaltkreistechnologie.

ix

Contents

The	ATOMIOO	
	ATOMICS experiment	5
2.1.	Basics	5
		5
		6
2.2.		8
		9
		10
2.3.	1	12
	1	13
		14
2.4.		20
		20
		20
		21
	2.4.4. Bragg-diffraction laser system	23
Dipo	le potentials based on conical refraction	27
-	•	28
		31
		31
		33
		37
		46
3.3.		49
		49
		54
3.4.		56
Aton	n Interferemetry with Bragg diffraction	57
		58
7.1.		58
		61
4.9	-	66
4.2.	•	67
4.0	· · · · · · · · · · · · · · · · · · ·	68
4.3.		70
		73
		83
	4.3.3. Summary	88
	2.3. 2.4. Dipo 3.1. 3.2. 3.4. Atom 4.1. 4.2.	2.1.1. Gaussian laser beams 2.1.2. Optical dipole potentials 2.2. Bose–Einstein condensation 2.2.1. Non-interacting Bose gas in harmonic traps 2.2.2. Interacting Bose gas in harmonic traps 2.2.2. Interacting Bose gas in harmonic traps 2.3. Experimental realisation at the ATOMICS experiment 2.3.1. Experimental control software 2.3.2. Evaporative cooling in all-optical crossed-dipole trap 2.4. Laser systems 2.4.1. Spectroscopy laser 2.4.2. MOT laser 2.4.3. Dipole-trap laser systems 2.4.4. Bragg-diffraction laser system Dipole potentials based on conical refraction 3.1. Fundamentals of conical refraction (CR) 3.2. The CR dark focus as bottle-beam trap 3.2.1. Properties of the dark focus 3.2.3. 3D trapping of ultracold ⁸⁷ Rb atoms in the CR dark focus 3.2.4. Improving the bottle-beam trap 3.3. Conical refraction with microlens arrays 3.3.1. Theoretical investigations 3.3.2. Experimental realisation of a dark-focus array 3.4. Summary Atom Interferometry with Bragg diffraction 4.1. Fundamentals 4.1.2. Experimental realisation 4.2. Mach-Zehnder interferometry with Bragg diffraction 4.2.1. Fundamentals of Mach-Zehnder atom interferometers 4.2.2. Statistical analysis 4.3. Phase-stable summation of interferometers 4.3.1. First-order Mach-Zehnder interferometer 4.3.2. Third-order Mach-Zehnder interferometer

	4.4. Dichroic mirror pulses	89 98
5.	Digital-micromirror-device potentials for ultracold ensembles	99
	5.1. Characterisation of the DMD system	100
	5.2. Bose–Einstein condensation in DMD potentials	103
	5.2.1. Adiabatic generation of Bose-Einstein condensates	104
	5.3. Summary	115
6.	Discussion and future perspectives	117
A.	ATOMICS setup supplementary material	121
В.	Conical refraction supplementary material	123
C.	Bragg diffraction supplementary material	127
D.	DMD potentials supplementary material	131
Ε.	Python environment	133
F.	List of publications	135
G.	Supervised theses	137
Re	eferences	139

Acronyms

AOM acousto-optical modulator

ATOMICS Atom Optics with Micro Structures

AWG arbitrary waveform generator

BC biaxial crystal

BEC Bose–Einstein condensate

BKB Belskii–Khapalyuk–Berry

CCD charge-coupled device

CDT crossed dipole trap

COM centre of mass

CR conical refraction

DDS direct digital synthesis

DMD digital micromirror device

DMP dichroic mirror pulse

ECDL external-cavity diode laser

FWHM full width at half maximum

GPE Gross–Piteavskii equation

GPIB general purpose interface bus

LMT large-momentum-transfer

LWG linear waveguide

MLA microlens array

MOPA master oscillator power amplifier

MOT magneto-optical trap

MTS modulation-transfer spectroscopy

MZI Mach-Zehnder interferometer

NA numerical aperture

PBS polarising beam splitter

PDF probability density function

RF radio frequency

RPI red-pitaya intensity stabilisation

SLM spatial light modulator

TA tapered amplifier

TBP time-bandwidth product

Ti:Sa titanium:sapphire

TOF time of flight

TTL transistor-transistor logic

1. Introduction

Interferometric measurement methods, exploiting the wave nature and coherence of light, are a cornerstone of fundamental physics and metrology. From the failed attempt to prove the existence of an ether, a medium in which electromagnetic waves were believed to propagate, by A. Michelson and E. Morley [1], to modern implementations such as gravitational wave detectors like Advanced LIGO and Virgo [2, 3], interferometry has continually pushed the boundaries of precision measurements. Moreover, optical-fibre Sagnac interferometers have become essential tools for inertial sensing and other phenomena such as electric currents [4]. The prediction from L. de Broglie that every massive particle can be associated with a wave-like behaviour, and its experimental confirmation by C. Davisson and L. Germer through the scattering of electrons off a nickel crystal, introduced a new research field studying matter-wave interference [5, 6]. The typically much shorter wavelengths associated with massive particles promise orders of magnitude improvements in precision compared to interferometric measurements conducted with light. Technical advances have enabled matter-wave interferometry with electrons, neutrons, atoms, and even large, complex molecules [7–9].

A key requirement for the successful and reliable realisation of matter-wave interferometers is a source of coherent matter waves, analogous to a laser for light-based interferometers. Bose–Einstein condensates, a state of matter predicted by S. Bose and A. Einstein, are dominated by the wave nature of particles and offer an excellent medium for matter-wave interferometers due to their predicted large coherence length despite the inter-particle interactions [10]. To achieve this exotic quantum state, atoms must be cooled close to absolute zero, such that the de Broglie wavelength of an individual particle, inversely proportional to the temperature, becomes much larger than the interatomic distance.

The development of laser-cooling techniques, pioneered by W. D. Phillips, S. Chu, and C. Cohen-Tannoudji, work recognised with the 1997 Nobel Prize, overcame the challenge of providing ultracold atomic ensembles [11–15]. Despite this tremendous improvement, an additional cooling method had to be implemented to cool atoms below the critical temperature for condensation. Two research groups, one led by E. Cornell and C. Wieman at the University of Colorado Boulder and the other one led by W. Ketterle at MIT, successfully used forced evaporative cooling in magnetic traps to achieve Bose–Einstein condensation of rubidium (Cornell and Wieman) and sodium (Ketterle) [16, 17]. This achievement earned them the 2001 Nobel Prize in Physics [18].

Further advances in laser technology made Bose–Einstein condensation in all-optical dipole traps possible, reducing the complexity of experimental setups associated with magnetic traps [19]. The dipole interaction between neutral atoms and laser light remains a vital tool for the manipulation of ultracold atomic ensembles such as Bose–Einstein condensates [20].

These advances in the preparation of ultracold atomic clouds consequently led to improvements in the field of matter-wave interferometry. The realisation of Raman or Bragg diffraction of atomic ensembles with gratings generated by interfering laser beams enables precise control over internal and external degrees of freedom, such as the population of hyperfine-structure and momentum states [21]. This can be used to implement interferometer schemes such as Mach–Zehnder or Sagnac interferometers, similar to their optical counterparts [22–24].

1

Atomic interferometers based on these techniques have been used to measure, for example, the fine-structure constant α [25, 26], the gravitational acceleration g [23], and the Einstein equivalence principle [27] with unprecedented precision. Current efforts include the investigation of atom interferometers in microgravity [28, 29] and in space [30–32], as well as the implementation of very-long-baseline atom interferometers for gravitational wave detection [33, 34]. Moreover, efforts to increase the sensitivity of atom interferometers include the development of large-momentum-transfer techniques [26, 35–37].

Increasing the interrogation time and by that sensitivity of the interferometer can be realised in microgravity environments, for example in free-falling experimental setups, atomic fountains, or by use of external guiding potentials [22, 23, 29, 38–40].

Guided interferometers can be realised by utilising external potentials generated by e. g. conical refraction or digital micromirror devices. Conical refraction, initially described by W. Hamilton, generating circular light fields with low-intensity regions produces potentials with reduced spontaneous scattering, making them ideal for high-precision measurements [41–46]. To realise arbitrary external guiding potentials, a multitude of techniques has been developed, including the use of digital micromirror devices, which offer immense control over the shape, depth, and dynamics of two-dimensional potentials [47, 48]. Other approaches include the use of spatial light modulators, painted potentials [49, 50]. Additionally, the reconfigurability of potentials generated by digital micromirror devices in combination with Bose–Einstein condensates as coherent matter-wave sources can be used to realise complex circuit-like structures, resembling electronic circuits, giving the field its name Atomtronics [40, 51, 52]. The idea behind such atomtronic circuits is, similar to atom interferometers, to use coherent matter-waves to realise measurements of rotation or acceleration [53–55].

The main focus of this work is the investigation and implementation of techniques aimed towards the improvement of large-momentum transfer atom interferometry. In the future, external guiding potentials can be used to extend interrogation times, overcoming the limitations imposed by the free fall of atoms in space.

This work has been carried out at the Atom Optics with Micro Structures (ATOMICS) experiment of the Atoms—Photons—Quanta (APQ) group at the Institute for Applied Physics (IAP), Technische Universität Darmstadt. A long-term goal of the ATOMICS project is the implementation of a continuously operating mode, generating multiple Bose—Einstein condensates in a pulsed fashion as a supply for, e. g. guided atom interferometers. The versatility of the ATOMICS experiment makes it an ideal setup for the combination of multiple techniques, showcasing proof-of-principle measurements, and the realisation of new methods, more specialised machines are unable to do.

In addition to this introduction, this work is organised as follows:

Chapter 2 introduces the ATOMICS experiment and presents the necessary fundamental background to navigate the experiments discussed in the following chapters. A brief introduction to Bose–Einstein condensation and optical dipole potentials is given. In addition, the basic operation of the all-optical process for the generation of BECs at the ATOMICS experiment is described.

Chapter 3 discusses optical potentials generated by a special case of birefringence in biaxial crystals, called conical refraction (CR). A general introduction to CR is given, with particular attention to the dark-focus regime. This regime is discussed in detail and is experimentally used as a bottle-beam potential to trap an ultracold ensemble of rubidium atoms. Finally, the combination of the dark-focus regime in CR with microlens arrays is numerically investigated, aimed towards large arrays of bottle beams for, e. g. quantum information processing with

single neutral atoms.

Chapter 4 is dedicated to atomic Bragg diffraction, a technique commonly used to implement atomic interferometers. A brief introduction to the theoretical concepts of atomic Bragg diffraction is given, combined with its experimental implementation at the ATOMICS experiment. Higher-order Bragg diffraction is experimentally realised and used to investigate Mach–Zehnder type atom interferometers (MZI). Various evaluation methods are presented and discussed for first- and third-order MZIs. State-selective measurements of the magnetic sub-states reveal the existence of a magnetic field gradient, which is discussed in detail using the presented evaluation methods. Finally, a new method for the generation of dichroic mirror pulses for MZIs is experimentally implemented, reducing the impact of parasitic paths in large-momentum-transfer (LMT) interferometers.

Chapter 5 introduces a new optical setup centred around two digital micromirror devices (DMD) used to generate arbitrary two-dimensional dipole potentials. This setup is built to provide external guiding potentials in combination with an additional light sheet potential, currently limited by corrugations of said light sheet. To progress towards a semi-continuous generation of BECs at the ATOMICS experiment, potentials supplied by the DMD setup are combined with a linear waveguide to implement the adiabatic generation of BECs from a thermal reservoir in dimple potentials. Single, double, and quadruple dimple setups are realised, and the free-space expansion of the produced ensembles is investigated. In addition to stationary potentials, dynamical potentials are implemented via the DMDs to generate successive ensembles from the same reservoir.

Chapter 6 summarises the experimental results of this work and discusses future perspectives for the experiments towards the realisation of guided-atom interferometers.

3

2. The ATOMICS experiment

The ATOMICS experiment provides a versatile platform for the experimental exploration of ultracold quantum gases, with a particular focus on Bose–Einstein condensates (BECs) confined in optical potentials [45, 46, 56, 57]. Advanced light-shaping techniques such as conical refraction (CR) and digital micromirror devices (DMDs) can be used and combined with atom interferometric methods. In this chapter, an overview of the essential experimental and theoretical concepts underpinning the manipulation of ultracold atoms at the ATOMICS experiment is provided.

The chapter starts by outlining the fundamental principles of laser cooling and optical trapping with a particular emphasis on the properties of Gaussian laser beams and the formation of optical dipole potentials. Furthermore, the theoretical framework for Bose–Einstein condensation in harmonic potentials is introduced for both the non-interacting and interacting regime, highlighting characteristic signatures of condensation such as critical transition temperatures and expansion properties of BECs. Finally, the experimental implementation at ATOMICS in its current form is presented, including the experiment infrastructure, evaporative cooling protocols and detection methods, providing a foundation for the detailed discussion of experimental results in the following chapters.

2.1. Basics

2.1.1. Gaussian laser beams

Gaussian laser beams emerge as the fundamental solution of the paraxial Helmholtz equation leading to the TEM_{00} mode of optical resonators. Hence, the electric field of an axially-symmetric beam with $r^2 = x^2 + y^2$, emitted from a laser resonator or an optical fibre can be described by

$$\mathbf{E}(r,z) = \frac{E_0}{\sqrt{1 + \left(\frac{z}{z_{\rm R}}\right)^2}} \exp\left(-\frac{r^2}{w_0^2 \left[1 + \left(\frac{z}{z_{\rm R}}\right)^2\right]}\right) \exp\left(\frac{\mathrm{i}kr^2}{2R(z)}\right) \exp\left(\mathrm{i}[kz - \Phi]\right) \mathbf{e} \qquad (2.1)$$

where E_0 denotes the electric field amplitude with ${\bf e}$ the unit polarisation vector, w_0 the minimal waist of the beam and $z_{\rm R}=\pi w_0^2/\lambda$ the Rayleigh length. For linear polarised light along the x-direction, the polarisation vector in Jones formalism is given by ${\bf e}={\bf e}_x=(1,0)$ [58]. The wavelength λ determines the wave vector $k=2\pi/\lambda$ of the beam. In addition to contributions that modify the electric field strength, there are also contributions that describe the local phase of the field. The curvature of the wavefronts is given by $R(z)=z[1+(z_{\rm R}/z)^2]$ and Φ gives the Gouy phase [59].

In most cases it is sufficient to discard the phase contributions and deal with the amplitude part of the electric field only. An exception arises in cases where this specific phase contribution is essential for accurately describing the interference effects of multiple beams, such as in the Talbot effect discussed later in Section 3.3.1 or Bragg diffraction discussed in Chapter 4 [60]. For the application in cold-atom trapping and manipulation with large detuning on the other hand, typically it is sufficient to describe the intensity distribution of Gaussian beams given by the square of the absolute value of the electric field

$$I(r,z) = \frac{2P}{\pi w_0^2 \left[1 + \left(\frac{z}{z_R}\right)^2 \right]} \exp\left(-\frac{2r^2}{w_0^2 \left[1 + \left(\frac{z}{z_R}\right)^2 \right]} \right)$$
(2.2)

where $P \propto |E_0|^2$ is the total optical power carried by the beam. In this description it is convenient to see that only λ , w_0 , and $z_{\rm R}$ are sufficient to characterise the beam completely with $z_{\rm R}$ denoting the length over which the beam waist $w(z) = w_0 \sqrt{1 + (z/z_{\rm R})^2}$ expands by $\sqrt{2}$ hence the peak intensity $I_0 = 2P/\pi w_0$ is halved.

Finally, a remarkable property of Gaussian beams is that they can be propagated and manipulated by optical elements while maintaining their fundamental characteristics. A Gaussian beam of initial waist w_0 can be focussed by a lens of focal length f producing again a Gaussian beam of waist w'. Assuming the system can be described in the paraxial approximation, the waist of the focused Gaussian beam is located in the focal plane of the lens and given by $w' = \lambda f/\pi w_0^2$ when the waist of the initial Gaussian beam is located at the aperture of the lens [61, Chap. 8].

Focused Gaussian beams play a major role in cold-atom trapping and manipulation ranging from large optical dipole traps in single-beam or crossed-beam setups to microlens arrays producing arrays of focused beams for single neutral atom trapping [62–65].

2.1.2. Optical dipole potentials

The ability to manipulate atoms through their interaction with light represents one of the major advances in the field of ultracold atoms and Bose–Einstein condensation. Light provided by lasers can be used to reduce their momentum by scattering photons hence reducing the kinetic energy and effectively cooling the atoms [12, 20, 21, 66]. Radiation pressure arising from the stimulated absorption of photons in a light beam tuned near the atomic transition frequency ω_0 forms the fundamental principle of laser cooling, which is universally employed as the initial magneto-optical trap (MOT) stage in every cold-atom laboratory.

Besides the reduction of kinetic energy by the absorption and emission of photons, far-detuned light can be used to trap atoms in potentials generated by the dipole interaction of atoms with light itself. In the following discussion, the central equations are presented to offer a general understanding of optical dipole potentials. Consider a two-level atomic system comprising ground state $|g\rangle$ and excited state $|e\rangle$, separated by an energy gap $\hbar\omega_0$, coupled to a monochromatic field of frequency $\omega_{\rm L}$. The electric field induces a dipole moment in the atom, oscillating at the driving frequency of the laser leading to an interaction potential U that is proportional to the intensity of the light field $|U| \propto I$. Hence, Gaussian beams as detailed in Section 2.1.1 with intensity gradients in both radial and axial directions create a position-dependent potential, leading to a conservative force $F = -\nabla U$.

Expanding this description to multi-level systems such as neutral alkali atoms, the following expression can be derived for the optical dipole potential

$$U(\mathbf{r}) = \tilde{U}_0 I(\mathbf{r}) \tag{2.3a}$$

$$\tilde{U}_{0} = -2 \cdot \frac{\pi c^{2} \Gamma_{D2}}{2\omega_{D2}^{3}} \left(\frac{1}{\omega_{L} - \omega_{D2}} + \frac{1}{\omega_{L} + \omega_{D2}} \right) +
-1 \cdot \frac{\pi c^{2} \Gamma_{D1}}{2\omega_{D1}^{3}} \left(\frac{1}{\omega_{L} - \omega_{D1}} + \frac{1}{\omega_{L} + \omega_{D1}} \right)$$
(2.3b)

where Γ_{Di} denotes the natural linewidth of the respective D-line with transition frequencies ω_{Di} [20, 67]. Here, fast rotating terms $\omega_{Di} + \omega_{L}$ can been discarded under the assumption that the detuning

$$\Delta = \omega_{\rm L} - \omega_0 \tag{2.4}$$

is small compared to the atomic transition frequencies $|\Delta| \ll \omega_{Di}$, applying the rotating wave approximation. The 2:1 weighting ratio between the D2 and D1 lines in dipole potential calculations arises from differences in their oscillator strengths for the relevant atomic transitions [20]. Alongside the optical dipole potential, spontaneous photon scattering may also take place, a process that is crucial for optical cooling of atoms, but is undesirable in optical traps designed for storing ultracold atoms without optical heating or decoherence. Again for neutral alkali atoms, the spontaneous scattering rate can be described by

$$\Gamma_{\rm Sc}(\mathbf{r}) = \tilde{\Gamma}_0 I(\mathbf{r})$$
 (2.5a)

$$\tilde{\Gamma}_{0} = 2 \cdot \frac{\pi c^{2} \Gamma_{D2}^{2}}{2\hbar \omega_{D2}^{3}} \left(\frac{\omega_{L}}{\omega_{D2}}\right)^{3} \left(\frac{1}{\omega_{L} - \omega_{D2}} + \frac{1}{\omega_{L} + \omega_{D2}}\right)^{2} + \\ 1 \cdot \frac{\pi c^{2} \Gamma_{D1}^{2}}{2\hbar \omega_{D1}^{3}} \left(\frac{\omega_{L}}{\omega_{D1}}\right)^{3} \left(\frac{1}{\omega_{L} - \omega_{D1}} + \frac{1}{\omega_{L} + \omega_{D1}}\right)^{2}.$$
(2.5b)

From these equations, the general scaling of the dipole potential U and scattering rate Γ_{Sc} can be deduced

$$U \propto \frac{I}{\Lambda}, \quad \Gamma_{\rm Sc} \propto \frac{I}{\Lambda^2}.$$
 (2.6)

These scaling relations reveal that increasing the intensity to offset a larger detuning Δ while maintaining a constant dipole potential results in reduced scattering rates, a desirable outcome for ultracold atom systems.

Generally, optical dipole potentials can be discriminated by the sign of the detuning Δ . For the remainder of this work, the convention red-detuned $\Delta < 0$ and blue-detuned $\Delta > 0$ optical dipole potentials is used. Blue-detuned optical potentials trap atoms in regions of low intensity while red-detuned potentials trap atoms in regions of high intensity. In Fig. 2.1, both scenarios are visualised using an intensity distribution of a red-detuned Gaussian beam [see Eq. (2.2)] and a blue-detuned potential based on the conical refraction [see Chapter 3]. For both potentials, a thermal atomic density distribution is visualised as purple dots.

Harmonic approximations provide a convenient framework for describing external potentials used to guide and manipulate atoms, and Gaussian beams remain the most widely employed optical potentials in this context. Here, the trapping frequencies for a standard Gaussian beam configuration and an atom of mass m are given:

$$\omega_{r,G} = \sqrt{\frac{8\tilde{U}_0 P}{\pi m w_0^4}}, \quad \omega_{z,G} = \sqrt{\frac{4\tilde{U}_0 P \lambda^2}{\pi^3 m w_0^6}} = \sqrt{\frac{4\tilde{U}_0 P}{\pi m w_0^2 z_R^2}}.$$
 (2.7)

Similar expressions can be derived for a large class of potential forms, allowing for a convenient way to compare potentials to each other. At the ATOMICS experiment, the main optical dipole

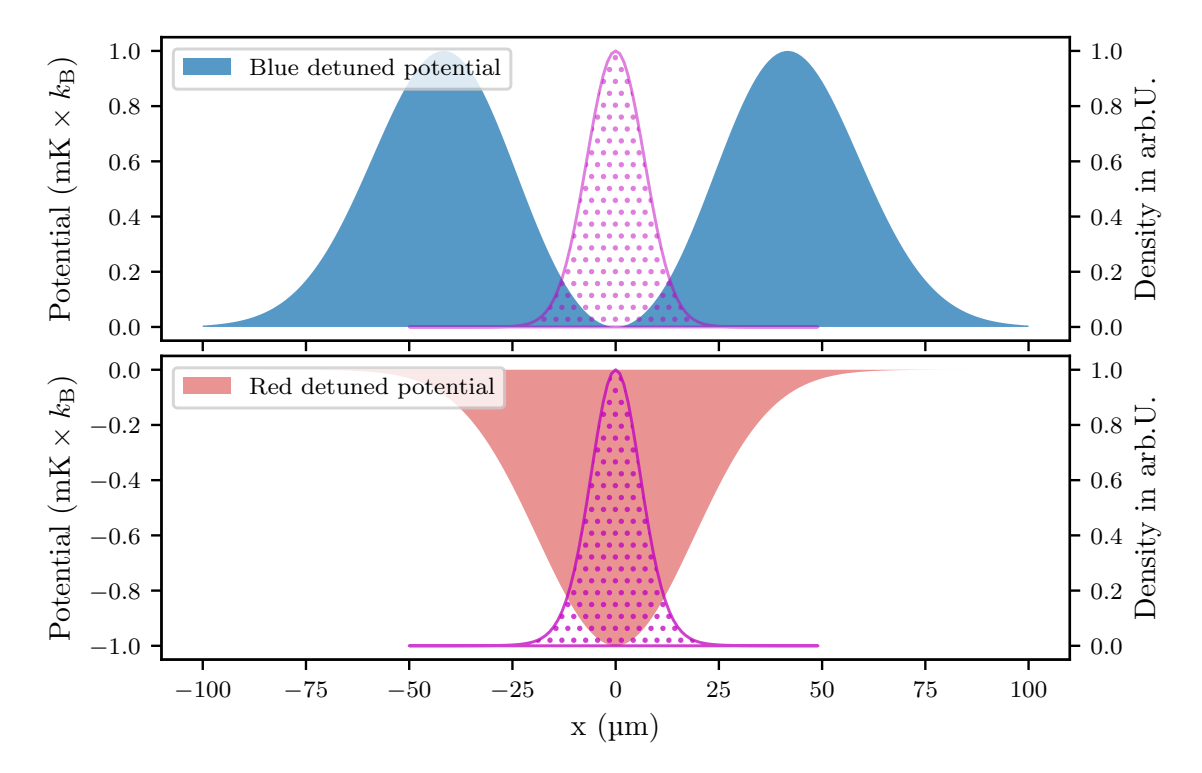


Fig. 2.1.: (top) Blue-detuned dipole potential based on a intensity distribution generated by the CR [see Chapter 3] with a thermal distribution depicted as dotted area trapped in the potential minimum (intensity minimum). (bottom) Red-detuned counterpart as generated by a focused Gaussian beam with the atomic distribution being trapped in the potential minimum (intensity maximum).

potential used to produce the BEC consists of two Gaussian beams, intersecting perpendicular. For a convenient description of potential depths, the recoil energy $E_{\rm rec}$ and recoil frequency $\omega_{\rm rec}$ are introduced as

$$E_{\text{rec}} = \hbar \omega_{\text{rec}} = \hbar \frac{\hbar k_{\text{D2}}^2}{2m_{87}} = \frac{k_{\text{B}}}{2} 362 \,\text{nK} = 2.5 \times 10^{-30} \,\text{J}$$
 (2.8)

with the Boltzmann constant $k_{\rm B}$, the wave number of the D2-line of $^{87}{\rm Rb}~k_{\rm D2}=2\pi/\lambda_{\rm D2}$ at $\lambda_{\rm D2}=780.2\,{\rm nm}$ and the mass of $^{87}{\rm Rb}~m_{87}$ [67].

2.2. Bose-Einstein condensation

Bose–Einstein condensation, first predicted by Satyendra Nath Bose and Albert Einstein in 1924–1925, represents a quantum phase transition where a macroscopic population of bosons occupies the same ground state of an external potential at ultralow temperatures. This phenomenon arises from the interplay between statistical mechanics and wave function symmetry: bosons, unlike fermions, are not restricted by the Pauli exclusion principle, enabling collective occupation of the lowest energy state when the thermal de Broglie wavelength $\lambda_{\rm dB,th} = \sqrt{2\pi\hbar^2/(mk_{\rm B}T)}$ exceeds interparticle distances with $k_{\rm B}$ the Boltzman constant, T the temperature and \hbar the reduced Planck constant. The critical temperature for condensation scales as $T_{\rm crit} \propto n^{2/3}/m$, where n is the density and m the mass [68, Chap. 3]. The experimental realisation of BECs in dilute atomic gases represented a major breakthrough, allowing for

precise control of interactions through Feshbach resonances and optical trapping techniques [18]. The condensate dynamics are governed by the Gross-Pitaevskii equation, a non-linear Schrödinger equation incorporating external potentials and self-interactions.

Key hallmarks include superfluidity, quantised vortices, and matter-wave interference-phenomena bridging quantum mechanics and many-body physics [69–71].

In this section, a fundamental framework for BECs is presented, highlighting key aspects of the condensation such as the critical temperature and the inversion of the aspect ratio, both clear indicators of Bose–Einstein condensation. Furthermore, the experimental realisation at the ATOMICS experiment is discussed.

2.2.1. Non-interacting Bose gas in harmonic traps

In terms of the grand-canonical ensemble, the average occupation of the single particle state i with energy ϵ_i can be described by

$$\bar{n}_i = \frac{1}{\exp\left(\beta(\epsilon_i - \mu)\right) - 1} \tag{2.9}$$

where $\beta=1/k_{\rm B}T$ with temperature of the ensemble T and $\mu<0$ is the chemical potential, fixed by the normalisation to the total particle number $N=\sum_i \bar{n}_i$ [68, Chap. 10]. Assuming a three-dimensional harmonic potential, e. g. given by a Gaussian beam in harmonic approximation as discussed in Section 2.1.1, of the form

$$U(\mathbf{r}) = \frac{m}{2} \left(\omega_x^2 x^2 + \omega_y^2 y^2 + \omega_z^2 z^2 \right)$$
 (2.10)

with ω_i being the trapping frequencies. For this case, the single-particle ground-state wave function of the Hamiltonian $H = p^2/2m + U(\mathbf{r})$ is given by

$$\Psi_0(\mathbf{r}) = \left(\frac{m\omega_{\text{ho}}}{\pi\hbar}\right)^{3/4} \exp\left(-\frac{m}{2\hbar} \left[\omega_x x^2 + \omega_y y^2 + \omega_z z^2\right]\right)$$
(2.11)

where $\omega_{\text{ho}}=(\omega_x\omega_y\omega_z)^{1/3}$ is the geometric average of the trapping frequencies [68, Chap. 10]. At finite temperatures, most particles occupy excited states, with only a small fraction in the ground state Ψ_0 . Bose–Einstein condensation occurs, when the chemical potential approaches the ground-state energy $\mu\nearrow\epsilon_0$, leading to a macroscopic occupation of the ground state. By calculating the thermal population N_T , the critical temperature is derived as

$$k_{\rm B}T_{\rm crit} = \hbar\omega_{\rm ho} \left(\frac{N}{\zeta(3)}\right)^{1/3}$$
 (2.12)

where $\zeta(x)$ is the Riemann zeta function and $T_{\rm crit}$ is the critical temperature, defined by $N_T(T_{\rm crit})=N$ [68, Chap. 11]. Normalising the total atom number $N=N_T+N_0$, the condensate fraction follows

$$\frac{N_0}{N_T} = 1 - \left(\frac{T}{T_{\text{crit}}}\right)^3 \tag{2.13}$$

describing the growth of N_0 as T drops below the critical temperature T_{crit} .

2.2.2. Interacting Bose gas in harmonic traps

The previous section discussed Bose–Einstein condensation for non-interacting particles in harmonic traps, yielding the critical temperature $T_{\rm crit}$ as a benchmark for condensation. However, experimental systems invariably involve interactions, necessitating a treatment of interatomic forces. These interactions are well captured by s-wave scattering, leading to the Gross–Piteavskii equation (GPE)

$$i\hbar \frac{\partial}{\partial t} \Psi_0(\mathbf{r}, t) = \left(-\frac{\hbar^2 \nabla^2}{2m} + U(\mathbf{r}, t) + g|\Psi_0(\mathbf{r}, t)|^2 \right) \Psi_0(\mathbf{r}, t)$$
 (2.14)

where $g=4\pi\hbar^2a_{\rm sc}/m$ quantifies the interaction strength via the s-wave scattering length $a_{\rm sc}$ [68, Chap. 11]. For repulsive interactions g>0, a stable BEC can be produced leading to an expansion and preventing the collapse of the cloud. The non-linear term $g|\Psi_0({\bf r},t)|^2$ in the GPE represents the mean field energy, which arises from averaging over all pairwise interactions and is commonly referred to as the mean field. Even for weakly interacting bosons, this energy dominates the kinetic energy in dense regions of the BEC. The balance between mean field energy, external potential $U({\bf r})$ and kinetic energy can be used to define distinct regimes. When interactions dominate, quantified by $Na_{\rm sc}/a_{\rm ho}\gg 1$, the kinetic energy term $-\hbar^2\nabla^2/2m$ in the GPE becomes negligible. This defines the Thomas–Fermi (TF) regime, where the condensate density adopts the inverted potential profile

$$n_{\rm TF} = \frac{1}{g}(\mu_{\rm TF} - U(\mathbf{r})) \quad \text{with} \quad \mu_{\rm TF} = \frac{\hbar \omega_{\rm ho}}{2} \left(\frac{15Na_{\rm sc}}{a_{\rm ho}}\right)^{2/5} \tag{2.15}$$

valid for $\mu_{\rm TF}>U({\bf r})$ and $n_{\rm TF}=0$ otherwise. Here, $a_{\rm ho}=\sqrt{\hbar/(m\omega_{\rm ho})}$ is the harmonic oscillator length. For harmonic potentials, $n_{\rm TF}({\bf r})$ forms a parabolic density distribution bound by the Thomas–Fermi radii

$$R_i = \sqrt{\frac{2\mu_{\rm TF}}{m\omega_i^2}} = a_{\rm ho} \left(\frac{15Na_{\rm sc}}{a_{\rm ho}}\right)^{1/5} \frac{\omega_{\rm ho}}{\omega_i}.$$
 (2.16)

The healing length

$$\xi = \sqrt{\frac{\hbar^2}{2mgn}},\tag{2.17}$$

defines the shortest scale over which density variations equilibrate. In the Thomas–Fermi regime ($\xi \ll R_{\rm TF}$) the condensate behaves hydrodynamically, suppressing density fluctuations. For the validity of the GPE, a dilute gas is assumed $n|a_{\rm sc}|^3 \ll 1$, where binary collisions dominate and the thermal component is negligible. This framework can be used to accurately predict static properties e. g. density profiles and dynamics like collective excitations in harmonically trapped BECs. In strongly interacting or low-dimensional systems, deviations arise necessitating beyond-mean field corrections.

Under adiabatic changes ($\dot{\omega}/\omega^2 \ll 1$ with $\dot{\omega} = d\omega/dt$) of the external potential $U(\mathbf{r})$, the condensate retains its shape as predicted by the Thomas–Fermi regime Eq. (2.15) without additional excitations. If the trapping potential is removed suddenly, the condensate will start to expand, converting the mean field into kinetic energy while maintaining its general shape. Hence, the Thomas–Fermi radii become time-dependent and can be described by a scaling approach using the scaling factors b(t) resulting in the time evolution

$$R_i(t) = R_i(0)b_i(t)$$
 (2.18)

with the initial values $R_i(0)$ given by Eq. (2.16) [72]. The scaling factors $b_i(t)$ obey

$$\ddot{b}_i = \frac{\omega_i^2}{b_i b_x b_y b_z} \tag{2.19}$$

with initial conditions $b_i(0)=1$ and $\dot{b}(0)=0$ [68, Chap. 12]. Rescaling time as $\tau=t\omega_x$, Eq. (2.19) becomes

$$\frac{\mathrm{d}^2}{\mathrm{d}\tau^2}b_i = \frac{\lambda_i^2}{b_i b_x b_y b_z} \tag{2.20}$$

where $\lambda_i = \omega_i/\omega_x$. Numerical solutions reveal a hallmark of BECs, the inversion of an initial aspect ratio R_i/R_j for anisotropic traps $R_i \neq R_j$ during free expansion. In contrast, a thermal cloud will isotropise $R_i/R_j \to 1$.

For the case of an axially symmetric external potential $\omega_x = \omega_y = \omega_r \neq \omega_z$ using the dimensionless time $\tau = \omega_r t$, Eq. (2.19) take the form

$$\frac{\mathrm{d}^2}{\mathrm{d}\tau^2}b_r = \frac{1}{b_r^3 b_z} \quad \text{and} \quad \frac{\mathrm{d}^2}{\mathrm{d}\tau^2}b_z = \frac{\lambda^2}{b_r^2 b_z^2}$$
 (2.21)

with aspect ratio $\lambda = \omega_z/\omega_r$. For small initial aspect ratios $\lambda \ll 1$ thus $\omega_z \ll \omega_r$, these can be solved analytically

$$b_r(\tau) = \sqrt{1 + \tau^2} \tag{2.22}$$

$$b_z(\tau) = 1 + \lambda^2 \left[\tau \arctan(\tau) - \ln(\sqrt{1 + \tau^2}) \right]$$
 (2.23)

describing the expansion in radial and axial direction. Clearly, the BEC will expand much faster along the radial direction of stronger confinement and for long expansion times the initial aspect ratio $R_r/R_z=\lambda$ will be inverted to $R_r/R_z=2/(\pi\lambda)$ for $t\to\infty$. This can be used as proof for Bose–Einstein condensation since a thermal cloud will always approach $R_r/R_z=1$ independently of the initial condition [16, 73].

2.3. Experimental realisation at the ATOMICS experiment

The ATOMICS experiment provides an ideal platform for experimental investigations of ultracold atomic ensembles, including BECs [45, 46, 56, 57, 74]. In contrast to other experimental setups, Bose–Einstein condensation is realised in an all-optical way, only utilising optical dipole potentials for the evaporation and manipulation of BECs [62]. Recently, all-optical BECs with a repetition rate of 2 Hz have been reported by Hetzel *et al.*, showing the potential of this technique for rapid BEC production [75]. In the following section, a brief overview of the current experimental implementation is given. Fig. 2.2 shows a schematic overview of the main vacuum chamber and visualises important laser beams.

The ATOMICS experiment is capable of producing a BEC of 87 Rb atoms within $20 \, \mathrm{s}$ including detection. Temperatures of typically $25 \, \mathrm{nK}$ and an atom number of $25 \, 000$ can be produced with a BEC fraction $N_0/N \geq 0.8$ [62].

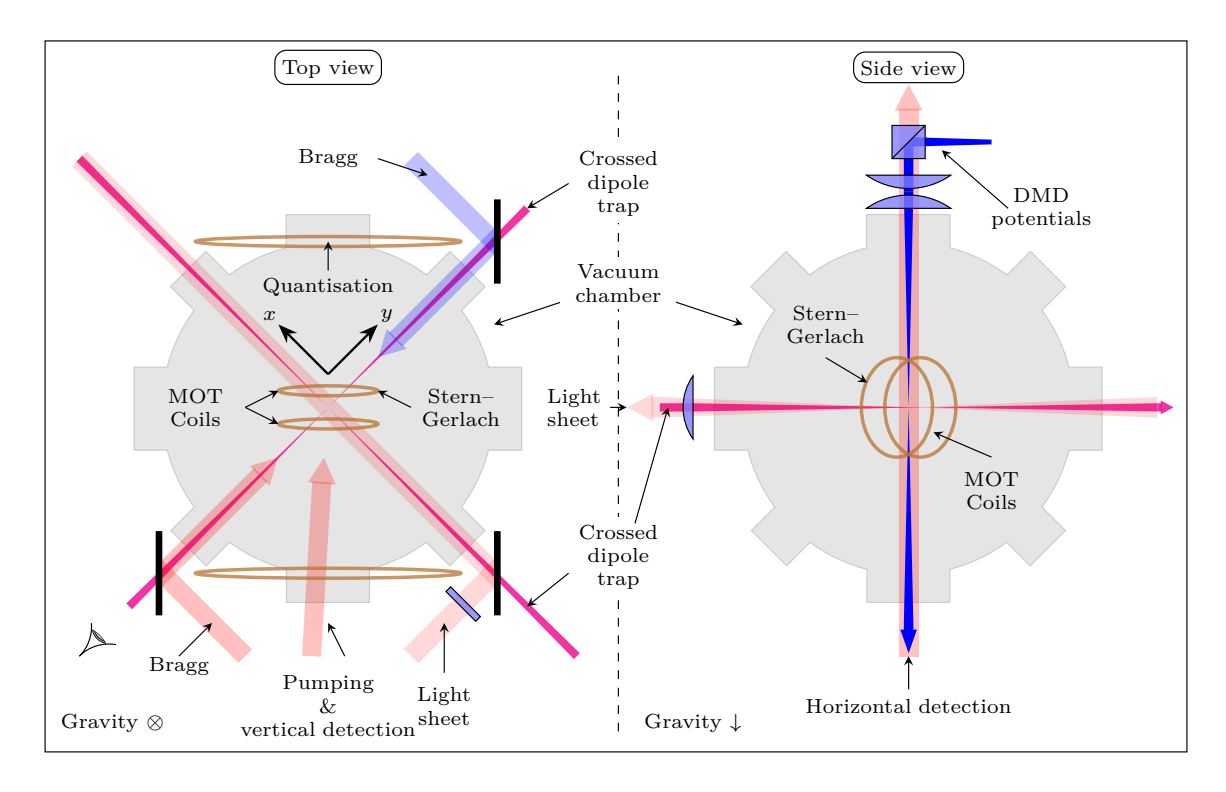


Fig. 2.2.: (left) Schematic view of the ATOMICS main vacuum chamber from the top with the main laser beams. Copper-coloured ellipses indicate the MOT coils located inside the vacuum chamber, as well as the coils that define the quantization axis for optical pumping. Blue and red arrows show the counterpropagating Bragg beams superimposed with one crossed dipole trap beam (magenta). (right) Side view of the chamber in the direction of one beam of the crossed dipole trap [see 'eye' on the left side]. Additional dipole potentials generated by e. g. the conical refraction [see Chapter 3] or the digital micromirror devices [see Chapter 5] light fields are reimaged into the vacuum chamber by achromatic lenses (top of the chamber). These are also used for the vertical detection path, reimaging the atomic plane onto the top detection camera (not shown). The oven where hot ⁸⁷Rb is produced is located to the right of the chambers connected via a differential pumping stage [74].

2.3.1. Experimental control software

In contrast to previous work at the ATOMICS experiment, a new control software has been implemented based on the *labscript suite* [76–78]. This Python-based software package is also employed in other experiments within the **APQ** group [79]. The implementation for ATOMICS was carried out as part of the master thesis of D. Derr, where a detailed description can be found [80].

Briefly summarised, the labscript suite is a powerful and extensible open-source framework designed for the composition, control, execution, and analysis of complex experimental sequences, with a primary focus on quantum science and ultracold atom research. The suite consists of three main programs, which work together to prepare, execute, and analyse experiments, as visualised in Fig. 2.3 [78]. Experimental sequences are defined in human-readable Python scripts, enabling modular design, version control (e. g. via GitHub), and straightforward reuse of experimental logic. Common elements of experimental sequences such as the MOT phase and evaporation steps at ATOMICS can be encapsulated in abstract layers, making it easy to update essential parts of the experiment without modifying each individual script.

To execute an experimental realisation (shot), the *runmanager* program compiles the experiment script, together with all chosen parameter values, into an .hdf5 file. A key advantage of this approach is the ability to investigate arbitrary combinations of experimental parameters, with *runmanager* generating a shot for each parameter set. This enables efficient exploration of n-dimensional parameter spaces; at ATOMICS, typically n=1 to 4 parameters are investigated in one measurement campaign.

Compiled shots are then queued in the BLACS program, which interfaces directly with the experimental hardware, such as the NI 6713 analogue and NI 6534 digital cards, as well as the SpinCore SP2-PB24-100-4k clock device. BLACS reads the instructions from each shot and executes them, controlling the hardware accordingly. Shots can be executed once or repeated multiple times to improve statistics, with execution continuing until manually stopped. If data acquisition devices (such as cameras) are integrated in BLACS, measurement data can be saved directly into the shots .hdf5 file. This enables the use of Lyse for automated analysis of single or multiple shots, with analysis routines again defined in Python scripts. Currently, at ATOMICS, this workflow is not fully realised due to the absence of camera integration, so acquired data is saved separately. The evaluation of experimental data is carried out using Python scripts written for each individual experiment [81–84]. The implementation of the labscript suite at ATOMICS has significantly enhanced the experiments capabilities. Automated measurement campaigns involving more than 1000 realisations and the ability to efficiently scan large, multi-dimensional parameter spaces have enabled many of the results presented in this thesis. Combined with substantial improvements in experimental hardware-including electronics, optics, and laboratory stability, measurement campaigns exceeding 12 h have become routine.

13

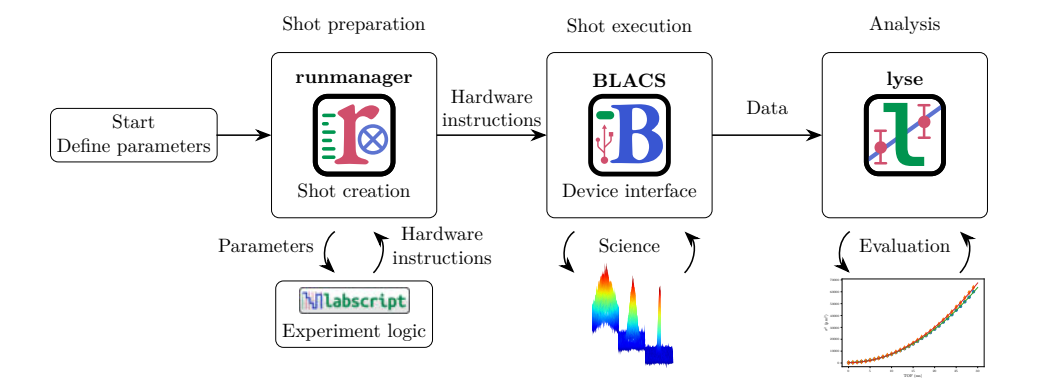


Fig. 2.3.: Schematic representation of the *labscript suite* software package and its workflow. An experiment is defined as a Python script containing all instructions for the experimental hardware. The *runmanager* compiles the script into an *.hdf5* experiment file. *BLACS* reads and executes the instructions, running one instance of the experiment (a *shot*). If experimental data is saved in the *.hdf5* file, *lyse* can be used for single- or multi-shot analysis. At ATOMICS, *lyse* is not used as data cannot currently be saved in the *.hdf5* files. (Image style inspired by [78], icons taken from [85, 86])

2.3.2. Evaporative cooling in all-optical crossed-dipole trap

In this section, the general experimental scheme to create a BEC at the ATOMICS experiment is described.

ATOMICS uses 87 Rb as the atomic species to produce BECs, which in contrast to 85 Rb has a positive s-wave scattering length of $a_{11}=100.4\,a_0$ for atoms in the $|5^2S_{1/2},F=1\rangle$ hyperfine ground states where a_0 denotes the Bohr radius [87]. Hence, with 87 Rb a stable BEC can be produced [57, 62, 74]. In Fig. A1, the hyperfine-structure of the D2-line of 87 Rb is shown with the cooling, repump and optical pumping transitions visualised. Furthermore, the stabilised operating frequencies of the MOT laser systems are included.

The 87 Rb is supplied to the experiment from an oven chamber, connected to the main vacuum chamber via a differential pumping stage, maintaining the ultra-high vacuum of 2×10^{-11} mbar to 5×10^{-11} mbar needed for Bose–Einstein condensation. In the oven chamber a constant pressure of 2×10^{-3} mbar is maintained using a turbo molecular pump Pfeiffer Vacuum TPU 240 (recently switched for a Pfeiffer Vacuum TPU 260). Glass ampoules containing 5 g to 20 g of rubidium are used to refill the oven with a typical consumption of below 5 g/a.

Resistive elements embedded within and surrounding the oven chamber are used to heat the oven to around $400\,\mathrm{K}$. This increases the vapour pressure within the oven and allows $^{87}\mathrm{Rb}$ to transfer into the main vacuum chamber, located approximately $1.5\,\mathrm{m}$ from the oven. Atoms diffuse through a differential pumping stage (diameter $3\,\mathrm{mm}$ and length $15\,\mathrm{cm}$), forming a narrow atomic beam with a high mean velocity ($\sim 300\,\mathrm{m/s}$). This velocity must be reduced to $\lesssim 50\,\mathrm{m/s}$ for efficient capture in the MOT [88, 89].

For this purpose, different methods can be utilised, such as Zeeman slowers based on magnetic field gradients, 2D-MOT setups or chirped laser cooling. At the ATOMICS experiment, the need for additional magnetic fields for Zeeman slowing is circumvented by using two frequency-chirped external-cavity diode laser (ECDL) systems. The two laser systems are frequency chirped around the $|5^2S_{1/2}, F=2\rangle \rightarrow |5^2P_{3/2}, F'=3\rangle$ (cooling) and $|5^2S_{1/2}, F=1\rangle \rightarrow |5^2P_{3/2}, F'=2\rangle$ (repump) transitions and propagate in opposite direction of the atom beam [12]. Two lasers are needed because atoms pumped into the $|5^2P_{3/2}, F'=2\rangle$

state by the cooling light can decay into the $|5^2S_{1/2},F=1\rangle$ ground state, which is inaccessible by the cooling light. The repump laser transfers atoms from this state back to the $|5^2P_{3/2},F'=2\rangle$ state via the repump transition. Since the atoms start with an initially large velocity, the lasers need to be strongly red-detuned with the respect to transition to compensate the Doppler shift $\Delta_{\rm dop}=|{\bf k}\cdot{\bf v}|$ with ${\bf k}$ the wave vector of the laser and ${\bf v}$ the velocity of the atoms. In order to keep the laser in resonance with the atoms slowing down after each scattering process, the laser detuning Δ is chirped towards smaller detuning giving this method its name, *chirp cooling* [see Fig. A1].

Atoms sufficiently slowed by the chirp cooling can be captured by the MOT built with three retro-reflective beams, with the cooling light intensity stabilised to $17.5\,\mathrm{mW}$ in each of the three beams for the MOT phase. Additionally, similar to the chirp cooling a repump laser has to be used to prevent atoms from accumulating in the $|5^2S_{1/2},F=1\rangle$ ground state. Typically, an optical power of less than $1\,\mathrm{mW}$ in two of the three beams is sufficient to prevent this accumulation. In the MOT, a minimum temperature of $T_{\mathrm{dop}}=146\,\mathrm{\mu K}$ can be reached, called the Doppler temperature limit [67]. To further decrease the temperature, a short compressed MOT stage is included with an higher magnetic field increasing the density, followed by a sub-Doppler cooling phase with larger detuning for the cooler laser and a drastically reduced intensity [90]. After the sub-Doppler cooling, typical temperatures of $20(5)\,\mathrm{\mu K}$ can be reached at the ATOMICS experiment.

The crossed dipole trap (CDT), used for the forced evaporative cooling to produce the BEC gets overlapped with the MOT starting with the compressed MOT stage, maintaining an initially high optical power of $6.5\,\mathrm{W}$ per beam to maximise the capture rate. At the end of the sub-Doppler phase, the repump laser is shut off $2\,\mathrm{ms}$ prior to the cooler, allowing the atoms to accumulate in the $|5^2S_{1/2}, F=1\rangle$ states with the atoms distributing in the magnetic sub-states $m_\mathrm{F}=0,\pm1.$

Initially at a high optical power, the CDT is ramped down to $2.5\,\mathrm{W}$ per beam over $125\,\mathrm{ms}$ in three linear sections, to prevent stimulated Raman transitions to the $|5^2S_{1/2},F=2\rangle$ states [62]. This process can occur since the used IPG Laser YLR-50-LP has a spectral width of $2.5\,\mathrm{nm}$ full width at half maximum (FWHM) producing pairs of photons with the appropriate detuning to drive stimulated Raman transitions [91]. The experimental MOT cycle is visualised in Fig. 2.4, including the proper values for all laser parameters involved.

After the initial linear ramp of the CDT optical power to 2.5 W per beam, for the remainder of the evaporative cooling cycle, a scaling law approach is chosen [92]. In previous works, the actual time dependency of the potential depth was approximated by a combination of linear ramps due to technical limitations [45, 46, 62]. The introduction of the labscript suite as the experimental control software allows for a direct implementation of the time-dependent optical potential given by

$$U(t) = \frac{U_0}{\left(1 - \frac{t}{\tau}\right)^{\beta}} \to P_{\text{CDT}}(t) = \frac{P_0}{\left(1 - \frac{t}{\tau}\right)^{\beta}}.$$
 (2.24)

Here β and τ describe the precise shape of the evaporation ramp with currently $\tau=3\,\mathrm{s}$ and $\beta=3$ used at ATOMICS with the initial optical power $P_0=2.5\,\mathrm{W}$ per beam. To reach quantum degeneracy and produce a BEC, the optical power is lowered according to Eq. (2.24) to a final power of typically $P_{\mathrm{end}}=30\,\mathrm{mW}$ where a BEC at a respective temperature of $25(5)\,\mathrm{nK}$ is produced consisting of approximately $25\,000^{87}\mathrm{Rb}$ atoms in a mixture of the m_{F} sub-states in the $|5^2S_{1/2},F=1\rangle$ ground state.

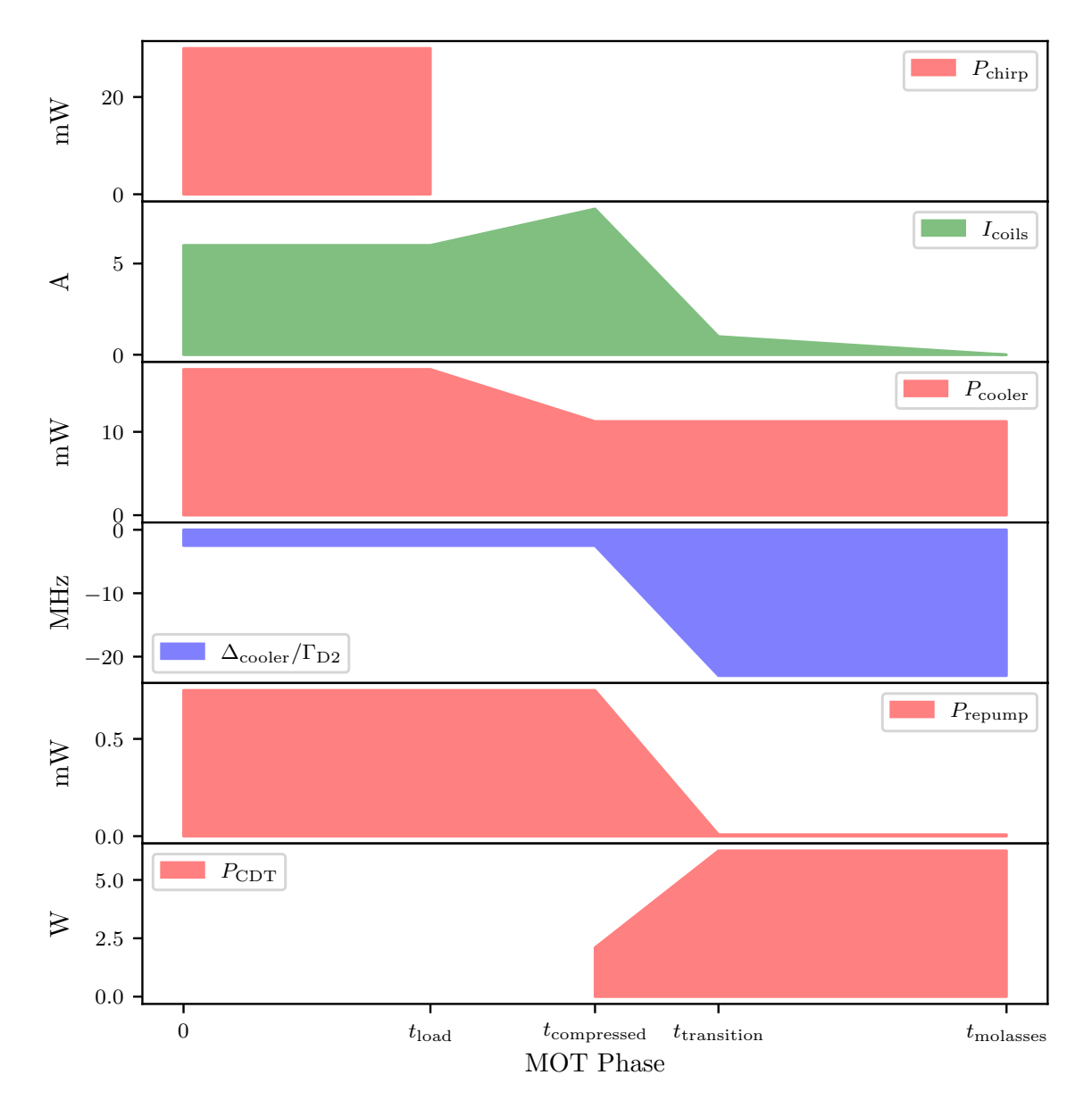


Fig. 2.4.: Schematic visualisation of the initial MOT phase at the ATOMICS experiment. The MOT is typically loaded for $t_{\rm load}=8\,{\rm s}$ after which the magnetic field is increased to compress the MOT for $t_{\rm comp}=100\,{\rm ms}$, increasing the density. A duration of $35\,{\rm ms}$ is employed to transition from the compressed MOT to the optical molasses, during which the optical power of both the cooling and repump lasers is reduced. Typically, an optical molasses of $50\,{\rm ms}$ to $100\,{\rm ms}$ is used to reduce the temperature of the atomic cloud to $20(5)\,{\rm \mu K}$. The CDT is turned on at the end of the compressed MOT and its optical power is increased to a maximum of $6.5\,{\rm W}$ per beam in the optical molasses to maximise the loading efficiency.

Optical pumping

As mentioned in the previous section, if no further action is taken, the BEC produced in the CDT will be a mixture of all three $m_{\rm F}$ magnetic sub-states of the $|5^2S_{1/2},F=1\rangle$ manifold in $^{87}{\rm Rb}$. This tripartite distribution splits the total atom population across three condensates, effectively reducing each condensate's atom number by a factor of three when equally distributed among the sub-states. In atom interferometry, where each $m_{\rm F}$ sub-state acts as a separate coherent matter-wave, this introduces complex interference patterns that must be accounted for [see Chapter 4]. This can be prevented by a method called optical pumping, which has been investigated in previous works [46, 57]. Since optical pumping was found not to have an effect on neither interferometric measurements nor any other experiments conducted, it was not finally included into the standard experimental scheme.

Recently, this method has been investigated again in the master thesis of S. Reißig [93]. To optically pump atoms into a dedicated $m_{\rm F}$ sub-state, first the energetic degeneracy needs to be lifted. This is achieved by using two additional coils in a Helmholtz-like configuration with winding number N=30, radius R=0.12 m and distance to the centre of the vacuum chamber $d=0.25\,\mathrm{m}$. Passing a current I through both coils in series generates a homogenous magnetic field, uniform on the spatial scale of the BEC, with a magnitude of 254(3) mG/A. Typically, a current of $I=2\,\mathrm{A}$ and respective field magnitude of $510(6)\,\mathrm{mG}$ is used. This field provides a sufficient quantisation axis and lifts the degeneracy of the $m_{\rm F}$ sub-states with $\Delta E_{\rm m_F}/\hbar=$ $-m_{\rm F} \times 2\pi \times 0.178(20)$ MHz/A. Light close to the $|5^2S_{1/2}, F=1\rangle \rightarrow |5^2P_{3/2}, F'=1\rangle$ transition, propagating along the horizontal detection beam path but oppositely aligned to the quantisation field, enables optical pumping of atoms into a specific magnetic sublevel $m_{\rm F}$. The $m_{\rm F}$ state into which atoms are pumped is determined by the combination of the quantisation axis orientation and the polarisation of the optical pumping light. In the typical orientation of the quantisation axis, as described above, using σ^- light induces transitions with $\Delta m_{\rm F} = -1$ hence the $m_{\rm F} = -1$ state becomes a dark-state accumulating atoms. The light for the optical pumping is generated by shifting a part of the light of the repump laser via an acousto-optical modulator (AOM) in double-pass configuration to the dedicated detuning Δ_{pump} and combining it with the beam path of the horizontal detection.

The precise detuning Δ_{pump} of the pumping light relative to the mentioned transition, optical power P_{pump} and pumping time τ_{pump} can be controlled via the experimental control software [see Section 2.3.1]. To decrease the effect of heating through photon scattering in the pumping process, the pumping is performed directly at the beginning of the evaporation ramp described in Section 2.3.2. Fortunately, a large number of combinations of Δ_{pump} and τ_{pump} result in similar pumping efficiencies, making the implementation robust against small drifts in frequency or optical power [93].

In order to quantify the results of the optical pumping, a state selective measurement method needs to be implemented. Here it is advantageous, that the states of interest are sensitive to magnetic fields and magnetic field gradients. This allows for a straight-forward implementation of the Stern–Gerlach method [94, 95]. At the ATOMICS experiment, one of the MOT coils can be used to generate a strong magnetic field gradient, resulting in a state-dependent force

$$\mathbf{F} = -\nabla m_{\mathbf{F}} g_{\mathbf{F}} \mu_B B \tag{2.25}$$

that separates the atoms spatially over a time of flight (TOF). The coil used for this gradient is the upper one in Fig. 2.2 (left), located on the left side of the MOT, when viewed from

the entrance window of the chirp beams in the direction of the oven¹. Therefore, the atoms are separated under a 45° angle relative to both CDT arms and the coordinate system of the vertical detection camera.

In Fig. 2.5, three averaged optical density distributions for different combinations of Δ_{pump} and τ_{pump} are shown, with the parameters based on [93, p.48, Tab.4.4]. The respective values are given in Tab. 2.1 including the average measured probability of an atom being in one of the m_{F} sub-state. Decreasing Δ_{pump} while keeping τ_{pump} and P_{pump} constant results in an increased pumping efficiency at the expense of reduced total atom number N_{tot} .

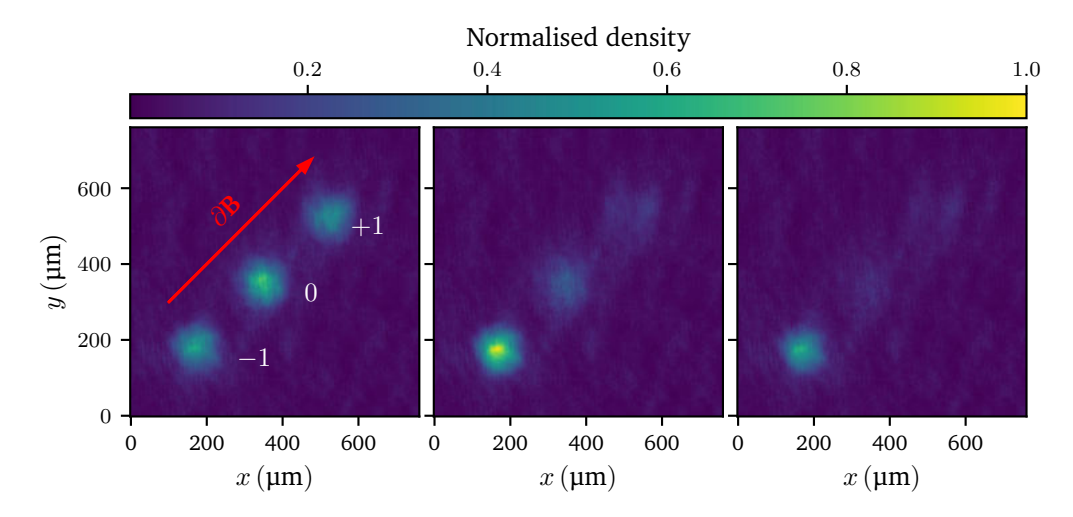


Fig. 2.5.: Averaged column densities for the reference without optical pumping (left), $\Delta_{\rm pump} = -2\pi \times 20.5(10)$ MHz with $\tau_{\rm pump} = 500\,\mu \rm s$ (centre), and $\Delta_{\rm pump} = -2\pi \times 10.5(10)$ MHz with $\tau_{\rm pump} = 500\,\mu \rm s$. Resulting probabilities for an atom being in one of the $m_{\rm F}$ sub-states given in Tab. 2.1. The pumping power was kept constant at $P_{\rm pump} = 25(5)\,\mu \rm W$ corresponding to an intensity $I_{\rm pump} = 2.0(4)\,\rm W/m^2$.

Tab. 2.1.: Corresponding values of Δ_{pump} and τ_{pump} to the measured densities in Fig. 2.5 with resulting probabilities of an atom being in one of the m_{F} sub-states.

$\frac{\Delta_{\mathrm{pump}}}{2\pi}$	Reference	$-20.5(10){\rm MHz}$	$-10.5(10){\rm MHz}$
$ au_{ m pump}$	unpumped	$500\mu s$	$500\mu s$
$m_{\rm F} = -1$	0.323(17)	0.569(11)	0.661(15)
$m_{\rm F} = 0$	0.381(24)	0.270(9)	0.185(11)
$m_{\rm F} = +1$	0.296(15)	0.161(8)	0.151(11)
N_{tot}	8790(690)	6610(580)	3990(400)

Detection and analysis of ultracold atomic clouds

To detect ultracold atomic clouds, several techniques can be deployed with absorption imaging being the most straightforward [73]. A laser beam, resonant to the cooling transition $|5^2S_{1/2}, F=2\rangle \rightarrow |5^2P_{3/2}, F'=3\rangle$ is used to illuminate the atomic cloud. Depending on the optical density, parts of the beam is absorbed, effectively casting a shadow in the beam. By taking a reference image without the atomic shadow as well as a dark image to remove

¹Which coil is used for the Stern–Gerlach field has been verified by tracing the cables from the power supply to the vacuum feed-through. At the feed-through, the coil used is label **R**.

external noise, the atomic density can be determined by the Lambert–Beer law, resulting in two-dimensional distributions of column density [73]. At the ATOMICS experiment, this technique is used with two distinct detection axis implemented [see Fig. 2.2]. The vertical axis is used as main detection with two achromatic lenses with focal lengths 300 mm and 400 mm projecting the shadow cast by the atoms onto the sensor of a PCO pco . panda 4.2 USB camera². Given the size of the achromatic lenses and the large distance to the plane of the atoms, the theoretical optical resolution of the detection system is given by $\Delta d = 1.22 \lambda f/D = 3.8 \, \mu \text{m}$ with $\lambda = 780 \, \text{nm}$ and $D = 75 \, \text{mm}$. The horizontal detection system offers an optical resolution of $\Delta d = 4.8 \, \mu \text{m}$ and is primarily employed for additional diagnostic purposes.

Fringes on the images, generated by the coherence of the laser beam used to perform the detection can pose a serious issue for the evaluation of the atomic images. An algorithm implemented in **Python** is used to correct the background of the images to remove interference fringes that are similar on each image of a measurement series. Typically, up to 200 images are combined in one set to correct the background of this set. For larger measurement campaigns containing more than 200 images, multiple sets of 200 images are used to endure proper correction, for details see [57].

Generally, two-dimensional Gaussian distributions

$$\tilde{n}(x,y) = \tilde{n}_0 \exp\left(-\frac{x^2}{2\sigma_x^2} - \frac{y^2}{2\sigma_y^2}\right) + \tilde{n}_{\text{off}}$$
(2.26)

are used to approximate most distributions to evaluate atom numbers and temperatures. The maximum column density is given by \tilde{n}_0 , σ_i denotes the Gaussian width and $\tilde{n}_{\rm off}$ accounts for any offset. Here a shift of the density along x or y is neglected assuming the density is centred around zero along both axes. Generally, an offset x_0 and y_0 along the x- and y-axis can be included if necessary. In special cases, other distributions are used to approximate the atomic density distributions which will be described when needed or atom numbers are determined by simple summation. The latter is typically employed when the atom number is anticipated to approach zero.

To estimate temperatures of atomic ensembles, Eq. (2.26) is fitted to a series of densities with varying TOFs. Assuming a Gaussian initial momentum distribution the expression

$$\sigma_i^2(t) = \frac{k_{\rm B}T}{m}t^2 + \sigma_{i,0}^2 \tag{2.27}$$

can be used to extract the temperature T of the ensemble [73, Sec. 4]. Here i=x,y and $\sigma_{i,0}$ denotes the initial width of the cloud at t=0. For thermal clouds this is a good approximation while for partially condensate ensembles, a bimodal distribution needs to be used given by

$$\begin{split} \tilde{n}_{\text{tot}}(t,x,y) &= \tilde{n}_{\text{therm}}(t,x,y) + \tilde{n}_{\text{BEC}}(t,x,y) \\ \tilde{n}_{\text{therm}}(t,x,y) &= \tilde{n}_{\text{therm}}(0)g_2 \left(\exp\left(\frac{\mu}{k_{\text{B}}T}\right) \exp\left(-\frac{x^2}{2\sigma_x^2} - \frac{y^2}{2\sigma_y^2}\right) \right) \\ \tilde{n}_{\text{BEC}}(t,x,y) &= \tilde{n}_{\text{BEC}}(0) \max\left(1 - \frac{x^2}{R_x^2} - \frac{y^2}{R_y^2}\right)^{3/2} \end{split} \tag{2.28}$$

with the thermal and condensate densities \tilde{n}_{therm} and \tilde{n}_{bec} , the poly-logarithmic function g_i and the Thomas–Fermi radii R_i [73]. Here it is important to note that one dimension from

²For Chapter 3 a Photometrics SenSys camera was used with a KAF-0401E sensor chip. For Section 4.4, the same camera model with a KAF-1400 sensor chip was used.

the three-dimensional density has been integrated as consequence of the absorption imaging. For this reason the recorded images display column densities. By integrating over one of the remaining axis, the one-dimensional line densities can be computed, that often perform better in experimental fitting routines. Nevertheless, the typically low atom numbers and high BEC fractions at the ATOMICS experiment prevents reliable evaluations based on Eq. (2.28).

2.4. Laser systems

This section provides a brief summary of the laser systems used at the ATOMICS experiments and their key properties. In the **APQ** research group most laser systems are based around in-house developed and build components, such as the current drivers and ECDL [96–98].

2.4.1. Spectroscopy laser

The spectroscopy master laser serves as an absolute frequency reference for stabilising down-stream laser systems at the ATOMICS experiment. An ECDL is the core of the system, incorporating a ThorLabs L785H1 laser diode. The master laser is frequency stabilised via modulation-transfer spectroscopy (MTS) at $\Delta\omega=+2\pi\times200\,\mathrm{MHz}$ relative to the $|5^2S_{1/2},F=2\rangle\to|5^2P_{3/2},F'=3\rangle$ transition in $^{87}\mathrm{Rb}$ [96, 99, 100] [see Appendix A]. For an enhanced mechanical stability of the laser system and an easier serviceability, the laser is placed on a daughter board and coupled via a fibre to the main board. Part of the light is used for the MTS stabilisation and guided to this section via $\lambda/2$ plates and polarising beam splitters (PBSs). The remainder of the light is further distributed by additional combinations of $\lambda/2$ plate and PBS towards the detection system and the fibre distribution of the master laser light for frequency stabilisation of other lasers.

For the absorption detection of ultracold 87 Rb atoms, the light has to be brought back to resonance with the $|5^2S_{1/2}, F=2\rangle \rightarrow |5^2P_{3/2}, F'=3\rangle$ transition. Therefore, a part of the light is guided to an AOM in double-pass configuration so the light is shifted by twice the AOM frequency. The detection AOM is driven by a combination of a direct digital synthesis (DDS) and a series of radio frequency (RF) power amplifiers at a frequency of approximately $2\pi \times 100\,\mathrm{MHz}$. To determine the precise resonance, the AOM frequency has to be scanned and the atom number determined. The distribution of the master laser light to further laser systems at the ATOMICS experiment has been transitioned to a fully fibre coupled system based on ThorLabs TN785R5A2 50/50 fibre couplers. This allows for a nearly lossless distribution and combination of the master laser light with the light from other laser systems to produce the frequency-beat signals for stabilisation.

2.4.2. MOT laser

In the following subsections, a brief overview of additional laser systems needed for the MOT at the ATOMICS experiment is given. This includes the chirp laser system as well as the MOT cooler and repump laser system. The experimental scheme of the ATOMICS MOT phase is visualised in Fig. 2.4.

Chirp laser system

As described above, at the ATOMICS experiment the chirp cooling method is used to slow the atoms emitted from the oven chamber with two frequency-chirped ECDLs deployed. These lasers are dynamically offset-locked to the master laser (chirp cooler) and MOT repumper (chirp repumper) and swept across ~ 400 MHz at repetition rate of 200 Hz to 300 Hz, synchronising with changing velocity of the atoms. The chirp compensates for the Doppler shift as atoms slow down, maintaining resonance with the $|5^2S_{1/2},F=2\rangle \rightarrow |5^2P_{3/2},F'=3\rangle$ cooling and $|5^2S_{1/2},F=1\rangle \rightarrow |5^2P_{3/2},F'=2\rangle$ repump transitions. This enables sufficient momentum transfer to reduce the beam velocity prior to MOT capture, achieving a sufficient loading of the MOT in typically 4 s.

To optimise the loading rate of the MOT, the frequency chirping profile was optimised, adding a flat top part at far-detuned section of the chirping profile [101].

MOT cooling laser

The MOT cooling laser system is build around a master oscillator power amplifier (MOPA) setup using an ECDL stabilised $\Delta\omega=-2\pi\times 105\, \mathrm{MHz}$ relative to the master laser to seed a tapered amplifier (TA) module, amplifying the available optical power to $600\,\mathrm{mW}$ [102]. In the MOT stage, a power of typically $17.5(25)\,\mathrm{mW}$ is used per MOT beam at a detuning of $\Delta=-2\pi\times 15\,\mathrm{MHz}\approx -2.5\,\Gamma_{\mathrm{D2}}$ relative to the cooling transition with Γ_{D2} the natural line width of the D2-line of $^{87}\mathrm{Rb}$ [67] [see Appendix A]. For the sub-Doppler cooling, the detuning is increased to $\Delta=-2\pi\times 140\,\mathrm{MHz}\approx -23\,\Gamma_{\mathrm{D2}}$ and the optical power lowered to $7.5\,\mathrm{mW}$ per MOT beam.

MOT repump laser

To prevent ⁸⁷Rb atoms from accumulating in the $|5^2S_{1/2}, F = 1\rangle$ ground state, where they cannot be excited with the MOT cooling laser, a repump laser is needed, similar to the chirp repumper. At ATOMICS a dedicated laser system is used for this purpose built around an ECDL similar to the other laser systems. Since only a low optical power is needed to prevent the accumulation in the $|5^2S_{1/2}, F=1\rangle$ state, the direct output power of the ECDL is sufficient and no further amplification is needed compared to the cooling laser. The repumper is frequency stabilised to an offset of $\Delta\omega = 2\pi \times 6568\,\mathrm{MHz}$ relative to the master laser, resulting in a detuning of $\Delta = +2\pi \times 200$ MHz relative to the repump transition in ⁸⁷Rb [see Appendix A]. An AOM is used to compensate for this detuning, shifting the light back to the resonance of the repump transition. The detuning of the repump laser remains unchanged during the experimental cycles and typically less than 1 mW in two of the three MOT arms is sufficient. Part of the optical power is additionally used to stabilise the chirp repump laser as well as the Bragg seed laser, described in Section 2.4.4. Additionally, a part can be used to drive optical transitions used for optically pumping atoms into one dedicated $m_{\rm F}$ sub-state of the $|5^2S_{1/2}, F=1\rangle$ ground state manifold in combination with a magnetic quantisation field. The optical pumping scheme is described in Section 2.3.2.

2.4.3. Dipole-trap laser systems

In the MOT, atoms can only be cooled to temperatures of approximately $20(5) \,\mu\text{K}$ using sub-Doppler polarisation gradient cooling [12]. To achieve the nanokelvin-scale temperatures

required for quantum degeneracy, optical dipole traps are employed to further cool thermal ensembles to reach Bose–Einstein condensation via forced evaporative cooling and manipulate BECs. The following subsections outline the dipole-trap laser systems at the ATOMICS experiment, highlighting their distinct configurations and applications in ultracold atomic physics.

Crossed Dipole Trap

As discussed in Section 2.3.2, Bose–Einstein condensation at the ATOMICS experiment is achieved exclusively in all-optical dipole potentials. To minimise spontaneous photon scattering and thus heating the primary dipole potential for evaporative cooling is operated at a large detuning Δ from both D-lines of ⁸⁷Rb. However, increasing the detuning reduces the trap depth for a given intensity, so a correspondingly higher optical power P is required [see Eq. (2.6)]. Recent advances in laser technology have made compact, commercial systems with continuous-wave optical powers in the kilowatt range readily available.

At the ATOMICS experiment, an off-the-shelf multimode IPG Laser YLR-50-LP fibre laser provides up to $50\,\mathrm{W}$ of optical power at a central wavelength of $\lambda_\mathrm{CDT}=1070\,\mathrm{nm}$ with a FWHM of $2.5\,\mathrm{nm}$. Typically, $20\,\mathrm{W}$ of this power is used, split into two beams with orthogonal polarisations to prevent interference within the vacuum chamber. The optical power in each beam is intensity-stabilised using a red-pitaya intensity stabilisation (RPI) feedback loop, which employs Koheron PDX10R-D-SI logarithmic photodiodes (positioned after the chamber viewport) and Crystal Technology 3110-125 & 3110-197 AOMs. Logarithmic amplifiers in the photodiodes are essential for stabilising the optical power over the full evaporative cooling range, from $6.5\,\mathrm{W}$ down to $30\,\mathrm{mW}$.

Both beams are focused into the vacuum chamber using $f=500\,\mathrm{mm}$ achromatic lenses, producing waists of $w_0=38(2)\,\mathrm{\mu m}$ [102]. The beams are aligned perpendicular to gravity and to each other, spanning a plane parallel to the optical table and intersecting at the position of the MOT [see Fig. 2.2 (left), magenta beams].

At the end of the evaporation sequence, with an optical power of 30 mW per beam, the measured trapping frequencies are $\omega_r = 2\pi \times 100(5)$ Hz and $\omega_z = 2\pi \times 140(10)$ Hz in the crossed-beam configuration with the z-axis aligned with gravity. The typical trap depth along the z-axis at the end of evaporation is 3.8×10^{-30} J = $k_{\rm B} \times 277$ nK = 1.53 E_{rec} including the gravitational potential that significantly lowers the actual depth.

Light sheet laser system

The CDT setup described above provides an optimal potential for evaporative cooling in optical traps, enabling the production of a BEC. Furthermore, if the BEC is transferred into a single CDT beam, this beam acts as a linear optical waveguide, suitable for applications such as atom-interferometric measurements [57].

For more complex trapping geometries beyond linear guiding, an additional setup is required. This involves creating a potential that confines atoms in a plane perpendicular to gravity, combined with a system that generates tailored potential structures within this plane. The latter system is introduced in Chapter 5.

To realise a quasi-one-dimensional potential perpendicular to gravity, a MOPA configuration is employed. The seed laser is an ECDL operating at $\lambda_{\rm LS}=797.8\,\rm nm$. Due to the large detuning from the nearest D1-line of $^{87}{\rm Rb}$ at $\lambda_{\rm D1}=794.98\,\rm nm$, no active frequency stabilisation is implemented, instead, the setup relies on the passive stability of the external resonator [67].

The seed laser output power is insufficient for trapping at this detuning, so a TA (Toptica A-795-02000) is used to amplify the optical power to approximately 600 mW.

The output of the TA is intensity-stabilised by a feedback loop using a RPI and an AA MT 110/B50/A 1.5-IR/S AOM, and delivered to the experiment via an optical fibre. At the experiment, the beam is out-coupled and expanded to a waist of 6.6(10) mm. A cylindrical achromatic lens with a focal length of 400 mm focuses the beam vertically, producing a waist of 15.4(20) µm inside the vacuum chamber.

The light sheet is spatially overlapped with one of the CDT beams at the chamber exit using a dichroic mirror, such that it propagates in the opposite direction to the CDT beam. The focal planes of the CDT and the light sheet are carefully aligned to coincide within the chamber [see Fig. 2.2 (left)].

Typically, an optical power of 230(5) mW is sufficient to support the atoms against gravity, resulting in trapping frequencies of $\omega_z=2\pi\times 365\,\mathrm{Hz}$ (vertical), $\omega_x=2\pi\times 0.8\,\mathrm{Hz}$, and $\omega_y=2\pi\times 4.3\,\mathrm{Hz}$, where gravity defines the z-axis and the beam propagates along the y-axis. Throughout this work, multiple iterations of light sheet systems have been used with the above described being the most current one. Experiments based on earlier versions are distinguished by the different wavelength being used.

Titanium:Sapphire laser systems

The light sheet laser system described in the previous section provides only a quasi-one-dimensional potential with a tight confinement in the vertical (aligned with gravity) direction while in the remaining two dimensions the atoms are effectively untrapped. Two additional laser systems constructed around Coherent 899-01 titanium:sapphire (Ti:Sa) ring lasers, which are pumped by Coherent Verdi V10 and V18 solid-state laser systems, provide power for additional optical dipole potentials. The main advantage of using a Ti:Sa laser for additional optical dipole potentials lies mainly in the available optical power provided over a large range of wavelengths. Both Ti:Sa lasers can be tuned in a range of 770 nm to 810 nm while maintaining a nearly unchanged output power. At the time of this work, the first Ti:Sa laser pumped typically at around 7 W provides 270(10) mW of output power, measured at the output of the Ti:Sa, at 800.3(1) nm, that can be used for red-detuned optical dipole potentials. This laser has been used for the experiments discussed in Chapter 3 at a wavelength of 793.96 nm but has been repurposed for later in this work.

The second Ti:Sa is generally used with a pumping power of $11 \,\mathrm{W}$, providing $1.0(1) \,\mathrm{W}$ at $776.4(1) \,\mathrm{nm}$ for blue-detuned potentials, measured at the output of the Ti:Sa.

In Chapter 5, a new optical setup based on two TI DLP® 3000 LightCrafter DMD modules is introduced. Each Ti:Sa is used on one of the individual DMDs to produce arbitrary two-dimensional optical potentials.

2.4.4. Bragg-diffraction laser system

In addition to the laser systems used for preparing ultracold atoms described above, the Bragg laser system is employed to coherently couple specific momentum states of the ultracold ensembles. The detailed scheme of Bragg diffraction for BECs is presented in Section 4.1.

A schematic of the complete Bragg laser system is shown in Fig. 2.6. Similar to the MOT laser systems, the seed laser is an ECDL [APQ-1069, see Fig. 2.6, top left], frequency-offset stabilised at $\Delta=2\pi\times3.0\,\mathrm{GHz}$ relative to the MOT repump laser described in Section 2.4.2. This results in a total detuning of $\Delta=2\pi\times3.2\,\mathrm{GHz}$ from the excited state manifold $|5^2P_{3/2},F'=2\rangle$ of

⁸⁷Rb.

Since the ECDL output power is limited to approximately $30\,\mathrm{mW}$, amplification is necessary to reach sufficient power for addressing higher-order momentum states and to compensate for optical losses [103]. Amplification is achieved via a MOPA setup incorporating a TA laser [see Fig. 2.6, top right] based on a Coherent Dilas I1N-TA-0780-2000-CM diode, delivering up to $\approx 1\,\mathrm{W}$ immediately after the amplifier module.

An AOM [Crystal Technology 3080-120], driven at 80 MHz, is used in combination with a photodiode on the laser table [see Fig. 2.6, bottom] and an RPI feedback loop to stabilise the intensity and enable fast switching of the Bragg light. For improved mechanical stability, the TA and switching AOM are mounted on a single optical board and fibre-coupled both to the seed ECDL and to the main optical setup on the laser table.

On the laser table, the light is coupled out from the optical fibre, and a small portion is directed onto a photodiode using a beam splitter to stabilise the intensity. The beam diameter is then reduced by a factor of two via a telescope, with an Uniblitz LS2T2 shutter placed at the telescope focal plane for fast beam switching. A $\lambda/2$ plate and a PBS split the beam into two equal-power paths, each guided to a Isomet 1205B-1 AOM. These AOMs shape the Bragg pulses and generate the required frequency difference $\Delta\omega$ [see Eq. (4.2)] to drive Bragg diffraction.

After blocking the zero-order beams behind the AOMs, the first-order diffracted beams are coupled into separate fibres that guide the light to the main experiment table. There, the beams are collimated to waists of $w_{\rm Bragg}=1070(50)\,\mu{\rm m}$. Two additional photodiodes monitor the beam powers for calibration and provide feedback on pulse shapes and timing. The beams are overlapped with the second CDT beam using two dichroic mirrors in a counter-propagating geometry, forming the moving standing wave lattice essential for Bragg diffraction. This setup differs from the typical retro-reflective setup.

On the laser table, the maximum optical power used is $P_{\rm Bragg} = 68(1)$ mW measured behind the shutter, calibrated at 6.8(1) mW/V. Prior to each Bragg experiment, a power calibration is performed, and the effective pulse area is measured to account for losses due to vacuum chamber window transmission and beam alignment. A detailed description of the experimental procedure is provided in Section 4.1.

The AOMs on the laser table are driven by an AD9959 DDS, providing up to four frequency outputs with an RF amplitude of $0\,\mathrm{dBm}$. An Arduino Nano and a Raspberry Pi control the DDS, allowing precise setting of frequencies and phases; further details are given in [46, 104]. Currently, three DDS outputs are used: one provides a fixed base frequency of $80\,\mathrm{MHz}$ to the first Bragg beam AOM, while the other two are offset to different values of $\Delta\omega$ relative to the base frequency, enabling addressing of two distinct momentum states.

Fast RF switches (Mini-Circuits ZYSWA-2-50DR+), controlled by transistor-transistor logic (TTL) signals from the main experiment computer, gate the RF power to the AOMs, ensuring that RF power is supplied only during pulse sequences. Another identical switch is used to select between the two secondary DDS frequency outputs, allowing rapid switching between preset frequencies. This frequency switching is controlled by a TTL signal from the experiment control system. A further fast switch is placed in series after the frequency selector to gate the RF power similarly to the first arm.

Since these switches operate in a binary on/off manner, time-dependent amplitude envelopes for the Bragg pulses are implemented using a Mini-Circuits ZAD-3+ mixer. This mixer attenuates the RF power transmitted to the amplifiers and AOMs via a control voltage, enabling smooth variation of pulse intensity.

A total of four HP 33120A arbitrary waveform generators (AWGs) generate the time-dependent

envelopes for the Bragg pulses. Outputs from pairs of AWGs are combined using voltage adders to produce pulses of varying lengths without reprogramming the AWGs via the general purpose interface bus (GPIB) interface. The envelope waveforms, consisting of up to 16000 points, are preloaded into the AWGs internal memory and triggered by an external TTL signal. The pulse length is controlled by setting the waveform frequency $f_{\rm pulse}=1/\tau_{\rm pulse}$, adjustable for each experimental run. Using four AWGs allows the generation of pulse sequences with non-uniform durations, avoiding the overhead of reprogramming during experiments.

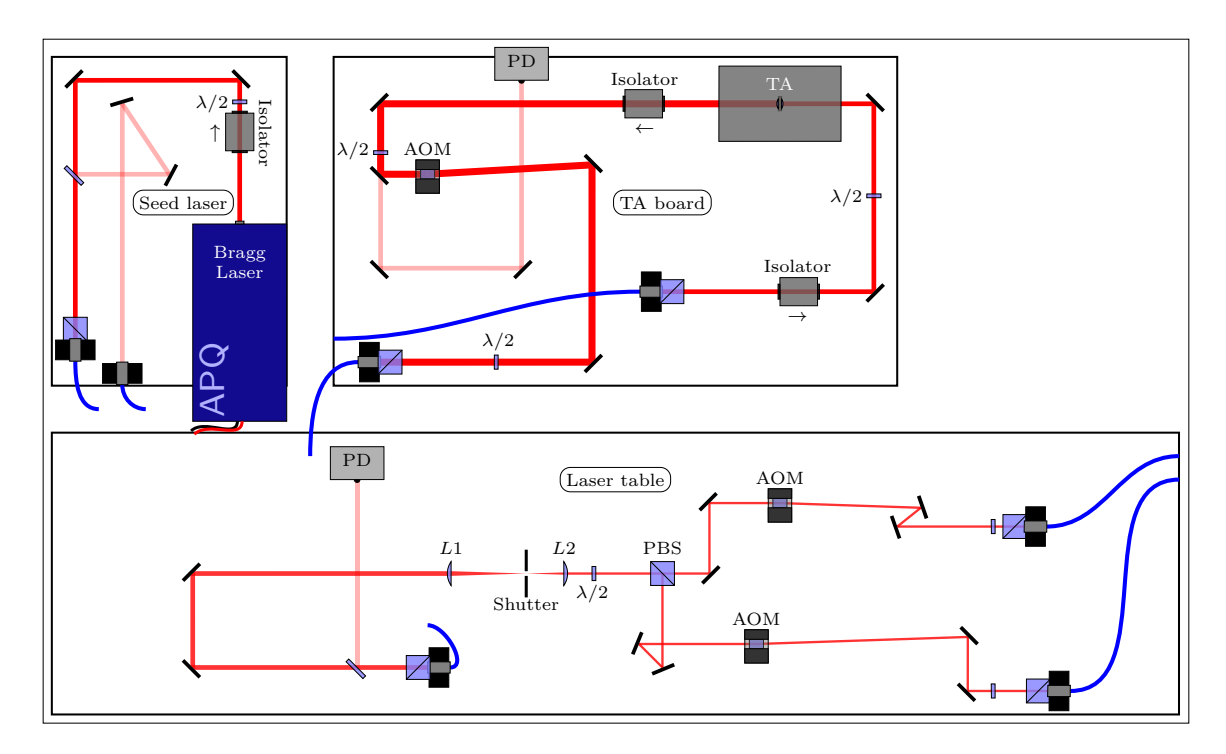


Fig. 2.6.: Schematic representation of the Bragg laser system. An ECDL laser stabilised to a frequency offset of $\Delta\omega_{\rm Bragg,tot}=+2\pi\times3160\,{\rm MHz}$ the state manifold $|e\rangle=|5^2P_{3/2},F'=2\rangle$ of $^{87}{\rm Rb}$ is used as seed for power amplification (top left). Since the ECDL provides a maximum output power of $\approx30\,{\rm mW}$, a MOPA setup based on a TA is used to amplify the power to $\geq400\,{\rm mW}$ (top right). The TA board includes an AOM used to stabilise the optical power guided to the laser table using the signal of a photodiode located on the laser table after the fibre coupler. On the laser table, the beam is split and two AOMs are used to shape the pulse envelope as well as to add the needed frequency difference $\Delta\omega$ to couple the desired momentum states. Two individual fibres are used to guide the light to the experiment table (bottom). Every fibre coupling is combined with a PBS cube aligned to the slow axis of the polarisation maintaining fibres to minimise polarisation drifts in the fibres.

3. Dipole potentials based on conical refraction

"Did everyone see that? Because I will not be doing it again."

– Captain Jack Sparrow, Pirates of the Caribbean: On Stranger Tides

Conical refraction (CR) as a special case of birefringence in biaxial crystals (BC) with three principal refractive indices offers a unique and efficient method for generating structured light fields, which are highly advantageous for optical trapping of ultracold atoms. Unlike conventional birefringence, CR produces a hollow cone of light when a circularly polarised beam propagates along one of the principal axes of a BC [41, 42], resulting in intensity distributions that can be utilized as advanced optical dipole potentials. First described already in 1832 [41, 42], CR has sparked interest again recently. References [44, 105] give an extensive review of the CR phenomenon, its fundamentals, and possible applications.

Optical dipole traps are a cornerstone of ultracold-atom experiments. Red-detuned traps, such as those based on focused Gaussian beams, like the CDT used to produce the BEC at the ATOMICS experiment, provide simple and robust geometries but inherently confine atoms at intensity maxima, leading to increased photon scattering and decoherence. The simplicity of red-detuned traps makes them especially attractive in scenarios where optical power is abundant so that the detuning can be increased to a point where scattering can be neglected on the timescales of the experiment. In contrast, blue-detuned traps confine atoms at intensity minima, significantly reducing scattering. This property makes them ideal for high-sensitivity and precision experiments like the investigation of BECs [43, 106], quantum information processing, or quantum sensing with neutral atoms [107–109]. Optimally, such potentials feature a central intensity minimum with large-intensity gradients, yielding high trapping frequencies in all directions. Creating high-quality so-called bottle-beams traps continues to present significant technical challenges. Different implementations of bottle beams have been reported based on techniques utilising spatial light modulators (SLMs) [110], or phase plates generating holograms [111], time-averaged potentials [112], conical lenses [113], interfering Laguerre–Gaussian or vortex beams [114–116], and using birefringent crystals [117].

Compared to the method based on CR, most of these approaches have known limitations like the need for increased precision regarding the alignment of multiple beams, a poor conversion ratio of optical input power to the actual potential, and a potential minimum with a non-zero intensity. The use of light fields produced by CR as optical potentials for ultracold atoms was first proposed in the context of two-dimensional CR double-ring configurations, which have already been employed to guide ultracold rubidium atoms [43, 45, 46, 57, 118]. Furthermore, an implementation of a CR bottle-beam potential for absorbing droplets has been reported by [119].

In the following chapter, a realisation of an optical bottle beam for ultracold atoms based on CR in biaxial birefringent crystals is presented with the results published in [120] and parts of the section taken verbatim from the article¹. In Section 3.1 the fundamentals of light fields generated by CR are presented followed by a detailed investigation of the dark focus regime

¹This article has been published in Physical Review A **108**, 053320 (2023), DOI: https://doi.org/10.1103/PhysRe vA.108.053320

in Section 3.2 including the realisation of a bottle-beam potential for ultracold ⁸⁷Rb atoms. Finally, the combination of CR and microlens array (MLA) as a path towards large arrays of bottle beams is investigated. These results demonstrate the significant potential of CR for next-generation quantum technologies

3.1. Fundamentals of conical refraction (CR)

Conical refraction is an optical phenomenon that occurs when light travels along an optic axis within a biaxial crystal. Instead of passing straight through, an unpolarised or circularly polarised Gaussian input beam emerges as a hollow cone or ring of light, creating distinctive ring-shaped intensity patterns. This effect arises from the unique way biaxial crystals refract light, and it can produce both internal and external conical refraction depending on the geometry [44, 105]. In Fig. 3.1 (right), a schematic setup for the creation of CR light fields is shown compared to the equivalent setup for a red-detuned optical dipole trap (left) based on a focused Gaussian beam. The incident light field is focused to a waist w_0 by a lens of focal length f. When a BC is positioned between the lens and the focal plane and the propagation axis of the beam is aligned with one of the optical axis of the BC, unpolarised or circularly polarised light is transformed into a ring-shaped intensity distribution at the focal plane. Depending on

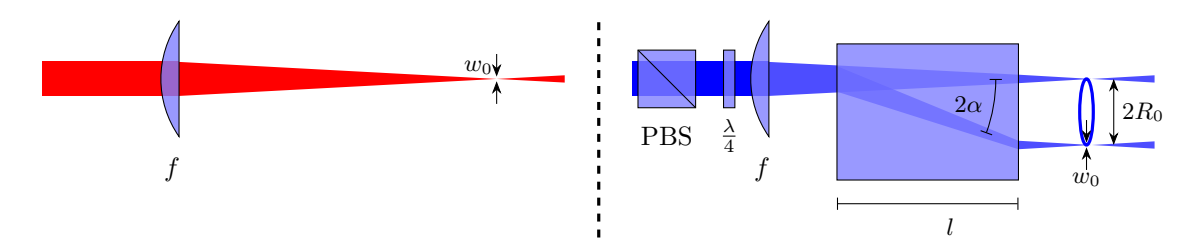


Fig. 3.1.: (left) Schematic of the simplest setup to create a red-detuned dipole potential based on a Gaussian beam focused to a waist w_0 by a lens of focal length f. (right) Schematic representation of the CR effect. An incident light beam is focused through the biaxial crystal by a lens of focal length f to a waist w_0 . If properly aligned, the emerging field forms a circular intensity distribution in the focal plane of the lens. The distribution size is determined by the principal ring radius R_0 . The qualitative structure of the intensity distribution depends on the ratio of the principal radius to the waist $\rho_0 = R_0/w_0$.

the length l of the BC crystal, the emerging ring has a principal radius of $R_0 = \alpha l$, describing the radius of the emerging intensity distribution, where α is the semi-angle determined by the three refractive indices $n_1 > n_2 > n_3$ [105] of the BC by

$$\alpha = \frac{1}{2}\arctan\left(\frac{\sqrt{(n_1^2 - n_2^2)(n_2^2 - n_3^2)}}{n_1 n_3}\right). \tag{3.1}$$

In addition to the interesting spatial properties of the emerging light field, its polarisation is linear everywhere with the polarisation angle depending on the position. Opposing azimuthal positions of the ring have orthogonal polarisation vectors with respect to each other [121, 122].

The transformation of an unpolarised or circularly polarised incident light field by the CR can be understood in terms of a unitary transformation acting on the plane wave spectrum $a(\mathbf{k})$ of

the incident light [123, 124]. Taking the full diffractive theory by Belskii and Khapalyuk [125] in the formulation by Berry [126], using a normalised coordinate system given by

$$\rho_0 = \frac{R_0}{w_0}, \quad \rho = \frac{r}{w_0}, \quad Z = \frac{z}{z_R} \quad \kappa = kw_0.$$
(3.2)

The field transformed by CR can be written in the form

$$\mathbf{D}(\rho, \phi, Z, \rho_0) = \frac{1}{\sqrt{2}} M_{\text{CR}} \mathbf{e}$$
(3.3)

with the waist w_0 of the focused light field, z_R the Rayleigh length, and **e** the polarisation unit vector. The 2×2 matrix M_{CR} takes the form

$$M_{\rm CR} = \begin{pmatrix} B_0(\rho,Z,\rho_0) + \cos(\phi)B_1(\rho,Z,\rho_0) & \sin(\phi)B_1(\rho,Z,\rho_0) \\ \sin(\phi)B_1(\rho,Z,\rho_0) & B_0(\rho,Z,\rho_0) - \cos(\phi)B_1(\rho,Z,\rho_0) \end{pmatrix} \tag{3.4}$$

and e denotes the polarisation vector of the incident light field in Jones formalism [127]. Here, B_0 and B_1 are the Belskii–Khapalyuk–Berry (BKB) integrals given by

$$B_0\left(\rho,Z,\rho_0\right) = \frac{1}{2\pi} \int_0^\infty \!\! \mathrm{d}\kappa \; \kappa \; a(\kappa) \cos\left(\kappa \rho_0\right) \exp\left(-\frac{\mathrm{i} Z \kappa^2}{2n}\right) J_0\left(\kappa \rho\right) \tag{3.5a}$$

$$B_{1}\left(\rho,Z,\rho_{0}\right) = \frac{1}{2\pi} \int_{0}^{\infty} d\kappa \,\kappa \,a(\kappa) \sin\left(\kappa \rho_{0}\right) \exp\left(-\frac{iZ\kappa^{2}}{2n}\right) J_{1}\left(\kappa \rho\right) \tag{3.5b}$$

where J_i refers to the i-th order Bessel function of the first kind, n is the mean refractive index, and $a(\kappa)$ the plane wave spectrum, defined via the Fourier transform of the incident field. For a circularly polarised beam with polarisation unit vector $\mathbf{e} = 1/\sqrt{2} \ (1, \mathbf{i})$ the intensity distribution simplifies to

$$I_{\text{CP}}(\rho, Z, \rho_0) = |B_0(\rho, Z, \rho_0)|^2 + |B_1(\rho, Z, \rho_0)|^2.$$
(3.6)

For cylindrically symmetric input light fields $E_{\rm in}$, $a(\kappa)$ is given by $a(\kappa)=2\pi\int_0^\infty\!\!{\rm d}\rho\,\rho E_{\rm in}\,(\rho)\,J_0\,(\kappa\rho)$. For Gaussian incident light fields as described in Section 2.1.1 [Eq. (2.1)], the plane wave spectrum is given by $a(\kappa)=\pi E_0\exp\left(-\kappa^2/4\right)$ with the electric field amplitude E_0 , so that the BKB integrals take the form

$$B_{0,\text{Gauss}}\left(\rho,Z,\rho_{0}\right) = E_{0} \frac{1}{2} \int_{0}^{\infty} \! \mathrm{d}\kappa \; \kappa \exp\left(-\frac{\kappa^{2}}{4}\right) \cos\left(\kappa \rho_{0}\right) \exp\left(-\frac{\mathrm{i}Z\kappa^{2}}{2n}\right) J_{0}\left(\kappa \rho\right) \tag{3.7a}$$

$$B_{1,\text{Gauss}}\left(\rho,Z,\rho_{0}\right) = E_{0} \frac{1}{2} \int_{0}^{\infty} \! \mathrm{d}\kappa \; \kappa \exp\left(-\frac{\kappa^{2}}{4}\right) \sin\left(\kappa \rho_{0}\right) \exp\left(-\frac{\mathrm{i}Z\kappa^{2}}{2n}\right) J_{1}\left(\kappa \rho\right). \tag{3.7b}$$

As mentioned, the normalised radius of the CR intensity distribution ρ_0 characterises the qualitative structure of the light field with $\rho_0 \ll 1$ resulting in super-Gaussian and with $\rho_0 \gg 1$ in clear double-ring distributions separated by a ring of low intensity, the so-called Poggendorf dark ring [126]. For values $0.9 \le \rho_0 \le 2$, the intensity distribution changes drastically from a doughnut-like mode at $\rho_0 = 0.924$ with a zero central intensity to a distribution forming a bright ring with a central intensity maximum at $\rho_0 \approx 1.5$ to the double ring mode at $\rho_0 > 2$. In Fig. 3.2 this transitional region is shown as a false colour plot for a fixed value of R_0 and values $0.924 \le \rho_0 \le 5$. In typical experimental setups, ρ_0 has a fixed value determined by the properties of the incident beam and the BC crystal. Using lenses of variable focal length, ρ_0 can

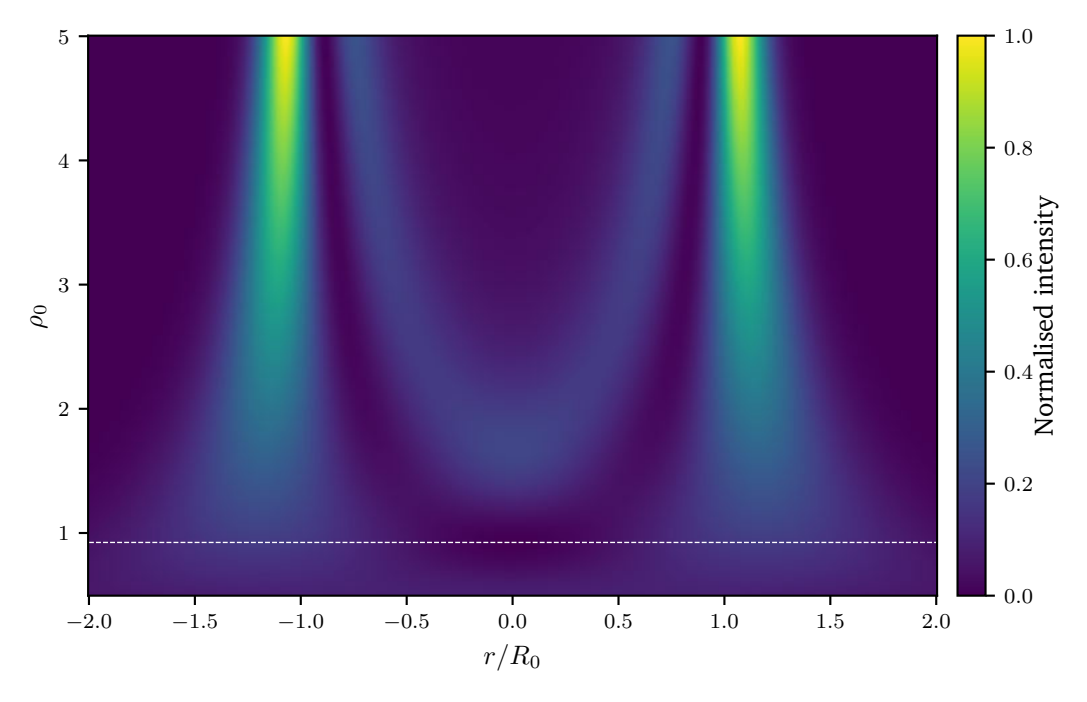


Fig. 3.2.: False colour plot of $I(\rho,Z=0)$ for ratios $0.5 \le \rho_0 \le 5$. By focusing the incident light to an ever smaller waist, different intensity distribution can be created by CR. Starting with super-Gaussian beams for $\rho_0 \ll 1$ followed by the dark focus (DF) regime at $\rho_0^{\rm DF} = 0.924$ two bright rings emerge, separated by the Poggendorf dark ring for $\rho_0 > 2$. A dashed white line marks the dark focus regime.

be dynamically changed as used in [128] to investigate the dynamics of BECs in dynamically changing trapping geometries based on CR. Furthermore, it can be shown that placing an aperture in the first focal plane of the lens focusing through the BC results in a truncation of the BKB integrals. This effect was used to dynamically change the effective ring regime to investigate topology changes of BECs [46].

Since Fig. 3.2 only visualises a one-dimensional cut through the intensity in the focal plane of the lens and does not show the behaviour along beam propagation, in Fig. 3.3 the two-dimensional (xy-plane) intensity distribution in the focal plane as well as a cut in the yz-plane for three distinct values $\rho_0 \in [0.924, 1.5, 5]$ are shown. The plot reveals that a dark focus (DF) configuration at $\rho_0^{\rm DF} = 0.924$ a central region of zero intensity is formed, surrounded by regions of high intensity along all three dimensions. Consequently, this configuration is ideally suited for implementing a blue-detuned, single-beam three-dimensional dipole trap for cold atoms.

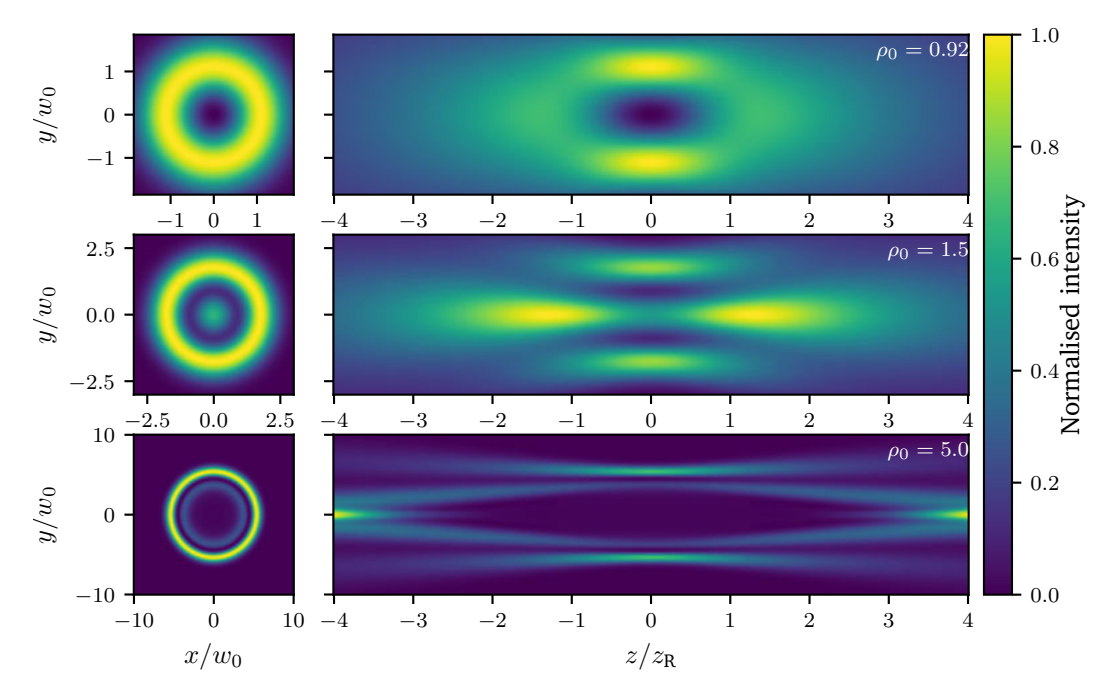


Fig. 3.3.: Intensity distributions in the xy (left) and yz-plane (right) for different values of ρ_0 . The top row shows the dark focus regime $\rho_0^{\rm DF}=0.924$ with the doughnut-like intensity distribution in the focal plane. In the centre row, an intermediate regime $\rho_0=1.5$ is shown where a local intensity maximum emerges in the centre of a bright ring, providing a dark ring structure in the focal plane. The bottom row shows a double-ring separated through the Poggendorf dark ring at $\rho_0=5$. For higher values of ρ_0 , the intensity distribution remains a double ring.

3.2. The CR dark focus as bottle-beam trap

As discussed in the previous section, for $\rho_0^{\rm DF}=0.924$ the light field produced by CR forms a dark region of zero intensity surrounded by high intensity in all directions. In the following, a detailed analysis of the resulting intensity distribution is given, investigating potential depth and trapping frequencies. Further, an experimental realisation of such a light field will be explored and compared to numerical calculations. The light field will be used to trap ultracold ⁸⁷Rb atoms in all three dimensions without the help of additional light fields. Finally, concepts to improve on this trapping technique are given. The results of this section have been published in [120].

3.2.1. Properties of the dark focus

To derive some key properties of the ideal dark focus at $\rho_0^{\rm DF}=0.924$, the intensity distribution is calculated numerically for $|Z|\leq 2$ and $\rho\leq 2$ using Eqs. (3.7a) and (3.7b) and finally Eq. (3.6). In Fig. 3.4 (top), the resulting intensity distribution is shown on a linear false colour map, normalised to the peak intensity in the focal plane. From this intensity distribution, relevant properties of this light field can be derived, where the given uncertainties refer to the numerical grid used to calculate the intensity distribution. For optical dipole potential applications, the magnitude and spatial positions of the limiting intensity thresholds are of particular importance, determining the maximum potential depth. In the focal plane at Z=0, the radial maximum forms a ring with radius $\rho=1.096(1)$ as can be seen in Fig. 3.3 (top left) with an intensity of

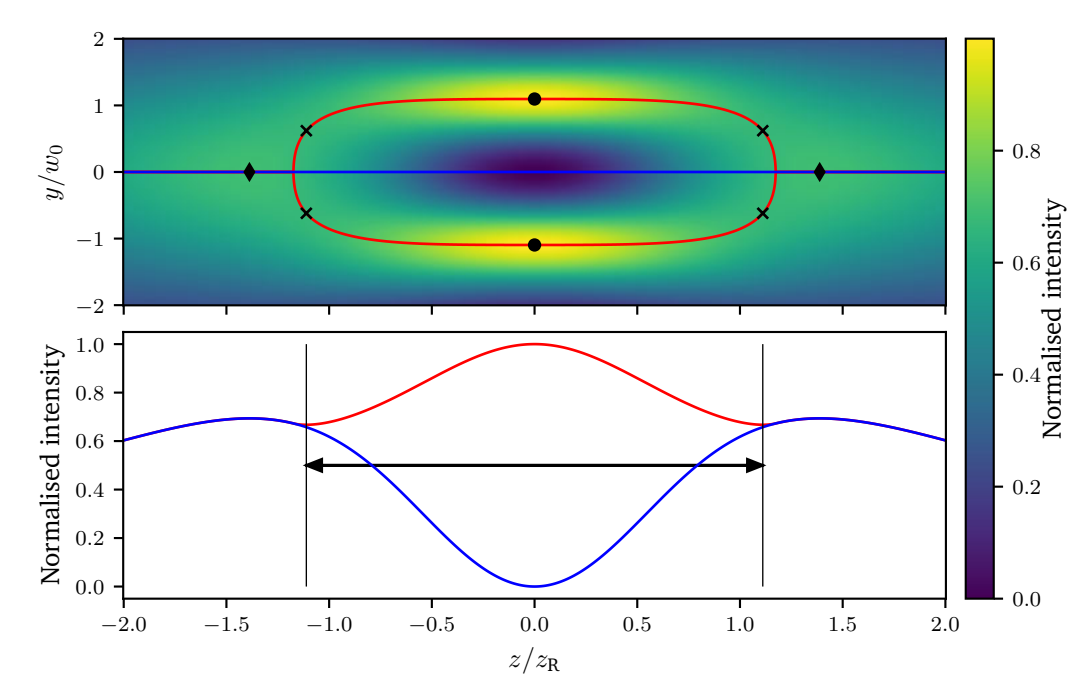


Fig. 3.4.: (top) False colour plot of a cut through the ρZ -plane of the normalised intensity distribution for $\rho_0^{\mathrm{DF}}=0.924$. The red curve traces the position of the radial maximum numerically extracted from the calculated intensities. Black diamonds mark the position of the maximum on-axis intensity at $Z=\pm 1.388(1)$, black dots mark the respective maxima on the radial direction for Z=0 at $\rho=1.096(1)$. Black crosses mark the locations of the weakest radial intensity maxima, which form a saddle point at $\rho=0.619(1)$ and $Z=\pm 1.111(1)$. (bottom) On axis $I(\rho=0,Z)$ (blue) and radial maximum values $I_{\mathrm{max}}(Z)$ (red) of the intensity. Vertical lines and a black arrow mark the location of the weakest points of the intensity at $Z=\pm 1.111(1)$.

 $I_{
ho, {
m max}}=0.199~I_0$. Here, $I_0=2P/(\pi w_0^2)$ denotes the peak intensity of the Gaussian input beam when focused to a waist w_0 . When used as a blue-detuned dipole trap, this point marks the potential maximum in the radial direction with a potential of $U_{
ho, {
m max}}=0.199~\tilde{U}I_0$. The position of the radial maximum is marked with black dots in Fig. 3.4 (top).

For $\rho=0$, the on-axis intensity reaches a maximum value of $I_{Z,\max}=0.138~I_0$ at $Z=\pm 1.388(1)$ (black diamonds in Fig. 3.4 (top)), marking the maximum length of the potential in axial direction. For $Z=\pm 0.598(1)$, the on-axis intensity reaches $50\,\%$ of this value $I_{50\%,z}=0.069~I_0$. A potential, suitable for trapping ultracold atoms is only provided for regions, where a radial intensity minimum is present. To find the axial position where the radial minimum vanishes, the radial maximum $I_{\rho,\max}(Z)$ is numerically determined for each value of Z in the calculated intensity distribution respectively. The red curve in Fig. 3.4 (top) traces the position of the radial maximum with the intensity values plotted in Fig. 3.4 (bottom). Comparing these values to the on-axis intensity [blue curve Fig. 3.4 (bottom)] gives a value of $I_{\rm fork}=0.134~I_0$ at $Z=\pm 1.174(1)$ for the point where the radial minimum vanishes and the radial maximum equals the on-axis intensity.

Further investigation of the radial maximum values shows, that at $Z=\pm 1.111(1)$ and $\rho=0.619(1)$ the radial maximum intensity $I_{\rho,\max}(Z)$ has a local minimum with a value of $I_{\rm trap}=0.133~I_0$ [black crosses in Fig. 3.4 (top)]. Since this value is smaller than the on-axis maximum $I_{\rm trap} < I_{Z,\max}$, this point is the weakest point of the trap when using this light field as a dipole potential. Given by the radial symmetry of the light field, this leads to two ring-shaped minima of the potential, located at $\rho=0.619(1)$ and $Z=\pm 1.111(1)$. In Tab. 3.1 a summary of the

discussed points is given with the intensities normalised to I_0 . In experiments with ultracold atoms, the potentials are often only sampled by the atomic

Tab. 3.1.: Specific intensity values and corresponding positions characterising the dark-focus beam for $\rho_0 = \rho_0^{\rm DF}$ in reference to the maximum intensity I_0 of a focused Gaussian beam with waist w_0 and identical power.

Intensity	Position			
$I_{\rho, \text{max}} = 0.199 I_0$	$\rho = 1.096(1)$	Z = 0		
$I_{Z,\text{max}} = 0.138 I_0$	$\rho = 0$	$Z = \pm 1.388(1)$		
$I_{\text{trap}} = 0.133 I_0$	$\rho = 0.619(1)$	$Z = \pm 1.111(1)$		
$I_{\text{fork}} = 0.134 I_0$	$\rho = 0$	$Z = \pm 1.174(1)$		
$I_{50\%,Z} = 0.069 I_0$	$\rho = 0$	$Z = \pm 0.598(1)$		
$I_{50\%,\rho} = 0.01 I_0$	$\rho = 0.593(1)$	Z = 0		

ensembles close to the minimum, which allows the use of a harmonic approximation for most potentials. Such an approximation was derived in [44, 120] close to $\rho_0^{\rm DF}=0.924$. Normalising the intensity distribution to I_0 and applying the harmonic approximation, the normalised intensity for $|Z|\approx 0$ and $\rho\approx 0$ can be described by

$$\frac{I(\rho, Z=0)}{I_0} \approx \chi_{\rho} \rho^2$$
, with $\chi_{\rho} = 4\rho_0^2 \left| {}_1F_1\left(2, \frac{3}{2}, -\rho_0^2\right) \right|^2 \approx 0.293$ (3.8a)

$$\frac{I(\rho=0,Z)}{I_0} \approx \chi_Z Z^2, \quad \text{with} \quad \chi_Z = \frac{1}{4}$$
 (3.8b)

where ${}_1\!F_1(a,b,c)$ is the Kummer confluent hyper-geometric function [129] and in the last step $\rho_0^{\mathrm{DF}}=0.924$ was inserted. In the radial direction, this approximation is only valid for values of $|Z|\leq 1.174$ where a radial minimum is present and in general χ_ρ becomes dependent on Z [see Appendix B]. Fig. 3.5 displays the normalized intensity profiles $I(\rho,Z=0)$ (top, blue) and $I(\rho=0,Z)$ (bottom, blue), alongside their harmonic approximations (orange curves) derived from Eqs. (3.8a) and (3.8b). From this plot, it is evident, that the harmonic approximation only describes the intensity well for small values around $\rho=0$ and Z=0.

3.2.2. Conical-refraction dark focus

At the ATOMICS experiment CR light fields can be created using different potassium gadolinium tungstate $[KGd(WO_4)_2]$ crystals of varying lengths from 2.2(1) mm to 16.0(1) mm. This type of crystal is optically transparent for a wide range of wavelengths between 350 nm and 5500 nm [130] which makes it an ideal candidate for the generation of optical potentials for all alkaline atoms [67, 131-136]. Furthermore, optical anti-reflective coatings are available with high quality, allowing in principle a conversion efficiency above 99 %.

Calculating the three principal refractive indices for this type of crystal and a wavelength of $\lambda_{\rm BB} = 793.96\,{\rm nm}$ with

$$n(A, B, C, D, \lambda) = A + \frac{B}{1 - \left(\frac{C}{\lambda}\right)^2} - D\lambda^2$$
(3.9)

leads to the values summarised in Tab. 3.2. Based on these values with Eq. (3.1) a semi angle of $\alpha = 19.07$ mrad can be calculated [137].

Therefore, principal radii of $R_0=41.95(190)\,\mu\text{m}$ to $305.0(19)\,\mu\text{m}$ can be realised for the available crystals without re-imaging the light field with additional optics. For the generation of

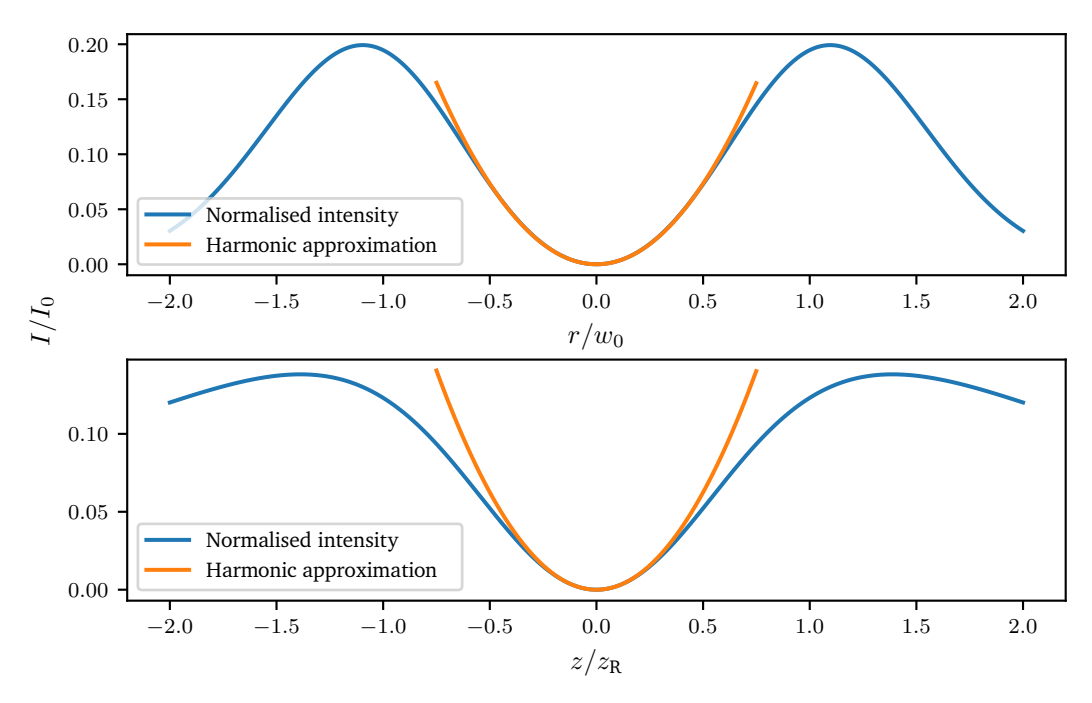


Fig. 3.5.: Radial (top) and axial (bottom) intensity for $\rho_0^{\rm DF}=0.924$ in blue normalised to the maximum intensity I_0 of the input Gaussian beam. Harmonic approximation based on Eqs. (3.8a) and (3.8b) are shown in orange.

Tab. 3.2.: Values of A to D for [KGd(WO₄)₂ and calculated refractive indices for $\lambda_{BB} = 793.96$ nm [137].

\overline{A}	В	C [1/nm]	$D [1/\mathrm{nm}^2]$	
1.3867	0.6573	170.02×10^{-9}	0.2913×10^{-27}	n_1 =2.0754
1.5437	0.4541	188.91×10^{-9}	2.1567×10^{-27}	n_2 =2.0237
1.5344	0.4360	186.18×10^{-9}	2.0999×10^{-27}	n_3 =1.9944

the dark focus regime, one of the CR-crystals with length 2.2(1) mm is chosen (APQ-1211). The light field in the focal plane is investigated to verify that a sufficient potential can be generated. To reach the desired value of $\rho_0^{\rm DF}=0.924$ a Gaussian beam with a focused waist of $w_0=45.4(21)$ µm is needed. The light fot the CR intensity distribution is produced by one of the Ti:Sa laser systems described in Section 2.4.3 and guided to the experiment with an optical fibre. After the light is coupled out of the fibre, a beam waist of $w_{\rm in}=1050(20)$ µm was determined by fitting a 2D Gaussian of the form Eq. (2.2) to an image taken of the beam with a COHU INC. 6410 RS-170 charge-coupled device (CCD) camera. A combination of $\lambda/2$ plate with a PBS ensures a pure linear polarisation of the light which can be converted to circularly polarised light by including an additional $\lambda/4$ plate. By using an achromatic lens with focal length $f_{\rm L1}=200$ mm, the initial Gaussian beam can be focused to a waist of $w_0=43.6(30)$ µm with a measured Rayleigh length of $z_{\rm R}=6.85(50)$ mm. Both values are extracted from Gaussian fits to the focused beam along its propagation axis. This gives an expected value of $\rho_0=0.96(8)$ which is close to the intended value for the dark focus.

The CR-crystal is mounted in a way allowing the control over the alignment between the optical axis of the crystal and the propagation axis of the beam. This is crucial to ensure a symmetric intensity distribution since even small misalignments can cause asymmetries in the produced light field, leading to additional weak points in the potential later on. It is known that for an

optimal output intensity the alignment of the axes of beam and crystal, the polarisation, and the overall optical quality of the crystal need to be optimised. Placing the BC in the focused beam and adjusting the polarisation produces an intensity distribution close to the numerically calculated dark focus. Again, the COHU INC. 6410 RS-170 camera is used to image the intensity

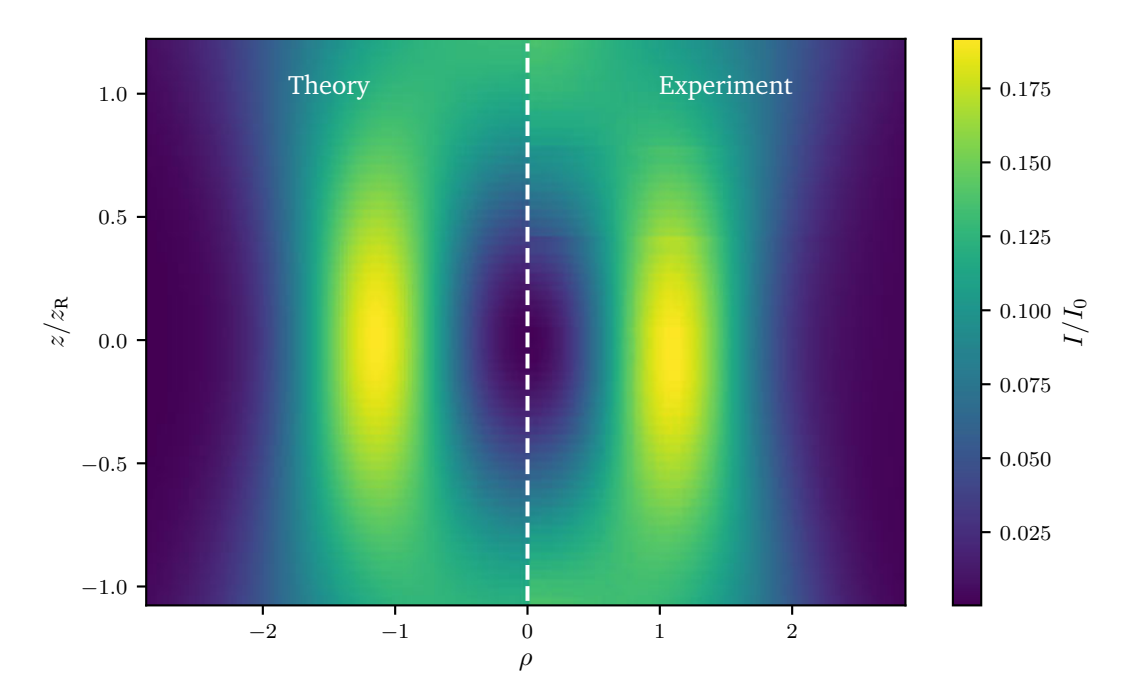


Fig. 3.6.: Comparison of the intensity distribution in the ρZ plane of the measured (right) and the numerically calculated (left) intensities for the experimentally obtained beam parameters $w_0=43.6(30)~\mu\text{m}$, $\rho_0=0.96(8)$, and $z_{\rm R}=6.85(50)~\text{mm}$. Both intensity distributions are scaled to the same optical input power to increase comparability and normalised to $I_0=2P/\pi w_0^2$.

produced by the combination of the focused beam and the CR crystal in the xy-plane. A series of 63 images is taken along the propagation axis of the beam equally spaced by $250(10) \, \mu m$ to capture not just the doughnut-like distribution in the focal plane but the full length of the dark focus which is expected to be on the order of $2 \times 1.174 \times 6.85(50)$ mm = 16.1(12) mm. For each image plane, the alignment of the crystal is adjusted to optimise the intensity distribution. Finally, all images are centred and scaled to an arbitrary optical power of 1 mW for comparison against the numerically calculated intensity with the same optical power. From the series of images, the radial mean intensity values are calculated and displayed as a false colour plot in Fig. 3.6 (right) next to the numerically calculated intensity (left) for the parameter set given in the caption of Fig. 3.6. For a quantitative comparison, similar to the discussion in Section 3.2.1 the axial intensity $I(\rho = 0, Z)$ as well as the radial maximum values $I_{\text{max}}(\rho, Z)$ are evaluated. In Fig. 3.7 (top), the radial maxima are represented by red diamonds and the axial values by blue dots. Both exhibit good agreement with the numerical results (indicated by dashed black lines). All values are normalised to the maximum of the numerical data. To evaluate the length of the potential where a radial minimum is present on the axis, the ratio $I(\rho = 0, Z)/I_{\text{max}}(Z)$ is evaluated and shown in Fig. 3.7 (bottom) with experimental values marked by green crosses and the numerical values as black dashed line. Taking a $5\,\%$ error into account, the length of the bottle can be evaluated as $I(\rho = 0, Z)/I_{\text{max}}(Z) \leq 0.95$ for $|Z| \le l_{\rm BB}/2$ leading to $l_{\rm BB} = 12.75(50)\,{\rm mm}$ which is slightly smaller than the value of 2×1.044 $z_{\rm R} = 14.3(10)$ mm derived from the numerical data based on the same criterium.

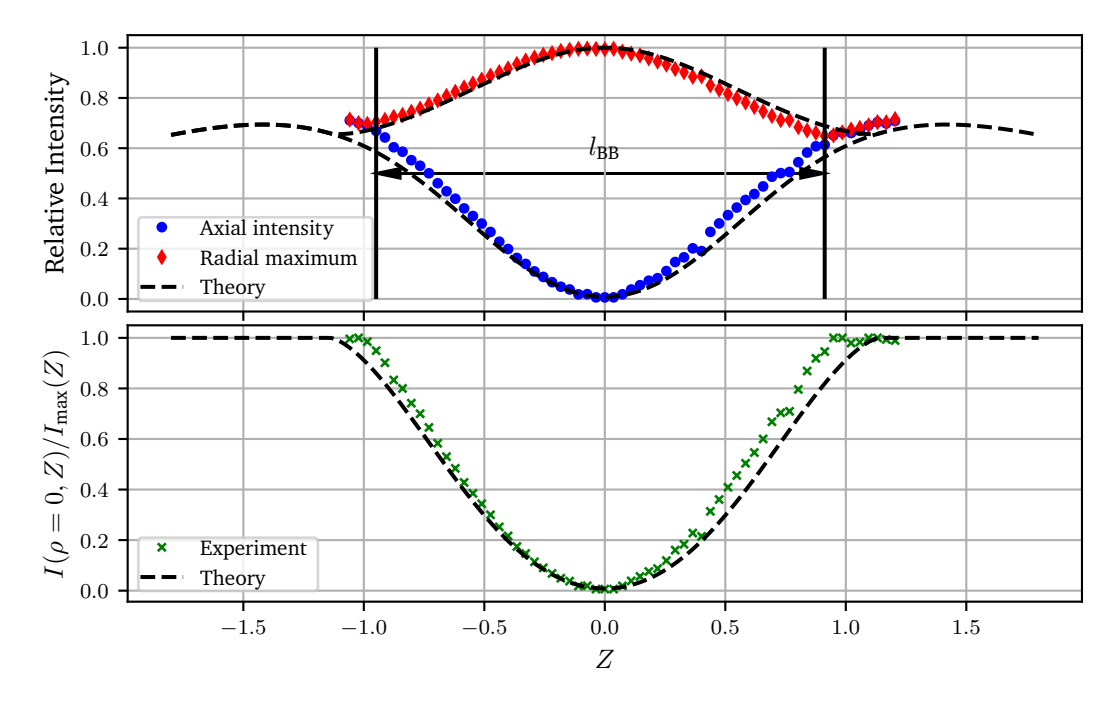


Fig. 3.7.: (top) Experimental values of the radial maximum $I_{\rm max}(Z)$ (red diamonds) and central axial intensity $I(\rho=0,Z)$ (blue dots) compared to the numerical values (black dashed) corresponding to the numerical and experimental intensity distributions shown in Fig. 3.6. (bottom) Ratio of $I(\rho=0,Z)/I_{\rm max}(Z)$ for the experimental values (green cross) and numerical results (black dashed). Defining the length of the bottle as $I(\rho=0,Z)/I_{\rm max}(Z) \leq 0.95$ for $|Z| \leq l_{\rm BB}/2$ gives $l_{\rm BB}=12.75(50)$ mm for the experimental data, shown as black arrow in the top plot. From the theoretical data a value of $2\times 1.044\times z_{\rm R}=14.3(10)$ mm can be derived which is slightly larger.

In Fig. 3.8, a comparison of the azimuthally averaged radial values $I(\rho,Z=0)$ of the experimental data (blue) and the numerical values $I(\rho,Z=0)$ (black dashed) is shown, which fit well. The shaded area marks the computed standard deviation for the experimental values. The Ti:Sa laser used to produce this intensity distribution can provide an intensity stabilised maximum optical power of $P_{\rm BB}=52(5)\,{\rm mW}$ to the experiment, including losses at the CR crystal and additional optics. Based on Eqs. (3.8a) and (3.8b) trapping frequencies in axial and radial direction can be calculated by switching back from normalised intensities to SI units and multiplying them with the corresponding dipole factor $\tilde{U}(\lambda)$ (Eq. (2.3))

$$\omega_r = \sqrt{2}\rho_0 \left| {}_1F_1\left(2, \frac{3}{2}, -\rho_0^2\right) \right| \sqrt{\frac{8\tilde{U}_0 P}{\pi m_{87} w_0^4}} = 0.357 \sqrt{\frac{8\tilde{U}_0 P}{\pi m_{87} w_0^4}} = 0.357 \omega_{r,G}$$
 (3.10)

and

$$\omega_z = \frac{1}{2} \sqrt{\frac{4\tilde{U}_0 P}{\pi m_{87} w_0^2 z_P^2}} = \frac{1}{2} \sqrt{\frac{4\tilde{U}_0 P \lambda^2}{\pi^3 m_{87} w_0^6}} = \frac{1}{2} \omega_{z,G}$$
(3.11)

where m_{87} denotes the mass of ⁸⁷Rb, w_0 the waist of the Gaussian beam and P the optical power. In the last step, $\rho_0 = 0.96$ was used and the known trapping frequencies $\omega_{r,G}$ and $\omega_{z,G}$ of a Gaussian beam were factored out.

Using the experimental parameter $P_{\rm BB}=52(5)$ mW, $w_0=43.6(30)$ µm, $z_{\rm R}=6.85(50)$ mm, and $\lambda_{\rm BB}=793.96$ nm, the resulting calculated trapping frequencies are $\omega_r=2\pi\times295(65)$ Hz and $\omega_z=2\pi\times1.87(23)$ Hz in the focal plane of the CR. Harmonic fits to the experimental axial and

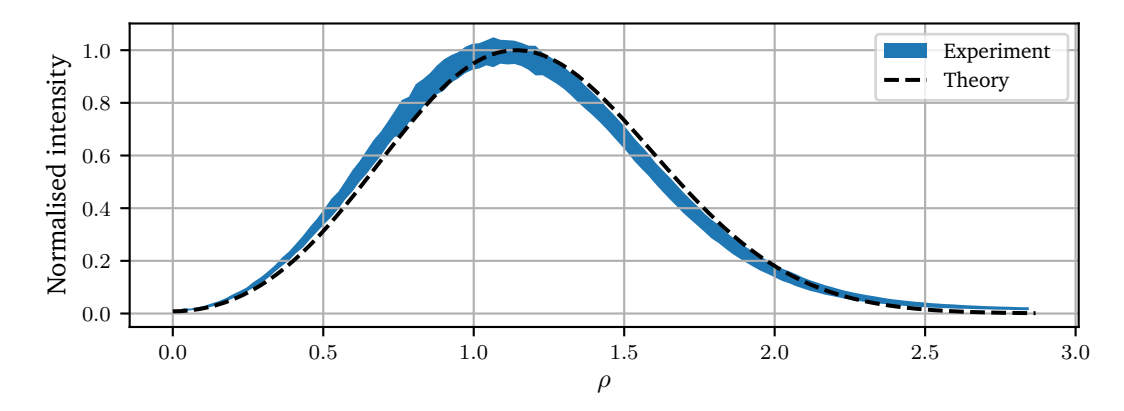


Fig. 3.8.: Radial intensity profile in the focal plane $I(\rho,Z=0)$ calculated for the experimental parameters ($w_0=43.6(30)\,\mu\text{m}$, $R_0=41.95(190)\,\mu\text{m}$, and $z_{\rm R}=6.85(50)\,\text{mm}$) (black dashed) and azimuthally averaged experimental values from Fig. 3.6 (blue shaded area). The width of the shaded area represents the standard deviation of the experimental intensity values. Both curves are normalised to the maximum of the numerical data.

radial intensity values shown in Fig. 3.7 (bottom) and Fig. 3.8 result in values for χ_{ρ} and χ_{Z} that can be converted to trapping frequencies. The resulting values are $\omega_{r}^{\rm exp}=2\pi\times325(38)\,{\rm Hz}$ and $\omega_{z}^{\rm exp}=1.97(21)\,{\rm Hz}$ which are in excellent agreement with the calculated values for the experimental optical powers and beam parameters.

3.2.3. 3D trapping of ultracold ⁸⁷Rb atoms in the CR dark focus

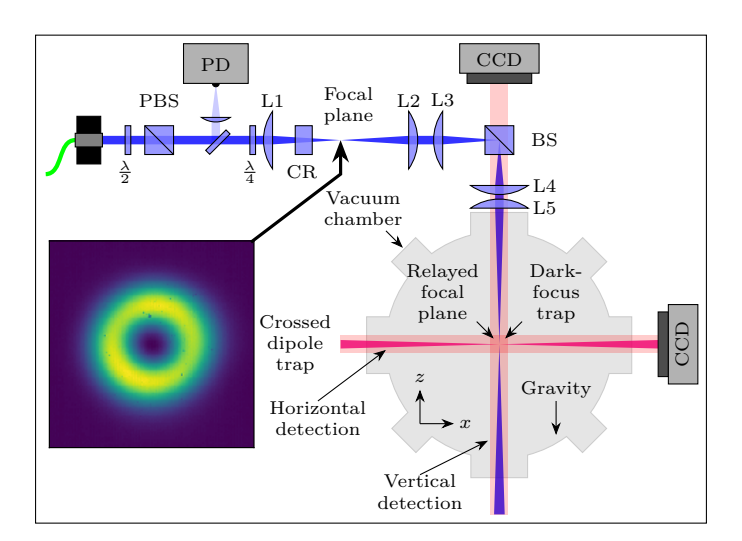


Fig. 3.9.: Schematic experimental setup for 3D trapping of cold atoms based on the CR bottle-beam potential. The intensity distribution of the dark focus is relayed into the vacuum chamber via the non-polarising beam splitter (BS), and demagnified by L2-L5. In the atom plane, the beam propagation axis is aligned with gravity. The inset shows the intensity distribution in the focal plane of L1. The two detection paths are marked as light-red beams with the CDT shown as magenta beam.

Since the focal plane at which the dark focus is created lies outside of the vacuum chamber of the experiment, additional optics are used to relay the intensity distribution to the atom plane

in the vacuum chamber. To ensure a sufficient potential to trap atoms in 3D, the relay optics are chosen to have a total magnification $|M_{tot}| < 1$. Reimaging scales the spatial dimensions of the light field while preserving the overall structure of the intensity distribution. The expected scaling for the beam waist w_0 and the radial size is linear with $|M_{tot}|$, while the Rayleigh length $z_{\rm R}$ and therefore the axial length of the bottle scale with $|M_{\rm tot}|^2$. For the trapping frequencies, a scaling of $1/|M_{\rm tot}|^2$ is expected for ω_r and $1/|M_{\rm tot}|^3$ is expected for ω_z which is beneficial for the case, where the direction of the beam propagation and hence the weak axis of the potential are aligned with gravity as is the case at the ATOMICS experiment. Taking these scaling relations and the weakest point of the bottle-beam potential at $I_{trap} = 0.133 I_0$ at $Z=\pm 1.111$, the maximally tolerated magnification can be calculated by equating the potential value $U_{\text{trap}} = 0.133 \ \tilde{U} I_0 / |M_{\text{max}}|^2$ with the gravitational potential at the weakest point $U_{\rm grav} = -1.111 \ m_{87} \ g \ z_{\rm R} \ |M_{\rm max}|^2$. Here, radiation pressure and other effects are neglected and it is assumed that the axial minimum of the bottle-beam potential is aligned with the plane of the CDT at z=0. Evaluating this leads to a maximum total magnification of $|M_{\text{max}}| \leq 0.39(1)$. The experimental setup illustrated schematically in Fig. 3.9 is employed for measurements involving ultracold atoms within the bottle-beam potential. The achromatic lenses L2 ($f_2 =$ $400 \,\mathrm{mm}$) and $L3~(f_3 = 200 \,\mathrm{mm})$ are used to demagnify the conical refraction (CR) intensity distribution and create an intermediate image plane, achieving a magnification of $|M_{2,3}| = 0.5(1)$. For precise positioning of the optical potential within the vacuum chamber, L3 is mounted on a z-axis translation stage, allowing for fine adjustment of the intermediate image plane. The intermediate image is then relayed into the vacuum chamber by a second pair of achromatic lenses, L4 ($f_4 = 400 \,\mathrm{mm}$) and L5 ($f_5 = 300 \,\mathrm{mm}$), which are fixed to the chamber and provide a magnification of $|M_{4.5}| = 0.60(3)$. This lens pair also projects the atom plane onto the Photometric Sensys CCD camera for imaging. A shift of $\Delta z_{
m shift}$ of the intermediate image will result in a shift of $|M_{4,5}|^2 \Delta z_{\rm shift}$ in the vacuum chamber. The total magnification of the system is expected to be $|M_{\rm tot}^{\rm th}|=0.3(2)<|M_{\rm min}|$ which would result in expected trapping frequencies of $\omega_r^{\rm AP}=2\pi\times 2881(730)$ Hz and $\omega_z^{\rm AP}=2\pi\times 57(13)$ Hz in the atom plane.

Measuring the axial trapping frequency

Since the radial trapping frequency is expected to be in the kHz range it is for technical reasons not experimentally accessible. The axial trapping frequency on the other hand can be measured by exciting dipole oscillations of the atomic ensemble in the bottle-beam potential. Along the vertical axis of the ATOMICS experiment no additional light fields are available to excite such oscillations. Therefore, the bottle-beam light field is shifted in such a way, that the plane of the CDT and the minimum of the bottle-beam potential no longer coincide by utilising the shift of the intermediate image via displacement of L3. In the following, the experimental procedure to excite dipole oscillations in the bottle-beam potential is described.

After the production of a BEC in the CDT via forced evaporative cooling (Section 2.2), the optical power of the CDT is again raised slightly to 41.7(20) mW to ensure a sufficient potential for the transition from CDT to the bottle-beam potential. The power in the bottle beam is raised in three distinct linear ramps from 0 mW to 2.4 mW in 20 ms, then from 2.4 mW to 19 mW in 2 ms and finally from 19 mW to 52 mW in 2 ms. After this transition, the CDT is switched off and the atoms are trapped in the bottle-beam potential where they start to oscillate around the minimum of the potential with an amplitude proportional to the initial displacement. The oscillation time T in the potential is varied from 2.5 ms to 70 ms in steps of 2.5 ms after which the atoms are detected via the horizontal detection following a TOF of 700 µs. In Fig. 3.10

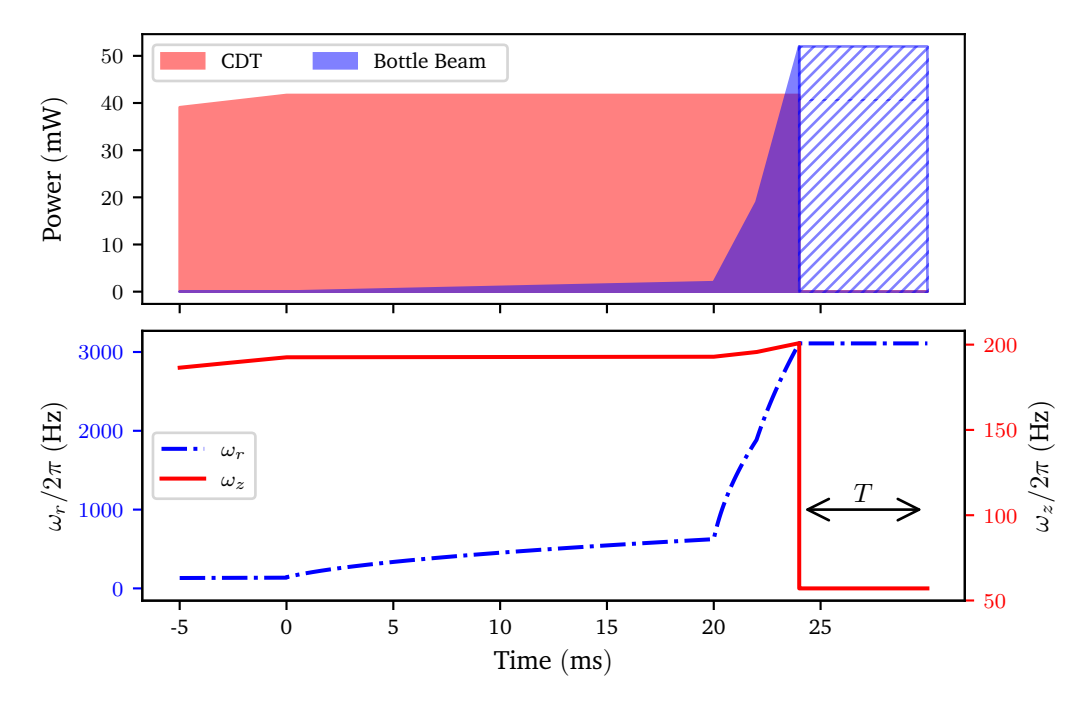


Fig. 3.10.: (top) Experimental scheme to measure the axial trapping frequency ω_z . The optical power in the bottle beam is increased to $52\,\mathrm{mW}$ in three distinct linear ramps while the CDT power is held constant. Following the turn off of the CDT, the atoms are left oscillating in the bottle beam for a variable time T from $2.5\,\mathrm{ms}$ to $70\,\mathrm{ms}$. (bottom) Total radial ω_r and axial ω_z trapping frequency of the combined potential of CDT and bottle beam.

(top) the experimental scheme is visualised in terms of the optical power of the CDT and the bottle-beam potential and in Fig. 3.10 (bottom) the calculated radial (blue) and axial (red) trapping frequencies are shown. The hatched region marks the variable time of oscillations T in the bottle beam. A total of seven individual positions of L3 are used to measure the oscillations of atoms in the bottle-beam trap. Fig. 3.11 shows the atomic distributions (averaged over three separate realisations) for each time step and lens position. It clearly can be seen that the amplitude decreases as the axial point where the atoms are loaded into the bottle beam approaches the potential minimum.

From the data shown in Fig. 3.11 the central position can be extracted by performing fits of 2D Gaussians $\tilde{n}(x,z) = \tilde{n}_0 \cdot \exp(-(x-x_0)^2/2\sigma_x^2 - (z-z_0)^2/2\sigma_z^2) + \tilde{n}_{\rm off}$ to the column density distributions. Here, \tilde{n}_0 denotes the maximum atomic column density, x_0 and z_0 the central position with $\sigma_{x,z}$ the width of the Gaussian along the respective axis, and finally $\tilde{n}_{\rm off}$ accounts for any offset of the background. The resulting z_0 component of the central position is shown in Fig. 3.12 for each time and initial displacement as coloured dots. A damped sinusoidal oscillation $z(t) = z_{\rm max} \exp(-\gamma t) \sin(\omega_z(t-t_0)) + z_{\rm off}$ is fit to each set of values to extract the oscillation amplitude $z_{\rm max}$ including the sign of the initial phase, damping constant γ , oscillation frequency ω_z and equilibrium position $z_{\rm off}$. Solid coloured lines in Fig. 3.12 show the resulting fit with excellent agreement to the experimental data.

From the amplitudes $z_{\rm max}$ and equilibrium points $z_{\rm off}$ the magnification $|M_{4,5}|$ can be extracted by a linear fit with slope m. Through $|M_{4,5}| = \sqrt{|m|}$ this results in $M_{4,5}^{\rm amp.} = 0.59(1)$ and $M_{4,5}^{\rm off.} = 0.59(1)$ which is in excellent agreement with the expected value $|M_{4,5}| = 0.60(3)$. In Fig. 3.13 (top), the values of $z_{\rm max}$ (blue dots) and $z_{\rm off}$ (orange diamonds) are shown with the

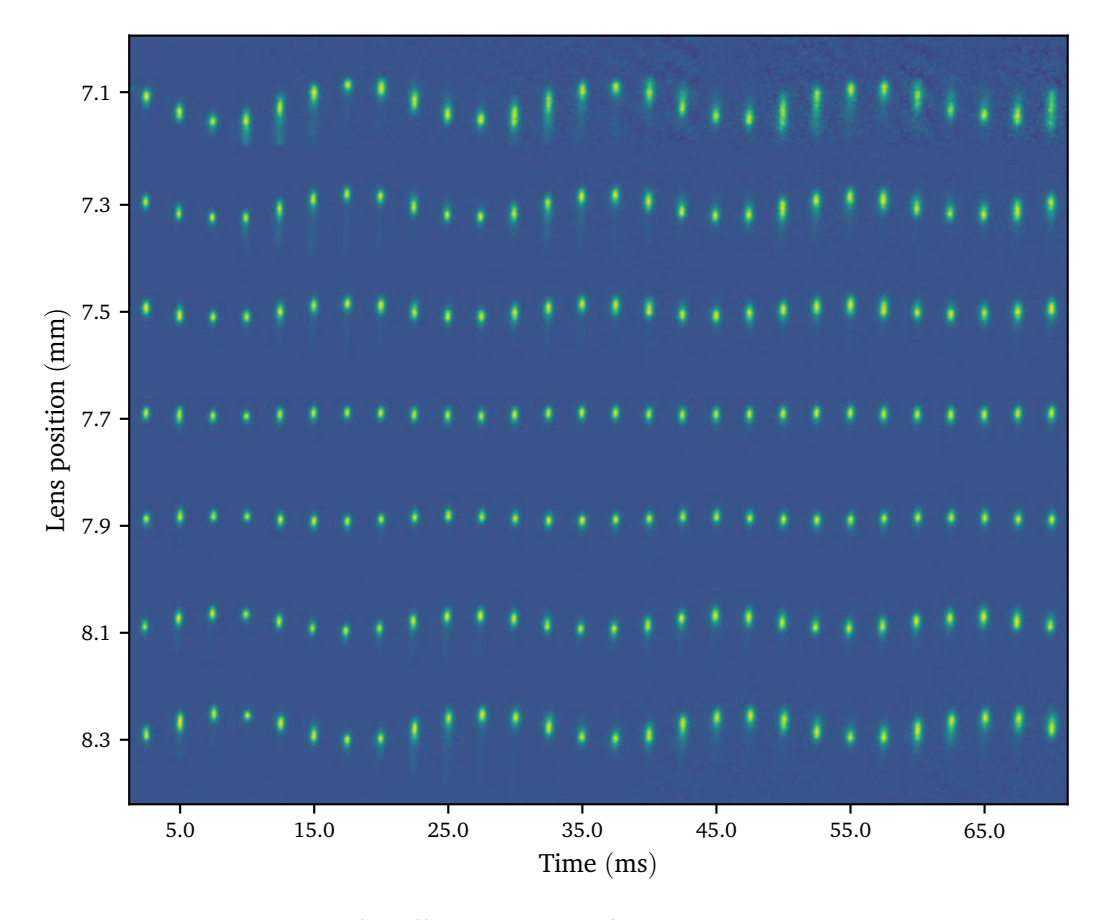


Fig. 3.11.: Averaged atomic densities for different positions of L3 resulting in varying initial axial displacements of the potential minimum from the plane of the CDT. For larger displacements, the oscillations of the atomic ensemble in the bottle beam are more pronounced. Extracting the position along the z-axis in dependency of the oscillation time can be used to determine the axial trapping frequency to $\omega_{z,\max} = 55.9(7)\,\mathrm{Hz}$ for the smallest initial distance from the potential minimum. The average frequency over all initial displacements is $\bar{\omega}_z = 2\pi \times 53.7(7)\,\mathrm{Hz}$.

corresponding linear fits (green solid and red dashed). The extracted oscillation frequencies shown in Fig. 3.13 (bottom) show a symmetric decline for larger displacements from the equilibrium position with a maximum value $\omega_{z,\text{max}} = 2\pi \times 55.9(7)\,\text{Hz}$ for the smallest shift and an average value of $\bar{\omega}_z = 2\pi \times 53.7(7)\,\text{Hz}$. For the following discussions $\omega_{z,\text{max}}$ will be used. An increasing anharmonicity of the potential for larger deviations from the potential minimum expected to be one reason behind this shift towards smaller oscillation frequencies. Interestingly, the largest damping constant $\gamma = 18.7(55)\,1/\text{s}$ is found for the smallest displacement from the equilibrium position Fig. 3.13 (bottom) which can also be seen in the raw data shown in Fig. 3.11. The average damping constant is evaluated to $\bar{\gamma} = 10.7(67)\,1/\text{s}$.

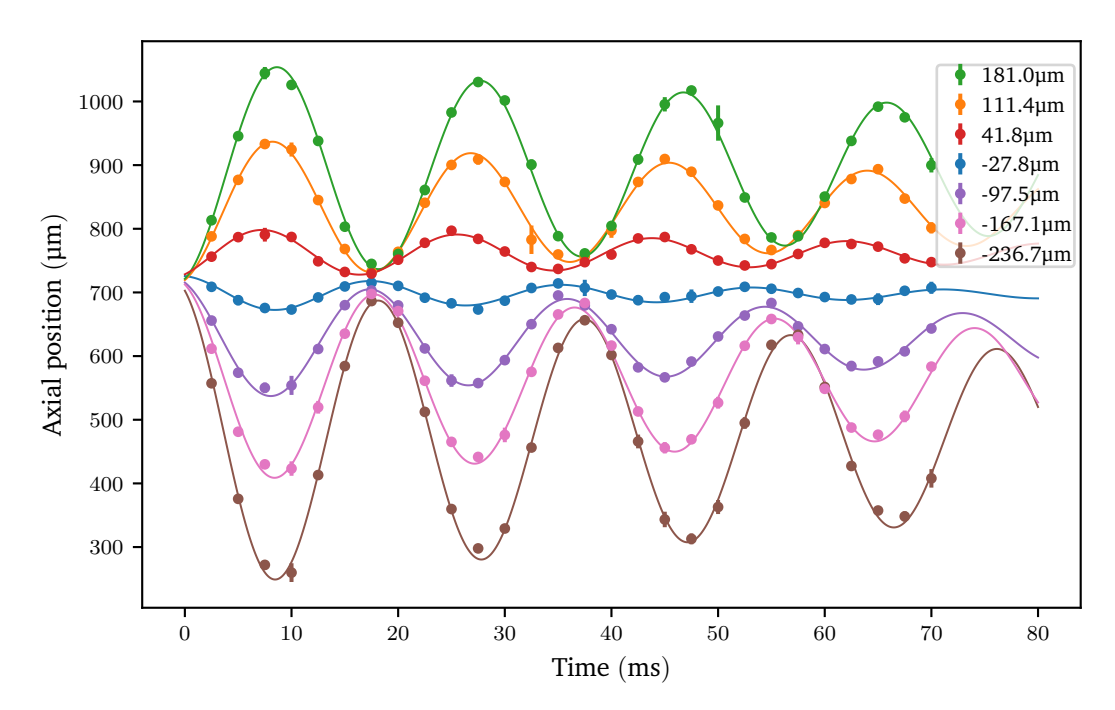


Fig. 3.12.: Position along the y-axis extracted from the column densities shown in Fig. 3.11 for each initial position (coloured dots). Solid lines with the corresponding colour show the fits to a damped oscillation for each data set.

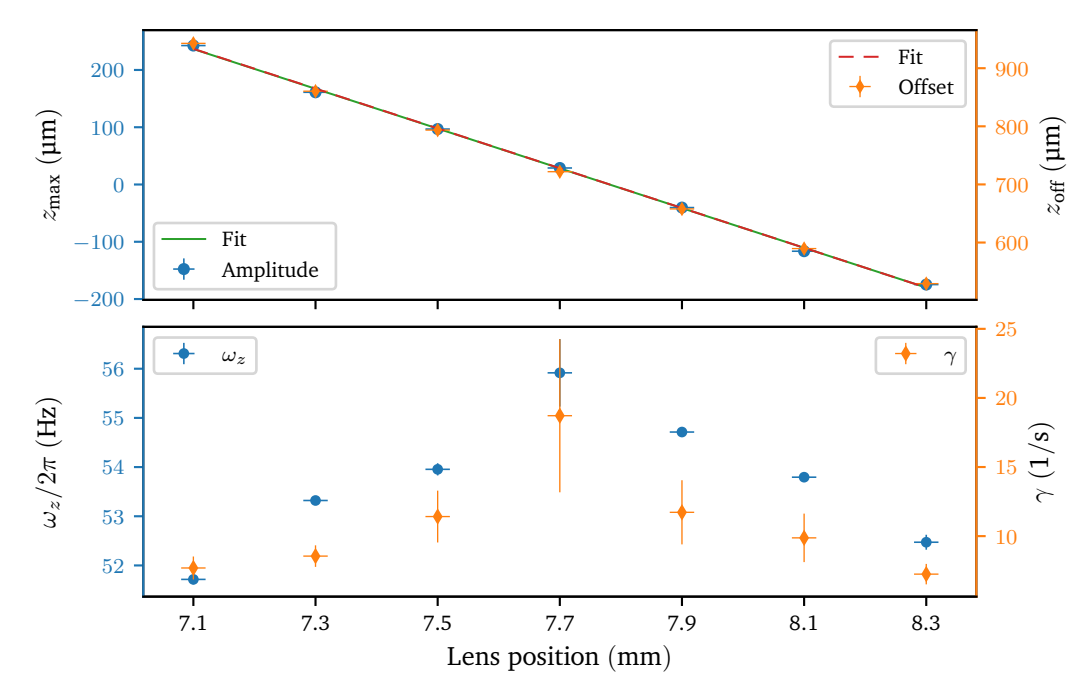


Fig. 3.13.: (top) Amplitudes $z_{\rm max}$ (blue dots) and offset $z_{\rm off}$ (orange diamonds) of the damped oscillation fits in Fig. 3.12 as a function of the initial position with linear fits shown and green solid and red dashed lines. From the slope of both amplitude and offset of the sinusoidal fits, the magnification value of the two lenses L4 and L5 can be extracted to $M_{4,5}^{\rm amp.}=0.59(1)$ and $M_{4,5}^{\rm off.}=0.59(1)$. (bottom) Oscillation frequencies ω_z (blue dots) and damping constants γ (orange diamonds) as a function of the initial position. The highest frequency is measured for the initial position closest to the potential minimum $\omega_{z,{\rm max}}=2\pi\times55.9(7)$ Hz coinciding with the highest damping rate $\gamma=18.7(55)$ $1/{\rm s}$ with an average value of $\bar{\gamma}=10.7(67)$ $1/{\rm s}$.

Spatial extent of the bottle-beam potential

In addition to the axial trapping frequency, the size of the bottle-beam potential in the atom plane is investigated. To confirm the spatial extent of the bottle-beam potential, a light-sheet (LS) potential [see Section 2.4.3] is used to sample planes of finite thickness of the bottlebeam potential in the plane of the CDT. The used ligh-sheet is built as a MOPA setup with a TA laser at 783.5 nm providing an attractive potential with a vertical trapping frequency of $\omega_{z,\mathrm{Ls}} = 2\pi \times 169.0(15)\,\mathrm{Hz}$ and axial trapping frequencies $\omega_{x,y} < 2\pi \times 10\,\mathrm{Hz}$. Therefore, the light sheet provides a quasi-uniform potential in the xy-plane where the atoms expand almost undisturbed. For typical atom numbers in a BEC and temperatures of thermal clouds, the resulting thickness of the density distribution inside the light sheet is below 10 µm which makes it an ideal tool to perform a tomographic measurement of the bottle-beam potential. Again, the measurement is performed for different axial positions of L3 with spacing of $500(10) \, \mu m$ which results in displacements of 174(8) µm of the bottle-beam potential in the atom plane. A BEC is produced in the CDT. By linearly decreasing the optical power of the CDT from 41.7 mW to 0 mW and simultaneously increasing the optical power in the light sheet from 0 mW to 137.5 mW in 40 ms [see Fig. 3.14] the atoms are transferred into the light sheet potential. Following this transfer, the atoms expand for a time of 7 ms to form a thin layer of atoms that samples the radial structure of the bottle-beam potential in the selected plane. Finally, the optical power in the bottle beam is raised from 0 mW to 9.4 mW over 3 ms and kept at that power for an additional 5 ms. Imaging is performed in vertical direction in situ. The low optical power in the bottle beam and short exposure times are chosen to decrease the spontaneous scattering rate for planes outside the CR focal plane with a non-vanishing intensity also for the central region.

Since the bottle-beam potential is repulsive, it decreases the atomic density in the light sheet

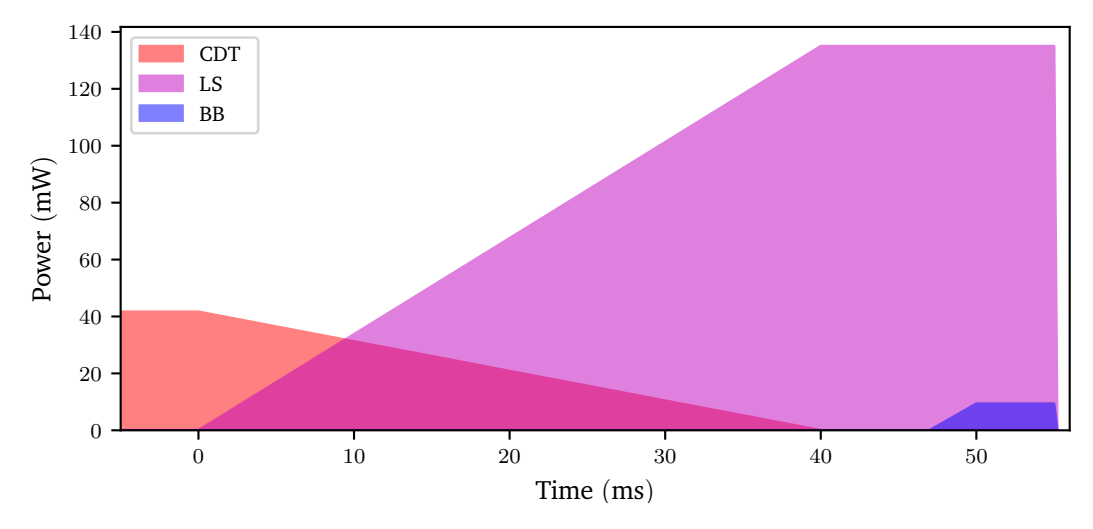


Fig. 3.14.: Schematic visualisation of the experiment to probe the radial potential in the atom plane. A BEC is created in the CDT and transferred to the light sheet potential by simultaneously increasing the optical power in the light sheet while decreasing the one in the CDT over $40\,\mathrm{ms}$. After an expansion time of $7\,\mathrm{ms}$ in the light sheet, the atoms form a thin layer and the bottle-beam potential is switched on for a total of $8\,\mathrm{ms}$ after which the resulting density distribution is detected. The resulting atomic column density distributions are shown in Fig. 3.15.

proportionally to the intensity gradient. This results in an imprint of the intensity distribution in the atomic density visualised in Fig. 3.15 for all selected planes. For planes where the bottle beam has a radial minimum, a part of the atoms remain in the centre of the density

distributions. The doughnut-shaped intensity of the bottle beam is clearly visible for all planes investigated though, which is counter-intuitive since the total displacement range is well above the expected length of the bottle-beam potential in the atom plane. An explanation for this observation is given by the vertical detection used to capture these atomic density distributions. Through this type of detection, all information regarding the position of atoms along the *z*-axis is lost, caused by the integrative nature of the vertical detection. This results in atoms scattered out of the light sheet potential but remaining radially trapped by the bottle beam to be detected in the central position of the bottle beam caused by the short exposure time and TOF.

The number of atoms that have been captured in the centre of the bottle beam in dependence

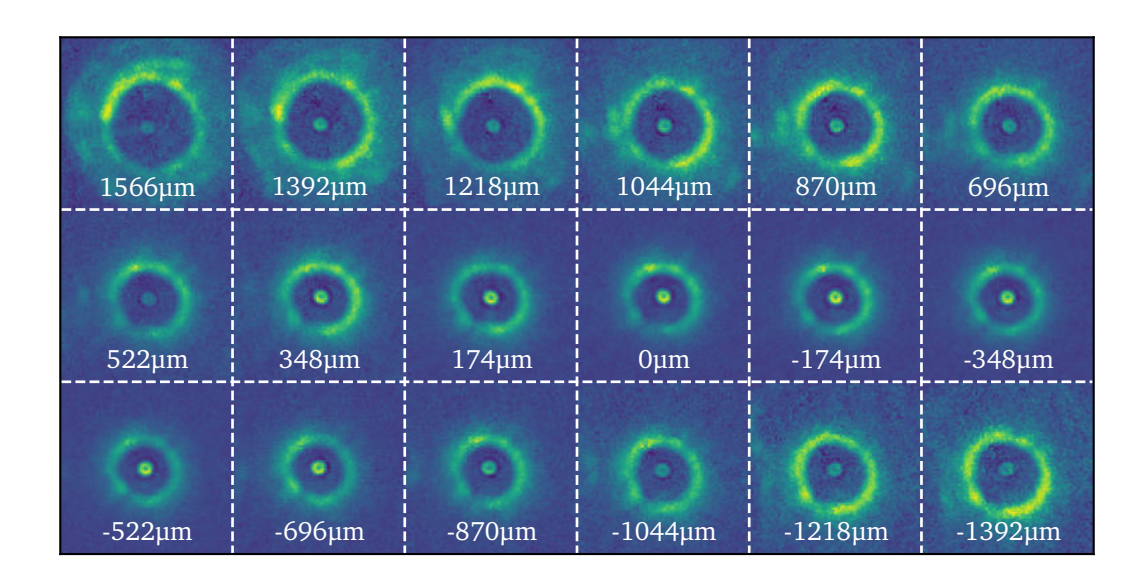


Fig. 3.15.: Atomic column density distributions obtained by the experiment for different axial positions of the intermediate image. The repulsive potential of the bottle beam pushes atoms away from regions of high intensity, leaving behind an imprint of the radial intensity distribution. From the atomic column density in the centre, the axial length of the bottle beam can be inferred.

on the axial position of L3 can be used to estimate the length of the bottle beam in the vacuum chamber. In Fig. 3.16 (top) the averaged line density is visualised, derived by selecting a square region containing the central column density from Fig. 3.15 integrating over both axes separately and taking the average. Integrating over both axes of the central column density gives the atom number trapped radially by the bottle beam as shown in Fig. 3.16(bottom). From this atom distribution, the length of the bottle-beam potential in the vacuum chamber can be inferred to $l_{\rm BB}^{\rm AP}=1570(174)\,\mu{\rm m}$ which is in good agreement with the expected value of $1465(224)\,\mu{\rm m}$ given by scaling the length of the dark focus with the total magnification $|M_{\rm tot}|=0.32(2)$. The offset of approximately 500 atoms for large shifts of the bottle beam can be explained by atoms being pushed out of the light sheet by spontaneous scattering while remaining radially trapped by the bottle beam as explained before. Furthermore, from the radial extent of the central column density distribution, the radial dimension of the bottle beam can be estimated to $R_0^{\rm AP}=13.2(26)\,\mu{\rm m}$ which is in excellent agreement with the expected value of $|M_{\rm tot}|\times R_0=0.32(2)\times 41.95(190)\,\mu{\rm m}=13.4(10)\,\mu{\rm m}$.

The experimentally determined value for the total magnification $|M_{tot}| = 0.32(2)$ used for

these estimates is extracted from a measurement characterising the axial position of the atomic density in relation to the optical power used for the bottle beam. Due to gravity, the axial equilibrium position of the atoms is dependent on the strength of the bottle-beam potential. Varying the optical power of the bottle beam shifts the equilibrium position in a known fashion, therefore leaving the magnification as a free parameter. To extract this information, a BEC is loaded into the bottle beam at maximal power. After an initial holding time, the optical power is lowered to the targeted value and an additional holding time is added to ensure minimum. From the axial position of the atom cloud as a function of the optical power, the magnification is determined to $|M_{\rm tot}|=0.32(2)$ in agreement with the value of $|M_{\rm tot}^{\rm th}|=0.30(2)$ calculated from the parameters of the optical reimaging system.

In conclusion, the axial and radial spatial extent of the bottle-beam potential were experimen-

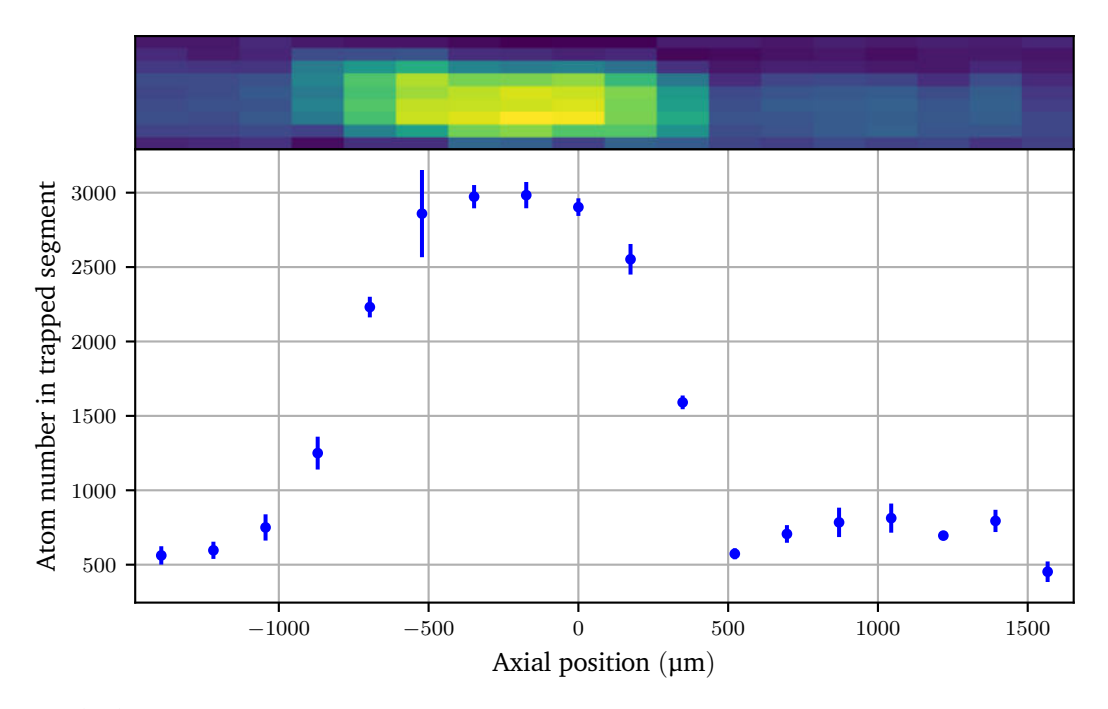


Fig. 3.16.: (top) Central atomic line density depending on the initial position of the bottle-beam potential extracted from the column densities in Fig. 3.15. (bottom) From the determined atom distribution, the length of the bottle can be inferred to $l_{\rm BB}^{\rm AP}=1570(174)\,\mu{\rm m}$ in the vacuum chamber. The background signal of approximately 500 atoms originates from atoms outside the light-sheet potential but radially confined by the bottle beam, which the detection system cannot differentiate from atoms in the light-sheet potential.

tally verified with good agreement with the expected values. Furthermore, the axial trapping frequency was determined from dipole oscillations of atomic ensembles for varying initial displacements of the potential equilibrium. In Tab. 3.3, a complete summary of all values calculated using the experimental properties of the Gaussian beam, the BC, the optical setup, as well as the values measured by the described experiments is given.

Tab. 3.3.: Comparison of measured and calculated parameters of the bottle beam: Experimental values are determined from the intensity distribution in the focal plane and the atom distribution in the atom plane. Calculated values in the focal plane: $l_{\mathrm{B}B}^{\mathrm{F}P}, \omega_r^{\mathrm{F}P}$, and $\omega_z^{\mathrm{F}P}$ are determined for $\rho_0=0.96(8)$ using Eqs. (3.10) and (3.11) and the experimental values for w_0 and z_{R} as input; the experimental value of R_0 is not applied for calculations since for its determination an assumption for the value of ρ_0 has to be made, leading to large uncertainties. Calculated values in the atom plane: w_0 , R_0 , $l_{\mathrm{B}B}$, U_{trap} , U_{trap} , ω_r , and ω_z are based on the calculated values in the focal plane and the magnification $|M_{\mathrm{tot}}|=0.32(2)$. The potential depth $U_{\mathrm{trap},g}$ includes the effect of gravity.

	Focal	plane	Atom plane		
	Calculation	Light field	Calculation	Experiment	
$\overline{w_0}$	44.0(19) μm	$43.6(30)\mu{\rm m}$	14.1(11) μm	_	
R_0	$42.0(19) \mu m$	$41.2(28)\mu\mathrm{m}$	$13.4(10)\mu{ m m}$	$13.2(26)\mu{\rm m}$	
$l_{ m BB}$	$14.3(10){ m mm}$	$12.75(50)\mathrm{mm}$	$1.47(22000)\mu{\rm m}$	1.570(174) mm	
ω_r	$2\pi \times 295(65)\mathrm{Hz}$	$2\pi imes 325(38)\mathrm{Hz}$	$2\pi \times 2881(730) \mathrm{Hz}$	_	
ω_z	$2\pi \times 1.87(23)\mathrm{Hz}$	$2\pi\times 1.97(21)\mathrm{Hz}$	$2\pi \times 57(13)\mathrm{Hz}$	$2\pi \times 55.9(7)\mathrm{Hz}$	
$U_{\sf trap}$	_	_	$k_{ m B} imes 166.5\mu{ m K}$	_	
$U_{trap,g}$	_	_	$k_{ m B} imes 87.0\mu{ m K}$	_	

Holding-time measurement

After successfully characterising the bottle-beam potential the holding time of an atomic ensemble is measured. To determine the holding time of an ensemble of ultracold atoms in such a potential, the number of residual atoms in the potential for varying holding times from 25 ms to 500 ms is performed. The measurement is done analogously to the oscillation measurement described in Fig. 3.10 with a longer TOF of 2 ms to ensure the atomic density has decreased enough to avoid full absorption of the detection light. In Fig. 3.17 (top), the atomic column densities (averaged over multiple realisations) for the selected holding times are shown as a false-colour plot, normalised to the maximum column density for the smallest holding time of 25 ms. Using a series of 2D Gaussian fits, the atom number can be determined and plotted over the holding time, see Fig. 3.17 (bottom). The holding time τ defined as the 1/e time can be determined by fitting an exponential decay $N(t) = N_0 \exp(-t/\tau)$ to the atom number. This results in a holding time of 205(3) ms which is an order of magnitude smaller than the holding time of the atoms in the CDT which typically is on the order of 10 s. The decreased holding in the bottle beam is due to several reasons, one being the small detuning necessary to produce a strong enough potential to hold the atoms against the gravitational potential paired with the large demagnification. This large demagnification results in a radial trapping frequency in the kHz range, effectively squeezing the atoms into a 1D line. The orientation of the bottle beam with the weak propagation axis parallel to gravity also leads to a drastically increased scattering rate, since the effective potential minimum is shifted away from the low-intensity region of the bottle beam. This counteracts the beneficial properties of the bottle beam. For this reason, in the next subsection, an idealised bottle-beam potential is compared against red-detuned potentials based on Gaussian beams in different experimental scenarios.

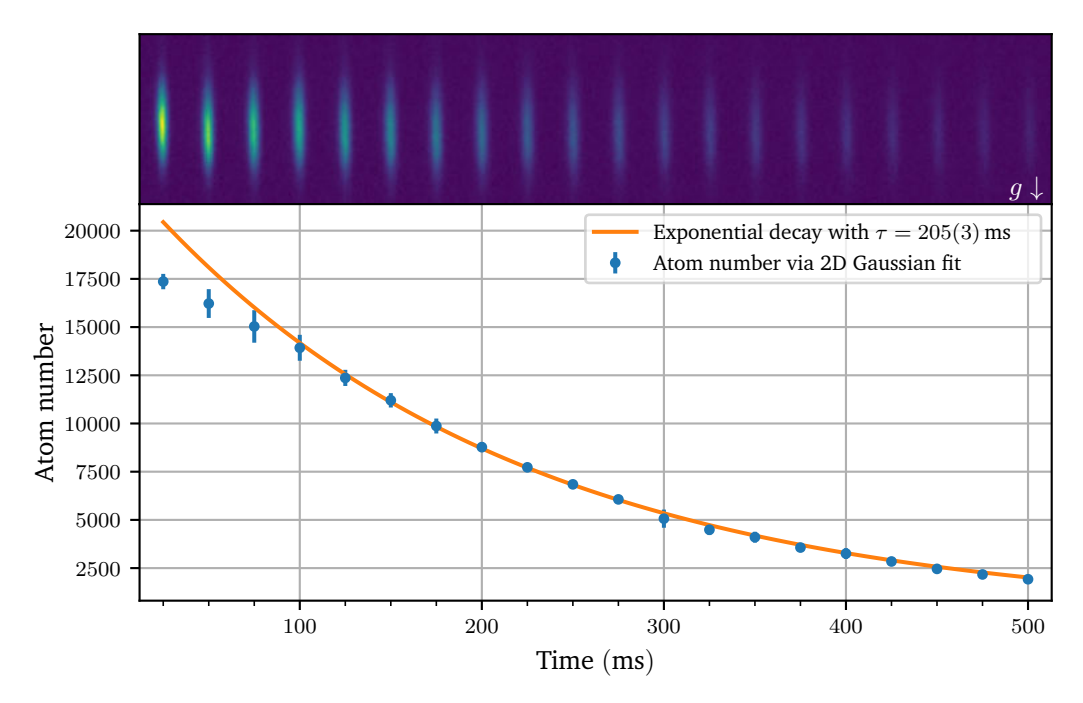


Fig. 3.17.: (top) Atomic column density in the bottle beam imaged by the horizontal detection as a function of the holding time in the bottle-beam potential. (bottom) Determined average atom number (blue dots) depending on the holding time. Through an exponential fit (orange) to the points for $t \geq 100\,\mathrm{ms}$, a lifetime of $\tau = 205(3)\,\mathrm{ms}$ can be extracted.

3.2.4. Improving the bottle-beam trap

As discussed in Section 3.2.2, the bottle-beam potential created by CR is capable of trapping atoms in 3D. Since the current setup at the ATOMICS experiment is not appropriate for further investigations for multiple reasons, leading to short lifetimes in the trap and the certain destruction of the BEC state, in this section advanced setups are discussed based on numerical calculations. For these comparisons it is assumed that the weak dimension of the potentials are oriented perpendicular to gravity so that the influence of the gravitational potential, especially the shift of the potential minimum, can be neglected. In detail, three experimental setups widely used in cold-atoms experiments are investigated: the single beam and crossed beam configuration for BEC experiments as well as a tweezer array setup for neutral-atom quantum computing. In Tabs. 3.4 to 3.6, trap setups based on attractive Gaussian beam and the bottle beam ($\rho_0^{\rm DF}=0.924$) are compared taking several key values like the radial and axial trapping frequencies ω_r and ω_z , the average harmonic oscillator frequency $\bar{\omega}_{\rm ho}$, the mean scattering rate $\bar{\Gamma}_{\rm TF}$ for a BEC in the Thomas-Fermi approximation, and the potential depth $U_{\rm trap}$ into account.

Single-beam trap

For the single beam setup, an optical power of $P_{\rm G}=1\,{\rm mW}$ at a detuning of $+1\,{\rm nm}$ with respect to the D_1 line of $^{87}{\rm Rb}$ at $\lambda_{\rm D1}=794.98\,{\rm nm}$ is chosen for the Gaussian beam with an equal detuning of opposite sign for the bottle beam. To match the radial trapping frequency of the Gaussian beam setup, the required optical power in the bottle beam $P_{\rm BB}$ can be calculated by dividing Eq. (3.10) by Eq. (2.7) which results in the condition

$$P_{\rm BB} = \frac{1}{0.383^2} \left| \frac{\tilde{U}_{0,\rm G}}{\tilde{U}_{0,\rm BB}} \right| P_{\rm G} = 6.82 \left| \frac{\tilde{U}_{0,\rm G}}{\tilde{U}_{0,\rm BB}} \right| P_{\rm G}. \tag{3.12}$$

In this context, matching the radial trapping frequencies provides a basis for comparing the traps, though matching the radial trapping depth could serve as an alternative criterion. With Eq. (3.12), the necessary optical power for the bottle beam can be calculated to $P_{\rm BB} = 9.00 \, {\rm mW}$. For this optical power and detuning, the axial trapping frequency of the bottle beam is slightly increased with respect to the Gaussian beam with the trap depth being fractionally smaller. Here, the trap depth of the bottle beam is given by the weakest point of the potential [see Tab. 3.1]. To compare both potentials in terms of the mean scattering rates, a BEC is assumed of 20 000 87 Rb atoms in the F=1 hyperfine state, with a scattering length $a_{11}=100.4\,\mathrm{a_0}$ where a_0 denotes the Bohr radius [87]. For both beams a waist of $38 \,\mu m$ is chosen to match the CDT at the ATOMICS experiment. The mean scattering rate is computed by determining the atomic density distribution in the Thomas-Fermi approximation. Transforming the density to a probability distribution by normalisation and multiplying it with the numerically computed intensities of the Gaussian beam and the bottle beam results in a mean scattering rate Γ that represents the real situation of an atomic ensemble in such potentials better than comparing just the central scattering rates. Here, the main advantage of the bottle beam is clearly evident since the mean scattering rate is reduced by a factor of about 700 compared to the Gaussian beam whilst the remaining parameters are nearly identical.

Tab. 3.4.: Comparison of Gaussian and bottle-beam based trap for BECs in a single-beam configuration. The dark-focus trap exhibits reduced rates for spontaneous scattering at comparable trapping properties.

Light-field parameters and calculated			
values for configuration based on			
Gaussian beam	Bottle beam		
$P_{\rm G} = 1{\rm mW}$	$P_{\rm BB} = 9.00\rm mW$		
$\lambda_{\rm G}=795.98{\rm nm}$	$\lambda_{\mathrm{BB}} = 793.98\mathrm{nm}$		
$2\pi \times 176.3\mathrm{Hz}$	$2\pi imes 176.3\mathrm{Hz}$		
$2\pi \times 0.831\mathrm{Hz}$	$2\pi\times1.083\mathrm{Hz}$		
$2\pi \times 29.6\mathrm{Hz}$	$2\pi imes 32.3\mathrm{Hz}$		
$k_{\mathrm{B}} imes -4.63\mathrm{\mu K}$	$k_{\mathrm{B}} imes 4.20\mathrm{\mu K}$		
$6.55 \frac{1}{s}$	$9.19 \times 10^{-3} \frac{1}{s}$		
	values for configances of values for configances of $P_{\rm G}=1~{\rm mW}$ $\lambda_{\rm G}=795.98~{\rm nm}$ $2\pi\times176.3~{\rm Hz}$ $2\pi\times0.831~{\rm Hz}$ $2\pi\times29.6~{\rm Hz}$ $k_{\rm B}\times-4.63~{\rm \mu K}$		

Crossed-beam trap

Next, the CDT setup of the ATOMICS experiment with a wavelength of 1070 nm and a typical optical power of 35 mW at the end of evaporation is compared to a bottle-beam setup with an equal power [Tab. 3.5]. From Eq. (3.12), the necessary wavelength can be determined, again under the constraint of equal radial trapping frequencies, which gives $\lambda_{\rm BB}=758.5$ nm. In both cases, the total potential is given by the sum of two individual single-beam potentials intersecting orthogonally. Again, the parameters are similar to the bottle beam providing an increased potential depth and reduced mean scattering rate. The scattering rate in the bottle beam can be further reduced by increasing the optical power and detuning. This showcases, that in scenarios where a large detuning is not available, the bottle-beam potential can offer a valuable alternative to fardetuned optical traps.

Single-atom tweezers

Finally, a setup for quantum computing based on neutral atoms in red-detuned Gaussian-beam tweezer arrays is compared to an array of bottle beams. Here, a typical waist of 1 µm is used

Tab. 3.5.: Comparison of Gaussian and bottle-beam based crossed-beam configuration for BECs.

Application	Light-field parameters and calculated				
case	values for configuration based on				
	Gaussian beam	Bottle beam			
BEC in	$P_{\rm G}=35{\rm mW}$	$P_{\rm BB}=35{\rm mW}$			
crossed-beam trap	$\lambda_{\rm G}=1070{\rm nm}$	$\lambda_{\mathrm{BB}} = 758.5\mathrm{nm}$			
ω_r (one beam)	$2\pi \times 124.8\mathrm{Hz}$	$2\pi \times 124.9\mathrm{Hz}$			
ω_z (one beam)	$2\pi \times 0.791\mathrm{Hz}$	$2\pi\times0.733\mathrm{Hz}$			
$ar{\omega}_{ ext{ho}}$	$2\pi \times 140.0\mathrm{Hz}$	$2\pi\times140.2\mathrm{Hz}$			
U_{trap}	$k_{\mathrm{B}} imes -2.32\mathrm{\mu K}$	$k_{ m B} imes 3.16\mu{ m K}$			
$ar{\Gamma}_{ ext{TF}}$	$16.1 \times 10^{-3} \frac{1}{s}$	$3.05 \times 10^{-3} \frac{1}{s}$			

which is readily achievable by quantum gas microscopes with large numerical aperture (NA) objectives. The goal is to create a number of 100 traps with a depth of $|U_{\rm trap}|=k_{\rm B}\times 1\,{\rm mK}$ with a total optical power of 1W available at $\lambda_{\rm G}=1051\,{\rm nm}$ and $\lambda_{\rm BB}=759\,{\rm nm}$. Since this setup is used with single atoms, for the mean scattering rate, the ground state wave function based on the trapping frequencies is calculated and the scattering rate is averaged over this wave function. For this setup, the biggest advantage for the bottle beam can be gained with the mean scattering rate being reduced by a factor of 10^5 compared to the Gaussian-beam tweezer. This result is not surprising, since the ground state wave function samples only a small area very close to the potential minimum where in the case of the Gaussian beam, the largest scattering rates are observed. Therefore, using bottle beams instead of conventional Gaussian beam traps as tweezer arrays would vastly decrease the scattering and heating of single neutral atoms and hence increase their lifetime. This would be beneficial for quantum computing efforts based on this approach since decreased heating means extended lifetimes and less decoherence.

The combination of tweezer arrays with CR has not yet been studied. In the following section, the combination of a technique based on MLA to create tweezer arrays in combination with CR is investigated numerically and an example of an implementation is given.

Tab. 3.6.: Comparison of Gaussian and bottle-beam based trap for an optical tweezer-arrays setup with possible applications in neutral-atom quantum computers.

Application	Light-field parameters and calculated				
case	values for configuration based on				
	Gaussian beam	Bottle beam			
Single-atom	$P_{\rm G} = 10{\rm mW}$	$P_{\rm BB} = 10{\rm mW}$			
tweezers	$\lambda_{\rm G}=1051{\rm nm}$	$\lambda_{\mathrm{BB}} = 759\mathrm{nm}$			
ω_r	$2\pi \times 98479\mathrm{Hz}$	$2\pi imes 98477\mathrm{Hz}$			
ω_z	$2\pi \times 23285\mathrm{Hz}$	$2\pi\times21976\mathrm{Hz}$			
$ar{\omega}_{ ext{ho}}$	$2\pi \times 60896\mathrm{Hz}$	$2\pi imes 59732\mathrm{Hz}$			
U_{trap}	$k_{\mathrm{B}} \times -1001\mathrm{\mu K}$	$k_{\mathrm{B}} imes 907\mathrm{\mu K}$			
$ar{\Gamma_{GS}}$	$3.87\frac{1}{s}$	$11.7 \times 10^{-6} \frac{1}{s}$			

3.3. Conical refraction with microlens arrays

Recent efforts to build experimental setups based on neutral atoms, for of quantum computing, quantum simulation, and quantum sensing, have led to increasing numbers of individual neutral atoms trapped in arrays of optical tweezers [64, 65, 138–141]. Different techniques are used to generate the tweezer arrays necessary to trap large numbers of neutral atoms like optical lattices [142], SLM based tweezers [143], and tweezer arrays based on MLAs [63, 64, 139, 144]. Typically, these tweezer arrays function as red-detuned optical dipole potentials, trapping the atoms in the intensity maximum. As discussed in the case of ultracold atoms in the previous Section 3.2.2 this leads to increased scattering and therefore increased heating and decoherence. Especially, since to reach large numbers of tweezers with limited optical power, the detuning has to be small increasing the scattering even further.

As mentioned, a common technique to create arrays of optical tweezers are microlens arrays consisting of a regular grid of small lenses typically with an aperture in the range of $10\,\mu\text{m}$ to $200\,\mu\text{m}$ with a separation (pitch) between the individual lenses on the same order. Such MLA can provide more than 10000 optical tweezers which makes them an ideal candidate for quantum computing and quantum simulation efforts based on neutral atoms. Additionally, setups based on such tweezer arrays can benefit from the Talbot effect [145]. This effect emerges, when multiple focused beams produced by the MLA interfere with each other in the direction of beam propagation, resulting in multiple planes with focal spots, so-called Talbot planes [60].

In this section, the combination of MLAs with the CR phenomenon is investigated in order to create arrays of bottle beams, providing trapping geometries with significantly reduced scattering rate and the capability to trap even atoms in highly excited Rydberg states [109].

3.3.1. Theoretical investigations

Generally, the Gaussian beam illuminating of the MLA is assumed to have a spatial extent much larger than the aperture of an individual microlens of the MLA. Therefore, the emerging fields can be described by focused plane waves, leading to a rather complex description of the intensity [146, Chapter 8.8]. The diffractive effects at the lens aperture become more pronounced as the lens diameter d decreases relative to the wavelength λ , characterized by the Fresnel number $\mathrm{FN} = d^2/4\lambda f_\mathrm{g}$, where f_g is the geometric focal length determined by the diffractive properties of the lens. This leads to a reduction of the focal length, resulting in an effective focal length f_e . For $\mathrm{FN} > 3$, this reduction remains small compared to the geometric focal length [147].

Since the focus of this section is the general investigation of the CR phenomenon combined with MLAs, for the remainder of this investigation it will be assumed, that the electric field of each microlens can be described by the field of a focused Gaussian beam and each microlens produces an identical field, shifted in space by the pitch of the MLA.

Given the pitch a_{MLA} , the position of the Talbot planes for quadratic MLAs can be calculated by [60, 148, 149]

$$z_{\rm T,quad} = \frac{2a_{\rm MLA}^2}{\lambda}.$$
 (3.13)

Calculating the electric fields for a 5×5 MLA with properties given in Tab. 3.7 results in the intensity distribution shown in Fig. 3.18. In the top part, the intensity distribution in the yz-plane is shown for $|z| \le z_{\rm T}$ and $|y| \le a$. Red vertical dashed lines indicate the Talbot planes

Tab. 3.7.: Properties of the APO-Q-P72-R1 . 45 MLA (for $\lambda=780\,\mathrm{nm}$) used for the numerical calculations of the Talbot planes in Fig. 3.18 and the bottle-beam array in Fig. 3.19.

MLA-type	$a_{\mathrm{MLA}} (\mu \mathrm{m})$	ROC (mm)	f_g (mm)	f_e (mm)	NA	FN	$w_{0,g}$ (µm)	$ ho_a$
AP0-Q-P72-R1.45	72	1.45	3.194	1.571	0.011	0.5	32.04	2.25

 $z_{\pm 1}$, $z_{\pm 1/2}$, and the focal plane z_0 for which the intensity distribution in the plane is shown in the lower part of Fig. 3.18. In the fractional Talbot planes $z_{\pm 1/2}$, focal spots are visible, shifted by $a_{\rm MLA}/2$ while in the principal planes $z_{\pm 1}$ a self-image of the focal plane z_0 is produced. As mentioned above, these calculations assume Gaussian beams for each microlens and effects like diffraction and a non-uniform illumination of the microlenses are neglected. Under these

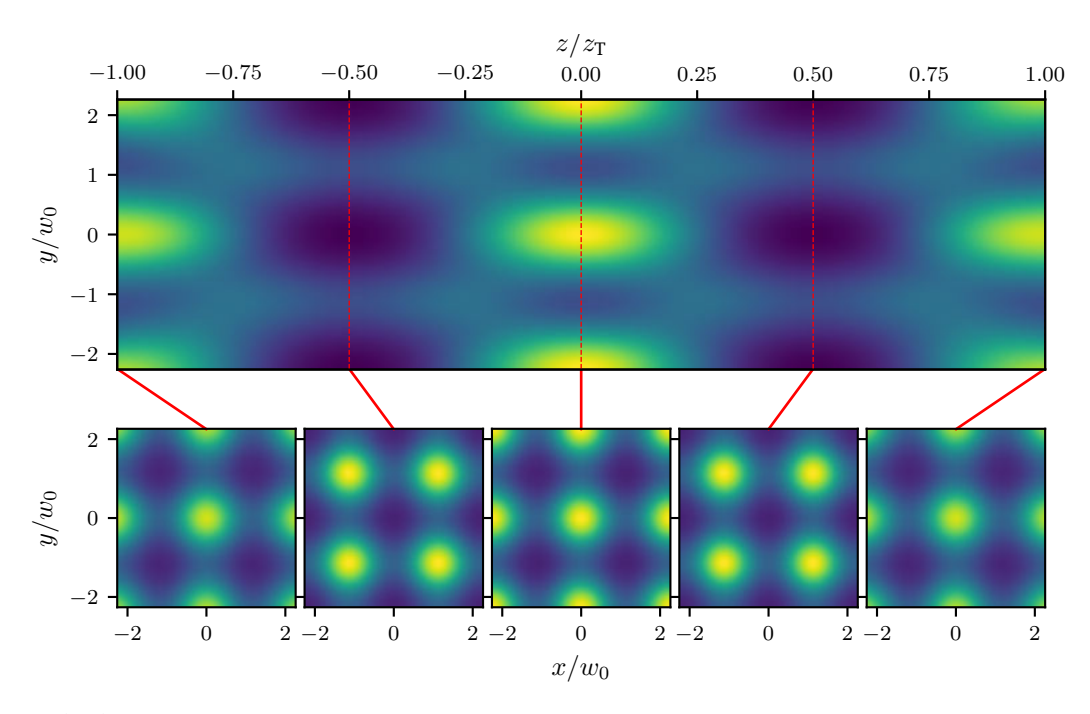


Fig. 3.18.: (top) Intensity calculated for a 5×5 array of microlenses with properties based on Tab. 3.7 in the yz plane for $|y|\leq a_{\text{MLA}}$ and $|z|\leq z_T$. For $|z|=z_T$ a self-image of the focal plane is formed. Here, an identical Gaussian beam for each microlens is assumed with equal optical power P, waist w_0 and Rayleigh length z_{R} . (bottom) Intensitiens in the xy-plane for the planes z_0 , $z_{\pm 1/2}$, and $z_{\pm 1}$.

assumptions, it is straightforward to calculate the expected intensity distribution for the CR in combination with the input field created by the microlens array described above. Since an array of bottle beams is of interest, $\rho_0^{\rm DF}=0.924$ is numerically implemented and similar to the MLA calculation above, a 5×5 setup is used. The electric field is numerically calculated for each input field using Eqs. (3.3), (3.7a) and (3.7b) and coherently added up to result in the total electric field, then the absolute square is taken to calculate the intensity distribution. In Fig. 3.19, analogously to Fig. 3.18, the intensity in the yz-plane is shown (top) with the intensity in the Talbot planes at the bottom of Fig. 3.19. Interestingly, the formation of multiple planes of bottle beams can be seen, similar to the formation of multiple planes of focal spots for the case without CR. This result is surprising since the electric field far outside of the focal plane of the CR resembles a Gaussian beam for $\rho^{\rm DF}=0.924$ as can be seen in Fig. 3.3. To gain a better understanding of the properties of such a potential, in Fig. 3.20, the axial intensity $I(\rho=0,Z)$ (top blue) is shown for a 1×1 configuration, therefore a single bottle beam, as

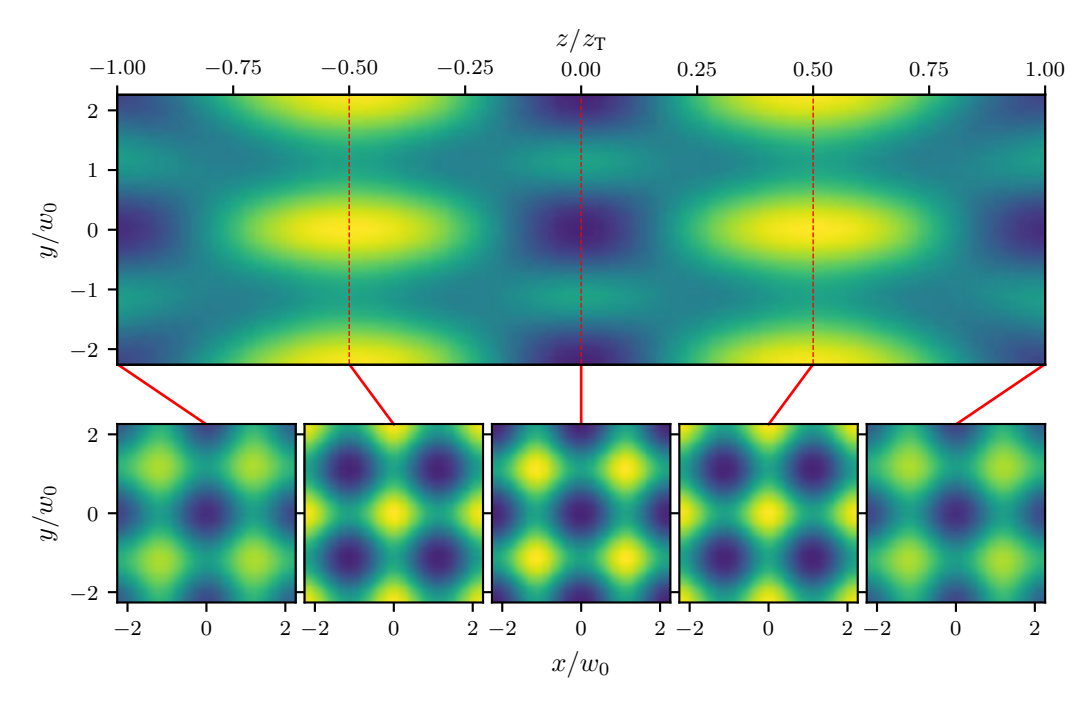


Fig. 3.19.: (top) Analogously to Fig. 3.18, the intensity is computed for the same 5×5 array of es including the CR effect based on Eq. (3.3). Similarly to the Talbot effect without the CR, the formation of self-images of the focal plane can be observed. (bottom) In the xy-plane intensity distributions for the different Talbot planes z_0 , $z_{\pm 1/2}$, and $z_{\pm 1}$, multiple dark foci are formed confirming the emergence of the Talbot effect in combination with CR.

well as for the 5×5 configuration (orange). Similarly, the radial intensity $I(\rho, Z=0)$ in the focal plane is shown for both setups Fig. 3.20 (bottom). For this plot, the intensities have been normalised to the maximum intensity of the input Gaussian beams $I_0 = 2P/\pi w_0^2$, hence the values for the single bottle beam are the same as in Fig. 3.5. From this comparison, it is already evident, that the midpoint intensity $I(\rho = 0, Z = 0)$ is increased drastically from $I_{1\times 1}(0,0) = 0$ to $I_{5\times5}(0,0)=0.077I_0$. Further, the radial and axial points of maximum intensity have shifted to $I_{5\times 5}(\rho=1.125,Z=0)=0.442$ and $I_{5\times 5}(\rho=0,Z=\pm 1.611)=0.767$. Performing harmonic fits based on Eq. (3.8) to the radial and axial intensity values of both the 1×1 and 5×5 configuration for $|Z|\leq 0.5$ and $|\rho|\leq 0.5$ results in $\chi_{\rho}^{1\times 1}=0.295(1)$ and $\chi_{\rho}^{5\times 5}=0.470(6)$ as well as $\chi_{Z}^{1\times 1}=0.239(10)$ and $\chi_{Z}^{5\times 5}=1.01(4)$. For the harmonic fits, the midpoint intensity was subtracted. This leads to a 26 % increase in the radial and 100 % increase in the axial trapping frequency. The increase of the midpoint intensity to $I_{5\times5}(0,0)=0.077~I_0$ is unintended and makes this configuration suboptimal for the trapping of BECs or single atoms. By leveraging the symmetries of the MLA as well as the $\sin(\phi)$ and $\cos(\phi)$ terms in Eq. (3.4), the midpoint intensity of the central trap can be written as

$$I(\rho = 0, Z = 0) = \left| \sum_{i,j=-m}^{m} D_{i,j}(\sqrt{i^2 + j^2}\rho_a, 0) \right|^2$$

$$= \left| \sum_{i,j=-m}^{m} B_0(\sqrt{i^2 + j^2}\rho_a, 0) \right|^2$$
(3.14)

$$= \left| \sum_{i,j=-m}^{m} B_0(\sqrt{i^2 + j^2} \rho_a, 0) \right|^2$$
 (3.15)

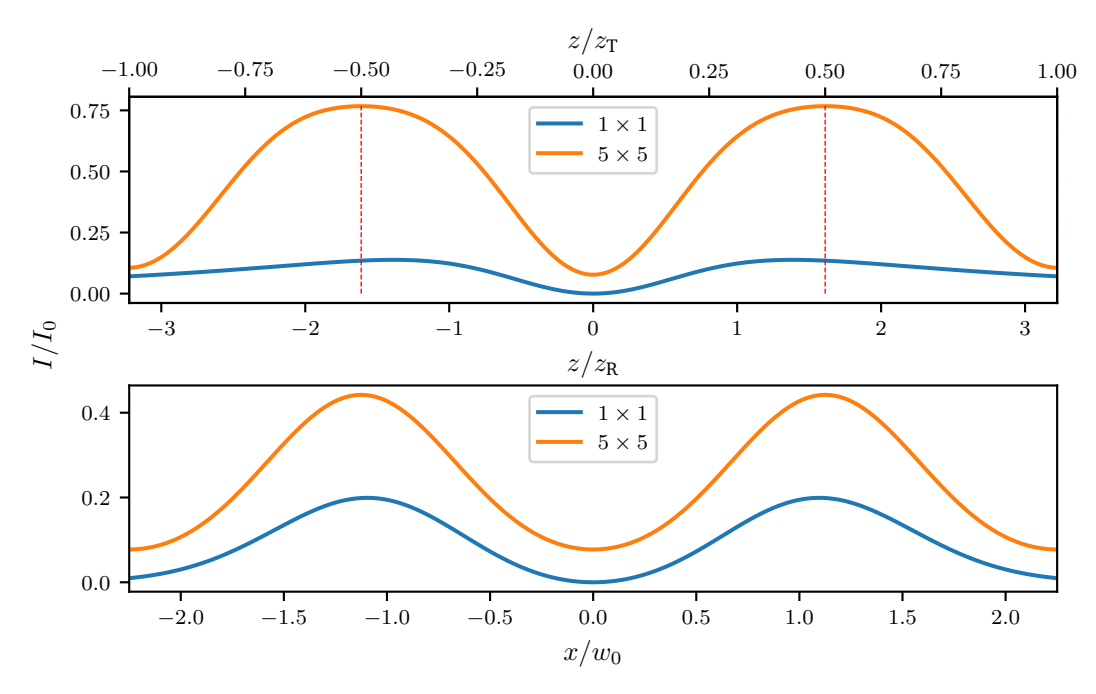


Fig. 3.20.: (top) Comparison of the axial intensity $I(\rho=0,Z)$, normalised to the maximum intensity I_0 of a single microlens, for the single (1×1) dark focus (blue) and the central field in a 5×5 microlens setup (orange). The latter shows an increased maximum value of $I_{5\times 5}(\rho=1.125,Z=0)=0.442\ I_0$ shifted further away from the focal plane. (bottom) Radial intensity $I(\rho,Z=0)$ in the focal plane, again for the single (1×1) dark focus (blue) and the central field in a 5×5 microlens setup (orange). Specifically, the elevated central intensity $I_{5\times 5}(0,0)=0.077\ I_0$ is suboptimal for applications employing this intensity distribution as potentials for ultracold or single neutral atoms.

where i and j enumerate the array positions of each lens contributing and $\rho_a = a_{\rm MLA}/w_0$ is the normalised pitch of the MLA. Calculating the dependency of this midpoint intensity value for different configurations leads to an interesting result shown in Fig. 3.21. The midpoint intensity for a single bottle beam is naturally equal to zero and adding the diagonal traps does not change this significantly. Only when by a factor of $\sqrt{2}$ closer traps are added in the 1×3 or + configuration, the midpoint intensity starts to increase. Finally, it reaches the maximum value for the 3×3 configuration with no further increase for the 5×5 setup at the numerical precision chosen. It is important to note, that these results have been obtained using a single value of ρ_0 and ρ_a and cannot be simply extrapolated to all combinations of these two parameters. Since the light fields produced by CR have a unique distribution of polarisations as discussed in Section 3.1, the behaviour of the midpoint intensity depending on ρ_0 or the pitch of the MLA $a_{\rm MLA}$ is non-trivial. The fact that ρ_a of the MLA does not change under (de-)magnification means that the waist can be adjusted to reach any value of ρ_0 for a given principal radius R_0 . To analyse the dependence of the midpoint intensity on this ratio and ρ_0 for a 3×3 array, it is calculated over the parameter ranges $2 \le \rho_a \le 4$ and $0.5 \le \rho_0 \le 2$ using

$$I_{3\times3}(0,0) = |B_0(0,0) + 4B_0(\rho_a,0) + 4B_0(\sqrt{2}\rho_a,0)|^2.$$
(3.16)

For these values of ρ_0 and ρ_a it was numerically verified, that the increase of intensity by the higher order 5×5 can be neglected. The results are visualised in Fig. 3.22 on a linear (left) and logarithmic (right) colour map. For better clarity, for each value of ρ_a the value of ρ_0 with the lowest midpoint intensity is marked in red. Interestingly, for $\rho_a>2.60(2)$ this value bifurcates. One branch asymptotically approaches $\rho_0^{\rm DF}=0.924$ which, for large values of

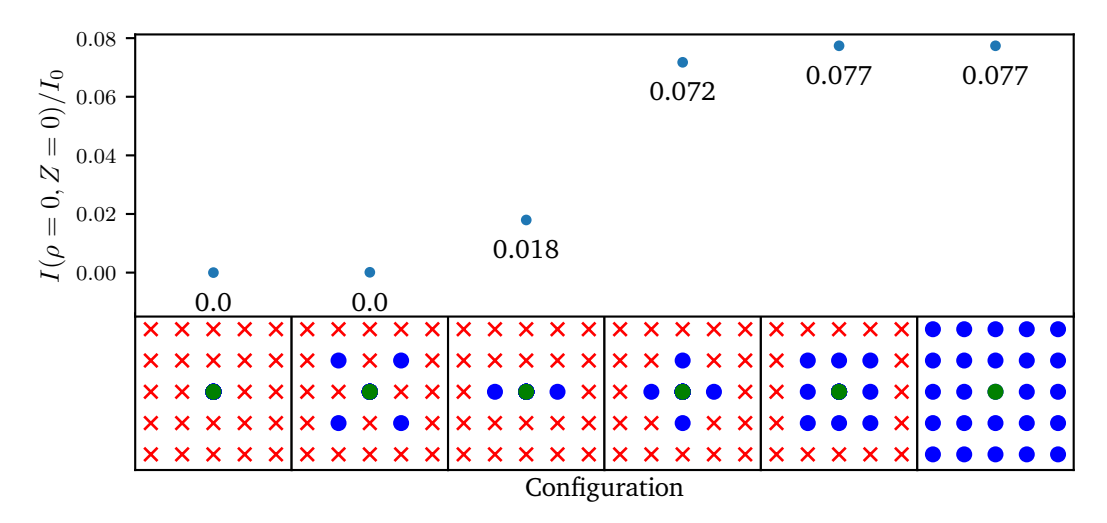


Fig. 3.21.: Midpoint intensity values $I(\rho=0,Z=0)/I_0$ for the central lens depending of different configurations. The contribution from the diagonal lens is suppressed due to its $\sqrt{2}$ -fold greater distance, whereas the on-axis lenses contribute appreciably. Therefore, between the 5×5 and 3×3 setup no further increase can be determined at the numeric precision chosen. For the properties of the assumed MLA the midpoint intensity is increased to $I_{5\times 5}(0,0)=0.077~I_0$.

 ho_a , is equal to separate bottle beams that show no interference. However, the other branch approaches the asymptote $ho_0 \approx 0.779
ho_a - 0.632$ which was determined by a linear fit. This can be understood by substituting $ho_0 = R_0/w_0$ which leads to $R_0 \approx 0.779 a_{\rm MLA} - 0.632 w_0$. Hence, for MLA pitch values close to the principal radius R_0 of the CR crystal, the light fields destructively interfere in the centre of each trap, leading to lower intensity values. Based on this evaluation, the optimal value is $ho_0 = 0.98$ with a midpoint intensity of $I_{\rm min}^{0.98} = 0.067 \ I_0$ which is only a marginal improvement. From the minimal intensities for each value of ho_a from Fig. 3.22, as shown in Fig. B1 in Appendix B, can be deduced that only for $ho_a > 2.5$ significant reduction of the midpoint intensity can be achieved.

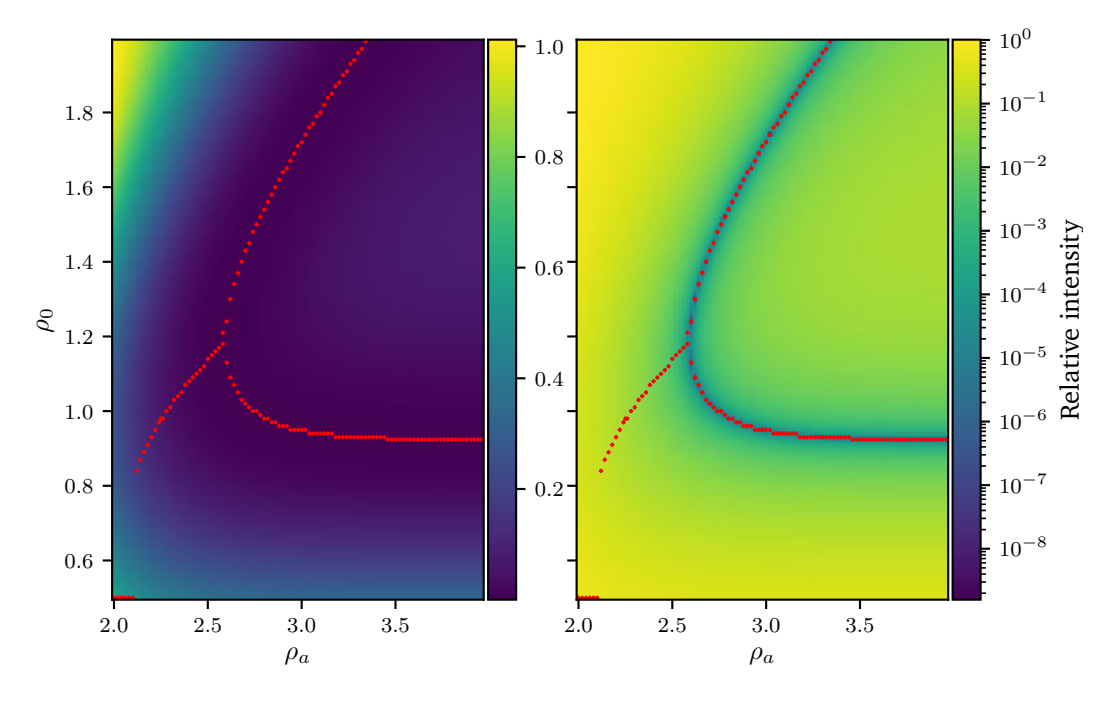


Fig. 3.22.: (left) Midpoint intensity of central lens for a 3×3 setup depending on the ratio of pitch to waist ρ_a and ρ_0 on a linear colour scale. Each value is normalised to the respective I_0 . Red dots mark the values of ρ_0 for which the lowest midpoint intensity can be reached. (right) Representation on a logarithmic colour map. Only for values $\rho_a>2.5$, the midpoint intensity decreases again to $I_{3\times 3}(0,0)\leq 1\times 10^{-3}\ I_0$.

3.3.2. Experimental realisation of a dark-focus array

As discussed in the previous Section 3.3.1, the optimal value of ρ_0 depends on the ratio $\rho_a=a_{\rm MLA}/w_0$ and can be extracted from Fig. 3.22. For the MLA APO-Q-P72-R1.45, in [150] an experimental investigation of the combination of MLA and CR was conducted. Since the principal radius of the available CR crystal (APQ-1211) is $R_0 = 42.0(19) \, \mu \text{m}$, an additional magnification by a factor of |M| = 1.5 is necessary to increase the waist. The resulting spot array had a measured pitch of $a_{\text{MLA}} = 106(2) \, \mu\text{m}$ and a waist of $w_0 = 36.7(20) \, \mu\text{m}$ which implies in a magnification of |M| = 1.47(3) based on the measured pitch and results in $\rho_a = 2.89(17)$. Restricted by the size of the crystal, a maximum number of ≈ 20 individual bottle-beams are realised in the experimental setup of [150]. Additionally, the Talbot planes $z_{1/2}$ to z_2 were experimentally confirmed and closely match theoretical predictions. Due to experimental constraints of the optical setup, the effect of destructive interference in the centre of the bottle beam traps could not be verified in [150] since individual control over each trap site is necessary requiring devices like DMDs or other SLMs. In addition to the comparison in the focal plane directly behind the crystal, another set of lenses was used to relay the intensity with a magnification of |M| = 0.48(2) producing a pitch of 51.5(20) µm. Fig. 3.23 presents a comparison of the reimaged experimental intensity distribution (bottom) in the yz-plane and numerical calculations (top) based on the experimental parameters $a_{\rm MLA}=106(2)\,\mu{\rm m}$, $w_0 = 36.7(20) \, \mu \text{m}$, $R_0 = 42.0(19) \, \mu \text{m}$, and $\lambda = 793.96 \, \text{nm}$. For the experimental distribution, a total of 181 images along the propagation axis z were taken and realigned manually. The theoretical data was calculated assuming 21×21 bottle beams and scaled down by |M| = 0.5to match the experimental reimaging. Dashed white lines in Fig. 3.23 mark the location of the z_0 and $z_{1/2}$ planes with $z_R = 1.33(15)$ mm and $z_T = 7.1(3)$ mm $\approx 5.3(5)$ z_R . Theory and

experiment show strong agreement. This way, the reproduction of the same effects under a reimaging with $|M| \neq 1$ could be verified. Therefore, a MLA with a large enough value of ρ_a can be chosen to produce an array of dark foci with significantly reduced midpoint intensities that can be reimaged with a magnification to match the desired pitch at the plane of interest.

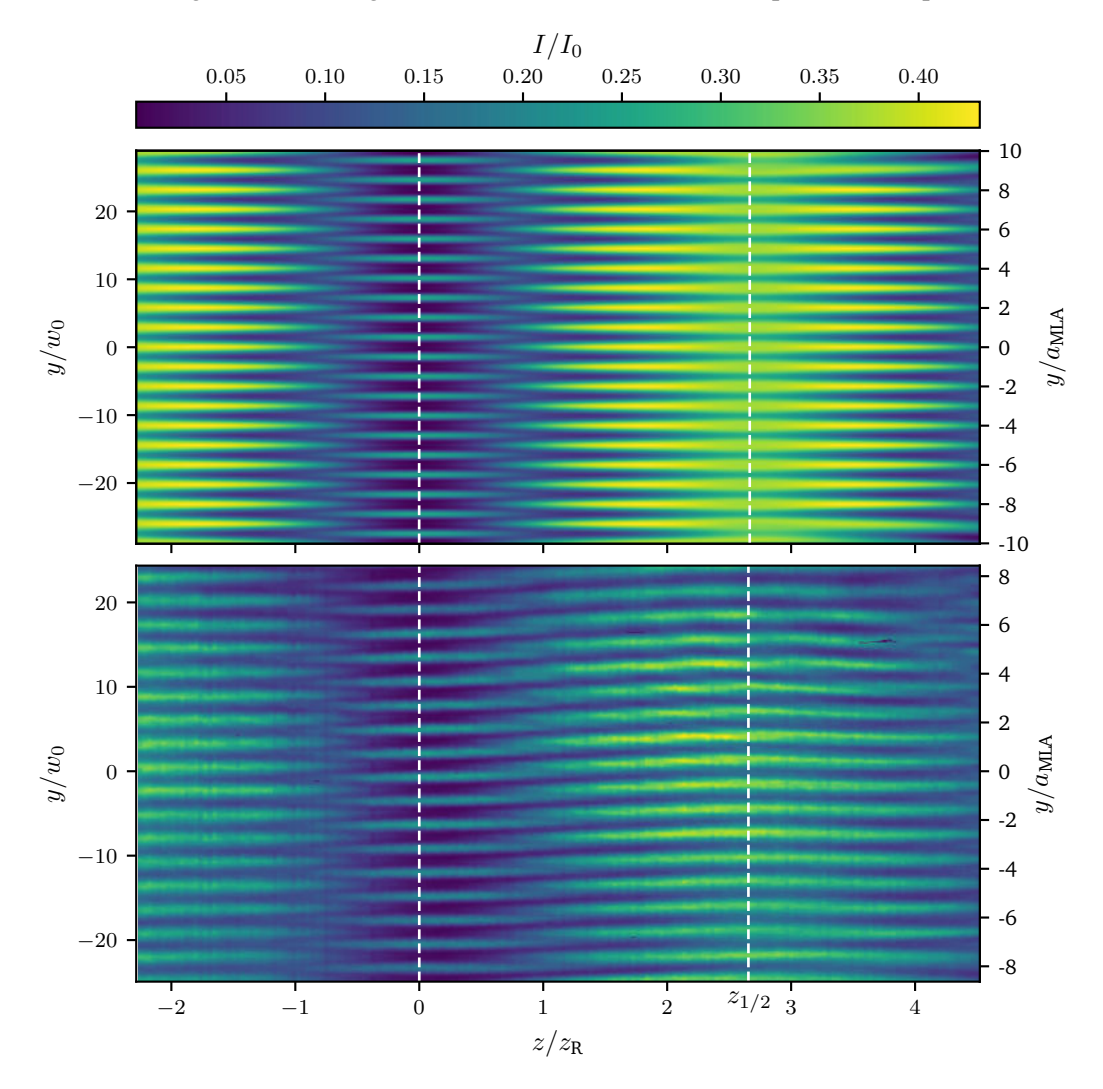


Fig. 3.23.: Qualitative comparison of the numerically calculated (top) and experimentally observed (bottom) intensity distribution in the yz-plane of a large number of microlenses in the reimaged focal plane (experimental data from [150]). The numerical results are based on the experimental values for ($a_{\rm MLA}=106(2)~\mu{\rm m},~w_0=36.7(20)~\mu{\rm m},~R_0=42(2)~\mu{\rm m})$ and a 21×21 setup was calculated since the size of the crystal limits the experimental number of lenses contributing to the final intensity distribution. The numerical data was scaled down with |M|=0.5 to match the reimaging of th experimental distribution. White dashed lines indicate the location of the z_0 and $z_{1/2}$ planes, located at z=0 and z=0.5 $z_{\rm T}=2.65$ $z_{\rm R}$.

3.4. Summary

This chapter presented an approach to blue-detuned bottle-beam potentials based on the phenomenon of conical refraction (CR). An in-depth numerical investigation of the light field produced by CR for $\rho_0^{\rm DF}=0.924$, known as the dark focus, was carried out, resulting in harmonic approximations for the light field. Key features of the intensity distribution were numerically determined to quantify both the spatial extent and the potential depths relevant for optical dipole trapping of ultracold $^{87}{\rm Rb}$ atoms.

At the ATOMICS experiment, a CR light field with a measured ring regime of $\rho_0 = 0.96(8)$ at a wavelength of 793.96 nm was generated. This light field was successfully used to trap ultracold ⁸⁷Rb atoms in the bottle-beam potential. Important trapping characteristics, including the axial trapping frequency ω_z , spatial dimensions in the atom plane, and trap holding times, were measured and found to be in excellent agreement with the numerically predicted values. The results have been published in [120].

Additionally, a numerical study of optimized configurations for bottle-beam potentials was conducted, highlighting their implementation in single-beam, crossed-beam, and microlens array setups.

Finally, a brief introduction to combining CR with microlens arrays (MLA) was presented, laying the groundwork for future applications in single neutral atom trapping for quantum computing or simulation. The presence of the Talbot effect under the CR phenomenon was both numerically predicted and experimentally verified for a specific MLA by [150]. Notably, the dependence of the traps midpoint intensity on the normalized pitch ρ_a revealed that the optimal ring regime ρ_0 for achieving minimal midpoint intensity is determined by the value of ρ_a relative to the waist.

4. Atom Interferometry with Bragg diffraction

"I do, like many of you, appreciate the comforts of the everyday routine, the security of the familiar, the tranquility of repetition."

– V, V for Vendetta

Atom interferometry has emerged as an essential tool for quantum sensing, metrology and the investigation of fundamental physics [26, 27, 33, 34, 36, 151]. In this context, atomic Bragg diffraction is a cornerstone of light-pulse atom interferometry. Interchanging the roles of light and matter, it is the matter-wave analogue of the well-known Bragg diffraction of X-rays on crystalline structures. When considering higher diffraction orders, an important property of atomic Bragg diffraction is the possibility to transfer large momenta [152–155]. This can also be realised via Bloch oscillations [156–160] or sequential pulses [161–163]. Often, a combination of several techniques is deployed [26, 36, 38, 155, 164, 165].

Especially the combination of large-momentum-transfer (LMT) with atomic interferometer schemes like Mach–Zehnder interferometers (MZIs) has attracted ever increasing interest with the goal of realising even more precise measurements [26, 36, 37, 166, 167].

At the ATOMICS experiment, in recent works a variety of Bragg diffraction implementations and interferometric realisations have been performed. Ranging from experimental realisations of double Bragg diffraction [45, 168] to atomic interferometers in external guiding potentials [46, 57]. One fundamental challenge encountered in all of these works is an apparently fast loss contrast in the interferometers, effectively prohibiting the successful realisation of long-interrogation-time MZIs [46]. The goal of this chapter is to gain a better understanding of the implementation of atomic interferometers at the ATOMICS experiment and find solutions to the underlying challenges. Essentially, the ATOMICS experiment is being prepared to enable long-interrogation-time MZIs with higher-order Bragg diffraction, thereby opening up new possibilities and avenues for research with this setup.

In the first section of this chapter, a fundamental understanding of atomic Bragg diffraction is built, introducing the theoretical framework to describe this effect. Concepts like beam splitter and mirror pulses are developed and a brief overview over the experimental implementation at the ATOMICS experiment is given. Bragg diffraction up to the fifth order is discussed.

In Section 4.3, experimental investigations of MZIs in first and third order are presented, leading to the discovery of an external magnetic field gradient in the ATOMICS vacuum chamber. The effective loss of visibility caused by the non-coherent summation of interferometer signals of different magnetic $m_{\rm F}$ sub-states is discussed and methods for differential measurement and evaluation of correlated MZIs are presented.

Finally, an additional challenge, i. e., the emergence of parasitic paths in higher-order Bragg diffraction and LMT atom interferometry is addressed. One solution based on dichroic mirror pulse (DMP) is experimentally verified in third and fifth order following a theoretical proposal by J. N. Kirsten-Siemß *et al.* [169, 170]. The result of this section have been published as an open-access research letter in *Physical Review Research* in collaboration with the group of Prof. E. Giese [171]. Parts of the section are taken verbatim from this publication¹.

¹This article has been published in Physical Review Research 7, L012028 (2025) under the terms of the Creative

4.1. Bragg diffraction

In the following section, the theoretical and experimental foundations required to describe atomic Bragg diffraction are established, with the goal of implementing Mach-Zehnder type light-pulse atom interferometers. A concise introduction to the quantum-mechanical treatment of light-atom interactions is given, formulating the necessary dynamics of Bragg transitions. Following this theoretical framework, the experimental implementation of Bragg diffraction at the ATOMICS experiment is described. A systematic investigation of Rabi oscillations for momentum transfers of $1\hbar k_{\rm eff}$ to $5\hbar k_{\rm eff}$ is presented, showcasing the non-linear dependency of higher-order Bragg transitions on the laser intensity. Furthermore, a reduction in transition efficiency and a heightened influence of velocity selectivity become evident. The theoretical description presented here includes only the most essential contributions needed to build an intuitive understanding of the experiments presented in the following sections and follows the notation from [172].

4.1.1. Fundamentals

In contrast to the well-known principle of Bragg diffraction of light waves from crystalline structures, governed by Braggs law [173]

$$n\lambda = 2d\sin(\theta) \tag{4.1}$$

in atomic Bragg diffraction the principle is inverted and an atomic ensemble diffracts off a light grating produced by interfering light waves of counterpropagating laser beams. Here λ is the wavelength of the light, d is the spacing between crystal planes, and θ is the glancing angle at which scattering of order n occurs. This effect can be described in terms of the atoms absorbing a photon with wave vector \mathbf{k}_a ($k_a = |\mathbf{k}_a|$) and frequency ω_a from one beam and subsequently emitting a photon with wave vector \mathbf{k}_b ($k_b = |\mathbf{k}_b|$) and frequency ω_b into the other beam by stimulated emission. Through this process, a total momentum of $\hbar k_{\rm eff} = \hbar (k_a + k_b)$ is transferred from the laser beams to the atom which therefore changes its momentum state from $p_{\rm in}$ to $p_{\rm in} + \hbar k_{\rm eff}$. In contrast to the similar process of Raman diffraction, in Bragg diffraction the internal state of the atoms remains unchanged, effectively coupling the two states $|g, p_{in}\rangle$ and $|g, p_{\rm in} + \hbar k_{\rm eff}\rangle$ with $|g\rangle$ being the atomic ground state [21]. In Fig. 4.1, the process of such a momentum transfer is shown schematically. Solid red and blue arrows depict the absorption and emission of photons from the two beams with coloured Gaussians visualising populations in the respective momentum states with a certain spread in momentum space. The parabolas drawn show the energy of the atomic ground $|g\rangle$ and excited $|e\rangle$ state that is only virtually populated. In order not to drive transitions to the excited state $|e\rangle$, a large detuning $\Delta = \omega_{eq} - \omega_a \approx \omega_{eq} - \omega_b$ has to be used. To conserve energy and momentum, all processes have to start and end on the parabola of the ground state $|g\rangle$. Processes that do not end on the parabola (dashed arrows) are out of resonance and therefore suppressed. To drive a resonant transition, the frequency difference of the laser field involved have to obey the resonance

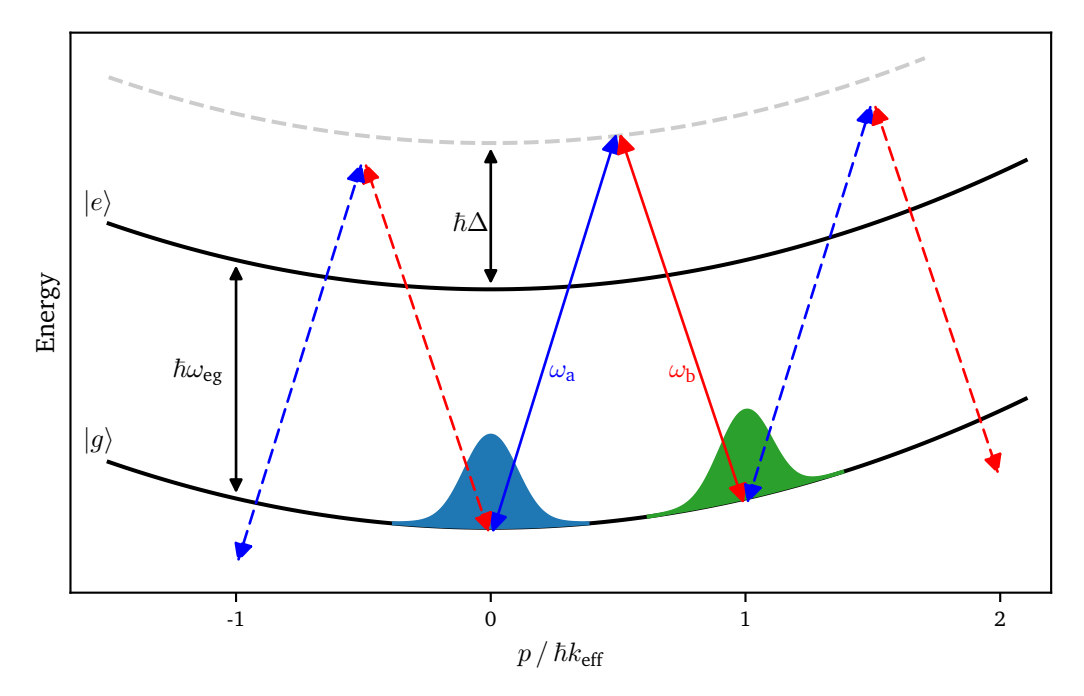


Fig. 4.1.: Schematic momentum-energy diagram for first-order Bragg diffraction. The absorption of a photon from one and subsequent emittance into the counterpropagating field leads to a momentum transfer of $\hbar k_{\rm eff}$ from the field to the atom. In order for the process to be resonant (solid arrows), the energy gained by the additional momentum needs to be accounted for by the energy difference of the two laser fields $\hbar(\omega_b-\omega_a)$. Dashed arrows depict non-resonant processes and the grey dashed parabola the detuning of the laser fields to the excited state $|e\rangle$.

condition

$$\Delta\omega = \omega_a - \omega_b \stackrel{!}{=} \frac{E_n - E_0}{n\hbar} = \frac{1}{n\hbar} \left(\frac{\left(n\hbar k_{\text{eff}} + p_{\text{in}}\right)^2}{2m} - \frac{p_{\text{in}}^2}{2m} \right)$$

$$= n\frac{\hbar k_{\text{eff}}^2}{2m} + \frac{k_{\text{eff}}p_{\text{in}}}{m} = n\omega_{k_{\text{eff}}} + \omega_{\text{D}}.$$
(4.2)

Here n denotes the Bragg diffraction order describing how many momenta $\hbar k_{\rm eff}$ are transferred to the atom by a 2n photon process, m the mass of the atom, $\omega_{\rm k_{\rm eff}}$ the recoil frequency of the two-photon momentum transfer, and $\omega_{\rm D}$ the Doppler frequency shift. The Doppler frequency shift is responsible for an effect called velocity selectivity. This effect emerges, when an atomic ensemble has a momentum distribution with a width large enough that for parts of the ensemble the Bragg transition is shifted out of resonance [174]. Applying short pulses with large amplitudes can be used to mitigate this effect since short pulses have broader frequency spectra therefore interact with broader momentum distributions [127, 175, Sec. 7.9]. Long pulses correspond to the deep Bragg regime, mitigating the population of additional momentum states at the cost of velocity selectivity [176]. Below, higher-order Bragg diffraction n > 1 will be discussed with the fundamental description given for an n = 1 first-order Bragg diffraction process.

The one dimensional Hamiltonian describing the dipole interaction of a two-level atom inter-

acting with the two ciunterpropagating light beams is given by

$$\hat{H} = \frac{\hat{p}^2}{2m} + \hbar \omega_{eg} |e\rangle \langle e| + \frac{\hbar}{2} \left\{ \left[\Omega_b \exp(i(k_b \hat{z} - \omega_b t)) + \Omega_a \exp(i(-k_a \hat{z} - \omega_a t)) \right] |e\rangle \langle g| + \text{h.c.} \right\}$$
(4.3)

where the rotating-wave approximation has already been applied to remove fast oscillating terms [172, 177]. Here Ω_a and Ω_b denote the single-photon Rabi frequencies coupling the ground $|g\rangle$ and excited $|e\rangle$ state of the two level atom, defined by

$$\Omega_{j} = -\frac{2}{\hbar} \langle e | \, \hat{d}E_{j} \, | g \rangle \tag{4.4}$$

with the dipole operator \hat{d} and the amplitude of the respective electric field E_j . Solving the Schrödinger equation $i\hbar \ d/dt \ |\Psi\rangle = \hat{H} \ |\Psi\rangle$ for an initial state given by

$$|\Psi\rangle = \int \!\!\mathrm{d}p \left(g(p) |g,p\rangle + e(p) |e,p\rangle\right)$$
 (4.5)

with time-dependent momentum distributions for the ground g(p) and excited state e(p) leads to a set of coupled differential equations. These differential equations can further be simplified by applying the adiabatic elimination of the excited state $|e\rangle$ and the method of averaging described in [172, 178]. Introducing the adiabaticity parameter

$$\epsilon = \frac{\Omega_{\rm R}}{2\omega_{k_{\rm eff}}} \tag{4.6}$$

which includes the two frequencies involved in Bragg diffraction

$$\Omega_{\rm R} = \left| \frac{\Omega_a \Omega_b^*}{2\Delta} \right|, \quad \omega_{k_{\rm eff}} = \frac{\hbar k_{\rm eff}^2}{2m}$$
(4.7)

the effective two-photon Rabi frequency $\Omega_{\rm R}$ and the two-photon recoil frequency $\omega_{k_{\rm eff}}$ allows to differentiate between different regimes in Bragg diffraction. For $\epsilon \ll 1$ the system is in the deep Bragg regime where higher-order momentum states are not populated while for $\epsilon \gg 1$ in the Kapitza–Dirac regime many momentum states are populated simultaneously. Most experiments are operating somewhere in between these extreme regimes in the so called quasi-Bragg regime, where population of higher-orders is suppressed but velocity selectivity does not decrease diffraction efficiency drastically [176, 179–181]. This enables the application of the method of averaging, which simplifies the system of coupled differential equations by eliminating rapidly oscillating terms, analogous to the rotating-wave approximation. For an initial momentum $p_{\rm in}=0$ and n=1, the solution for the probability amplitude $g_0(t)$ of an atom being in the state $|g,0\rangle$ or $g_1(t)$ for $|g,\hbar k_{\rm eff}\rangle$ are given by

$$\begin{pmatrix} g_0(t) \\ g_1(t) \end{pmatrix} = \begin{pmatrix} \cos\left(\frac{\Omega_R t}{2}\right) & i\sin\left(\frac{\Omega_R t}{2}\right) \exp(i\phi) \\ i\sin\left(\frac{\Omega_R t}{2}\right) \exp(i\phi) & \cos\left(\frac{\Omega_R t}{2}\right) \end{pmatrix} \begin{pmatrix} g_0(0) \\ g_1(0) \end{pmatrix}$$
(4.8)

where the phase is given by $\phi = \arg(\Omega_a \Omega_b^*/4\Delta)$. Finally, the probabilities for an atom being the states $|g,0\rangle$ or $|g,\hbar k_{\rm eff}\rangle$ for the initial condition $g_0(0)=1$ and $g_1(t)=0$ are given by

$$\mathcal{P}_0(t) = |g_0(t)|^2 = \cos^2\left(\frac{\Omega_R t}{2}\right) \tag{4.9a}$$

$$\mathcal{P}_1(t) = |g_1(t)|^2 = \sin^2\left(\frac{\Omega_R t}{2}\right). \tag{4.9b}$$

Experimentally these probabilities are determined by measuring the atom number in a given momentum state and normalising it to the total atom number.

Based on these probabilities, beam splitter and mirror pulses can be defined. A beam splitter pulse is defined with an effective pulse area $\Omega_{\rm R} t_{\pi/2} = \pi/2$ leading to a probability of $\mathcal{P}_0(t) = \mathcal{P}_1(t) = 1/2$ in the optimal case, effectively transferring half of the atoms into the state $|g,\hbar k_{\rm eff}\rangle$. Analogously, a mirror pulse with an effective pulse area $\Omega_{\rm R} t_\pi = \pi$ transfers all atoms into the $|g,\hbar k_{\rm eff}\rangle$ state leading to $\mathcal{P}_1(t) = 1$. Pulses fulfilling these conditions can later be used to build the atom interferometric analogue of the well known Mach-Zehnder interferometer by combining them to the pulse sequence $\pi/2 - \pi - \pi/2$.

So far, the Rabi frequency was treated as time-independent, but generally it is advantageous to use smooth pulse envelope functions such as Gaussians or the Blackman window function since they have a narrow spectral bandwidth, suppressing off-resonant transitions [182]. In that case, the Rabi frequency becomes time dependent which leads to an effective Rabi frequency given by an integral over time [176]. Therefore, the discussed pulse areas for a beam-splitter and mirror pulse are given by

$$\frac{\pi}{2} = \int_{-\infty}^{\infty} dt \, \Omega_{R}^{\pi/2}(t), \quad \pi = \int_{-\infty}^{\infty} dt \, \Omega_{R}^{\pi}(t)$$
(4.10)

translating into different pulse envelopes depending on the desired diffraction outcome. As mentioned above, transferring multiple momenta $\hbar k_{\rm eff}$ is possible through n two-photon scattering processes. This can be done by adjusting the detuning according to Eq. (4.2) and increasing the optical power, typically called higher-order Bragg diffraction [152–155]. Calculating the effective Rabi frequency for higher-order Bragg diffraction is non trivial, since more intermediate momentum states have to be taken into account. Here, methods like adiabatic elimination of intermediate states and the averaging approach mentioned above have to be used to describe the time evolution of the states involved [172, 176, 178, 183]. For the case of constant two-photon Rabi frequencies $\Omega_{\rm R}$ the effective 2n-photon Rabi frequency can be calculated via

$$\Omega_{\text{eff},n} = \frac{\Omega_{\text{R}}^n}{\left(2\omega_{\text{rec}}\right)^{n-1} \left((n-1)!\right)^2} \tag{4.11}$$

where n denotes the diffraction order and for n=1 it gives $\Omega_{\text{eff},1}=\Omega_{\text{R}}$ [176].

4.1.2. Experimental realisation

At the ATOMICS experiment a dedicated laser system, described in Section 2.4.4, is used to realise Bragg diffraction. The two beams necessary for Bragg diffraction are produced on the laser table and guided to the vacuum chamber via optical fibres. Furthermore, a counterpropagating setup is used where both beams are out coupled on opposite sides of the chamber and overlapped with one of the CDT beams. The size of the Bragg beams has been evaluated to $w_0=1170(50)\,\mu\mathrm{m}$ by fitting a 2D Gaussian to an image of the beams intensity distribution. The image has been taken at the entrance window of the vacuum chamber. By utilising a TA system that provides more than $100(10)\,\mathrm{mW}$ on the laser table, higher-order Bragg diffraction can be achieved, although with drastically limited efficiency. For the following sections, a maximum order of n=5 has been used.

To optimise the efficiency of Bragg diffraction, smooth pulse envelopes have proven to be beneficial. For the experiments described in this chapter, a pulse envelope based on the

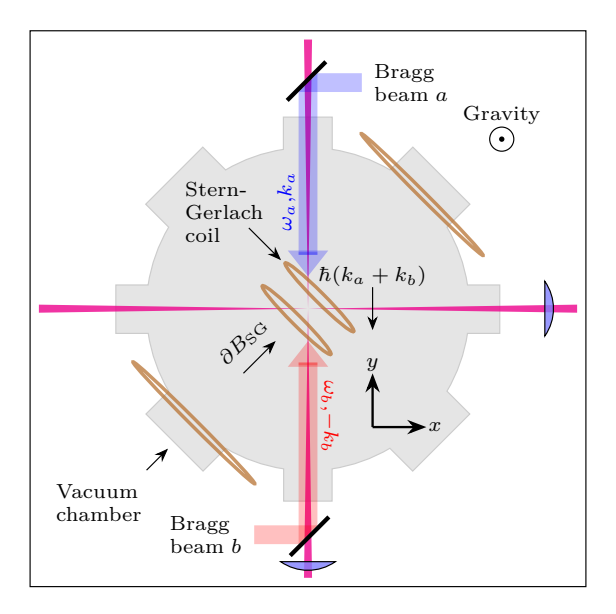


Fig. 4.2.: An atom ensemble with narrow momentum distribution is prepared via Bose-Einstein condensation in a crossed dipole trap (transparent red). Two counterpropagating laser beams (blue and red) induce Bragg diffraction and transfer momenta $n\hbar k_{\rm eff}$ as beam splitters and mirrors.

simplified Blackman window function is used given by

$$\Omega_{\rm R}(t) = \Omega_{\rm R,max} \times \left[0.42 - 0.5 \cos\left(\frac{2\pi t}{\tau}\right) + 0.08 \cos\left(\frac{4\pi t}{\tau}\right) \right] \tag{4.12}$$

defined for $0 \le t \le \tau$ and $\Omega_{\rm R}(\tau/2) = \Omega_{\rm R,max}$ and with FWHM $\approx 0.405\tau$. The effective two-photon Rabi frequency is given by the integral of Eq. (4.12) from 0 to τ resulting in $\Omega_{\rm eff,1} = 0.42~\Omega_{\rm R,max}\tau$. A comparable Gaussian pulse of shape $f_{\rm G} = \exp\left(-t^2/(2\sigma^2)\right)$ has a width of $\sigma = 0.17~\tau$.

The envelope function is pre-loaded onto the HP33120A AWGs mentioned in Section 2.4.4 as a waveform containing 16 000 data points and can be triggered by the experimental control computer. To correct for the non-linearity of the ZAD-3+ mixer component that is used to combine the envelope with the RF frequency provided by the AD9959 DDS, the resulting pulse shape has been measured with a photodiode. Subtracting the measured intensity from the expected envelope allows the calculation of the required correction to the waveform.

Currently, the AOM included in the TA setup is used to ensure a stable intensity prior to the pulse shaping. The direct stabilisation of the pulses based on the two Bragg AOMs on the laser table would further improve the stability of the system.

To calibrate the Bragg system, a scan of the two-photon Rabi frequency $\Omega_{\rm R}$ for a fixed length of a single Bragg pulse is realised by varying the optical power of the Bragg system. Choosing $\Delta\omega=2\pi\times15.084\,{\rm kHz}$ allows for resonant Bragg diffraction on first order n=1 coupling the momentum states $p_0=0\hbar k_{\rm eff}$ and $p_1=1\hbar k_{\rm eff}$. Since the atomic ensembles produced in the CDT are initially at rest with $p_0=0\hbar k_{\rm eff}$ in the direction of the Bragg beams, the Doppler term in Eq. (4.2) can be neglected. Typically, the BECs produced at the ATOMICS experiment have a temperature of $T_{\rm BEC}=25(5)\,{\rm nK}$ which corresponds to a momentum width of $\Delta p=0.13(3)\hbar k_{\rm eff}$ after the mean field energy has been converted into kinetic energy by a TOF. Fixing the pulse length to $\tau=100\,{\rm \mu s}$ and varying the optical power and therefore $\Omega_{\rm R,max}$ can be used to determine the pulse amplitudes necessary for a $\pi/2$ and π pulse. Estimating the width of this

pulse in momentum space results in a FWHM value of $\Delta p = 0.06\hbar k_{\rm eff}$ [see Appendix C]. Further, when using first-order Bragg diffraction, this approach can be used to calibrate the relation of optical power $P_{\rm Bragg}$ to effective two-photon Rabi frequencies $\Omega_{\rm eff,1}$. The experimentally determined values can be compared to the calculated Rabi frequencies based on

$$\Omega_{\rm eff,1}^{\rm th}(P_{\rm Bragg}) = 0.42 \times \frac{4P_{\rm Bragg}\tilde{U}_0}{\hbar\pi w_0^2} \tag{4.13}$$

where w_0 and P_{Bragg} denote the average waist and power of the Bragg beams while the factor 0.42 stems from the integration of the time-dependent two-photon Rabi frequency with a Blackman envelope [20, 45, 66, 184].

In Fig. 4.3 scans of the effective two-photon Rabi frequency $\Omega_{\rm eff,1}$ are shown for different orders of Bragg diffraction $n \in \{1,2,3,4,5\}$. For each Rabi scan, the pulse length has been fixed to $\tau = 100\,\mu \rm s$ and the frequency difference $\Delta\omega$ was adjusted according to Eq. (4.2) to realise a resonant process for the target order. The selected frequency differences and corresponding AOM frequencies are summarised in Tab. 4.1. Using Eq. (4.13) and the known calibration of

Tab. 4.1.: Frequency detuning $\Delta\omega$ calculated with Eq. (4.2) for 87 Rb with $p_0=0\hbar k_{\rm eff}$ and corresponding AOM frequencies. A pair of two different Bragg orders can be realised by choosing the corresponding AOM frequencies and programming the AD9959 DDS. Switching between the two chosen frequencies can be carried out during the experiment by employing a fast RF switch controlled via a TTL signal. The second AOM has a fixed frequency of $80\,\mathrm{MHz}$.

Bragg order n	$\Delta\omega/2\pi$	$\omega_{\text{AOM}}/2\pi$
1	$15084\mathrm{Hz}$	$79984916\mathrm{Hz}$
2	$30168\mathrm{Hz}$	$79969832\mathrm{Hz}$
3	$45252\mathrm{Hz}$	$79954748\mathrm{Hz}$
4	60 336 Hz	$79939664{\rm Hz}$
5	75 420 Hz	$79924580\mathrm{Hz}$

the optical power, $\Omega_{\text{eff},1}$ can be calculated for each of the Rabi scans.

The Rabi scans were carried out by producing a BEC in the CDT and releasing it by turning the CDT off instantaneously. This allows for the mean field energy to be converted into kinetic energy by free expansion prior to applying the Bragg pulse. An expansion time of 3 ms is used in these experiments followed by the Bragg pulse. To separate the different momentum states, a TOF of 15 ms is used to map each state to a different spatial location. Since it can be expected that non-resonant momentum orders are occupied for higher values of Ω_R , the probability \mathcal{P}_i of measuring atoms in the momentum state p_i with $i \in \{-1, 0, 1, 2, 3, 4, 5\}$ is evaluated by summing the atomic density for each component and normalising to the sum of all evaluated components. The resulting probabilities are shown in Fig. 4.3 (left) for each Rabi scan adjusted to a different resonance with a false colour density plot visualised for $\mathcal{P}_n \approx \mathcal{P}_0$ for each resonance (right). For n=1, a maximum diffraction efficiency of 85(2) % at $\Omega_{\rm eff,1}=2\pi\times3.8(7)\,{\rm kHz}$ was determined which is limited by velocity selectivity. In Tab. 4.2 the diffraction efficiencies for all Rabi scans are given with the corresponding calculated values of $\Omega_{\text{eff},1}$. Generally, optimising the pulse length can be done to maximise the diffraction efficiency for each Bragg order but for pulse lengths greater than the 100 µs, velocity selectivity of plays an increasing role.

Tab. 4.2.: Measured diffraction efficiencies for resonant Bragg diffraction of orders $n \in \{1,2,3,4,5\}$ with the corresponding effective two-photon Rabi frequencies $\Omega_{\rm eff,1}$ calculated using Eq. (4.13). The large error of $\Omega_{\rm eff,1}$ is mainly reasoned in uncertainty of the optical power used to generate the Bragg pulses.

Bragg order n	Maximum efficiency	$\Omega_{\mathrm{eff},1}/2\pi$
1	85(2)%	$3.8(7)\mathrm{kHz}$
2	63(2) %	$8.1(14)\mathrm{kHz}$
3	68(3) %	$15.3(26){\rm kHz}$
4	67(3) %	$24.4(42)\mathrm{kHz}$
5	61(2)%	$36.4(63)\mathrm{kHz}$

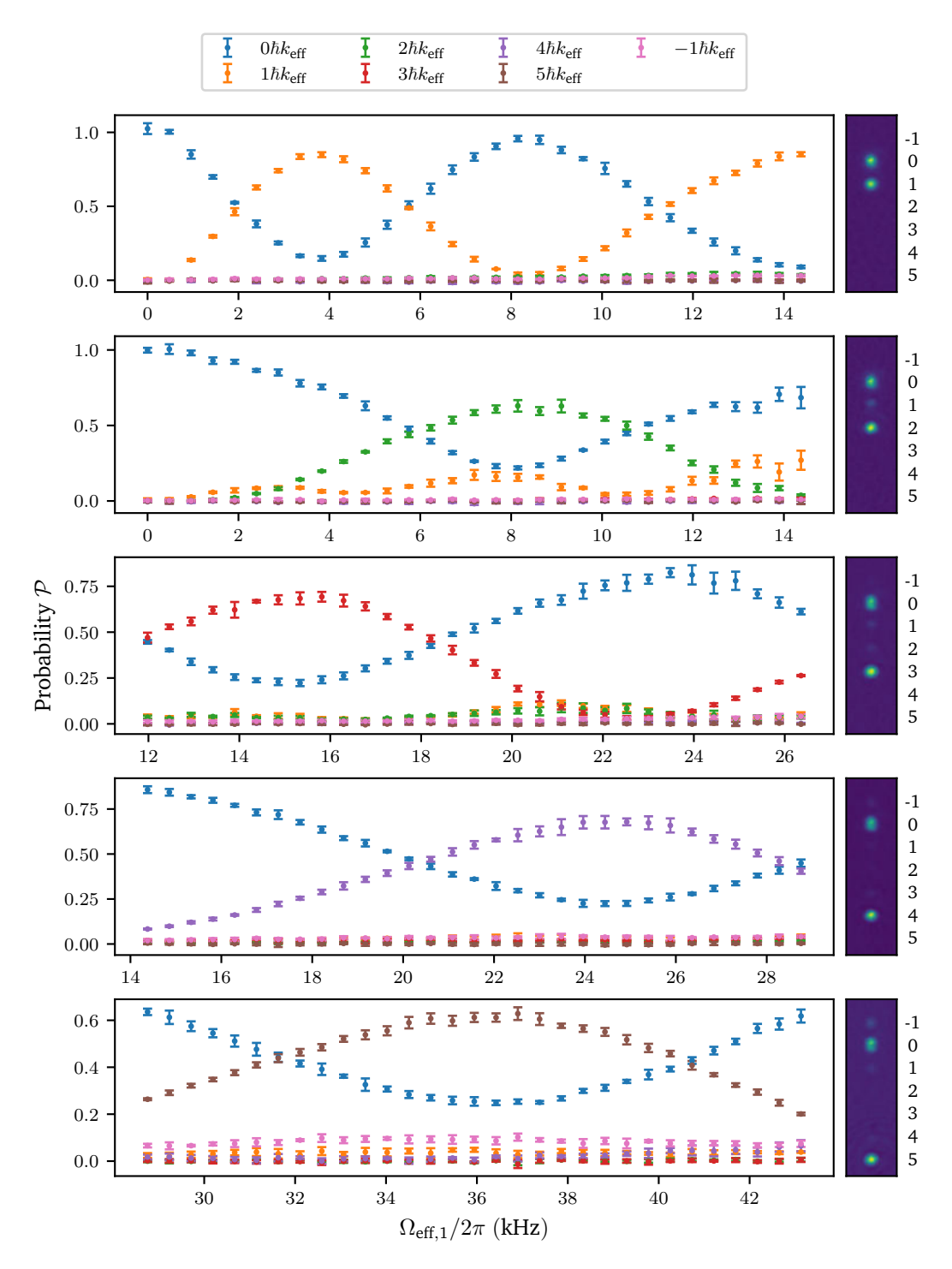


Fig. 4.3.: (left) Scan of the effective two-photon Rabi frequency $\Omega_{\rm eff,1}$ for a fixed pulse length $\tau=100~\mu \rm s$ and resulting probabilities \mathcal{P}_i for $i\in\{-1,0,1,2,3,4,5\}$. The frequency difference $\Delta\omega$ was adjusted to be resonant with different Bragg orders $n\in\{1,2,3,4,5\}$ according to Eq. (4.2). The diffraction efficiency is drastically reduced for n>1 which can be addressed to a degree by optimising the pulse length. (right) False colour column density plots for $\mathcal{P}_0\approx\mathcal{P}_n$. The density plots have a size of $381~\mu m\times 1334~\mu m$.

Fixing $\Delta\omega=2\pi\times15\,084\,\mathrm{Hz}$, $\tau=100\,\mathrm{\mu s}$, and $\Omega_\mathrm{R,eff}=2\pi\times3.8(7)\,\mathrm{kHz}$ results in a constant effective pulse area. By varying the time between the release of a BEC from the CDT and the application of the Bragg pulse, the spatial extend of the Bragg beams in the vacuum chamber can be measured. Since the atoms are in free fall and the Bragg beams are aligned perpendicular to gravity, they experience a spatially varying effective Rabi frequency depending on the free-fall time. Therefore, the measured probability \mathcal{P}_1 for an atom to be in the $p_1=\hbar k_\mathrm{eff}$ component is expected to behave like

$$\mathcal{P}_{1}(t) = \mathcal{P}_{1,\text{max}} \sin \left(\frac{\tau}{2} \Omega_{\text{R,max}} \exp \left(-\frac{2\left(\left(\frac{gt^{2}}{2} \right) - z_{0} \right)^{2}}{w_{0}^{2}} \right) \right)^{2}$$
(4.14)

with the maximum diffraction probability $\mathcal{P}_{1,\text{max}}$, maximum two-photon Rabi frequency $\Omega_{\text{R,max}}$, displacement z_0 along gravity relative to the CDT and waist of the Bragg beams and w_0 . For values of 3 ms to 10 ms between the release of the atoms from the CDT and the Bragg pulse, the measured population is shown in Fig. 4.4. A fit based on Eq. (4.14) is shown as solid orange line with average parameters $\mathcal{P}_{1,\text{max}} = 0.92(1)$, $\Omega_{\text{R,max}} = 2\pi \times 4.9(2)$ kHz, $z_0 = 26(22)$ µm, and $w_0 = 966(66)$ µm based on five individual experimental realisations and corresponding fits. The resulting $\Omega_{\text{R,max}}$ agrees well with the expected value of $2\pi \times 5$ kHz for an effective pulse area of π , and the extracted waist is consistent with the value determined from the imaged intensity distribution.

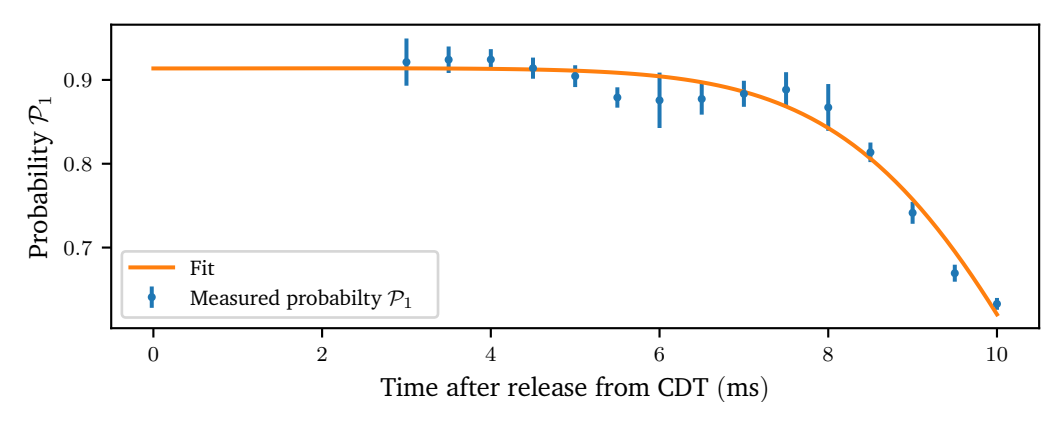


Fig. 4.4.: Measured probability \mathcal{P}_1 of atoms being in the momentum state $p_1 = \hbar k_{\mathrm{eff}}$ depending on the time between release from the CDT and the applied Bragg pulse. The effective pulse area is kept constant, adjusted to be a π pulse for the first measuring point at $3\,\mathrm{ms}$.

4.2. Mach-Zehnder interferometry with Bragg diffraction

Based on the technique of atomic Bragg diffraction described in the previous section, light-pulse atom interferometers can be implemented. At the ATOMICS experiment different interferometer geometries like well-known MZI based on a sequence of $\pi/2 - \pi - \pi/2$ pulses, and the Ramsey type $(\pi/2 - \pi/2)$ interferometer have been realised in free space as well as in a multitude of external guiding potentials [45, 46, 56, 57]. One main challenge encountered in these previous works is the loss of contrast in the conducted experiments. In the work of F. Schmaltz, a coherence time of $\tau_{\rm coh} = 3.3\,{\rm ms}$, defined as the total interferometer time where the contrast of the interferometer decreased to $1/{\rm e}$, was determined for a first-order MZI experiment in

a linear waveguide provided by the CDT [46]. Perspectively, the aim of of the ATOMICS experiment is to implement interferometers in external guiding potentials like ring-shaped waveguides with a spatial dimension requiring interferometer times of $T_1 = T_2 \gg 10\,\mathrm{ms}$, defining the times between the beam splitter and mirror pulses. In a ring-shaped waveguide with a radius of $50\,\mathrm{\mu m}$, the time it takes a BEC, accelerated to $p_1 = \hbar k_\mathrm{eff}$, to travel once around the circumference is $27\,\mathrm{ms}$. To realise interferometers in such potentials either the coherence time needs to be increased or higher-order Bragg diffraction needs to be used.

In the following sections, different methods to evaluate the signals generated by symmetric MZIs in free-space are introduced, providing the possibility to extract information about the experiment even in non-phase stable conditions. These methods are employed to investigate the apparent loss of visibility in first and third-order MZIs leading to the identification of an external magnetic field gradient present in the vacuum chamber of the ATOMICS experiment. To gain deeper insights, a state-selective detection method that enables correlation measurements of individual MZIs associated with the magnetic sub-levels ($m_{\rm F}$) of the hyperfine ground state of $^{87}{\rm Rb}$ is implemented. This approach allows to analyse each interferometer separately, specifically examining their interferometric contrast and coherence times. For first-order Bragg interferometers, a detailed discussion of the magnetic field gradient and its impact on interferometric measurements is given with additional experiments in third-order Bragg diffraction showing consistent scaling of the effect. Finally, in Section 4.4, a new method to improve higher-order Bragg diffraction MZIs is experimentally implemented and discussed based on a proposal made in [169, 170].

4.2.1. Fundamentals of Mach-Zehnder atom interferometers

Atomic MZIs use the wave properties of ensembles of ultracold atoms to detect phase shifts, caused by external accelerations. To realise such an interferometer with Bragg diffraction, a series of Bragg pulses is used to split the atom cloud in momentum space, redirect, and recombine it to close the interferometer, similar as it is done in the optical case [185]. In Fig. 4.5, a simple schematic of a free-space MZI at the ATOMICS experiment is shown. A BEC is created in the CDT and then released for a period of free expansion, allowing the intrinsic mean field energy to be completely converted into kinetic energy. Since the laser beams used to generate the Bragg diffraction are perpendicular to gravity, the initial momentum with respect to the direction of the Bragg diffraction is only given by the momentum distribution of the atoms resulting from the mean-field energy. Additionally, this prevents the setup from being used as a gravimeter. To implement such an interferometer using Bragg diffraction, a sequence of Bragg pulses successively splits the atom cloud in momentum space, redirects its trajectory, and recombines it to close the interferometric loop, analogous to optical implementations [185]. If the times T_1 and T_2 are equal, the interferometer is called closed, for $T_1 \neq T_2$ it is an open interferometer where spatial interference fringes can be observed depending in the difference between T_1 and T_2 [46, 57]. In this work, only closed interferometers are investigated, for which the interferometer signal S is defined by

$$S = \frac{N_0 - N_n}{N_0 + N_n} = \mathcal{V}_0 \cos(\varphi) + B$$

$$(4.15)$$

with the measured atom number in the $0\hbar k_{\rm eff}$ and $n\hbar k_{\rm eff}$ output ports N_0 and N_n . The signal S varies with the total acquired phase φ with the visibility \mathcal{V}_0 and an offset B. Here, the total phase φ includes all relative phases acquired by the atoms within the interferometer sequence which generally is the sum of various phase contributions. The phase of the last beam

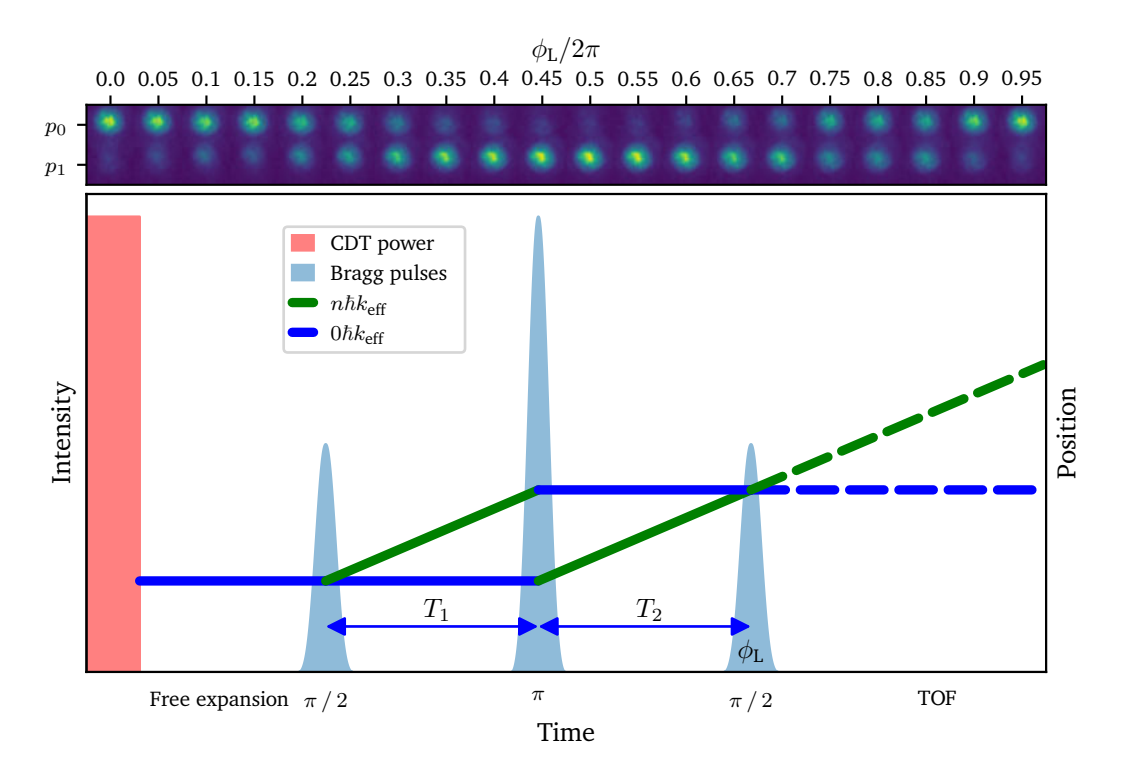


Fig. 4.5.: (top) False colour series of atomic column densities after an MZI in first-order Bragg diffraction with $\phi_{\rm L} \in [0,2\pi)$ being scanned from left to right in 20 distinct values². (bottom) Schematic visualisation of a MZI experiment in free-space at the ATOMICS experiment. A BEC is produced in the CDT and the mean field energy is released through a free expansion time prior to the $\pi/2-T_1-\pi-T_2-\pi/2$ sequence of Bragg pulses forming the MZI. In a closed MZI, $T_1=T_2=T$ is set and the atomic population oscillates between the interferometer outputs depending on the total phase φ . The pulse phase $\phi_{\rm L}$ for the second $\pi/2$ pulse can be scanned to provide a controllable source of external phase for the MZI. Solid lines trace the spatial paths of the wave packets with colours encoding the momentum state. A TOF is used to separate the output ports (dashed lines) of the MZI for a better readout.

splitter pulse can be adjusted by changing the phase of the RF frequency driving the AOMs [see Section 2.4.4] and for the remainder of this work is indicated by ϕ_L . In Fig. 4.5 (top), a sequence of 20 averaged atomic column densities (averaged over 10 realisations for each phase ϕ_L) is shown for a MZI in first order with ϕ_L linearly scanned across $[0, 2\pi)^2$. Additionally, external accelerations can contribute to the total phase φ via

$$\theta = \mathbf{a} \cdot \mathbf{k}_{\text{eff}} T^2 \tag{4.16}$$

where **a** is the external acceleration vector, \mathbf{k}_{eff} the effective Bragg wave vector and T the interferometer time [186]. The sensitivity of an interferometer therefore increases linearly with \mathbf{k}_{eff} and quadratically with T, hence higher-order Bragg diffraction and long interferometer times are the main goal in current research efforts [33, 34].

4.2.2. Statistical analysis

In a typical MZI, the external phase can be varied using, e.g. the phase of the light field ϕ_L in the second $\pi/2$ pulse of the interferometer. If the experiment operates in a phase-stable

²The step size is given by $\delta\phi_L = 2\pi/20$ and the phase scales as $\phi_L = j \cdot \delta\phi_L$ with $j \in [0, 19]$.

configuration, meaning that φ in Eq. (4.15) is dominated by the scanned pulse phase $\varphi \approx \phi_{\rm L}$ which can be externally controlled, an interference fringe can be generated by scanning $\phi_{\rm L} \in [0,2\pi)$. Such an numerically generated interference fringe is shown in Fig. 4.6 (red) where $\phi_{\rm L}$ is scanned linearly over 1000 individual points with a random phase noise added uniformly distributed over $[-\pi/50,\pi/50]$ and a maximum visibility $\mathcal{V}_0=0.75$. The signal is calculated based on Eq. (4.15) with the baseline B sampled from a normal distribution Eq. (4.17b) centred around the mean $\bar{b}=0$ with a standard deviation of $\sigma=0.025$. These baseline fluctuations include effects like a limited diffraction efficiency with atoms remaining in the p_0 momentum state that cannot be discarded for short interferometer times and therefore contribute to the interferometer signal S. If external noise sources, such as vibrations in the

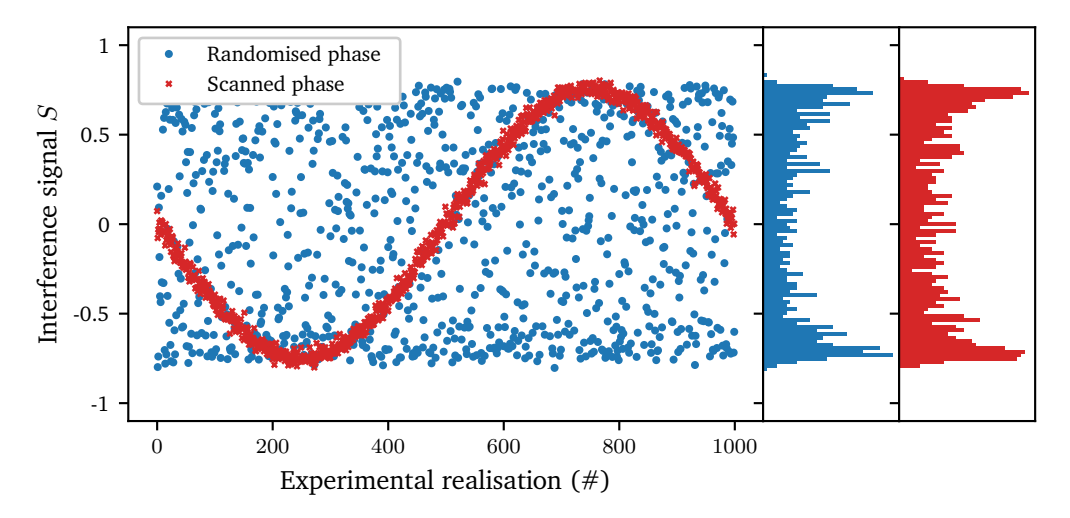


Fig. 4.6.: Demonstration of the statistic analysis of MZI signals in a phase-stable (red) and non-phase-stable (blue) situation. While in the phase-stable case, the interference fringe can be extracted from the interferometer signal, in the case of a dominating random phase, no discrete signal can be extracted. Using the statistic analysis based on the histogram of the interferometer signal (right) can provide insights on especially the visibility $\mathcal V$ of the interferometer. Both sets of data points have been numerically generated using Eq. (4.15) with a linear phase scan $\phi_{\rm L} \in [0,2\pi)$ and a added random phase noise $[-\pi/50,\pi/50]$ the phase-stable and $[-\pi,\pi]$ for the phase-unstable case. The offset B was chosen to be identical for both and sampled from a normal distribution centred around the mean value $\bar b=0$ with a standard deviation of $\sigma_b=0.025$.

experimental setup, introduce a random phase contribution to the laser field, the interference fringes disappear. Similarly, if the laser or the electronic components generating the Bragg pulses are not phase-stable on the timescale of the MZI, the MZI signal becomes random (blue). Assuming the phase noise is uniformly distributed over $-\pi$ to π and the baseline B in Eq. (4.15) can be treated as an independent random variable based on a probability density function (PDF) described by a normal distribution [see Eq. (4.17b)], another random variable can be introduced $A = \mathcal{V}_0 \cos(\phi)$ which is described by the PDF given in Eq. (4.17a) assuming a non-fluctuating visibility \mathcal{V}_0 [187]

$$f_A(x) = \begin{cases} \frac{1}{\nu_0 \pi \sqrt{1 - (x/\nu_0)^2}} & \text{if } |x| < \nu_0 \\ 0 & \text{otherwise} \end{cases}$$
 (4.17a)

$$f_B(b) = \frac{1}{\sqrt{2\pi}\sigma} \exp\left(-\frac{(b-\bar{b})^2}{2\sigma_b^2}\right). \tag{4.17b}$$

Therefore, the interferometer signal is described by the sum of two independent random variables $S = \mathcal{V}_0 \cos(\phi) + B = A + B$ with the PDF given by the convolution (*) of A and B $f_S = (f_A * f_B)$ [188, 189].

$$f_S(u) = \frac{1}{\sqrt{2\pi^3 \nu_0 \sigma_b}} \int_{-\nu_0}^{\nu_0} dz \frac{1}{\sqrt{1 - (z/\nu_0)^2}} \exp\left(-\frac{(u - z - \bar{b})^2}{2\sigma_b^2}\right)$$
(4.18)

The resulting PDF given by Eq. (4.18) can be used to extract information about the visibility \mathcal{V}_0 of the MZI by using either a least-square method to fit Eq. (4.18) to the histogram of the interferometer signal S generated by the experiment or using a Bayesian estimator approach [189–191]. This approach yields valuable insights into the overall performance of the studied MZI and enhances understanding of the BECs coherence properties. However, it inherently discards all phase information, which cannot be reconstructed from the acquired data. In the following sections, an extension of this method is used to extract information about a differential phase in a MZI by utilising the beating of independent MZIs generated by the magnetic $m_{\rm F}$ sub-states of $^{87}{\rm Rb}$.

4.3. Phase-stable summation of interferometers

In order to quantify the current capabilities of the ATOMICS experiment for realising MZIs with interferometer times $T \ge 10$ ms, an estimate of the coherence time is needed. To get this estimate, a series of MZI experiments in free space is conducted with interferometer times T ranging from 1.1 ms to 2.1 ms. For each experiment, a BEC is produced in the CDT and the mean field energy is released prior to the MZI by shutting off the CDT followed by a free expansion time of 3 ms. As discussed in Section 4.1, the pulse areas can be calibrated using a scan of the two-photon Rabi frequency Ω_R via the pulse amplitude. The phase of the second $\pi/2$ pulse can be scanned using the electronic setup described in Section 2.4.4, providing the possibility to observe an interference fringe if the experiment operates in a phase-stable mode. For each interferometer time T, the phase is varied from 0 to 2π in 20 discrete steps² and multiple realisations (7) of each phase are conducted. After the interferometer, a TOF of 15 ms is used to separate the output ports and the atom number in each port is determined by summation. The interferometer signal is then computed using Eq. (4.15). Utilising the statistical analysis approach discussed in in Section 4.2.2, histograms of the signals are computed for each interferometer time using 51 bins ranging from -1 to 1. In Fig. 4.7 (left), the stacked histograms for the $m_{\rm F}$ distribution $\mathcal{P}(m_{\rm F}=-1)=0.50(3),\,\mathcal{P}(m_{\rm F}=0)=0.17(4)$ and $\mathcal{P}(m_{\rm F}=+1)=0.33(2)$ are shown on a colour map indicating the bin counts. High bin counts are mapped to bright and low bin counts to dark colours. From this visualisation, it is clear that the visibility vanishes completely for $T \approx 2$ ms while for T = 2.1 ms an increase in the visibility can be seen. Conducting the same MZI experiment but optically pumping the atoms to the $m_{\rm F}=-1$ sub-state prior to the evaporative cooling leads to drastically different results of the MZI (Fig. 4.7 (right)) for the $m_{\rm F}$ distribution $\mathcal{P}(m_{\rm F}=-1)=0.68(4), \, \mathcal{P}(m_{\rm F}=0)=0.21(4)$ and $\mathcal{P}(m_{\rm F}=+1)=0.10(2)$. For this case, the visibility of the MZI shows a reduction for $T \approx 2 \,\mathrm{ms}$ but remains at a minimal value of $\mathcal{V}_0(2 \,\mathrm{ms}) \approx 0.5$. The difference between these two experimental realisations suggests that different $m_{\rm F}$ sub-states acquire a state-dependent phase.

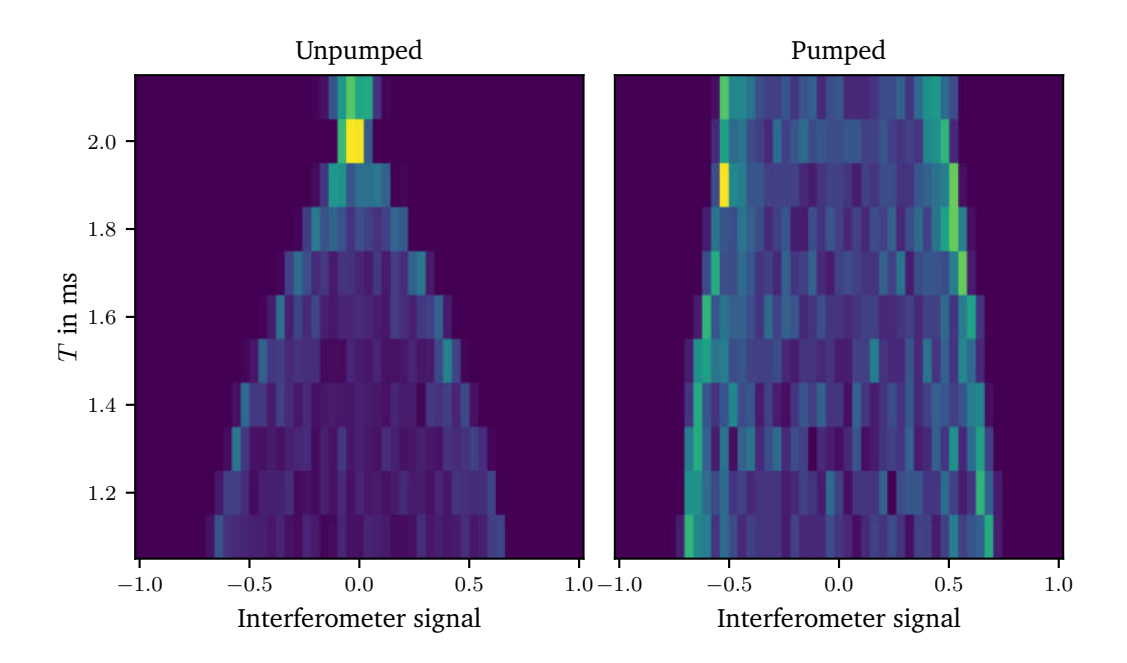


Fig. 4.7.: (left) Stacked histograms of the interferometer signal for interferometers time $1.1\,\mathrm{ms} \leq T \leq 2.1\,\mathrm{ms}$. The bin count is encoded on a colour map with brighter colours encoding a higher bin counts. From the width of the histograms, the visibility \mathcal{V}_0 of the MZI can be estimated with a clear minimal visibility for $T=2\,\mathrm{ms}$. (right) Similar visualisation of the interferometer signal histograms for a BEC that has been optically pumped to the $m_{\mathrm{F}}=-1$ sub-state. The optically pumped BEC shows a reduced decrease of the visibility compared to the BEC consisting of a mixture of all three $m_{\mathrm{F}}=\pm 1,0$ sub-states.

This behaviour can be understood by realising, that for the unpumped case, the three $m_{\rm F}=\pm 1,0$ sub-states form three distinct MZIs with signals $S_{m_{\rm F}}$

$$S_{+1} = \mathcal{P}(m_{\text{F}} = +1)(\mathcal{V}_0 \cos(\varphi + \theta_{\text{B}}) + B) \tag{4.19a}$$

$$S_0 = \mathcal{P}(m_{\rm F} = 0)(\mathcal{V}_0 \cos(\varphi) + B) \tag{4.19b}$$

$$S_{-1} = \mathcal{P}(m_{\rm F} = -1)(\mathcal{V}_0 \cos(\varphi - \theta_{\rm B}) + B). \tag{4.19c}$$

Here, φ denotes the common phase accumulated by all three interferometers, $\theta_{\rm B}$ an external phase only accumulated by the $m_{\rm F}=\pm 1$ sub-state interferometers and $\mathcal{P}(m_{\rm F}=\pm 1,0)$ the probability of atoms being the respective $m_{\rm F}$ sub-state with $\sum_{m_{\rm F}} \mathcal{P}(m_{\rm F})=1$. This approach neglects additional state-dependent phase contributions that generally could be present and additionally assumes that the external phase $\theta_{\rm B}$ is imprinted with opposite sign to the $m_{\rm F}=\pm 1$ sub-states as it is the case if magnetic fields are the source of $\theta_{\rm B}$ [192]. If no state-selective detection can be performed, the signals of the interferometers incoherently add up to the total signal $S_{\rm tot}=S_{-1}+S_0+S_{+1}$. Assuming the same maximum visibility \mathcal{V}_0 and baseline fluctuation B for all three interferometers, the total signal evaluates to

$$S_{\text{tot}} = \mathcal{V}_C \cos(\varphi) - \mathcal{V}_S \sin(\varphi) + B \tag{4.20a}$$

$$\mathcal{V}_C = \mathcal{V}_0 \left[\cos(\theta_{\rm B}) + \mathcal{P}(m_{\rm F} = 0)(1 - \cos(\theta_{\rm B})) \right] \tag{4.20b}$$

$$V_S = V_0 \Delta P \sin(\theta_{\rm B}) \tag{4.20c}$$

where $\Delta P = P(m_F = +1) - P(m_F = -1)$ is the difference of probabilities for $m_F = \pm 1$. This form results from the summation of the three interferometer signals, simplified using trigonometric angle-sum identities [193, Sec. 2.5.2]. Here the different contributions modulating

the visibility \mathcal{V} as a function of θ_B , $\mathcal{P}(m_F=0)$, and $\Delta \mathcal{P}$ become clear. For $\mathcal{P}(m_F=0)=0$ and $\Delta \mathcal{P}=0$, the visibility as a function of θ_B is given by $\mathcal{V}(\theta_B)=\mathcal{V}_0\cos(\theta_B)$. The signal can be rewritten in the form as Eq. (4.15)

$$S_{\text{tot}} = \mathcal{V}\cos(\varphi + \beta) + B \tag{4.21a}$$

$$\mathcal{V} = \sqrt{\mathcal{V}_C^2 + \mathcal{V}_S^2} \tag{4.21b}$$

$$\beta = \arctan\left(\frac{\mathcal{V}_S}{\mathcal{V}_C}\right) \tag{4.21c}$$

where $\mathcal V$ is the visibility of the combined interferometer signal depending on $\mathcal V_C$ and $\mathcal V_S$ [193, Sec. 2.5.2]. The additional contribution of β results in a constant phase offset for a fixed interferometer time, restricted by the arctan to the interval $(-\pi/2,\pi/2)$. In the case of large phase noise, φ becomes a random variable equally distributed over $\varphi \in [0,2\pi)$. Hence, the constant and restricted phase offset β only shifts the total phase which can neglected when the statistical analysis method is used. Rewriting S_{tot} into this form allows again to introduce two random variables analogously to Section 4.2.2 resulting in the same PDFs with $\mathcal V$ substituted for $\mathcal V_0$ assuming φ is uniformly distributed.

To visualise this effect, in Fig. 4.8, two sets of numerically generated MZI signals are shown for $|\theta_B| = \pi/4$ (top) and $|\theta_B| = \pi/2$ (bottom) with S_{+1} shown as blue dots, S_{-1} as red crosses, and their sum as orange diamonds³. Here, $\Delta \mathcal{P} = 0$ and $\mathcal{P}(m_F = 0) = 0$ are assumed and the same random phase noise as in Fig. 4.6 was used to calculate the signals with a chosen maximum visibility $\mathcal{V}_0 = 0.75$. This showcases, how the sum of the two interferometers can lead to a complete loss of visibility for $|\theta_B| = \pi/2$ caused by the phase-stable summation of the two interferometers [192, 194, 195]. In the general case of $\Delta \mathcal{P} \neq 0$ and $\mathcal{P}(m_F = 0) \neq 0$, the visibility has a richer structure as a function of θ_B as can be seen from Eq. (4.20a).

As demonstrated by the model given above, the summation of individual MZI signals can drastically influence the perceived signal if no state-selective measurement can be performed and the experiment operates in a phase-unstable configuration. The differential phase measured in Fig. 4.7 can therefore be explained by an external force, effecting the $m_{\rm F}=\pm 1$ sub-states with an equal absolute value but opposing directions generated by an external magnetic field gradient. An external force generates a time-dependent phase following Eq. (4.16) and in the case of a magnetic field gradient, the external force and therefore the acceleration **a** become dependent on the $m_{\rm F}$ sub-states Eq. (2.25). In order to verify the assumption of a magnetic field gradient in the ATOMICS experiment and to improve the experimental situation, in the following sections a method of state-selective measurement of the three independent MZIs is implemented. Furthermore, different evaluation techniques are introduced that allow for precise measurements of differential phases in the future. Finally, the linear scaling of the differential phase with $k_{\rm eff}$ is shown by measuring the magnetic field gradient in a third-order Bragg MZI.

³Additionally in Appendix C [Fig. C2] a version of the signals is shown with reduced phase noise, visualising the shift of $S_{\pm 1}$ in opposite directions.

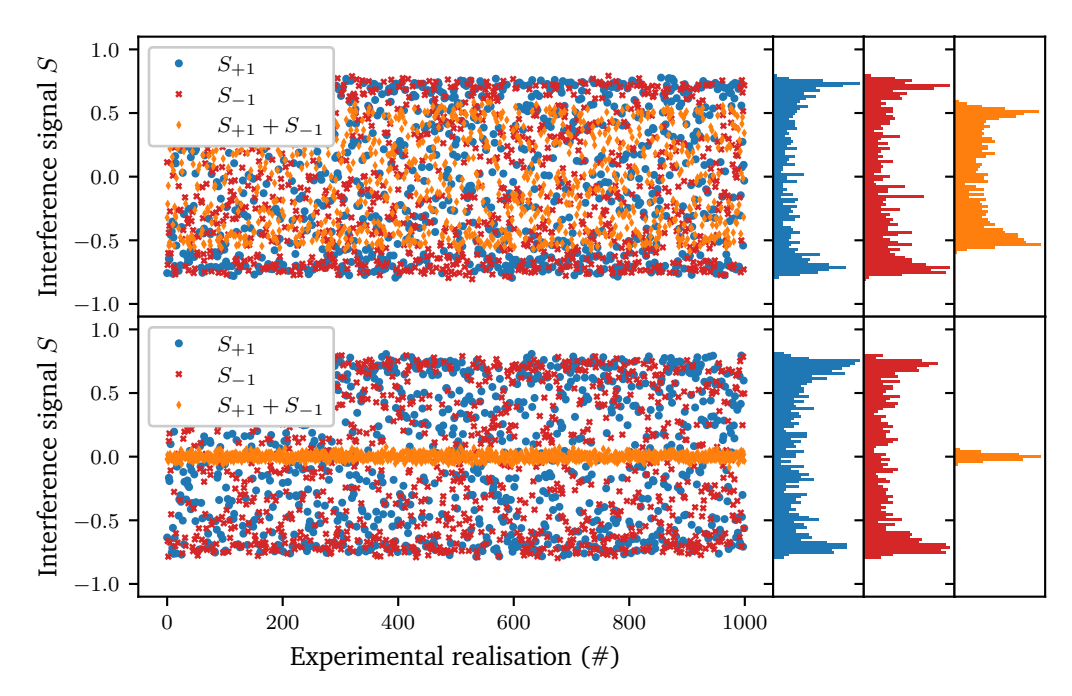


Fig. 4.8.: Schematic visualisation of the phase-stable summation of correlated MZIs for $\theta_{\rm B}=\pi/4$ (top) and $\theta_{\rm B}=\pi/2$ (bottom). Red crosses and blue dots show the individual MZI signals $S_{\pm 1}$ with orange diamonds showing their sum. On the right side the histograms of the positive S_{+1} , negative S_{-1} and total $S_{\rm tot}$ signals are shown in corresponding colours, showcasing a reduces apparent visibility for $\theta_{\rm B}=\pi/4$ and a complete loss for $\theta_{\rm B}=\pi/2$.

4.3.1. First-order Mach-Zehnder interferometer

To verify the hypothesis of a magnetic field disturbing the measurements by applying a state dependent acceleration and thus a phase, the Stern-Gerlach method is implemented to separate the $m_{\rm F}$ sub-states after the MZI. This allows for a state-selective readout of the interferometer signals and therefore a direct measure of the differential phase θ_B . In Fig. 4.9, a schematic visualisation MZI experiment including the Stern-Gerlach method is shown. The MOT coil providing the Stern-Gerlach field is only engaged after the second $\pi/2$ pulse closing the MZI and the current is ramped up an additional 1 ms later to ensure the Stern-Gerlach field does not interfere with the MZI. A current of 12.5 A is set in the experimental control software labscript and the field is left on for a total time of 24 ms until detection. The Delta Elektronika SM15-200 D power supply, used for both the MOT and Stern-Gerlach coils, exhibits a response time too slow to achieve the target current during the coils engagement period. Consequently, the actual current and resulting magnetic field strength remain undetermined. The parameters for the Stern-Gerlach subsequent to the MZI have been experimentally optimised using a heuristic approach. Including the 1 ms interval between the MZI and the onset of the 24 ms Stern–Gerlach sequence yields a total TOF of 25 ms after the MZI. In the following sections, three methods of evaluation are presented, each allowing to extract the external acceleration and hence the magnetic field gradient.

Interference-fringe evaluation

Choosing small interferometer times $T \leq 1$ ms ensures the experiment operates in a phase-stable configuration, making an interference fringe visible. The phase stability for these

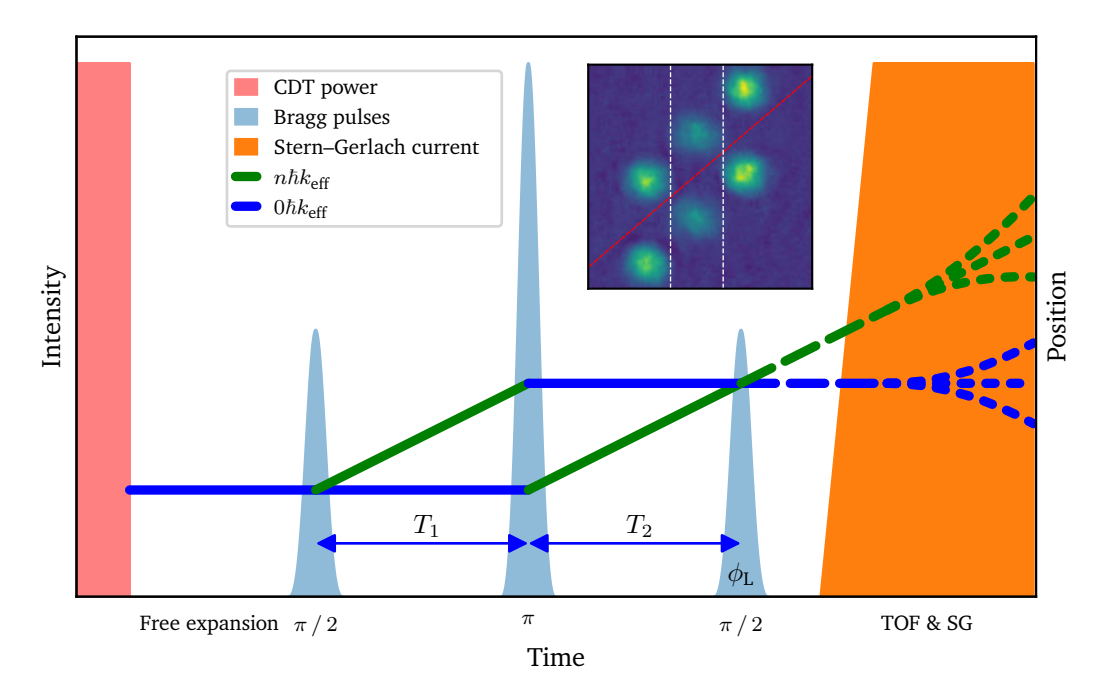


Fig. 4.9.: Schematic visualisation of a first-order Bragg MZI including the separation of the $m_{\rm F}$ sub-states via the Stern–Gerlach method. After the MZI is closed by the second $\pi/2$ pulse, one of the MOT coils is engaged. To ensure the Stern–Gerlach field does not interfere with the MZI, the current is ramped up $1~{\rm ms}$ after the MZI is closed. The Stern–Gerlach field stays turned on for the remainder of the TOF to spatially separate the $m_{\rm F}$. An averaged atomic density of the three MZIs is shown in the inset. A red dashed line depicts the separation of the MZI outputs with white dashed lines isolating the $m_{\rm F}$ sub-states.

interferometer times has been experimentally verified in agreement with previous works [46]. In Fig. 4.10, such an interference fringe is shown for $T_{1,2}=100\,\mu\text{s}$, $500\,\mu\text{s}$, and 1 ms averaged over 10 individual realisation of a phase-scan in $\phi_{\rm L}\in[0,2\pi)$. The data points visualise the mean interferometer signal with the error bars showing the standard deviation. Each individual realisation of the phase scan is used to fit a function $S=\mathcal{V}\cos(\phi_{\rm L}+\theta)+B$. Solid lines of corresponding colour in Fig. 4.10 show the resulting interferometer signal calculated with the mean fit parameters.

In Tab. 4.3 the averaged fit parameters are summarised for each interferometer time and $m_{\rm F}$ sub-state. From the values of $\theta_{\rm B}$ for $m_{\rm F}=\pm 1$, the differential phase $\Delta\phi$ and further the absolute value of the external phase $\theta_{\rm B}$ can be calculated. The resulting values for $\theta_{\rm B}$ are given in the most right column of Tab. 4.3. Relatively large uncertainties in $\Delta\phi$ and consequently $\theta_{\rm B}$ indicate that fringe-fitting for differential phase extraction is unreliable given the noisiness of the experimental data presented here.

From the combination of the external phase θ_B and interferometer time T the external acceleration and hence the external magnetic field gradient can be computed. Assuming a force described by Eq. (2.25), the magnetic field gradient measured by the MZI is given by

$$\left| \frac{\boldsymbol{\nabla} B \cdot \mathbf{k}_{\text{eff}}}{k_{\text{eff}}} \right| = \left| \partial B_{\parallel} \right| = \left| \frac{\theta_{\text{B}} m_{87}}{\mu_{B} g_{\text{F}} m_{\text{F}} k_{\text{eff}} T^{2}} \right|$$
(4.22)

with the Bohr magneton μ_B , the hyperfine Landé g-factor $g_{\rm F}=-1/2$ for the hyperfine ground state $|5^2S_{1/2},F=1,m_{\rm F}=\pm 1\rangle$ of $^{87}{\rm Rb}$. This results in a magnetic field gradient $|\partial B_{\parallel}|$ along the direction of $k_{\rm eff}$ of $1100(200)\,{\rm T/m}$ ($11(2)\,{\rm G/m}$) calculated using the value of $\theta_{\rm B}$ for $T=1000\,{\rm \mu s}$. Taking multiple devices such as the ion-getter pump and the vacuum pressure gauge into

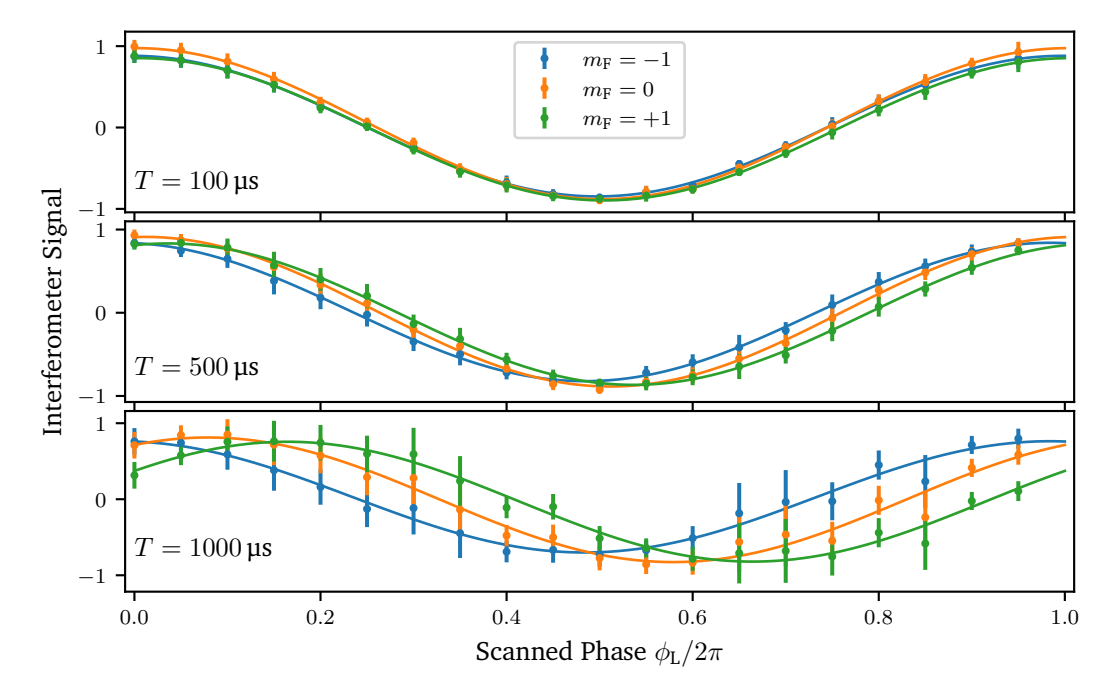


Fig. 4.10.: Interferometer signal depending on the controlled pulse phase $\phi_{\rm L}$ for different interferometer times. (top) Interference fringe for $m_{\rm F}=\pm 1,0$ and $T=T_1=T_2=100~\mu{\rm s}$. (centre) $T=T_1=T_2=500~\mu{\rm s}$ and (bottom) $T=T_1=T_2=1000~\mu{\rm s}$. Solid lines show the fits of Eq. (4.15) to the data to extract the differential phase depending on $\theta_{\rm B}$.

account, both generating magnetic fields in close location to the vacuum chamber, the measured gradient is on a realistic scale.

Additionally to extracting θ from an interference fringe of the phase scan and determining the differential phase $2\theta_B = |\theta_{-1}| + |\theta_{+1}|$ from these values, another method can be used.

Ellipse fitting

In contrast to the direct fitting of the interference fringe, the following method described here has the advantage of removing the common phase φ [see Eq. (4.19)] including common noise from the determination of the differential phase and not to be reliant on phase stability of the system. The idea is to correlate two sets of interference signals, effectively doubling the data point contribution. Here, it is clear that regarding the external phase θ_B , the interferometer signals $S_{\pm 1}$ are correlated. Therefore, they form an ellipse when used as coordinates of a vector $(S_{-1}, S_{+1})^T$ in a parametric plot [22, 196–199].

Generally, an ellipse can be described by the conic section equation

$$0 = Ax^{2} + Bxy + Cy^{2} + Dx + Ey + F$$
(4.23)

with the additional constraint $B^2 - AC < 0$ [196, 200]. However, since this is not a proper function but a constraint, determining the conic parameters can be a challenge, that fortunately has been solved leading to different approaches. Here, to compute the values of A to F, an implementation of the ellipse-fitting algorithm of Halíř and Flusser [200] is used which breaks the task down to solving an eigenvalue equation which can be easily done numerically [201, 202]. To employ this technique, for each of the ten individual phase scans an ellipse is fitted and the conic parameters are computed. In Fig. 4.11, the three resulting parametric plots are

•						
$T_{1,2}$	$m_{ m F}$	\mathcal{V}	θ [rad]	В	$\Delta\phi$ [rad]	$\theta_{\rm B}$ [rad]
	-1	0.86(6)	0.02(3)	0.02(4)		
$100\mu s$	0	0.83(10)	0.02(2)	0.05(6)	0.05(3)	0.02(2)
	+1	0.87(4)	-0.03(1)	-0.02(4)		
	-1	0.83(4)	0.10(3)	0.01(3)		
$500\mu s$	0	0.90(4)	-0.07(2)	0.01(6)	0.33(4)	0.16(2)
	⊥1	0.85(2)	-0.23(3)	-0.02(4)		

0.10(13)

-0.50(13)

-1.03(14)

0.03(5)

-0.01(5)

0.03(5)

1.13(20)

0.57(10)

0.73(6)

0.82(6)

0.79(6)

 $1000 \, \mu s$

0

Tab. 4.3.: Averaged fit parameters for each interferometer time and $m_{\rm F}$ sub-state and the resulting value for the differential phase $\theta_{\rm B}$.

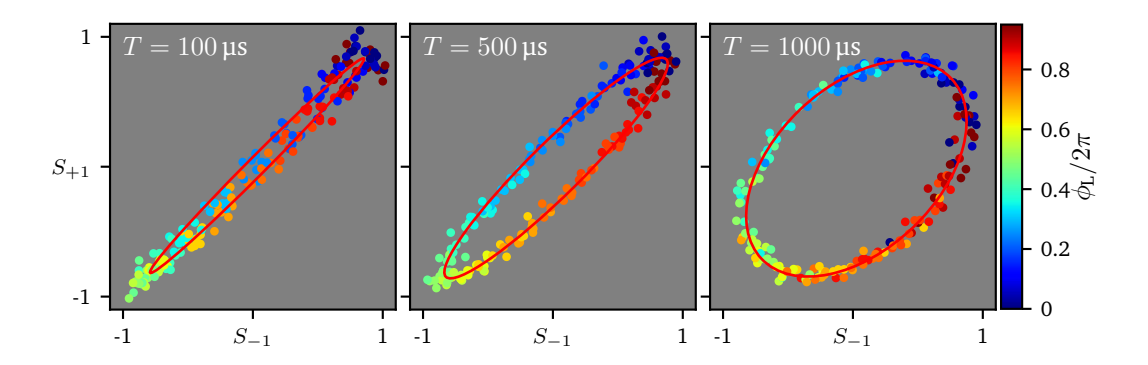


Fig. 4.11.: Parametric plots of the interferometer signals $S_{\pm 1}$ for $T=T_1=T_2=100\,\mu s,\ 500\,\mu s$ and $1000\,\mu s$. Each dot represents an individual measurement with their colour encoding the pulse phase ϕ_L (see colour bar). For these measurements the experiment is in a phase-stable situation, visualised by the ordered colour gradient. Red solid lines represent the ellipses, drawn for the averaged conic parameters.

shown as coloured dots. The colour is used to encode the scanned pulse phase ϕ_L which shows an ordered colour gradient indicating the phase stability for the investigated interferometer times. Solid red lines plot the ellipses for the mean conic parameters A to F. Through

$$\Delta \phi = \arccos\left(\frac{-B}{2\sqrt{AC}}\right) = 2\theta_{\rm B} \tag{4.24}$$

the differential phase $\Delta\phi$ can be calculated from the conic parameters [196]. Similar to the fringe fitting routine, the determined external phases can be converted to a magnetic field gradient. This results in the averaged differential phases and magnetic field gradients summarised in Tab. 4.4. For $T=1000\,\mu s$ the resulting magnetic gradient has an absolute value of $\left|\partial B_{\parallel}\right|=1.1(2)\, \mathrm{mT/m}$. Compared to the value extracted from the interference fringe for the same T, the error is an order of magnitude reduced, showcasing the advantage of the ellipse fitting approach compared to standard fringe fitting. Anyhow, as can be seen from Fig. 4.11 (left), for $\Delta\phi=j\pi$ with $j\in\mathbb{N}_0$ the ellipse collapses onto the (anti-)diagonal effectively forming a straight line that fluctuates with B. Therefore, this method of ellipse fitting struggles to properly extract the correct differential phase for values that are close to $\Delta\phi=j\pi$ where the experimental data point form a broadened line due to fluctuating B [196, 198].

Tab. 4.4.: Average external phase θ_B and resulting magnetic field gradient calculated from the conic parameters.

	100 μs	500 μs	1000 μs
$\theta_{\rm B}$ [rad]	0.06(1)	0.17(1)	0.56(1)
$ \partial B_{\parallel} $ [mT/m]	11.6(20)	1.3(1)	1.1(2)

Long interferometer times

Since the expected sensitivity of an MZI scales with T^2 , additional measurements are conducted for T in the range of 1 ms to 3 ms. For these longer interferometer times it can be expected, that the experiment operates in a non-phase-stable mode. Therefore, only the statistical analysis based on the histograms of the interferometer signals and the ellipse fitting routine are used to evaluate the results of the MZIs. The MZI experiments are carried out analogously to the ones described above and shown in Fig. 4.9 with the Stern–Gerlach method utilised to separate the $m_{\rm F}$ sub-states. Prior to the MZI experiment, the pulse areas for each interferometer time T are calibrated by performing scans of the two-photon Rabi frequency $\Omega_{\rm R}$ which is especially necessary for $T \geq 2.5$ ms. Including the 24 ms needed for the Stern–Gerlach method, for the maximum interferometer time T = 3 ms the total time of the atoms in free fall adds up to 34 ms, being close to the detection limit at the ATOMICS experiment restricted by technical limitations.

Even though no phase-stable operation is expected for longer interferometer times, a phase-scan is performed using 20 distinct equally spaced phase values $\phi_L \in [0, 2\pi)^2$. A total of 7 phase-scans per interferometer time are conducted, totalling the number of individual MZI realisations to N=140 for each interferometer time T.

Evaluation of the individual magnetic sub-state MZIs

To gain an understanding of the coherence time of the BEC produced at the ATOMICS experiment, first the three individual MZIs generated by the three $m_{\rm F}$ sub-states are evaluated. For each $m_{\rm F}$ sub-state and interferometer time T the interferometer signal S is computed using Eq. (4.15). Using the statistical analysis, all N=140 individual realisations for each T are combined in one data set and a histogram is computed using a constant number of 25 bins ranging from -1 to 1 for the interferometer signal S[see Fig. 4.12]. Stacking these histograms for each T and $m_{\rm F}$ leads to a 2D distribution with the binned interferometer signal S on the x-axis and the interferometer time T as the y-axis. The resulting two-dimensional distributions exhibit no discernible reduction in visibility, indicating perceived interference contrast [see Fig. 4.12 (top)]. Using the one-dimensional PDF Eq. (4.18), for each $m_{\rm F}$ sub-state the visibility $\mathcal{V}(T)$ is determined by a fit. A summary of the determined values averaged over all interferometer times T is given in Tab. 4.5. Here it is important to note, that generally also σ_b and \bar{b} can be extracted from these fits with a precision fundamentally tied to the bin width of the histogram and therefore the number of data points available [203]. Since all N=140 data points are used to generate the histograms, only one value of $\mathcal V$ for each Tcan be extracted. The resulting values are shown in Fig. 4.12 (bottom) as coloured markers. This confirms that over the range of interferometer times used, no loss of visibility can be determined. Therefore, no clear coherence time can be identified. Nevertheless, these results showcase that the coherence time, at least for free-space MZIs has to be in the order or multiple 6 ms which is a drastic improvement over previous works [46, 168].

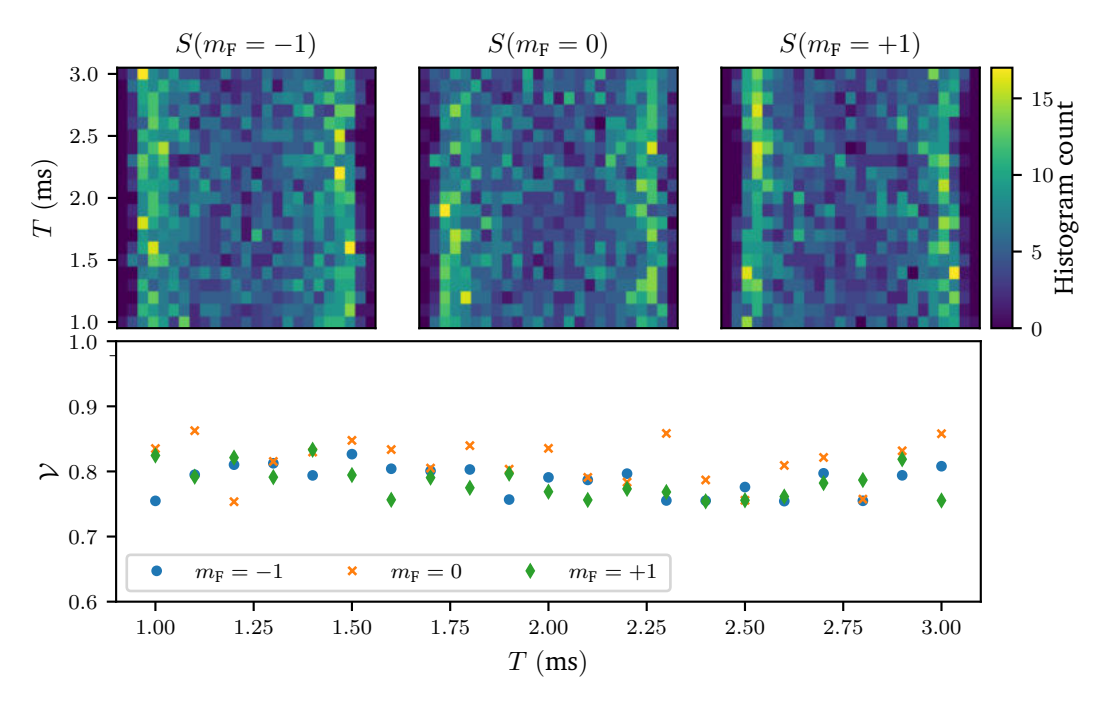


Fig. 4.12.: (top) Stacked histograms of the interferometer signal S for each $m_{\rm F}$ sub-state evaluated individually. The colour scheme indicates the bin count of the interferometers. None of the $m_{\rm F}$ sub-states shows a clear loss of visibility over the interferometer times T investigated. (bottom) Visibility $\mathcal{V}_{m_{\rm F}=0,\pm 1}$ determined by fitting Eq. (4.18) to the histograms for each T. No clear loss of visibility can be detected, hence the coherence time has to exceed $6\,{\rm ms}$.

Tab. 4.5.: Visibility $\mathcal V$ averaged over all interferometer times $1\,\mathrm{ms} \le T \le 3\,\mathrm{ms}$. All $m_{\mathrm F}$ sub-states show the same visibility with no discernible drop over the investigate interferometer times.

$m_{\rm F}$	-1	0	+1
\mathcal{V}_0	0.79(3)	0.81(3)	0.78(1)

Ellipse fitting

Following the evaluation of the individual $m_{\rm F}$ sub-states, the ellipse fitting routine described above is used to investigate the correlation between the $m_{\rm F}=\pm 1$ states and gain a better understanding of the differential phase imprinted by the external magnetic field gradient. For each interferometer time T, all N=140 pairs of $S_{\pm 1}$ are used for the parametric plots spanning the ellipses and the conic parameters A to F are computed using the ellipse fitting algorithm [200, 202]. In Fig. 4.13 (top), three resulting ellipses are shown for 1.0 ms, 1.7 ms and 2.3 ms as coloured dots with the colour encoding the pulse phase $\phi_{\rm L}$. From the emerging disorder of the phase-encoding colour of the data points, it can be estimated that the experiment transitions from a phase-stable to a phase-unstable operation at around T=1.5 ms for first-order Bragg MZIs. Therefore, even in first-order MZIs for $T \ge 1.5$ ms, only correlated measurements like the experiments discussed here and the stochastic analysis method can be used to extract information from the interferometer signals. Next, the differential phase $\Delta \phi$ is calculated for each T from the conic parameters using Eq. (4.24). Finally, the resulting values of $\Delta\phi$ need to be phase-unwrapped, since the ellipse fitting projects the differential phase onto $[0,\pi]$. Since all N=140 data points acquired for each T are used to fit the ellipses, a measure for the uncertainty of the calculated differential phase needs to be generated differently.

A bootstrapping approach is employed here to estimate the uncertainty, operating under the assumption that the experimental data accurately represents the true probability distribution [204]. These uncertainties characterise the specific evaluation method chosen. The deviation of the values for the acceleration $a_{\rm B}$ and the magnetic field gradient ∂B_{\parallel} , as determined by different evaluation methods, provides another way of estimating the uncertainty. From the original dataset (N=140), we generate 1000 randomised subsets (each with $N_{\rm rand}=140$) through resampling with replacement⁴. Each subset is fitted to an ellipse, yielding 1000 distinct conic parameter sets for every T. The solid red lines in Fig. 4.13 (top) display ellipses derived from averaged conic parameters obtained via bootstrapping. These parameters are then used to compute differential phases, which are averaged in the final analysis step. The subsequent discussion utilises the mean and standard deviation.

In Fig. 4.13 (bottom) green diamonds show the averaged differential phase $\Delta\phi$ determined from the conic parameters of the bootstrapped ellipse fitting. Here it becomes clear, that this approach struggles to properly identify differential phases of $\Delta\phi=j\pi$. Especially for $T=2.5\,\mathrm{ms}$ where $\Delta\phi\approx2\pi$, the mean differential phase determined by the ellipse fit is $\Delta\phi/\pi=1.93(2)$. Additionally, blue crosses show the differential phase extracted from the fringe fits for short times T discussed above. In the last step, the phase-unwrapped values of $\Delta\phi$ can be used to fit a function $\Delta\phi(T)=2~k_{\mathrm{eff}}a_{\mathrm{B}}T^2$ to extract the acceleration generated by the external magnetic field gradient a_{B} . A solid red line in Fig. 4.13 plots this function $\Delta\phi(T)$ for the average acceleration.

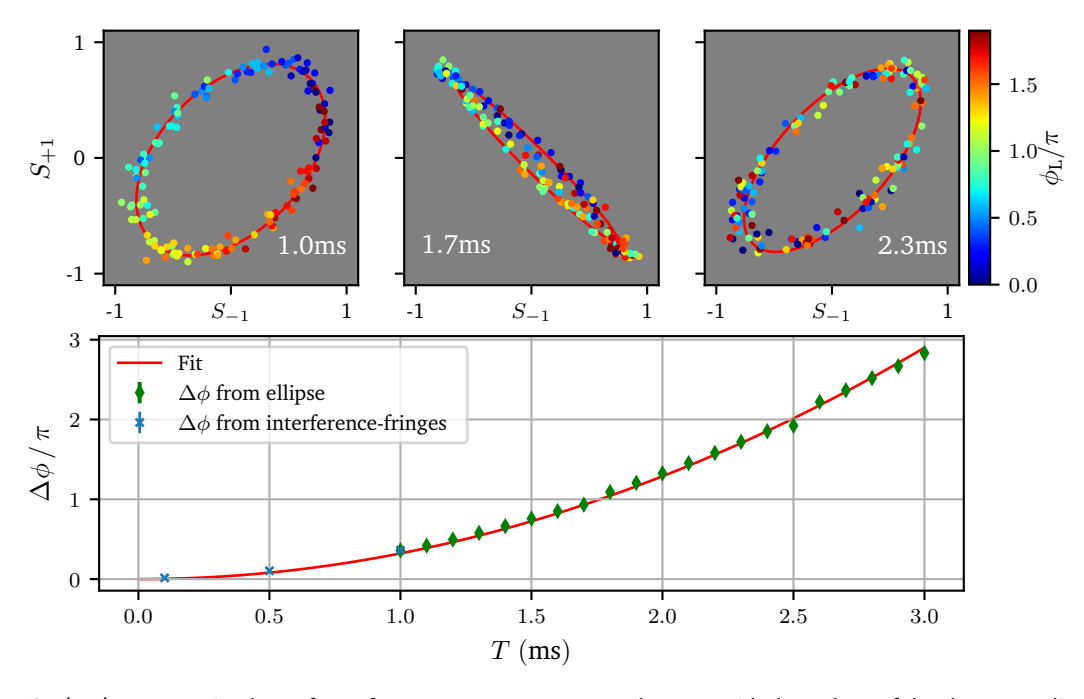


Fig. 4.13.: (top) Parametric plots of $S_{\pm 1}$ for $T=1.0\,\mathrm{ms},\ 1.7\,\mathrm{ms}$ and $2.3\,\mathrm{ms}$ with the colour of the dots encoding the experimental pulse phase ϕ_L (see colour bar). The emerging disorder of the colour shows the transition from a phase-stable to a phase-unstable operation of the experiment at around $T=1.5\,\mathrm{ms}$. Red solid lines show the ellipses plotted for the conic parameters from the fit to the original data. (bottom) Average differential phase $\Delta\phi$ computed from the conic parameters generated by the bootstrapping method (green diamonds) and extracted from the interference-fringe evaluation for short interferometer times (blue crosses). A solid red line shows $\Delta\phi(T)=2\,k_\mathrm{eff}a_\mathrm{B}T^2$ for the average acceleration value of $a_\mathrm{B}=31.40(3)\,\mathrm{mm/s^2}$.

⁴Implemented using Pythons numpy package and its numpy.random.default_rng().choice() function [82].

From the acceleration determined by the fit, the magnetic field gradient can be calculated by

$$\left|\partial B_{\parallel}\right| = \left|\frac{a_{\rm B} m_{87}}{\mu_{\rm B} g_{\rm F} m_{\rm F}}\right| \tag{4.25}$$

and results in $\left|\partial B_{\parallel}\right| = 980(1) \,\mu\text{T/m}$ which is in good agreement with the value determined by the fringe fit for $T=1000\,\mu\text{s}$ [see Tab. 4.4].

Phase-stable summation

Finally, the phase-stable summation of the individual interferometers generated by the three $m_{\rm F}$ sub-states is introduced as an additional method. As discussed at the beginning of this section, the coexistence of three BECs in separate $m_{\rm F}$ sub-states leads to three individual MZIs. If no state-selective measurement can be performed and hence no interference-fringe or ellipse fitting is available, the T-dependent summation of the interferometer signals can be used to extract a differential phase $\Delta\phi$. In the following part this method is discussed based on the data presented above.

The separation of the MZIs opens up the opportunity to artificially recombine them again simply by summing up the individual interferometer signals $S_{\pm 1,0}$ leading to the phase-stable summation signal already observed at the start of this section. In Fig. 4.14 (left top), the three signals have been combined according to the measured distribution of the $m_{\rm F}$ sub-states taken from the atom number in the individual interferometers normalised to the total combined atom number. A summary of the measured probabilities $\mathcal{P}_{m_{\rm F}}$ averaged over the full experimental data is given in Tab. 4.6.

After the recombination of the interferometer signals, the statistical approach is used to display

Tab. 4.6.: Measured probabilities $\mathcal{P}_{m_{\rm F}}$ of atoms being in the respective $m_{\rm F}$ sub-state averaged over the complete experimental data set of 2940 individual measurements.

$$m_{\rm F} = -1$$
 $m_{\rm F} = 0$ $m_{\rm F} = +1$ $\mathcal{P}_{m_{\rm F}}$ $0.37(3)$ $0.23(4)$ $0.40(3)$

the stacked histograms similar to Fig. 4.7 and Fig. 4.12. Qualitatively, it is immediately visible, that the same behaviour emerges that has been described at the beginning of this section. Similar to the data shown in Fig. 4.7 (right) where no state-selective evaluation was performed, the visibility almost vanishes for $T=1.9\,\mathrm{ms}$ where $\theta_\mathrm{B}=\pi/2$ ($\Delta\phi=2\theta_\mathrm{B}=\pi$). Since in this experiment interferometer times longer than 2 ms have been used, the revival of the visibility can be observed. The second maximum is reached for $T=2.5\,\mathrm{ms}$ with a value of $\mathcal{V}(2.5\,\mathrm{ms})=0.37(2)$ which is significantly lower than the visibility of the individual MZIs [see Fig. 4.12]. Considering Eq. (4.20a), this can be understood by the contribution of the $m_\mathrm{F}=0$ component reducing the maximum visibility at $\theta_\mathrm{B}=\pi$ to $\mathcal{V}(\Delta\phi=2\pi)=\mathcal{V}_0|2\mathcal{P}_0-1|$. In contrast, if only the $m_\mathrm{F}=\pm 1$ sub-states are recombined, the visibility reaches $\mathcal{V}(2.5\,\mathrm{ms})=0.75(2)$ which is close to the maximum value. The stacked histograms for this case are shown in Fig. 4.14 (top right).

To evaluate these data sets, again a bootstrapping approach is chosen, since all N=140 values of S are needed for each time T to generate a histogram that is not sparsely populated. Using the description of S_{tot} given in Eq. (4.21) and the resulting PDF including the general visibility $\mathcal V$ results in a function that can be fitted to the stacked histograms which is done for 1000 bootstrapped data sets generated from the original data by sampling with replacement. For the combination $m_{\rm F}=\pm 1$, the fit function was restricted by setting $\mathcal P_0=0$. A summary of

the parameters extracted from the fit is given in Tab. 4.7, averaged over the experimental realisations. Both fits return similar results for the external acceleration and maximum visibility \mathcal{V}_0 . Furthermore, the value of \mathcal{P}_0 is determined with excellent agreement to the experimental value given in Tab. 4.6. Red solid lines in Fig. 4.14 (top) trace the visibility $\mathcal{V}(T)$ as calculated for the averaged parameters determined by the two-dimensional fits. Additionally, for each

Tab. 4.7.: Average parameters extracted from a two-dimensional fit to the bootstrapped stacked histograms. The fit is based on the PDF given in Eq. (4.18) with a modified visibility term given by Eq. (4.21b).

	\mathcal{V}_0	\mathcal{P}_0	$\Delta \mathcal{P}$	a_{B}	σ_b	\overline{b}
				$31.2(1)\mathrm{mm/s^2}$		
$m_{ m F}=\pm 1$	0.77(1)	_	0.08(3)	$31.5(1){\rm mm/s^2}$	0.054(4)	-0.005(3)

interferometer time T, the visibility $\mathcal{V}(T)$ is determined by performing a one-dimensional fit of Eq. (4.18) to the bootstrapped dataset. In Appendix C, two histograms (1.6 ms and 2.5 ms) and the corresponding PDF for the averaged fit parameters are shown. The resulting averaged visibility values are shown in Fig. 4.14 (bottom) as coloured markers with the error bars indicating the standard deviation. Dotted black lines represent the $\mathcal{V}(T)$ as calculated from the two dimensional fits. Coloured solid and dashed lines plot the fits of Eq. (4.21b) with the dashed lines representing a restricted fit where \mathcal{P}_0 and $\Delta \mathcal{P}$ were taken from the experimental values [see Tab. 4.6]. All fits show excellent agreement.

In Tab. 4.8, a summary of all approaches to determine the magnetic field gradient is given. All approaches result in a consistent magnetic field gradient of $1.0(6)\,\mathrm{mT/m}$ along the direction of Bragg diffraction summarised in Tab. 4.8. Since the gradient can only be evaluated along the direction of Bragg diffraction, it's absolute direction and value cannot be determined. Hence, the precise origin of the magnetic field remains unknown. Future measurements including additional magnetic fields to compensate parts of the gradient are conceivable. Using one of the coils providing the quantisation field for the optical pumping ($N=30, R=0.12\,\mathrm{m}, d=0.25\,\mathrm{m}$) would allow to compensate part of the gradient using a current of approximately 5 A. Since the angle between the Bragg diffraction and any coils available is 45° , a combination of at least two coils is needed to compensate the gradient completely. Then again, this gradient provides a known differential phase and hence a known signal allowing for correlation measurements between the $m_{\rm F}=\pm 1$ sub-states rejecting common-mode noise to a high degree. In the future, this approach could enable longer interferometer times in guiding potentials without requiring phase-stable operation of the experiment.

Tab. 4.8.: Summary of the magnetic field gradients as determined by the different evaluation approaches.

		$ \partial B_{\parallel} $ [$\mu T/m$]
Phase scan ($T = 1000 \mu s$)	Interference-fringe evaluation	1100(200)
Finase scali $(I - 1000 \mu\text{s})$	Ellipse fits	1100(200)
Ellipse fits	$\mathbf{a}\mathbf{k}_{ ext{eff}}T^2$ fit	980(1)
_	2D fit $(m_{ m F} = 0, \pm 1)$	970(3)
Statistic Analysis	2D fit ($m_{ m F}=\pm 1$)	980(3)
Statistic Analysis	$\mathcal{V}(T)$ fit ($m_{ m F}=0,\pm 1$)	963(7)
	$\mathcal{V}(T)$ fit ($m_{ m F}=\pm 1$)	975(4)

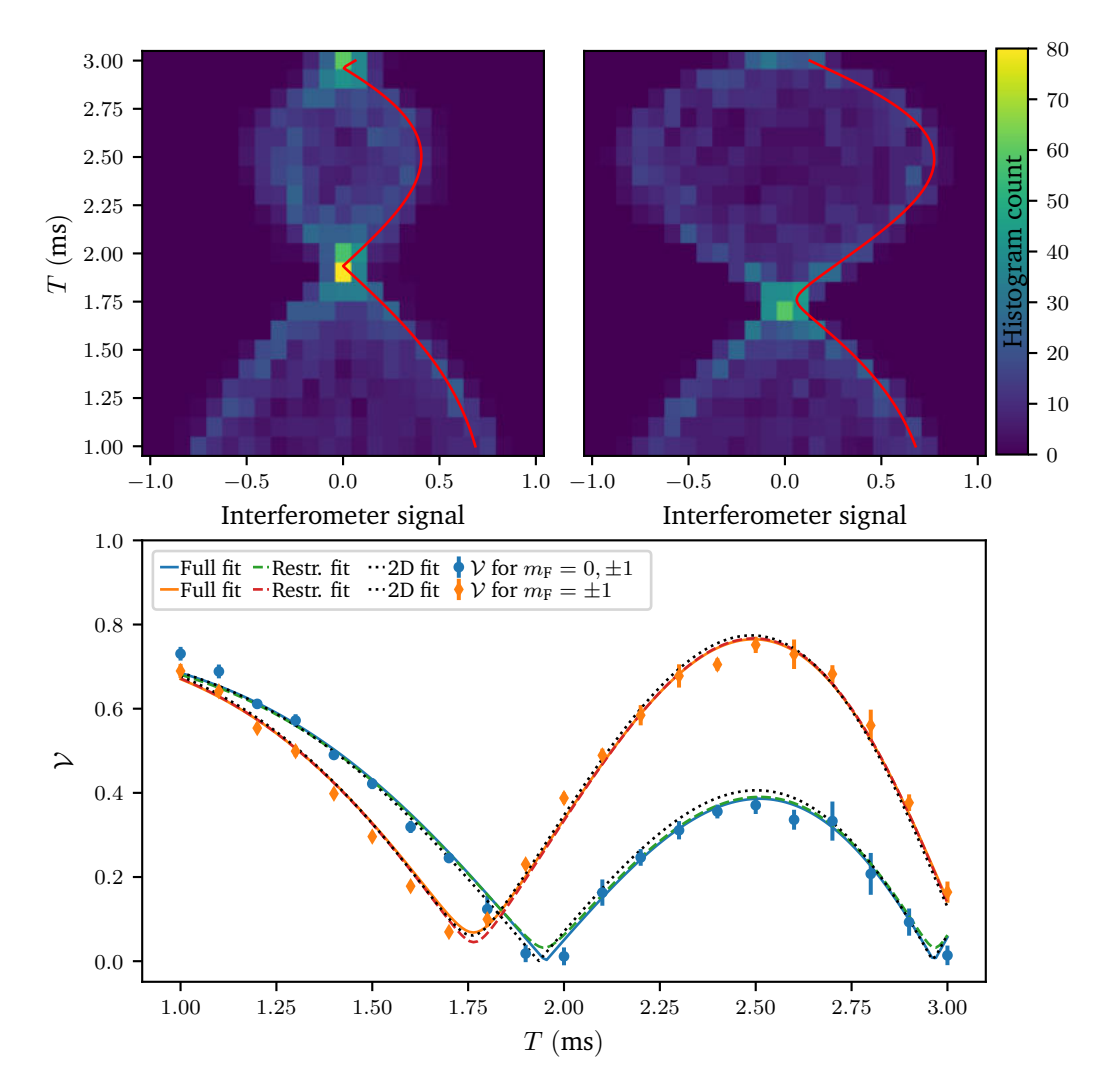


Fig. 4.14.: (top) Stacked histograms as generated by combining the interferometer signals of all $m_{\rm F}$ sub-states $S_{-1}+S_0+S_{+1}$ (left) and only the $m_{\rm F}=\pm 1$ sub-states $S_{-1}+S_{+1}$ (right). The colour map shows higher bin counts as brighter colours (see colour bar). Here, the same experimental data is used as discussed above and artificially recombined to model the output of interferometers without state-selective measurement [see e. g. Fig. 4.7]. Red solid lines trace $\mathcal{V}(T)$ as calculated by Eq. (4.21b) with the averaged fit parameters from two-dimensional fits to the bootstrapped stacked histograms. (bottom) Average visibility values $\mathcal{V}(T)$ determined by one-dimensional fits of Eq. (4.18) to the bootstrapped data for $S_{0,\pm 1}$ (blue dots) and $S_{\pm 1}$ (orange diamonds). Dotted black lines show $\mathcal{V}(T)$ calculated from the two-dimensional fits, dashed and solid lines plot a full (solid) and restricted (dashed) fit of Eq. (4.21b). For the restricted fit, \mathcal{P}_0 and $\Delta \mathcal{P}$ were taken from the experimental values and are therefore no fit variables [see Tab. 4.6].

4.3.2. Third-order Mach-Zehnder interferometer

Since in the future, MZI experiments with higher-order Bragg diffraction are planned, the behaviour of a third-order Bragg diffraction MZI is investigated in this subsection. Furthermore, the linear scaling of the external phase imprinted by the external acceleration can be verified by performing MZIs similar to the experiments discussed prior. In order to perform these experiments, the detuning $\Delta\omega$ is tuned to the third order and scans of the effective two-photon Rabi frequency $\Omega_{\rm eff,1}$ are used to determine the necessary optical power to generate pulses with an effective pulse area of $\pi/2$ and π [see, e. g. Fig. 4.3]. Here, a constant pulse time of $\tau_{\rm pulse}=100~\mu s$ is used for both pulses and the pulse area is solely tuned by the amplitude. Again, interferometer times in the range of 1 ms to 3 ms are investigated and the individual interferometers created by the three $m_{\rm F}$ sub-states are separated by the Stern–Gerlach method described above. First, the three individual MZIs are evaluated separately to gain an understanding of the visibility $\mathcal V$ and possible coherence times $\tau_{\rm coh}$ in third-order Bragg diffraction. The measured probabilities $\mathcal P_{m_{\rm F}}$ to be in the corresponding $m_{\rm F}$ sub-state are given in Tab. 4.9 with very similar values compared to the first-order experiments.

Tab. 4.9.: Measured probabilities $\mathcal{P}_{m_{\rm F}}$ of atoms being in the respective $m_{\rm F}$ sub-state averaged over the complete experimental data set of 2520 individual measurements.

	$m_{\rm F} = -1$	$m_{\rm F}=0$	$m_{\rm F} = +1$
$\mathcal{P}_{m_{\mathtt{F}}}$	0.36(3)	0.23(5)	0.41(4)

Evaluation of the individual m_F sub-state MZIs

From the raw atomic column densities, again in the first step the interferometer signals $S_{0,\pm 1}$ are determined for every interferometer time T and the statistical analysis approach is choses. This generates the stacked histograms already discussed for the first-order MZIs and fits of PDF Eq. (4.18) are performed for every $m_{\rm F}$ sub-state and interferometer time T. In Fig. 4.15 (top) the resulting stacked histograms are visualised, containing all data points generated from six realisations of the experiment. The visibility values $\mathcal{V}(T)$ determined by the one-dimensional fits of Eq. (4.18) to the histograms are visualised in Fig. 4.15 (bottom). Similar to the firstorder individual MZIs, no clear loss of contrast can be detected over the interferometer times investigated here. The average visibilities for each $m_{\rm F}$ sub-state are given in Tab. 4.10 showing slightly lower values than in first order. This may be a result of a lower overall efficiency or the contribution of parasitic orders generated by the higher-order Bragg diffraction processes [169, 170]. A possible solution to this challenge is given in the next section of this chapter. Furthermore, atoms not taking part in the MZI cannot be fully discarded for interferometer times smaller than approximately 5 ms and might lead to systematic errors in the interferometer signals. From the data presented here, no proper estimation of a coherence time can be made, similar to the first-order MZIs with the total duration of the interferometers of 2T = 6 ms being a lower limit. To investigate coherence times, experiments require guiding potentials e.g., a linear waveguide from the CDT or a two-dimensional potential generated by the optical setup detailed in Chapter 5.

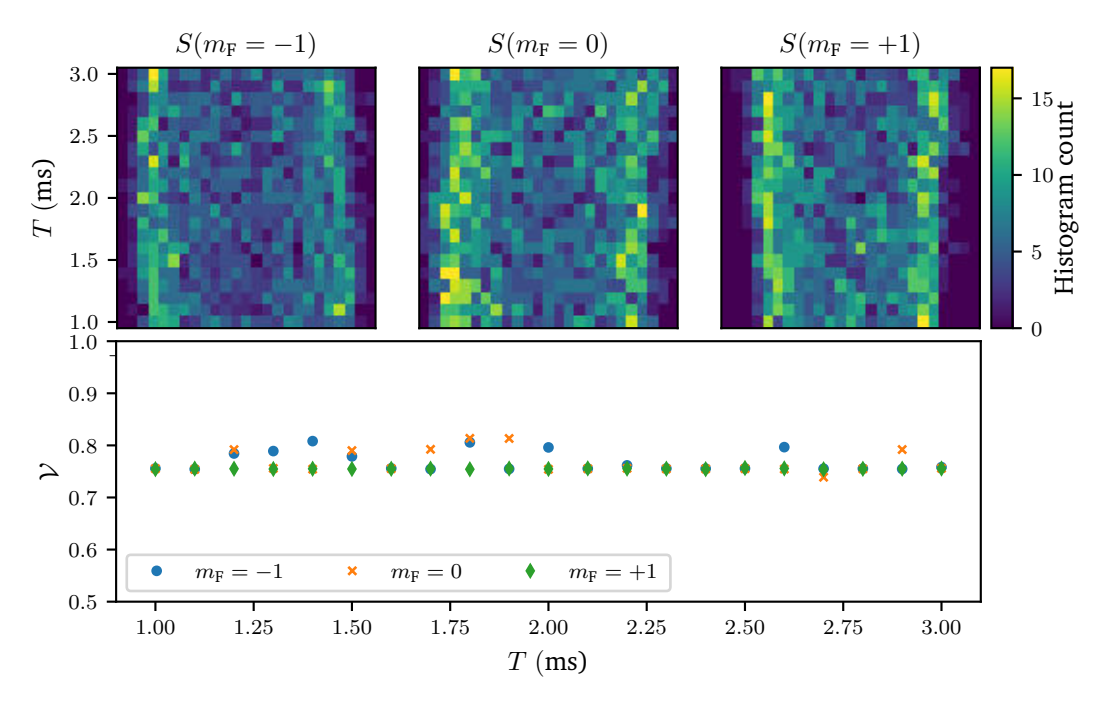


Fig. 4.15.: (top) Stacked histograms of the interferometer signal S for each $m_{\rm F}$ sub-state evaluated individually. The colour scheme indicates the bin count of the interferometers. None of the $m_{\rm F}$ sub-states shows a clear loss of visibility over the interferometer times T investigated. (bottom) Visibility $\mathcal{V}_{m_{\rm F}=0,\pm 1}$ determined by fitting Eq. (4.18) to the histograms for each T. No clear loss of visibility can be detected, hence the coherence time has to exceed $6\,\mathrm{ms}$.

Tab. 4.10.: Visibility $\mathcal V$ averaged over all interferometer times $1\,\mathrm{ms} \le T \le 3\,\mathrm{ms}$. The values are slightly decreases compared to the first-order visibilities. Possible reasons are a reduced diffraction efficiency and parasitic diffraction orders. A method to mitigate the latter issue is introduced in Section 4.4.

$m_{\rm F}$	-1	0	+1
\mathcal{V}_0	0.77(2)	0.77(2)	0.76(1)

Ellipse fitting

Additionally to the evaluation of the individual interferometers, following behaviour regarding the external phase θ_B is discussed. Similar to the first order, it is expected that the external magnetic field gradient imprints a phase $\theta_{\rm B}=k_{\rm eff}~a_{\rm B}T^2$ to the $m_{\rm F}=\pm 1$ sub-states. Changing the Bragg diffraction order to n=3 also increases the absolute value of $k_{\rm eff}$ by a factor of three. Hence, the imprinted phase $\theta_{\rm B}$ for each interferometer time T is increased and the time where $\theta_B = \pi/2$ decreases by $\sqrt{3}$. Again, the signals of the $m_F \pm 1$ sub-states are bootstrapped to generate 1000 random sets and the ellipse fitting algorithm is used to extract the conic parameters A to F. In Fig. 4.16 (top) three selected parametric plots of S_{+1} are shown for 1.0 ms, 1.6 ms and 2.4 ms as coloured dots with the colour encoding the applied pulse phase ϕ_L . Here in contrast to the first-order MZIs, even for the shortest interferometer time $T=1\,\mathrm{ms}$, no ordered phase gradient can be seen. This further hardens the suspicion, that vibrational noise or phase instability of the electronics or laser randomises the effective phase of the Bragg pulses. Since in third order, the number of photons scattered from the Bragg beams is three times higher, phase noise is transferred to the atoms three times faster leading to a phase-unstable operation of the experiment for shorter interferometer times. Fundamentally, for the ATOMICS experiment this means efforts have to be made in order to reduce the phase noise by changing

the optical layout to a retro-reflective setup to reduce optical components that can transfer vibrational noise. Also, the electronic elements such as AOM drivers and amplifiers should be considered as source of electronic phase noise. If the phase-stability cannot be drastically increased by these measures, only the statistical analysis can be used to extract information about the general visibility of the MZIs but does not provide phase information. Here, the differential measurement using the $m_{\rm F}$ sub-states provides an ideal tool, since common-mode noise is drastically suppressed.

As in the first-order discussion [see Section 4.3.1], the differential phase $\Delta \phi$ can be calculated,

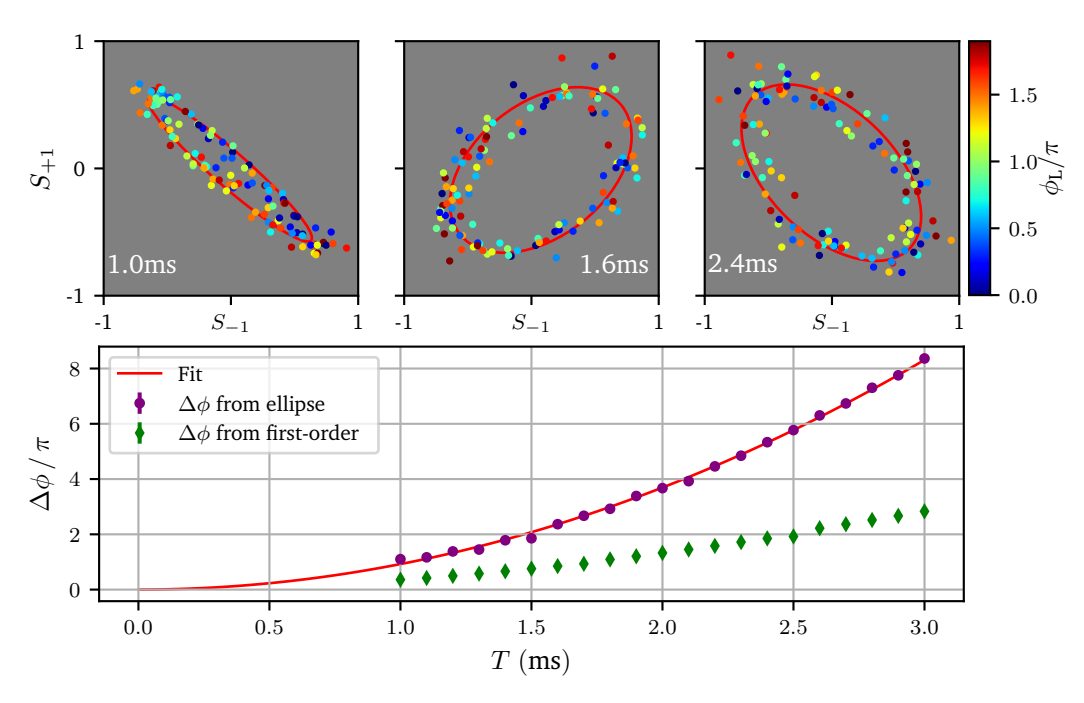


Fig. 4.16.: (top) Parametric plots of $S_{\pm 1}$ for $T=1\,\mathrm{ms},\,1.6\,\mathrm{ms}$, and $2.4\,\mathrm{ms}$ with the colour of the dots encoding the adjusted pulse phase ϕ_L (see colour bar). In contrast to the first-order ellipses in Fig. 4.13, no order can be seen in the phase-encoding colour of the dots, hence in third-order Bragg diffraction the experiments is phase-unstable already for $T=1\,\mathrm{ms}$. Red solid lines show the ellipses plotted for the conic parameters from the fit to the original data. (bottom) Average differential phase $\Delta\phi$ computed from the conic parameters generated by the bootstrapping method (purple dots). Green diamonds show the phase values determined from the first-order ellipse fitting for comparison, showcasing the scaling with k_eff . A solid red line shows $\Delta\phi(T)=2\,k_\mathrm{eff}a_\mathrm{B}T^2$ for the average acceleration value of $\bar{a}_\mathrm{B}=30.00(2)\,\mathrm{mm/s^2}$.

and a fit of form $\Delta\phi=k_{\rm eff}a_{\rm B}T^2$ is used to extract the external acceleration. In Fig. 4.16 (bottom) the unwrapped differential phase $\Delta\phi$ calculated from the conic parameters of the bootstrapped data is shown as purple dots. A red solid line plots the fit function for the average acceleration $\bar{a}_{\rm B}=30.00(2)\,{\rm mm/s^2}$ which is in good agreement with the values determined from the first-order MZIs. Green diamonds further illustrate the differential phase extracted from first-order Bragg diffraction measurements, highlighting the distinct scaling relationship with the effective wave vector $k_{\rm eff}$. The averaged differential phases yield a scaling factor of 2.80(15), consistent with the theoretically expected dependence of 3.

Phase-stable summation

Finally, the three interferometer signals can be combined again and the statistical evaluation based on the stacked histograms is performed. In Fig. 4.17 (top) the stacked histograms of all three $m_{\rm F}$ sub-states (left) and only $m_{\rm F}=\pm 1$ (right) are shown. In this visualisation again the scaling of $\Delta\phi$ with respect to $k_{\rm eff}$ becomes clearly visible already in the qualitative structure. As in the first-order Bragg interferometers the first minimum of the visibility is reached for $T\approx 1.9\,{\rm ms}$, in third order this time is reduced by $\sqrt{3}$ to approximately 1 ms. Furthermore, the summation of the three interferometer signals $S_{0,\pm 1}$ is clearly visible, producing periodic minima and maxima in the visibility. Again, the influence of the population in the $m_{\rm F}=0$ state shifts not only the times for which minima and maxima in the visibility occur, but also decreases the maximal visibility reached for every second maximum. If mixing only $m_{\rm F}=\pm 1$, the maximal visibility is reached for every local maximum. As in first-order, the data is bootstrapped and the modified PDF Eq. (4.18) is fitted resulting in the averaged fit parameters summarised in Tab. 4.11, showing excellent agreement with the values determined by the individual evaluation of the $m_{\rm F}$ sub-states and the bootstrapped ellipse fitting routine. A solid

Tab. 4.11.: Parameters extracted from a two dimensional fit to the stacked histograms using the modified PDF Eq. (4.18).

	\mathcal{V}_0	p_0	Δp	a_{B}	σ_b	\bar{b}
$m_{\rm F}=\pm 1,0$	0.72(1)	0.23(1)	0.03(2)	$30.1(6){\rm mm/s^2}$	0.061(3)	0.037(3)
$m_{ m F}=\pm 1$	0.71(1)	_	0.01(2)	$30.2(3){\rm mm/s^2}$	0.054(3)	0.033(3)

red line in Fig. 4.17 (top) traces the visibility $\mathcal{V}(T)$ for the averaged fit parameters from these two-dimensional fits. Additionally, the bootstrapped histograms for each T are fitted with the one-dimensional PDF Eq. (4.18) extracting the values of $\mathcal{V}(T)$, shown in Fig. 4.17 (bottom). Again, dotted black lines plot the corresponding $\mathcal{V}(T)$ for the averaged fit parameters from the two-dimensional fits. Solid and dashed lines plot the full and restricted fit of Eq. (4.21b) to the visibility values. All fits show excellent agreement with each other and the visibility values. Finally, in Tab. 4.12, a summary of the determined magnetic field gradients calculated from the external accelerations is given. All methods show excellent agreement. Again, an average value of $937(2)\,\mu\text{T/m}$ is determined, confirming the measurements in first-order Bragg diffraction [see Tab. 4.8]. The difference compared to the measurements in first-order Bragg diffraction are likely reasoned in a systematic differences in the experimental realisation of first- and third order Bragg diffraction. First-order diffraction processes have a higher diffraction efficiency and lower population in parasitic paths due to a lower effective two-photon Rabi frequency.

Tab. 4.12.: Summary of the magnetic field gradients as determined by the different evaluation approaches for the third-order Bragg MZIs.

		$\left \partial B_{\parallel}\right \left[\mu \mathrm{T/m}\right]$
Ellipse fits	$\mathbf{a}\mathbf{k}_{\mathrm{eff}}T^2$ fit	934(1)
Statistical analysis	2D fit ($m_{ m F} = 0, \pm 1$)	938(2)
	2D fit ($m_{\rm F}=\pm 1$)	938(1)
	$\mathcal{V}(T)$ fit ($m_{ m F}=0,\pm 1$)	939(4)
	$\mathcal{V}(T)$ fit ($m_{ m F}=\pm 1$)	941(2)

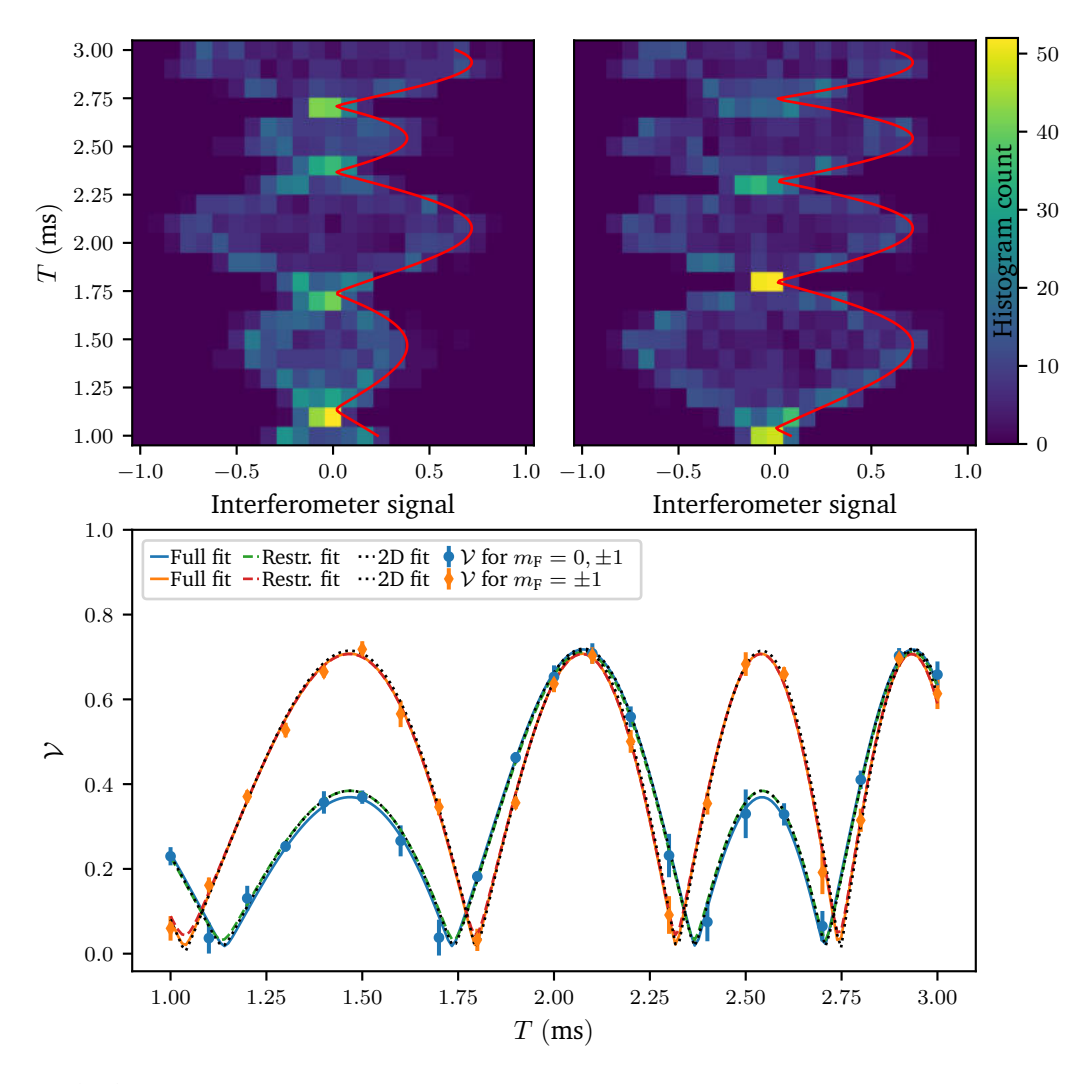


Fig. 4.17.: (top) Stacked histograms as generated by combining the interferometer signals of all $m_{\rm F}$ sub-states $S_{-1}+S_0+S_{+1}$ (left) and the $m_{\rm F}=\pm 1$ sub-states $S_{-1}+S_{+1}$ (right). The colour map shows higher bin counts as brighter colours (see colour bar). Red solid lines trace $\mathcal{V}(T)$ as calculated by Eq. (4.21b) with the averaged fit parameters from two-dimensional fits to the bootstrapped stacked histograms. (bottom) Average visibility values $\mathcal{V}(T)$ determined by one-dimensional fits of Eq. (4.18) to the bootstrapped data for $S_{0,\pm 1}$ (blue dots) and $S_{\pm 1}$ (orange diamonds). Dotted black lines show $\mathcal{V}(T)$ calculated from the two-dimensional fits, dashed and solid lines plot a full (solid) and restricted (dashed) fit of Eq. (4.21b). For the restricted fit, \mathcal{P}_0 and $\Delta\mathcal{P}$ were taken from the experimental values [see Tab. 4.10]

4.3.3. Summary

To summarise, in this section improvements to the capabilities of the ATOMICS experiment in regard to atom-interferometric measurements have been discussed. By evaluating the visibility of MZIs in first-order Bragg diffraction for various interferometer times $100\,\mu s \le T \le 3\,m$ s, a phase-stable summation of the individual MZI signals generated by the magnetic m_F sub-states in combination with an external magnetic field gradient of approximately $1\,m$ mT/m could be found. This summation leads to the total loss of the visibility of the interferometer if no state-selective detection is performed. Similar effects have been proposed for quantum-clock interferometry to measure relativistic effects with claimed geometric phase amplifications and metrological gains at the point of no visibility [205]. In contrast to quantum clocks, where a coherent superposition in internal degrees of freedom is needed, in the case presented here, a similar effect is observed without coherence between the m_F sub-states. Hence, this effect may be used in experiments where no coherent superposition can be generated, but multiple interferometer signals are summed.

Reasoned on this summation of the interferometer signals, a state-selective measurement procedure based on the Stern-Gerlach method was implemented allowing for correlation measurement and the individual evaluation of the MZIs. In the experiments discussed here, no loss of visibility could be detected for the individual MZIs indicating that the true coherence time has to be significantly longer than the 6 ms of total interrogation time in the longest interferometer investigated. This opens the opportunity to investigate MZIs in external guiding potentials for increased interferometer times. In addition, two methods to evaluate correlated interferometer were used to evaluate the MZIs (i) ellipse fitting and (ii) phase-stable summation of interferometer signals. The latter makes use of the summation of the interferometer signals for correlated interferometers and uses the loss of visibility as a signal to evaluate the differential phase. This technique shows promising results with similar precision to the ellipse fitting in this case. Further investigations of this techniques is subject of current ongoing research in collaboration with the research group of Prof. E. Giese. Finally, MZIs in third-order Bragg diffraction were investigated, proving the linear scaling of the differential phase with the effective wave vector k_{eff} . Again, similar to the first-order MZIs, no loss of contrast could be detected for the interferometer times investigated when evaluating the individual $m_{\rm F}$ sub-states. This opens up the opportunity for future LMT interferometers at the ATOMICS experiment. Overall, this highlights the capabilities of the ATOMICS experiment in new facets compared to previous works [46, 56, 57, 168].

4.4. Dichroic mirror pulses

As discussed in the previous section, scaling to higher-order Bragg diffraction at the ATOMICS experiment is possible, with behaviour similar to that of the first-order Bragg diffraction when used in an MZI. Increasing the sensitivity of light-pulse atom interferometers progressively relies on LMT techniques. Precise control of such methods is imperative to exploit the full capabilities of these quantum sensors. One key element is the mitigation of deleterious effects such as parasitic paths deteriorating the interferometric signal, as mentioned above. In this section, the experimental realisation of dichroic mirror pulses for atom interferometry, its scalability to higher-order Bragg diffraction, and its robustness against initial momentum spread are presented. This approach has been inspired by a proposal [169, 170] of momentumselective, i. e. dichroic mirror pulse (DMP) based on Bragg diffraction [172, 180] that only redirects the two intentionally populated, i. e. resonant paths (distinguishable through their momenta), while being made transparent for the dominant parasitic paths, which are not redirected to the detected output of the interferometer. Such an evolution is induced by applying a pulse area of π to the resonant paths, while parasitic orders experience pulse areas of multiples of 2π . This method effectively isolates the desired interferometric signal from noise induced by unwanted paths. The scalability of this technique is established through an examination of resonant third- and fifth-order diffraction. It can be readily applied to existing setups capable of higher-order Bragg diffraction.

First, the mechanism of the proposed DMP is briefly introduced with an presentation of the theoretical background given in [169, 170]. Following this introduction, the initial approach in MZIs using *conventional* mirror pulses is discussed, leading to an experimental scheme to design a DMP. Finally, DMPs are realised in third-order Bragg diffraction and showcasing the scalability of this approach in fifth-order Bragg diffraction.

In this section, an experimental approach to find the parameters for a DMP in third order is presented and the results are based on the Letter published in *Physical Review Research* [171]. Some parts have been taken verbatim from this publication. The theoretical data shown is taken from the Letter and was provided by the research group of Prof. E. Giese⁵.

Mechanism of the dichroic mirror pulse

As mentioned, the approach of using a dichroic mirror pulse in a MZI light-pulse atom interferometer has been inspired by the proposal by J. N. Kirsten-Siemß et~al. and an investigation is given in their work [169, 170]. Here, only the fundamental idea behind the DMP is discussed to give a better intuition of the mechanism that drives this approach. In Fig. 4.18 a third-order Bragg diffraction is depicted in terms of the energy-momentum conservation. For every Bragg diffraction process of order n, the dominating parasitic momenta p_i are inherently given by i=1 and i=n-1 [169, 170]. As visualised in Fig. 4.18 atoms occupying these states, mainly due to imperfections of the initial $\pi/2$ pulse, are coupled to the other parasitic order by a resonant n-4 photon process. In the case of n=3 the states p_1 and p_2 are therefore coupled by a resonant two-photon transition as can be verified by calculating the necessary detuning $\Delta \omega$ with Eq. (4.2). This results in two distinct effective Rabi frequencies driving transitions between the states $p_0 \to p_3$ as well as $p_1 \to p_2$. For higher orders n>3, more resonant transitions are possible, coupling the states p_{n-i} and p_i hence more distinct effective

⁵Numerical data kindly provided by M. Dietrich and P. Schach for the Letter and visualised here for the sake of completeness.

Rabi frequencies need to be taken into account. To find the parameters for a DMP, the effective two-photon Rabi frequency and the pulse length τ have to be chosen such that the effective pulse area is π for the desired transition while being multiples of 2π for all other transitions. For time-independent pulse envelopes, i. e. box-pulses, this may be calculated using Eq. (4.13). As discussed, for a third-order setup, only one additional transition has to be taken into account

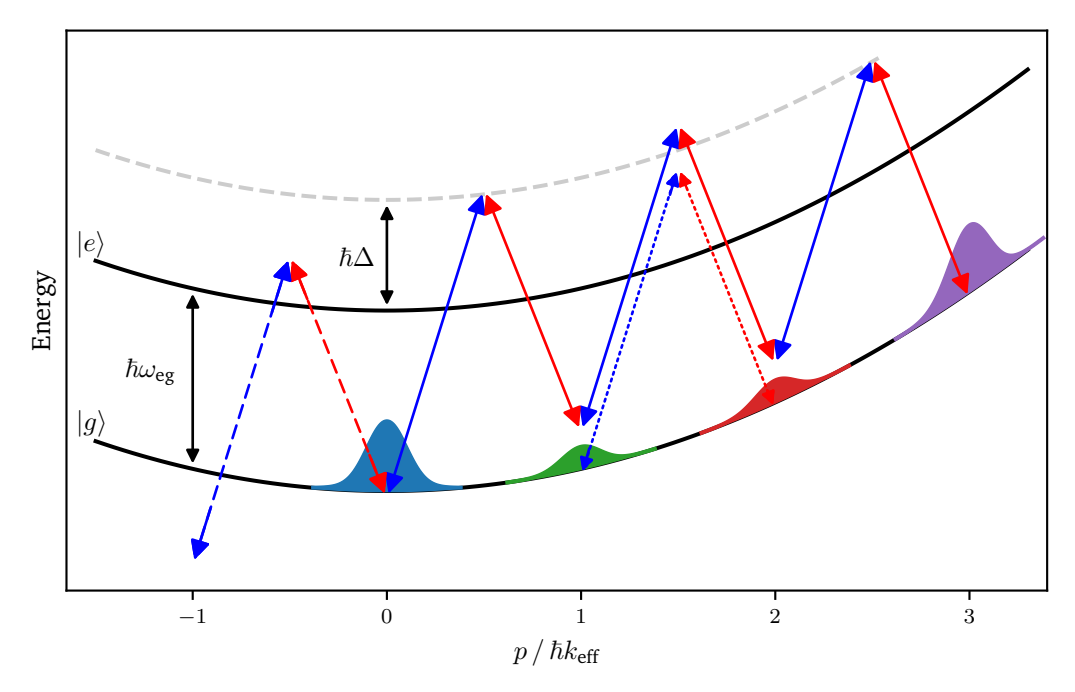


Fig. 4.18.: Energy-momentum conservation in a third-order Bragg process. Blue and red arrows denote the induced absorption and emission of photons of the corresponding Bragg beams. The light is strongly detuned (Δ) with respect to one-photon transitions ω_{eg} such that the excited state $|e\rangle$ is only virtually populated. Dashed arrows indicate a off-resonant transitions that are suppressed while the dotted arrows show a resonant two-photon process between the momentum states $p_1=1\hbar k_{\rm eff}$ and $p_2=2\hbar k_{\rm eff}$.

while generally all possible transitions should be considered. If no combination of Ω_R and τ is found that fulfils the pulse-area condition, the relative population of the parasitic paths should be taken into account to adjust the DMP parameters.

Experimental realisation of a DMP

Higher-order diffraction requires longer pulses or increased laser power, implying an increased $\Omega_{\rm R}$. The two parameters are balanced to minimise velocity selectivity while still observing a two-level behaviour between resonant momenta. However, this quasi-Bragg regime [176, 179–181] leads to inevitable population of parasitic orders p_i [see Fig. 4.3]. By using smooth pulse envelopes [like Blackman pulses Eq. (4.12)] this issue can be mitigated, but not eliminated. Fixing $\tau=90\,\mu{\rm s}$ and scanning $\Omega_{\rm R}$ by varying the optical power of the pulse, and therefore the effective two-photon Rabi frequency $\Omega_{\rm eff,1}$, when tuned to third-order resonance n=3, the probability \mathcal{P}_i of populating momenta p_i is determined by extracting the atom numbers in the relevant orders i=0,1,2,3 and normalising to their sum. In Fig. 4.19 the probabilities of p_0 (purple diamonds) and $p_3=p_0+3\hbar k_{\rm eff}$ (blue dots) is shown as a function of $\Omega_{\rm eff,1}$. From this scan the needed effective two-photon Rabi frequency $\Omega_{\rm eff,1}$ for beam splitter $(\pi/2)$ and mirror (π) pulses for third-order diffraction can be extracted. The transfer to momentum p_3 is limited

to 65%, which can be attributed to velocity selectivity, visible by the spatial structure of the atomic density remaining in the p_0 momentum state for $\Omega_{\rm eff,1}=2\pi\times23(2)\,\rm kHz$ [174]. The experimental observations are supported by simulations implementing the effective Hamiltonian [176]

$$\hat{H} = \frac{\hat{p}^2}{2m} + 2\hbar\Omega_{\rm R}f(t)\cos^2\left(\frac{k_{\rm eff}\hat{x} - \Delta\omega t + \phi}{2}\right),\tag{4.26}$$

with the phase of the Bragg beams ϕ and $[\hat{x},\hat{p}]=i\hbar$, since atomic interactions can be neglected due to the low atom density after expansion. For these simulations, a Split-Step-Fourier method implementing the palindromic *PP 3/4 A scheme* [206] was used. Numerical simulations have been performed by M. Dietrich and P. Schach of the group of Prof. E. Giese for the collaboration that led to the publication of these results [171]. Since the figure of merit, the diffracted population, is not expected to depend on the pulse phase in Bragg diffraction, $\phi_{\rm L}=0$ was chosen for the simulations. Furthermore, since no interferometric measurements are carried out including the DMP, there is no experimental access to this phase. The numerical model was fitted to the data using the experimental values of $\Omega_{\rm eff,1}$ and τ and only leaving the initial momentum spread Δp as a free parameter. The results are shown as solid lines in Fig. 4.19 and agree well with the experiments with some numerical noise visible. Applying the same routine to a larger data set varying $50\,\mu s \le \tau \le 150\,\mu s$, $\Delta p = 0.13(1)\hbar k_{\rm eff}$ can be inferred, matching the experimental value. Using the parameters obtained from this fit, the simulations can be

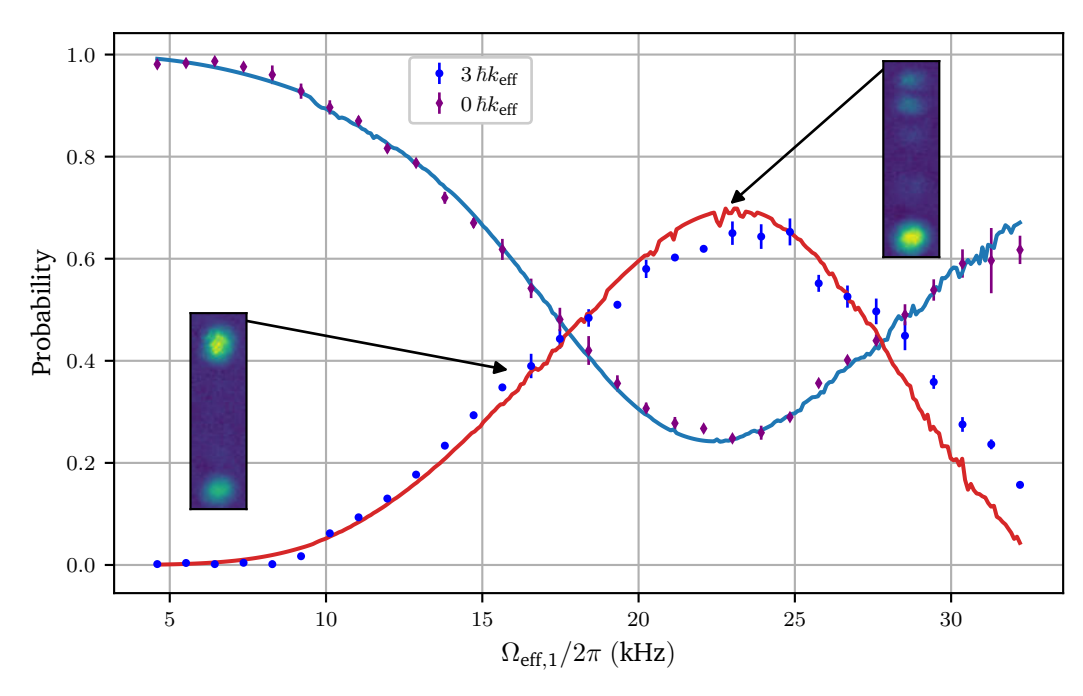


Fig. 4.19.: Experiment and simulation of third-order Bragg diffraction. Resonant Rabi scan for a fixed duration $\tau=90\,\mu s$ of a Blackman pulse. Scanning $\Omega_{\rm eff,1}$ induces Rabi oscillations between momentum states p_0 and p_3 (measured probabilities as purple diamonds and blue dots). Solid lines show a corresponding simulation with a fitted width $\Delta p=0.13(1)\hbar k_{\rm eff}$ of a Gaussian momentum distribution. False-color insets depict momentum distributions after a beam splitter (left) and mirror pulse (right) with population in p_0 at the bottom and in p_3 on top. The undeflected density lobes of p_0 are caused by momentum selectivity. (Numerical data courtesy of M. Dietrich and P. Schach of group of Prof. E. Giese)

extended to a full MZI sequence discussed in [171]. A supplementary plot of the numerical simulations can be found in Appendix C [Fig. C3]. Besides the resonant paths p_0 and p_3 ,

parasitic paths emerge after the first beam splitter as schematically shown in Fig. 4.20 (top). To demonstrate their impact, in Fig. C3a a path-resolved version of the MZI simulation is shown. The resonant paths 0 and 3 suffer loss from velocity selectivity, but the bulk of the population

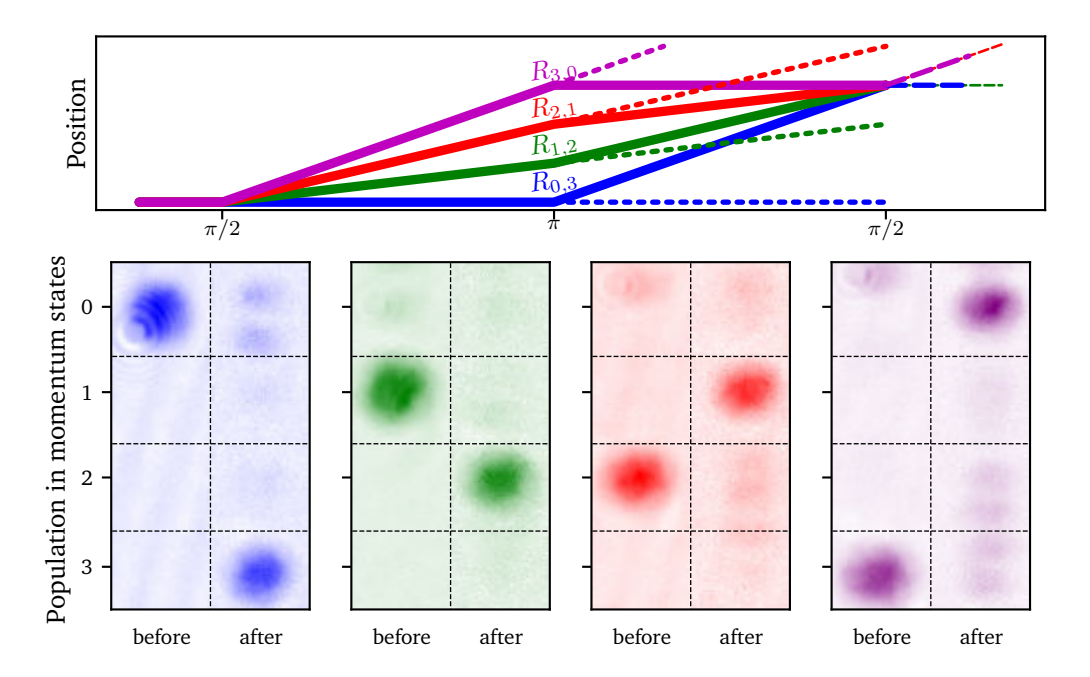


Fig. 4.20.: (top) Schematic visualisation of the four dominant order in a third-order MZI (colours correspond to Fig. 4.18). Solid lines show that all orders are effectively reflected towards the interferometer output by the conventional mirror pulse and dotted lines mark atoms not reflected by the mirror because of e. g. velocity selectivity. Hence, the parasitic paths contribute to the interferometer signal depicted by thin dashed lines in the exit ports. A numerically calculate version, courtesy of M. Dietrich and P. Schach is shown in Fig. C3a. (bottom) Experimental absorption images of momentum distributions before (left columns) and after (right columns) the mirror pulse with parameters obtained from the Rabi scan in Fig. 4.19. The resonant orders (purple and blue) are efficiently reflected, but so are the parasitic orders (red and green), which are redirected to the exit ports with high efficiency.

couples into the output ports as intended. Because the mirror pulse also redirects the parasitic paths 1 and 2, they are coupled into the relevant output ports, interfering with resonant paths and corrupting the signal. While the effect is small for adiabatic pulses that suppress the initial population of parasitic paths, it can limit the sensitivity of the interferometer [169].

To verify the numerical observation that the mirror pulse redirects both resonant and parasitic paths, atoms in four input states $p_{\rm in} \in \{p_0, p_1, p_2, p_3\}$ are selectively prepared by applying Bragg pulses at the respective resonance, as shown in the left columns of Fig. 4.20 (bottom) by absorption images in the far field. The colour scheme has been adapted to match the colours chosen for the respective diffraction order. After 4 ms of propagation, the third-order mirror pulse ($\tau = 90\,\mu\text{s}$, $\Omega_{\rm eff,1} = 2\pi \times 23(2)\,\text{kHz}$) is applied. The experimental scheme is visualised in Fig. 4.21 with the length of the Bragg pulses increased for visual purposes. Solid coloured lines trace the centre of mass (COM) motion and are exemplary shown for $p_{\rm in} = p_1$ with colours corresponding the colour scheme chosen in Fig. 4.20. The right column of Fig. 4.20 shows the resulting momentum distributions after applying the conventional mirror pulse with parameters taken from the Rabi scan [see Fig. 4.19]. The resonant orders (purple and blue) are efficiently reflected, but so are the parasitic orders (red and green), which are redirected to the exit ports with high efficiency.

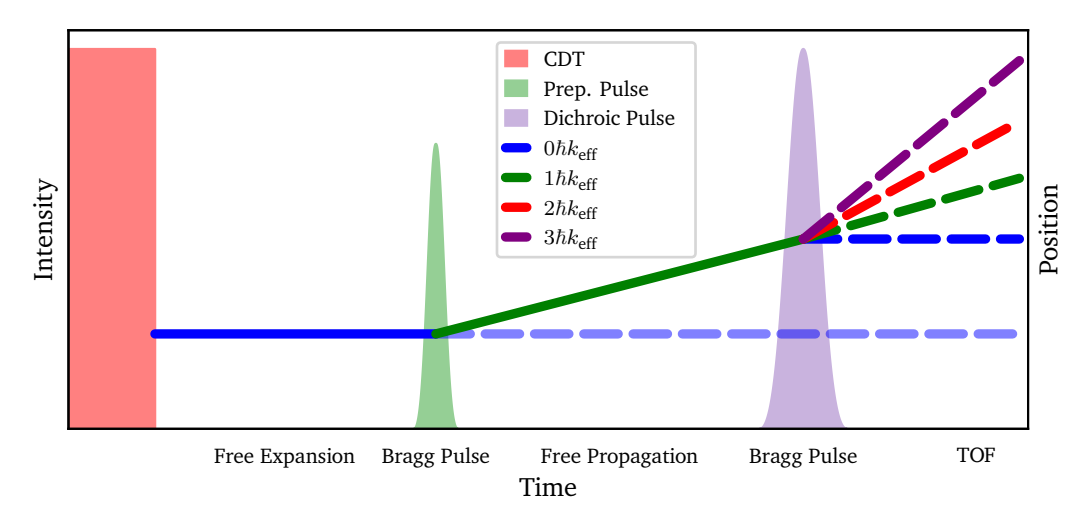


Fig. 4.21.: Schematic visualisation of the experiments carried out to determine the parameters for a DMP. After a BEC is released from the CDT, a free expansion of $3\,\mathrm{ms}$ is used to convert the mean field energy into kinetic energy. An initial π pulse with the resonance tuned to order $n\in\{0,1,2,3\}$ (here n=1) is used to transfer the atoms in the momentum state p_n . Separated by a free propagation of the BEC of $4\,\mathrm{ms}$, the second Bragg pulse tuned to resonance of the third order n=3 is applied with varying lengths τ and maximum two-photon Rabi frequency Ω_R and thus $\Omega_\mathrm{eff,1}$. The resulting momentum distribution is spatially separated with a TOF of $15\,\mathrm{ms}$ and detected.

To overcome this problem, a DMP is implemented that is reflective only for the resonant paths 0 and 3 while not redirecting the parasitic paths 1 and 2. Similar to the experiment presented in Fig. 4.20 and Fig. 4.21, ensembles in all four relevant $p_{\rm in}$ are prepared and a mirror pulse resonant to third-order diffraction, varying τ and $\Omega_{\rm eff,1}$ is applied. To obtain the reflectivity $R_{\rm in,out}$ for each path, the final probability of all four output momenta $p_{\rm out}$ is measured by integrating over the respective momentum distribution in the far field and normalising it. The resulting probabilities for all $p_{\rm in}$ and $p_{\rm out}$ are shown in Fig. 4.22, strikingly visualising the resonant coupling between $p_0 \leftrightarrow p_3$ and $p_1 \leftrightarrow p_2$ and the different scales of effective Rabi frequencies at play. From the measured probabilities, it is evident that the reflectivities $R_{0,3}$ and $R_{3,0}$ as well as $R_{1,2}$ and $R_{2,1}$ behave symmetrically. Therefore, it is sufficient to only take $R_{0,3}$ and $R_{1,2}$ (marked by a red frame in Fig. 4.22) into account.

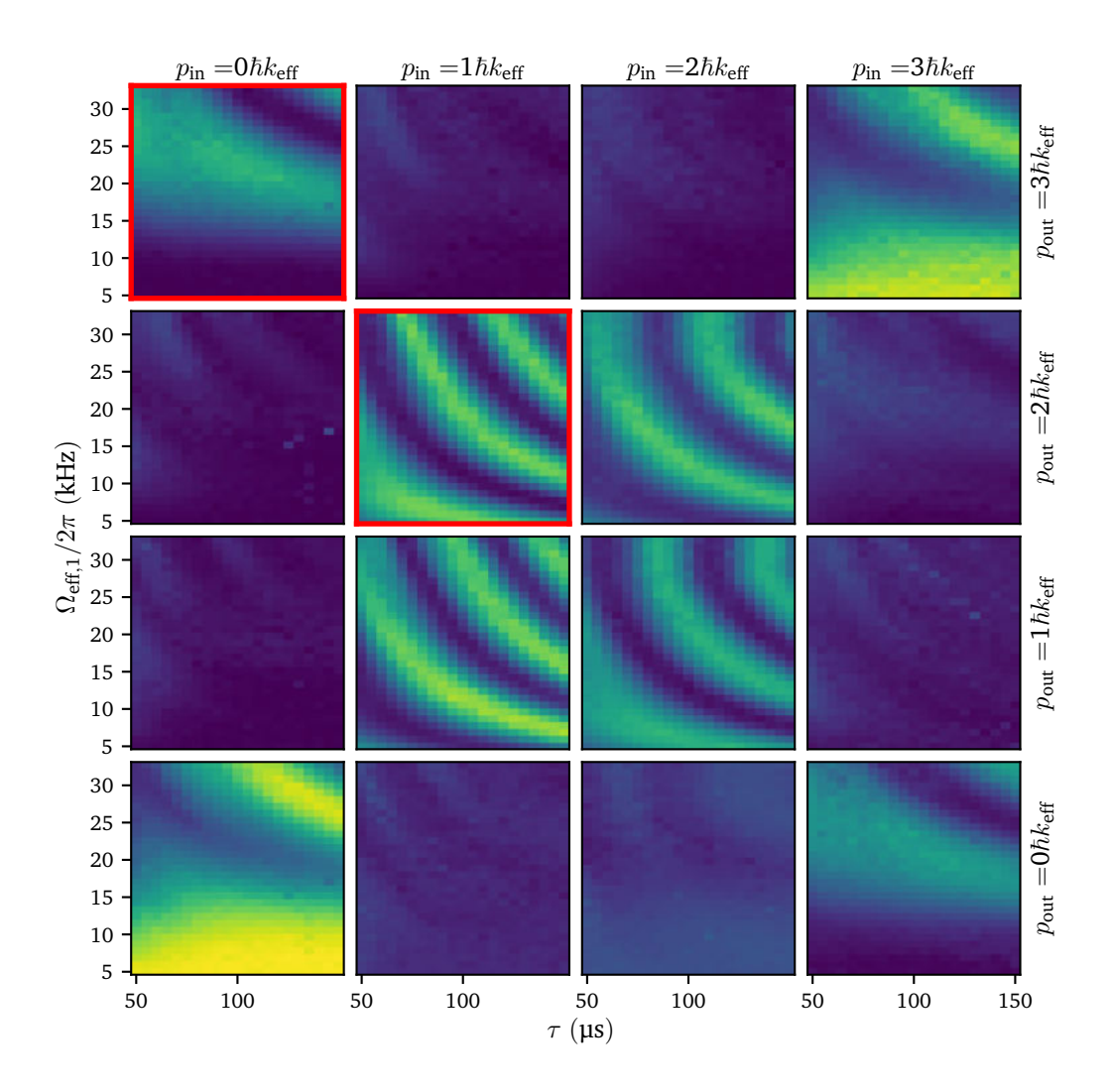


Fig. 4.22.: Experimental probabilities to find atoms in the state p_{out} for every $p_{\text{in}} \in \{p_0, p_1, p_2, p_3\}$ after the application of a Bragg pulse tuned to the third-order resonance. The pulse length τ is varied from $50~\mu \text{s}$ to $150~\mu \text{s}$ with the effective two-photon Rabi frequency ranging from $2\pi \times 4.6(4)~\text{kHz}$ to $2\pi \times 32.2(31)~\text{kHz}$ giving rise to different effective pulse areas. From this plot the symmetry between $R_{0,3}$ and $R_{3,0}$ as well as $R_{1,2}$ and $R_{2,1}$ is evident, making it sufficient to take $R_{0,3}$ and $R_{1,2}$ (red frame) into account when searching for a DMP.

In Fig. 4.23 (left column) the measured values for $R_{0,3}$ and $R_{1,2}$ are shown. Corresponding

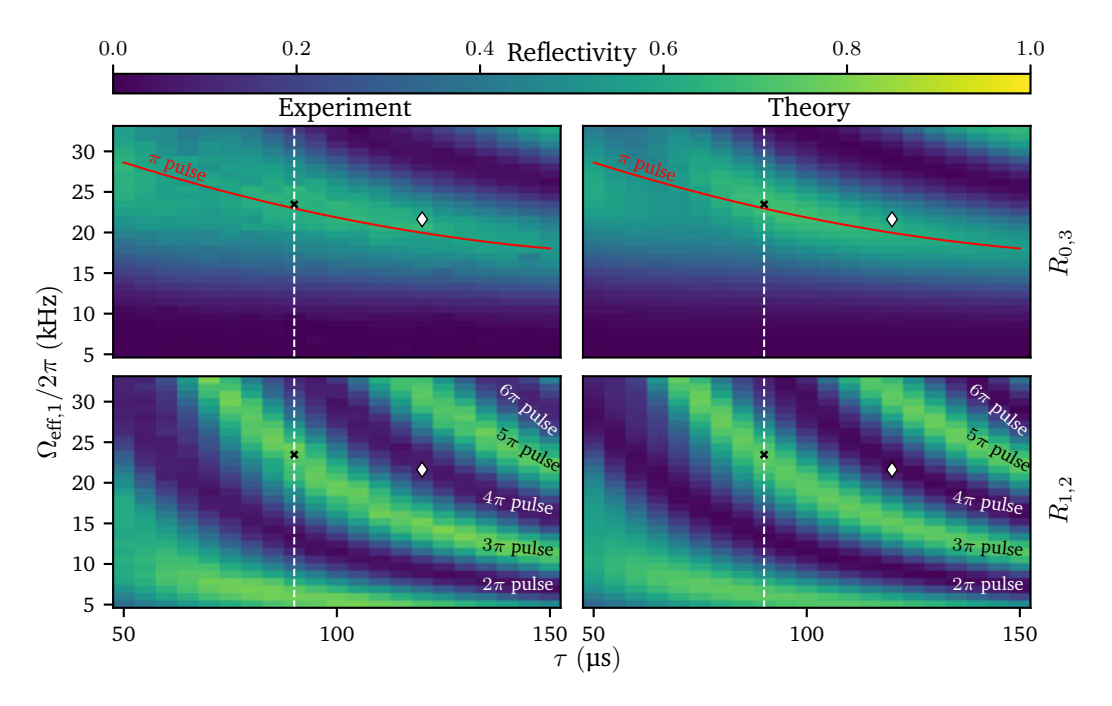


Fig. 4.23.: Experiment and simulation of third-order Bragg diffraction with DMP. Comparison of experimental (left) and numerical (right) reflectivities $R_{0,3}$ (top) for resonant six-photon and $R_{1,2}$ (bottom) for parasitic two-photon diffraction. Scanning τ and $\Omega_{\rm eff,1}$ reveals different effective Rabi frequencies for both cases. The white diamonds indicate the DMP [$\tau=120~\mu s$, $\Omega_{\rm eff,1}=2\pi\times21(2)~kHz$] with significantly improved performance over the mirror pulse (black cross) obtained in Fig. 4.19. The labels indicate pulse areas of multiples of π . (Numerical data courtesy of M. Dietrich and P. Schach of group of Prof. E. Giese)

simulations are depicted in the right column, showing excellent agreement. The white dashed line indicates the Rabi-frequency scan of Fig. 4.19. Since resonant paths are redirected by six-photon processes but parasitic paths by two-photon transitions, their effective multi-photon Rabi frequencies differ, as can be seen from different oscillation periods in the top and bottom panels. This behaviour suggests a parameter set where resonant orders experience a pulse area π , while parasitic orders experience pulse areas of multiples of 2π . In fact, for $\tau=120\,\mu s$ and $\Omega_{\mathrm{eff},1}=2\pi\times21(2)$ kHz a DMP with $R_{0,3}=0.62(1)$ and $R_{1,2}=0.08(1)$ (white diamonds) can be observed. In comparison to the parameters of Fig. 4.19 with $R_{0,3} = 0.65(2)$ and $R_{1,2} = 0.72(1)$ (black crosses), the reflectivity of parasitic paths drops significantly while the one of resonant paths remains almost unaltered. The pronounced reflectivity of resonant paths combined with the low reflectivity of parasitic paths implements the intended DMP schematically visualised in Fig. 4.24 (top). As in Fig. 4.20 (bottom), the momentum distributions before (left) and after (right) the DMP are shown to confirm the dichroic behaviour. Indeed, the DMP is reflective for resonant paths and redirects them to the exit ports, while maintaining near-perfect transparency for both parasitic paths where the output momentum distribution resembles the input. Additionally, a path-resolved MZI simulation in Fig. C3 is displayed in the supplementary material Appendix C.

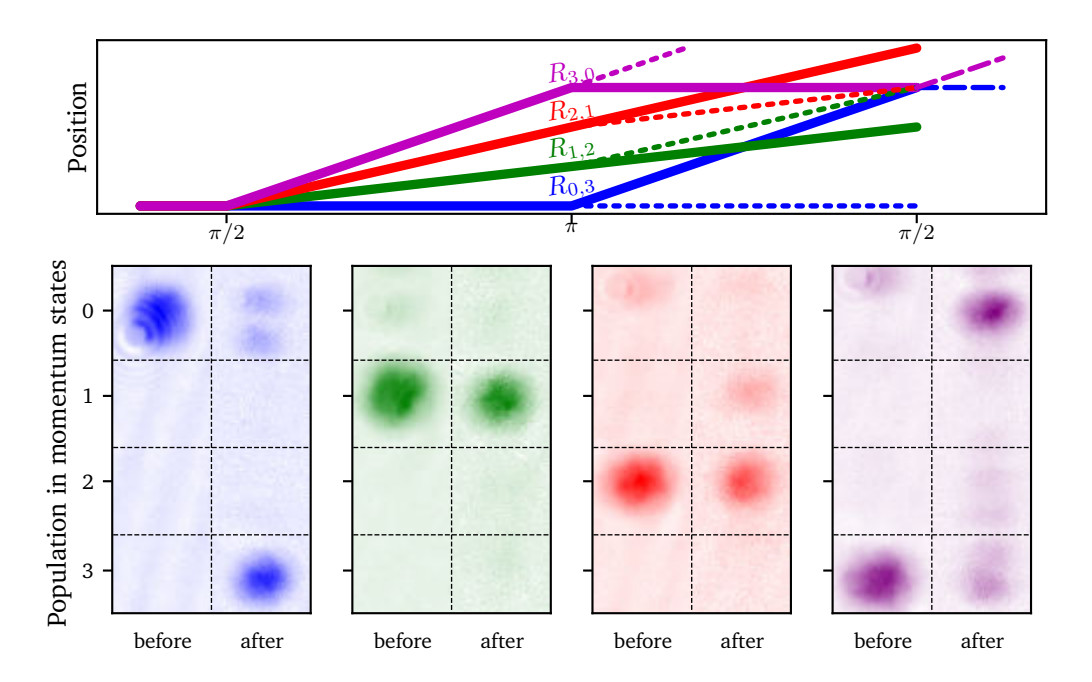


Fig. 4.24.: (top) Schematic visualisation of the four dominant order in a third-order MZI with a DMP (colours correspond to Fig. 4.18). Solid lines show that the parasitic orders are not reflected towards the interferometer output as was the case for the conventional mirror [see Fig. 4.20]. Hence, the parasitic paths do not significantly contribute to the interferometer signal. A numerically calculate version, courtesy of M. Dietrich and P. Schach is shown in Fig. C3b. (bottom) Confirming this dichroic behaviour experimentally by absorption images of the momentum distribution before (left columns) and after (right columns) the DMP, where parasitic paths are not reflected by the DMP and almost fully remain in their input momentum class.

Expansion to fifth order

These results can be transferred to any odd diffraction order, in particular to fifth order, which is a good compromise [174] between available laser power, velocity selectivity, and loss from spontaneous emission. This scalability is experimentally verified by implementing a fifth-order DMP and measuring $R_{0,5}$, $R_{1,4}$, and $R_{2,3}$ (Fig. 4.25 (bottom)). The latter two reflectivities are associated with parasitic paths as shown in Fig. 4.25 (top). The different scaling of the multi-photon Rabi frequencies [176] allows to identify parameters ($\tau=100\,\mu s$, $\Omega_{\rm eff,1}=2\pi\times52(5)\,{\rm kHz}$) where the pulse area is close to π for the resonant path, but 4π and 6π for the parasitic ones, giving reflectivities $R_{0,5}=0.57(1)$, $R_{1,4}=0.16(1)$, $R_{2,3}=0.10(1)$.

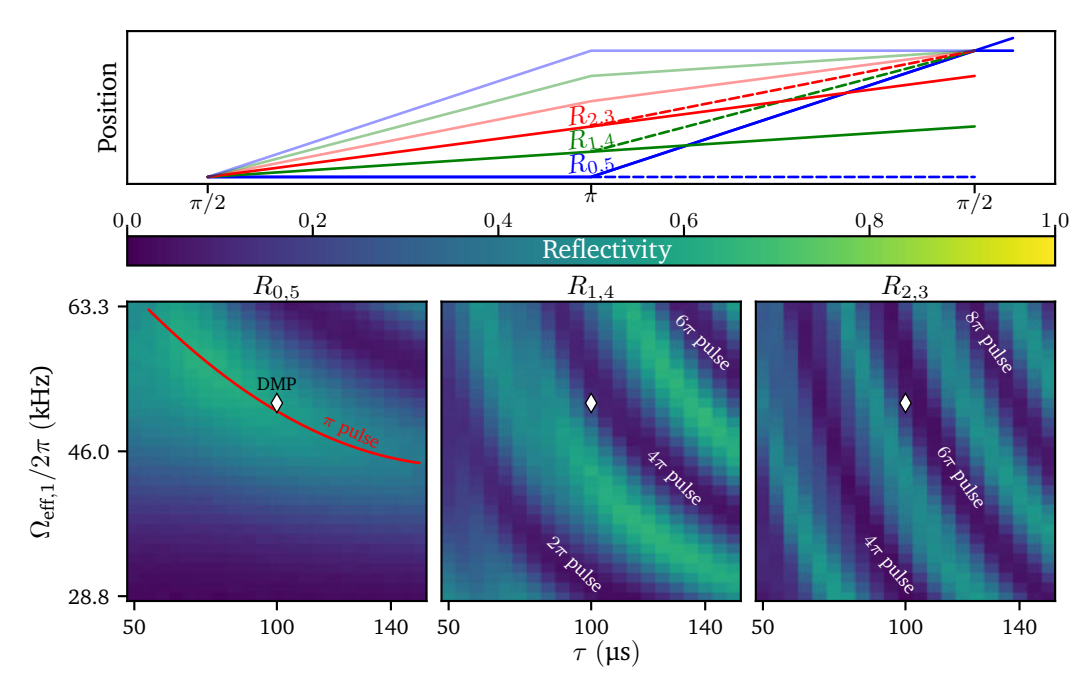


Fig. 4.25.: Fifth-order MZI (top) highlighting the paths associated with the reflectivities $R_{0,5}$, $R_{1,4}$, and $R_{2,3}$ as measured in (bottom) for different pulse lengths τ and effective two-photon Rabi frequencies $\Omega_{\rm eff,1}$. The DMP is marked by a white diamond ($\tau=100~\mu \rm s$, $\Omega_{\rm eff,1}=2\pi\times52(5)~\rm kHz$), where the resonant path experiences a pulse area close to π , while the parasitic paths undergo 4π and 6π pulses, respectively.

4.5. Summary

To summarise, in this chapter the requirements for long-interrogation time Mach–Zehnder interferometers (MZIs) in combination with higher-order Bragg diffraction were discussed and implemented. In Section 4.3, a magnetic field gradient in combination with a mixture of different magnetic sub-states was identified as the dominant cause for an apparent loss of visibility in the signal of MZIs. Furthermore, the magnitude of the gradient along the direction of Bragg diffraction was measured to be approximately $960(20)\,\mu\text{T/m}$ ($9.6(2)\,\text{G/m}$), confirmed by multiple evaluation techniques introduced in this section like fringe and ellipse fitting. Based in the loss of the visibility, a theoretical model was described, explaining the underlying mechanism that leads to the observed behaviour: a phase-stable summation of the interferometer signals of correlated MZIs with a differential phase.

Following this mechanism, an evaluation method was introduced that can be used to extract a differential phase with surprising precision, even when no state-selective measurements can be performed. The proper scaling of these effect for higher-order Bragg processed was investigated, realising MZIs in third-order Bragg diffraction. To complete the set of evaluation tools available for future interferometric experiments at the ATOMICS experiment, a state-selective detection scheme was implemented based on the Stern–Gerlach method allowing for an individual evaluation of the MZIs generated by the $m_{\rm F}$ sub-states. Neither in first nor third-order MZIs, a significant drop of the visibility could be observed on the time scales of investigated interferometer times, hence it can be expected that the coherence time $\tau_{\rm coh}$ is at least 6 ms.

Finally, an implementation of a dichroic mirror pulse (DMP) was discussed, complementing the possibility of realising large-momentum-transfer (LMT) atom interferometers in the future. The results of Section 4.4 have been produced in cooperation with the research group of Prof. E. Giese at the TU Darmstadt and have been published as an open access research letter in *Physical Review Research* [171].

5. Digital-micromirror-device potentials for ultracold ensembles

"When I see a bird that walks like a duck and swims like a duck and quacks like a duck, I call that bird a duck."

- James Whitcomb Riley

The development of techniques for configurable optical potentials has opened the possibility to investigate ultracold atomic ensembles including BECs in arbitrary potentials, giving rise to the research field of ATOMTRONICS striving to utilise the coherent and superfluid properties of such ensembles [40, 51, 52, 207]. Using two acousto-optical deflectors combined to control a beam in the xy-plane has been used to "paint" potentials guiding ultracold atoms, realising waveguides similar to optical fibres for light, splitters and recombiners [50, 208, 209]. Recently, quasi one-dimensional potentials implementing so-called prime number potentials have been implemented using spatial light modulators (SLMs) generating the potential using holographic methods [49]. Next to these approaches, digital micromirror devices (DMDs) that can primarily be found in data projectors have become an established method for the generation of arbitrary dynamic potentials [47, 210]. This has enabled studies from vortex dynamics and animatronic oscillator circuits to large persistent currents in BECs [55, 211–214]. Furthermore, DMDs have been deployed studying persistent currents and Kelvin-Helmholtz instabilities in fermionic systems [48, 215–217].

The advantages of a DMD-based system offering high flexibility while being relatively easy to implement make them an ideal expansion for the ATOMICS experiment, especially since a DMD has already been used in combination with the CR [46]. Replacing the complexity of the CR potentials, prone to misalignment, beam and polarisation errors with a direct imaging of the DMD surface reduces the complexity of the setup while increasing the flexibility.

In the following chapter, a new optical setup is introduced combining two DMDs allowing for the combination of attractive and repulsive potentials. This system has partially been built by L. Lind in his master thesis and since then has been extended for the operation of a second DMD [218]. Projects utilising the capabilities of this optical setup are being investigated in ongoing close collaborations with the research group of Prof. A. Yakimenko from the Taras Shevchenko National University of Kyiv and Prof. M. Edwards from the Georgia Southern University [54, 219].

Corrugations on the light sheet potential prevent this system to be fully utilised for experiments in arbitrary potentials at the time of this work (June 2025), which are briefly discussed. Finally, the DMD system is deployed to realise the adiabatic generation of ultracold atom ensembles in dynamic dimple potentials, paving the way for the generation of multiple consecutive BECs from one thermal reservoir.

99

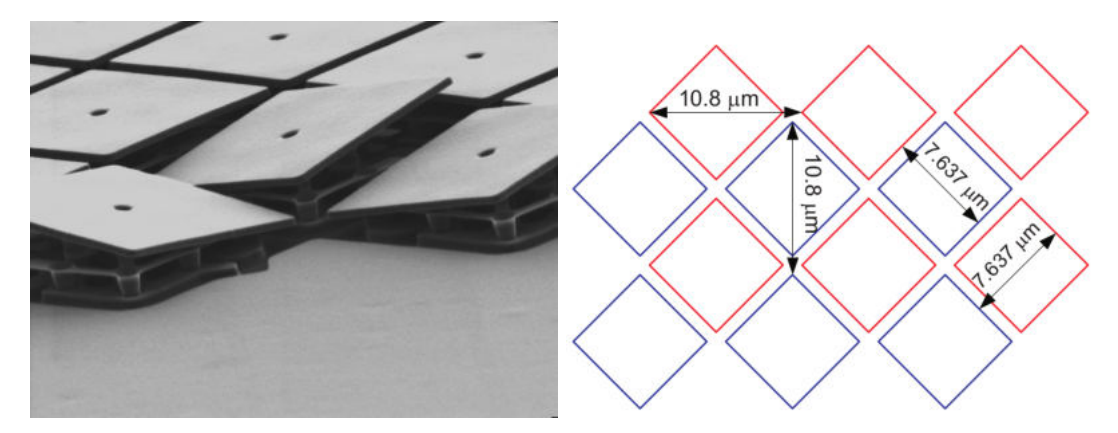


Fig. 5.1.: (left) Micro mirror arrays of a DMD. Each mirror is a built as an individual micro-electromechanical system (MEMS) and can be tilted by $\pm 12^{\circ}$ relative to its neutral position reflecting light towards the experimental beam path or into a beam dump [220]. (right) Schematic drawing of the micro mirror array with a pitch of $7.4\,\mu\mathrm{m}$ generating a blaze grating [221].

5.1. Characterisation of the DMD system

The DMD system at the ATOMICS experiment was conceptualised and partially built in the master thesis of L. Lind [218]. It is based on two TI DLP® 3000 LightCrafter modules, with a separate beam path for each of the DMDs. The micromirror array of this DMD consists of 608×684 individual quadratic mirrors with a pitch of $7.4\,\mu m$ [see Fig. 5.1 (right)] spanning a total area of $6.57\,mm \times 3.7\,mm$. Each mirror can be tilted by $\pm 12^\circ$ relative to the DMD surface, reflecting light either towards the experimental beam path or into a beam dump.

Which way each mirror is tilted is controlled by a binary image file displayed on the DMD, in the following called potential mask. At the ATOMICS experiment, a set of Python scripts is available to convert calculated potentials into corresponding potential masks. Initially, the desired potential is calculated and the script determines the necessary optical power to realise the potential. Since the DMD can only display binary files, a dithering algorithm is used to convert the target potential into a binary potential mask. Here, a dithering approach based on the Bayer-16 method is implemented [222]. To calculate the potential mask properly, the properties of the optical setup such as the wavelength, optical power and magnification as well as the waist of the illuminating beam need to be supplied.

A total of up to 96 potential masks can be stored on the internal buffer of the DMD. These can be cycled by applying a TTL signal to the trigger input of the DMD which allows to generate semi-dynamic potentials by cycling between changing potential masks. The minimum time a potential mask has to be displayed when using 96 masks is 385 µs [221].

As mentioned in Section 2.4.3, two individual Ti:Sa laser systems are used to supply the laser light for this system. A schematic overview of the DMD setup in its current form is shown in Fig. 5.2. Since both paths are constructed analogously, the red-detuned path will be described in the following with a summary of the properties for both paths given in Tab. 5.1. The light generated by the Ti:Sa laser is outcoupled from an optical fibre guiding the light from the laser system to the optical table. A combination of a $\lambda/2$ waveplate and a PBS is used to ensure a linear polarisation of the light. Following, part of the light is sampled and guided to a photodiode for intensity stabilisation via an RPI. The beam is then guided to the DMD surface with the incident angle matched such that the part reflected towards the experiment is perpendicular to the DMD surface. Here it is important to mention, that the surface of the DMD

Tab. 5.1.: Properties of the DMD system at the ATOMICS experiment at the time of this work (June 2025). The maximum optical power $P_{\rm max}$ is measured between the beamsplitter (Bs) and the last two lenses (L4, L5) mounted on top of the vacuum chamber.

	λ	P_{max}	w_{DMD}	M	U_{max}
Red-detuned DMD	$800.3\mathrm{nm}$	$19.2(10)\mathrm{mW}$	$1.0(1){\rm mm}$	0.148(20)	$-5.7(5){\rm E}_{\rm rec}$
Blue-detuned DMD	$776.3\mathrm{nm}$	$41.4(10)\mathrm{mW}$	$1.2(1)\mathrm{mm}$	0.178(20)	$26.1(5)\mathrm{E}_{\mathrm{rec}}$

generates a reflective diffraction grating. To maximise the diffraction efficiency, the incident angle has to be close to the third-order diffraction angle along both axis of the micromirror arrays [223]. Furthermore, these diffractive properties of the DMD make it necessary to realign the optical system in case of a wavelength change. The waists of the Gaussian beams illuminating the DMDs are measured as $w_{\rm DMD,red}=1.0(1)\,{\rm mm}$ and $w_{\rm DMD,blue}=1.2(1)\,{\rm mm}$. For both beampaths two achromatic lenses with focal lengths $f_{L1r}=f_{L1b}=400\,\mathrm{mm}$ and $f_{L2r} = f_{L2b} = 100$ mm remap the surface of the DMD to an intermediate image plane with a magnification of $|M_{1,2}| = 0.25$. Additionally, these lenses are configured in a $2(f_1 + f_2)$ setup giving access to the Fourier plane where an aperture is placed allowing the manipulation of the k-vector distribution. Hence, the image can be smoothed out by reducing the opening of the aperture, removing large k-vector components associated with sharp edges [127, Chap. 11]. In a PBS, both beams of the red-detuned and blue-detuned path are combined with both intermediate image planes overlapped. Prior to entering the vacuum chamber, a 50:50 non-polarising beam splitter cube splits the combined beam with one part being reflected towards the chamber. The combination of two achromatic lenses (L4 with = $75 \,\mathrm{mm}$ and $f_{\rm L4} = 400 \, \rm mm$, L5 with = 75 mm and $f_{\rm L3} = 300 \, \rm mm$), permanently mounted on top of the vacuum chamber and also used for the vertical detection path, remap the intermediate image to plane of the CDT in the chamber with a magnification |M| = 0.60(3).

A second pair of achromatic lenses ($L1_{\rm mon}$, $L2_{\rm mon}$) with focal lengths $f_{1\rm mon}=400\,{\rm mm}$ and $f_{2\rm mon}=300\,{\rm mm}$ is used to relay the intermediate image in the transmitted beam of the non-polarising beam splitter to a monitoring camera Point Grey CM3-U3-13S2M. This monitoring beam path can be used to observe a twin-image of the intensity distribution in the vacuum chamber with similar properties.

The optical resolution of both DMD paths is limited by the lenses mounted to the vacuum chamber and is given by $\Delta d=3.8\,\mu\text{m}$. Here, Δd is the diffraction limited spot size calculated at $780\,\text{nm}$ for L_5 according to the Rayleigh criterion $\Delta d=1.22f\lambda/[61$, Sec. 5.7]. Using the DMDs to display potentials of a known size, the total magnification for the red-detuned path is measured to $|M|_{\rm r}=0.148(20)$ and for the blue-detuned path $|M|_{\rm b}=0.178(20)$ from the DMD surface to the plane of the atoms in the vacuum chamber. For the monitoring beam path, the magnification is measured to $|M|_{\rm mon}=0.168(20)$ from the DMD surface to the monitoring image plane.

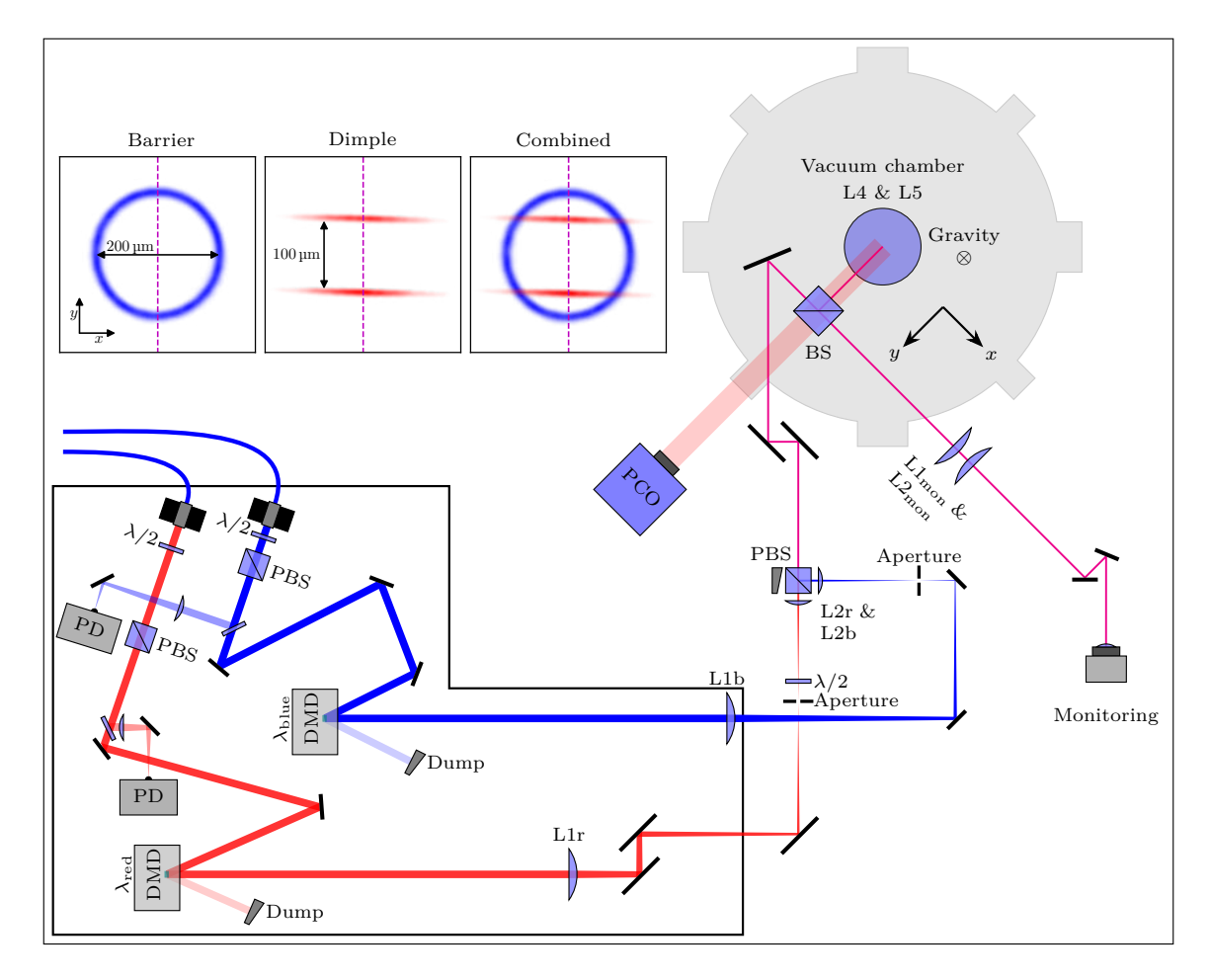


Fig. 5.2.: Schematic visualisation of the DMD optical setup. The light produced by two separate Ti:Sa lasers $(\lambda_{\rm red}=800.3~{\rm nm}$ and $\lambda_{\rm blue}=776.3~{\rm nm})$ is outcoupled from optical fibres with a combination of a $\lambda/2$ waveplate and a polarising beam splitter cube (PBS) ensuring a linear polarisation. Part of the beam is sampled and focused onto a photodiode (PD) for intensity stabilisation. The remainder of the beam is illuminating the DMDs with a combination of two achromatic lenses $(f_1~{\rm and}~f_2)$ in $2(f_1+f_2)$ configuration reimaging the surface to an intermediate plane with magnification |M|=0.25 and giving access to manipulate the k-wave spectrum in the Fourier plane. A PBS is used to combine the two beams with the two lenses fixed to the vacuum chamber (L4,L5) reimaging the intermediate plane into the vacuum chamber. The non-polarising 50:50 beam splitter (BS) cube combines the DMD beam path with the vertical detection light (light red) propagating in opposite direction. The secondary output of this BS is used as a monitoring path for the DMD potentials. Insets in the top left show a blue-detuned ring barrier with a radius of $100~{\rm \mu m}$ as used for the adiabatic generation of BECs and the red-detuned dimple potentials spaced $100~{\rm \mu m}$ apart (sizes given for the atom plane in the vacuum chamber). Right inset shows the combination of both potentials with the linear waveguide (LWG) oriented perpendicular to the dimple potentials (dashed line).

5.2. Bose-Einstein condensation in DMD potentials

As described above, the DMD system can be used to generate arbitrary two-dimensional potentials by reimaging the surface of the DMDs into the plane of the atoms. Since these potentials provide no confinement in the vertical direction and hence against gravity, an additional potential needs to be used. This can be generated by the light sheet system described in Section 2.4.3, ideally providing a strong confinement in the vertical direction and close to no confinement in the horizontal plane.

The combination of light sheet and the DMD potentials provides the opportunity the extent the interferometric measurements discussed in Chapter 4 using arbitrary external guiding potentials. Furthermore, the direct creation of BECs in such potentials, especially ring-shaped potentials opens up the possibility to investigate the dynamics of BECs including rotational states and the Josephson effect [54, 219, 224–226]. Moreover, the investigation of the topology change of a BEC in a dynamic trap becomes feasible, opening the opportunity to expand further on the understanding of excitations in such systems, discussed in the theses of J. Teske and F. Schmaltz [46, 227].

Additionally, the research field of ATOMTRONICS, investigating various approaches to utilise the properties of ultra cold atoms and BECs from quantum sensors to fundamental physics, relies heavily on arbitrary guiding potentials that can be generated by, e.g. a DMD system [40].

While the system can generally be used to trap atomic ensembles in combined potentials from the light sheet and DMD system, an additional challenge has been encountered. To fully utilise the capabilities of the DMD system, the light sheet potential needs to have a potential roughness well below the chemical potential of, e.g. a BEC. If the potential has corrugations larger than the chemical potential, the BEC will sample the potential landscape leading to uneven atomic densities or the separation of the BEC into smaller sub-ensembles effectively destroying the BEC. In the master thesis of D. Derr such corrugations on the light sheet system used at that time (2022) have been found and investigated in detail [80]. Several approaches to mitigate these corrugations, including a rebuild of the laser system and optical setup has been found ineffective at the time of this work (June 2025). By altering the optical setup, the qualitative structure of the corrugations can be affected in unpredictable ways. So far, no configuration was found that produced a section of the light sheet sufficiently smooth to allow atomic ensembles to expand uniformly within the potential.

By changing the optical layout from the laser providing the optical power, including a change in wavelength from $783.5\,\mathrm{nm}$ to $797.8\,\mathrm{nm}$, to the vacuum chamber window through which the beam is guided to the atoms with corrugations appearing for any setup, multiple causes were ruled. A possible reason is the interference of the light sheet beam with a reflection, generated as the beam passes through the windows of the vacuum chamber. Since the spatial expansion of the beam in the horizontal direction is larger than the lateral offset of the reflection, this is the most likely reason for the unevenness. Recently, J. Henning has investigated additional compensation potentials based on blue- and red-detuned DMD potentials with limited success [228]. Additionally, the possibility to build a new light sheet system at $\lambda=1070\,\mathrm{nm}$ using the laser generating the CDT is currently being investigated.

5.2.1. Adiabatic generation of Bose-Einstein condensates

To create a BEC by forced evaporative cooling in the CDT takes typically 18 s including the MOT loading phase. Furthermore, to create a BEC, the majority of the atoms are discarded despite being already close to quantum degeneracy. Ideally, techniques to create multiple BECs from one pre-cooled yet thermal reservoir could be implemented to increase the repetition rate of an atomic interferometer. Since the CDT only provides a single potential, this cannot be realised in this configuration.

Using the DMD system on the other hand, allows for a reconfigurable potential landscape that can be used to implement a technique based on the adiabatic generation of BECs [68, Sec. 10.7]. The underlying idea behind this method is that a thermal ensemble in a reservoir potential with a temperature above the critical temperature has a chemical potential $\mu_{\rm res} < 0$. By introducing a narrow (dimple) potential with depth $U_{\rm dimp} = -\mu_{\rm res}$ the atoms will start to macroscopically occupy the new lowest potential state, effectively forming a BEC. This effect cannot simply be understood in terms of an increase in the critical temperature in the dimple since increasing the trapping frequency will increase the temperature of the thermal ensemble, even if done adiabatically [68, Sec. 10.7].

Already in the early stages of experimental BEC research, this method has been successfully used to create BECs [229, 230]. Recently, an adapted version of this method has been used to create a BEC in a thermal reservoir continuously refilled with thermal atoms extending the lifetime of the BEC [231]. The growth dynamics and kinetics of BECs in such dimple potentials have been studied experimentally for various dimple depths [232] with a kinetic model describing the dynamics studied by S. Dutta and E. Müller [233].

Experimental reservoir and dimple potentials

To realise this method at the ATOMICS experiment, a combination of the light sheet potential and the DMDs potentials could be used, opening up the possibility to transfer the BECs directly into a guiding potential for, e.g. guided atom interferometric measurements. Increasing the smoothness of the light sheet potential is a necessary step to realise such experiments. Hence, for an initial implementation of this method, the CDT is chosen as a thermal reservoir, described in the following section. In Fig. 5.3, the combination of potentials used to implement the dimple method is shown. A magenta solid line depicts the main reservoir potential depth as generated by one arm of the CDT. The blue-detuned DMD system is used to generate a repulsive ring-shaped potential with a height of $U_{\text{barr}} = 5 \, \text{E}_{\text{rec}}$ [see also inset of Fig. 5.2] constraining the reservoir along the y-axis. A small dimple is generated by a Gaussian-shaped potential with a waist of approximately $5 \mu m$ along the y-axis (red). The reconfigurability of the DMD allows to introduce multiple of such dimple potentials [see inset of Fig. 5.2]. Furthermore, the dynamic properties of the DMD can be used to move the dimples after the creation of an ensemble in order to create secondary dimples. In Tab. 5.2, a summary of the dimple potential properties is given for a depth of $|U|_{\text{dimp}} = 1 \, \text{E}_{\text{rec}}$. The large uncertainties in the expected trapping frequencies, especially along the y-axis are reasoned in the uncertainties of the magnifications $|M|_{mon}$ and $|M|_{red}$ as well as the short Rayleigh length along this axis. For an expected waist of $w_y = 6.6 \,\mu\text{m}$, the Rayleigh length is $z_{\text{R},y} = 170 \,\mu\text{m}$ which is comparable to the positioning precision of the potentials along the propagation axis i. e. the precision with which the focal plane of the DMD potentials can be overlapped with the plane of the CDT [see also Section 3.2.3].

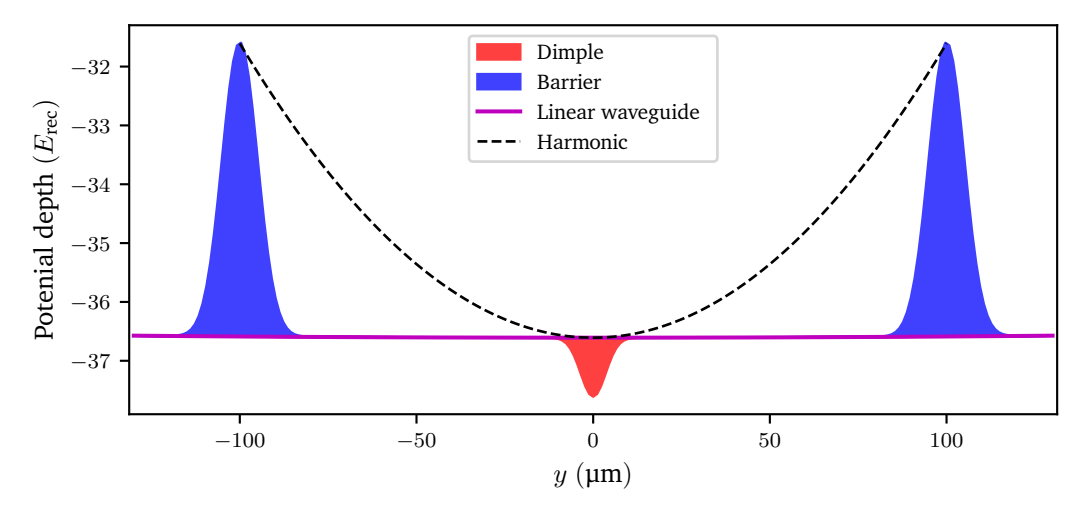


Fig. 5.3.: Potentials along the y-axis as used in the ATOMICS experiment to realise the adiabatic generation of BECs. A magenta solid line depicts the main reservoir potential realised by using one of the CDT beams as LWG. The reservoir is restricted by a repulsive barrier potential (blue) generated by a blue-detuned ring-shaped DMD potential. Using the red-detuned DMD beam, a dimple potential can be introduced (red) with the narrow dimension perpendicular to the weak reservoir axis. A dashed black line shows a harmonic potential used to estimate a critical temperature in the reservoir.

Tab. 5.2.: Properties of the dimple potentials for $|U|_{\rm dimp}=1.0(1)\,{\rm E}_{\rm rec}$ as measured by the monitoring camera. Spatial dimensions are equal for the dimple with $|U|_{\rm dimp}=2.0(2)\,{\rm E}_{\rm rec}$. For the expected waists and trapping frequencies, the measured waists in the monitoring image plane are scaled by the magnifications $|M|_{\rm red}=0.148(20)$ and $|M|_{\rm mon}=0.168(20)$ to infer the waist at the atom plane. For an uncertainty estimation of the trapping frequencies, a 10% error in the potential depth is assumed. Here, only the properties of the dimple potentials are presented. The total potential is given by a combination of dimple and reservoir potential. The y-direction is dominated by the dimple while x- and z direction are dominated by the reservoir potential [see Tab. 5.3].

Monitoring	Vacuum chamber		Monitoring	Vacu	ıum chamber
w_x	w_x	ω_x	w_y	w_y	ω_y
$105(2)\mu\mathrm{m}$	$92.5\mu\mathrm{m}$	$2\pi \times 14^{+1}_{-3}{\rm Hz}$	$7.5(10)\mathrm{\mu m}$	$6.6\mu m$	$2\pi \times 203^{+10}_{-94}\mathrm{Hz}$

Thermal reservoir

Employing the single beam of the CDT alongside the blue-detuned ring-shaped potential (inset of Fig. 5.2) as a reservoir for adiabatic BEC generation presents distinct advantages over light-sheet-based reservoirs [see Section 2.4.3]. This approach combines large detuning with high optical power to create deep potentials while maintaining scattering rates negligible on experimental timescales. To load the reservoir, a pre-cooled ensemble generated in the CDT with initial atom number $N_{\rm init}=84\,000(1200)$ at $T_{\rm init}=760(30)$ nK is used. The critical temperature for this ensemble in the CDT with $\omega_r=2\pi\times210\,{\rm Hz}$ and $\omega_z=2\pi\times300\,{\rm Hz}$ is $T_{\rm crit}=465\,{\rm nK}$ which is below the measured temperature of the ensemble. Hence, it can be assured that the initial ensemble is purely thermal.

A linear ramp is used to transfer the atoms from the CDT to the reservoir potential, simultaneously increasing the power in the LWG, i. e. the CDT beam along y, and blue-detuned DMD potential and decreasing the power in the second CDT beam along x. For all experiments discussed in this work, the length of the ramp was chosen to be $100\,\mathrm{ms}$. To ensure a thermal equilibrium, after the transfer from the CDT to the reservoir, an additional waiting time of

250 ms is added.

Upon the transition to the reservoir, i. e. linear-wave guide potential, the atom number decreases to $N_{\rm res}(1250\,{\rm ms})=56\,000(4300)$ with a temperature of $T_{\rm res}(1250\,{\rm ms})=350(10)\,{\rm nK}$ for a hold time of $1250\,{\rm ms}$. A summary of the reservoir parameters is given in Tab. 5.3. Through evaporation, this atom number decreases further with increased holding time to $N_{\rm res}(5000\,{\rm ms})=47\,900(1000)$ with a temperature of $T_{\rm res}(5000\,{\rm ms})=240(10)\,{\rm nK}$.

Since the reservoir potential is provided by one arm of the CDT, the trapping frequency along the propagation axis of the LWG decreases to $2\pi \times 1.3\,\mathrm{Hz}$, hence the critical temperature decreases to $70\,\mathrm{nK}$ for this configuration. This provides a lower bound for the critical temperature only, since the atoms are restricted by the blue-detuned DMD potential to a length of $l_{\mathrm{res}} = 200\,\mathrm{\mu m}$ effectively increasing the density and hence the critical temperature. To calculate an upper bound, a harmonic potential is assumed, centred in the middle of the reservoir with a potential height of $5\,\mathrm{E}_{\mathrm{rec}}$ at the radius of the DMD potential [see Fig. 5.3]. The critical temperature for this configuration is evaluated to $170\,\mathrm{nK}$ which is still well below the temperature of the ensemble determined by the TOF measurement. This again ensures, that the ensemble in the reservoir remains thermal without the dimple potentials.

Finally, the aspect ratio of the atom ensemble is evaluated as ratio of σ_x/σ_y taken from the two-dimensional Gaussian fits used in the TOF measurement to determine the temperature. The ensemble has an initial aspect ratio of 0.18 which increases to a value of 0.97 for the maximal TOF of $30\,\mathrm{ms}$.

Tab. 5.3.: Summarised reservoir parameters for this work. The value of $|U_z|$ includes the reduction of the potential by the gravitational potential.

$\overline{N_{ m res}}$	$T_{\rm res}$	$\omega_r = \omega_x = \omega_z$	ω_y	$ U_y $	$ U_z $	$ U_x $
56 000 (4300)	350(10) nK	$2\pi \times 210\mathrm{Hz}$	$2\pi \times 1.3\mathrm{Hz}$	$5\mathrm{E}_{\mathrm{rec}}$	$11.7\mathrm{E}_{\mathrm{rec}}$	36.6 E _{rec}

Single dimple

To investigate the interaction between the thermal reservoir and an additional narrow dimple potential, the experimental procedure schematically shown in Fig. 5.4 is realised. First the reservoir is loaded from the CDT in $t_{\rm load}=100\,{\rm ms}$ as discussed in the previous section. After the equilibration time of $t_{\rm eq}=250\,{\rm ms}$, the potential depth of the dimple is linearly increased to its maximum value over $t_{\rm init}=100\,{\rm ms}$. The dimple potential is kept constant for a varying holding time $250\,{\rm ms} \le t_{\rm hold} \le 5000\,{\rm ms}$ while the reservoir barrier is switched off $t_{\rm purge}=150\,{\rm ms}$ prior to the end of $t_{\rm hold}$. Following the purging of the reservoir, all potentials are switched off and a TOF measurement can be performed. A summary of the experimental times and dimple potential depths used is given in Tab. 5.4.

It was observed that the atomic density in the dimple potentials remains below the detection threshold when the reservoir is present. Even normalisation and background-subtraction measurements of the reservoir (with and without dimple potentials) and subsequent subtraction of the averaged reservoir density from the measurements with dimple potential failed to enhance

Tab. 5.4.: Parameters used for the measurements with static dimple potentials.

$\overline{t_{ m init}}$	$t_{ m hold}$	$t_{ m purge}$	$ U _{\mathrm{dimp}}$	TOF
100 ms	$250\mathrm{ms}$ to $5000\mathrm{ms}$	$150\mathrm{ms}$	$1\mathrm{E}_{\mathrm{rec}},2\mathrm{E}_{\mathrm{rec}}$	$0\mathrm{ms}$ to $10\mathrm{ms}$

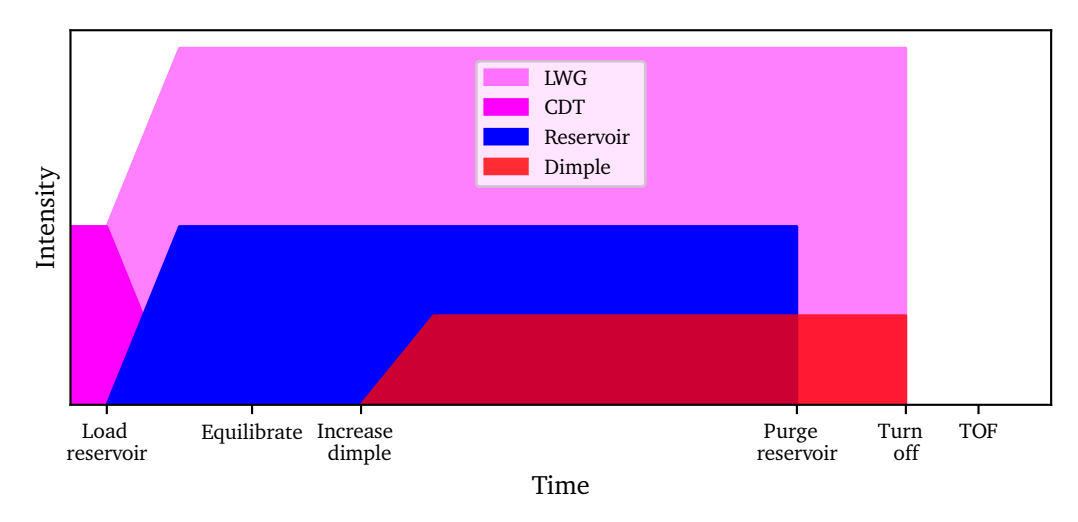


Fig. 5.4.: Schematic visualisation of the experimental protocol used for the static dimple experiments. The reservoir is loaded from the CDT (red) by transitioning to the LWG (light red) while increasing the barrier potential (blue). After an equilibrium time, the dimple potential (magenta) depth ins linearly increased and all potentials are kept constant for the holding time. To purge the reservoir, the barrier potential is removed ahead of the TOF measurement.

the detectability of dimple potential signals. In order to lower the density of the reservoir atoms prior to the detection, a purge of the reservoir is implemented by removing the repulsive barrier potential ahead of time while the dimple and LWG are kept at constant depth. This allows the thermal atoms of the reservoir to distribute along the LWG, drastically reducing the density at the location of the dimple, hence, improving the detection. In addition to lowering the density of the reservoir, enhancing the detectability of the dimple ensembles, this might provide some form of evaporative cooling which is currently being investigated by L. Lind at the ATOMICS experiment. Furthermore, for every measurement, a comparative realisation with the same parameters but $|U|_{\rm dimp}=0$ is carried out. In the evaluation of the experimental data, these comparative measurements are averaged and subtracted from the realisations with $|U|_{\rm dimp}\neq 0$. The remaining densities resemble the atoms present in the dimple potentials. In the following, the results for a holding time of $t_{\rm hold}=1000\,{\rm ms}$ are discussed. For the remaining holding times, the resulting observations are similar.

In Fig. 5.5 (top), the atomic densities are depicted for dimple potential depths of $|U|_{\rm dimp}=1~{\rm E}_{\rm rec}$ and $2~{\rm E}_{\rm rec}$ and the TOF of 0 ms to 10 ms. Here, the reservoir atoms have been subtracted via the comparative measurement without any dimple potential as described above. To evaluate the expansion behaviour, two-dimensional Gaussian functions [see Eq. (2.26)] are fitted to the resulting densities to extract the time dependent widths $\sigma_{x,y}$. The resulting widths can be used to estimate a temperature both along the x- and y-axis using Eq. (2.27). For a dimple potential of $|U|_{\rm dimp}=1~{\rm E}_{\rm rec}$, temperatures of $T_y=40(2)~{\rm nK}$ and $T_x=250(20)~{\rm nK}$ are determined, averaged over six experimental realisations. Comparing T_x to the temperature of the reservoir atoms evaluated from the comparative measurements without a dimple $T_{x,{\rm res}}=360~{\rm nK}$ shows that the ensemble from the dimple has a similar temperature along the x-axis. Computing the aspect ratio of the widths σ_x/σ_y for each TOF [see Fig. 5.5 (centre)] reveals a remarkable behaviour. Initially, the ensemble has an aspect ratio of 1.02(7) which approaches an asymptotic value of 2.2(2) for an increasing TOF. This is in stark contrast to the behaviour of a purely thermal ensemble, which invariably becomes isotropic. Using the atom number in the dimple N=1040(200), determined by summing over the density distribution, combined

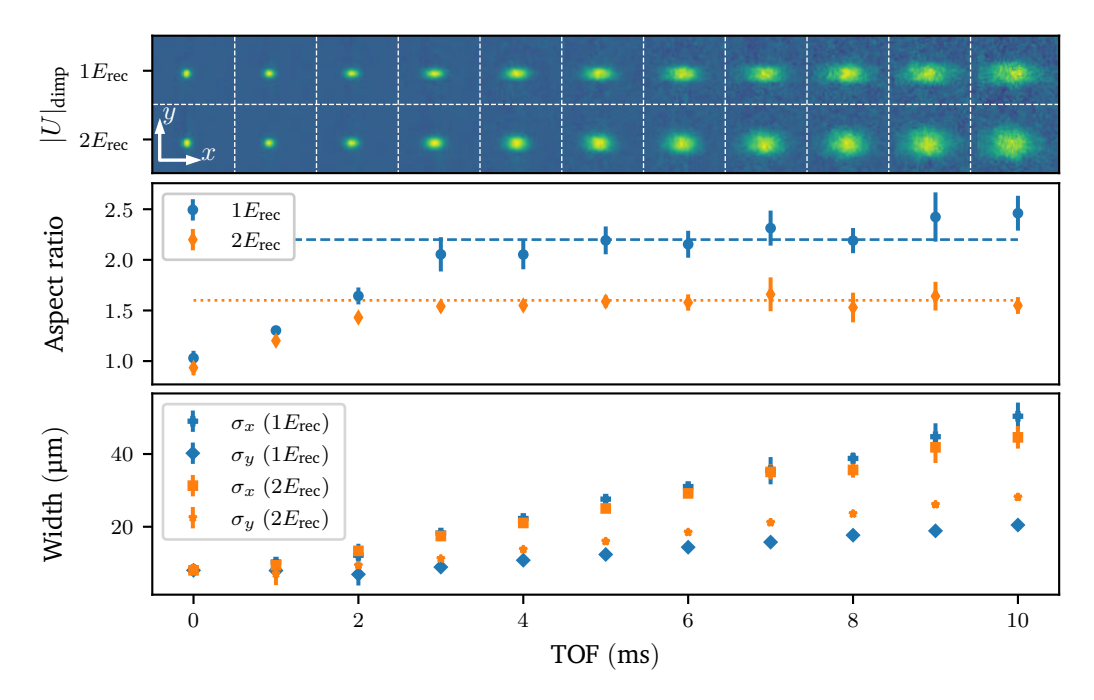


Fig. 5.5.: (top) Column density plots for $|U|_{\mathrm{dimp}}=1\,\mathrm{E}_{\mathrm{rec}}$ and $2\,\mathrm{E}_{\mathrm{rec}}$ dimple potentials and all TOF values from $0\,\mathrm{ms}$ to $10\,\mathrm{ms}$. (centre) Aspect ratio σ_x/σ_y for the time-dependent widths $\sigma_{x,y}$ extracted by two-dimensional Gaussian fits [see Eq. (2.26)]. For both dimple potential depths investigated, the final aspect ratio (dotted and dashed lines) differs significantly from 1 the value that would be expected for a purely thermal distribution. (bottom) Gaussian widths $\sigma_{x,y}$ used to determine the aspect ratio and estimate the temperatures of the ensembles.

with the expected trapping frequencies for the reservoir [see Section 5.2.1] and the dimple [see Section 5.2.1] the value $Na_{\rm sc}/a_{\rm ho}$ can be calculated. As discussed in Section 2.2, this value needs to be greater than 1 to justify the Thomas–Fermi approximation in the case that the ensemble would be on a BEC state. For this dimple depth, a value of $Na_{\rm sc}/a_{\rm ho}\approx 7$ is calculated, ensuring the validity of the Thomas–Fermi approximation in the case of a BEC. Similarly, for the dimple with $|U|_{\rm dimp}=2$ Erec the temperatures $T_y=70(5)$ nK and $T_x=270(40)$ nK are estimated with an initial aspect ratio of 0.94(7) asymptotically approaching 1.8(1) for longer TOFs. With an atom number of 1200(240), a value of $Na_{\rm sc}/a_{\rm ho}\approx 13$ again ensures the validity of the Thomas–Fermi approximation in the case of a BEC. In Tab. 5.5, these parameters are summarised for both dimple potential depths investigated.

The difference in the aspect ratio, with the larger value for the dimple with a higher trapping

Tab. 5.5.: Averaged properties extracted by fitting a two-dimensional Gaussian to the column density distributions. The asymptotic aspect ratio σ_x/σ_y is calculated by averaging over the aspect ratios for TOFs from $3~\mathrm{ms}$ to $10~\mathrm{ms}$.

$ U _{\text{dimp}}$	T_x	T_y	N	$Na_{\rm sc}/a_{ m ho}$	σ_x/σ_y
1 E _{rec}	$250(20)\mathrm{nK}$	$40(2)\mathrm{nK}$	1040(200)	$7.4_{-0.8}^{+0.1}$	2.2(2)
2 E _{rec}	$270(40)\mathrm{nK}$	$70(5)\mathrm{nK}$	1200(240)	$13.00^{+0.15}_{-1.40}$	1.8(1)

frequency ω_y confirms, that the shape of the density distributions is dominated by the radial trapping frequency of the reservoir i. e. the linear waveguide. Furthermore, the large asymptotic value for $|U|_{\rm dimp}=1\,\rm E_{rec}$ does not match the ratio of trapping frequencies expected by the

dimple parameters, pointing towards significantly smaller values of ω_y . Since the optical power carried by the dimple potential in the atom plane cannot be measured, the true value of ω_y and $|U|_{\text{dimp}}$ need to be determined using methods like, e. g. Bragg scattering to excite dipole oscillations in the future.

Double dimple

Since the results with a single dimple are promising, it is of interest to investigate whether two separate dimple potentials can produce identical ensembles with properties similar to those observed in the single dimple case. Again, the same routine as described above is used with the new dimple potential containing two identical dimples, offset to $y=\pm 50\,\mu m$ respectively along the y-axis of the reservoir [see Fig. 5.2], totalling in $100\,\mu m$ distance between the dimples to prevent crosstalk. The resulting densities for the same potential depths as in the single dimple case are visualised in Fig. 5.6 (top). Qualitatively, each dimple shows a similar expansion behaviour as the single dimple discussed in above.

Again, using two-dimensional Gaussian fits the time-dependent widths $\sigma_{x,y}$ are determined.

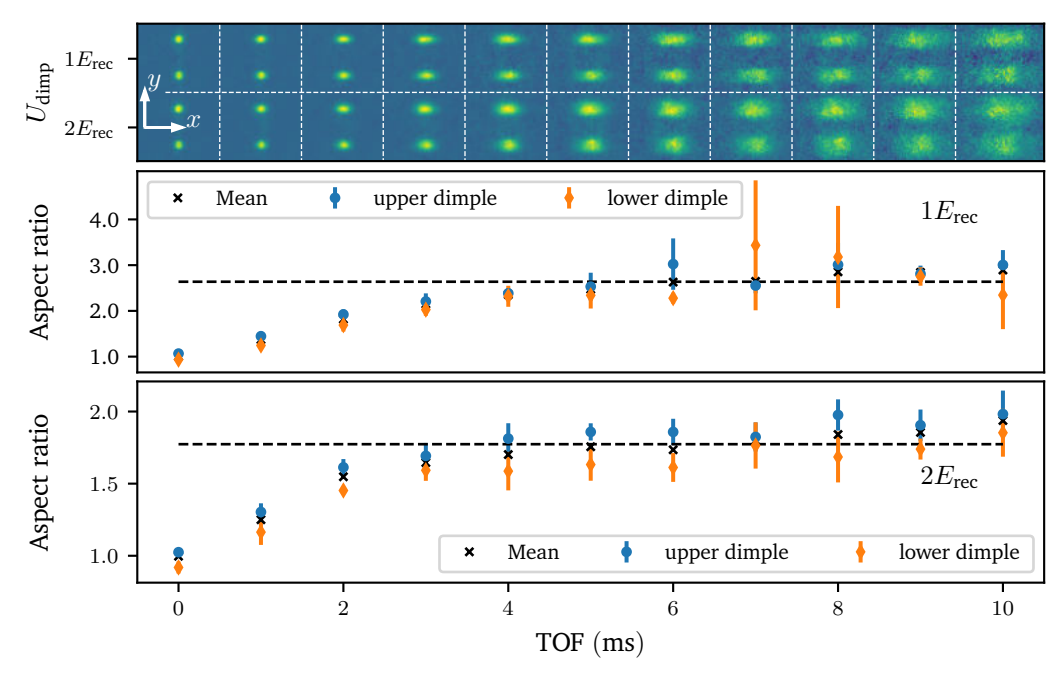


Fig. 5.6.: (top) Column density plots for the TOF expansion of a double-dimple setup for $|U|_{\rm dimp}=1\,\rm E_{rec}$ and $2\,\rm E_{rec}$. (centre) and (bottom) changes of the aspect ratio σ_x/σ_y during the TOF of $0\,\rm ms$ to $10\,\rm ms$ for the upper dimple a $+50\,\rm \mu m$ (blue) and lower dimple at $-50\,\rm \mu m$ (orange). Both dimples show a similar behaviour to the single dimple case with the asymptotic aspect ratio (dashed lines) agreeing well for both dimple potential depths.

The resulting aspect ratios, averaged over 5 experimental realisations, are depicted in Fig. 5.6 (centre and bottom) for both dimples and potential depths. A summary of the determined temperatures, atom numbers and aspect ratios, averaged over upper and lower dimple is given in Tab. 5.6. Comparing the parameters of the double-dimple system no significant difference to the single dimple can be found. Both dimples show the same expansion behaviour as the single dimple for both potential depths used with similar asymptotic aspect ratios. This opens the opportunity to create multiple ensembles from one thermal reservoir without any

Tab. 5.6.: Averaged properties for the double-dimple system. Compared to the single dimple, the expansion behaviour has not changed significantly.

$ U _{\mathrm{dimp}}$	T_x	T_y	N	$Na_{ m sc}/a_{ m ho}$	$\sigma_x/\sigma_y(10\mathrm{ms})$
1 E _{rec}	280(60) nK	$30(8)\mathrm{nK}$	780(230)	$5.6^{+0.1}_{-0.6}$	2.6(4)
2 E _{rec}	$270(40)\mathrm{nK}$	$70(5)\mathrm{nK}$	1200(240)	$9.2^{+0.1}_{-1.0}$	1.8(1)

drawback compared to the single dimple setup. Therefore, the next phase investigates the dynamic displacement of a dimple potential alongside the simultaneous implementation of a second dimple, advancing toward a setup capable of dynamically generating multiple ultracold ensembles with similar properties in pulsed operation.

Dynamic dimple systems

As discussed in the previous sections, a dimple potential can be used to produce an ultracold ensemble with properties indicating increased phase-space density. Furthermore, it has been shown that not only a single ensemble can be produced but multiple ensembles from the same thermal reservoir are possible. On the roadmap from a single BEC produced in the CDT to a setup that produces many consecutive BECs, the next logical step is to introduce dynamical dimple potentials, showcasing the possibility to move these ensembles without changing their properties. Ultimately, this will allow to remove the ensemble from the reservoir potential, allowing for the successive generation of a new ensemble.

To realise such an experiment, the dynamic properties of the DMDs, mainly the red-detuned DMD path, are used. Initially, the reservoir is loaded from the CDT and two dimple potentials symmetrically displaced by $|\Delta y|=20\,\mu\mathrm{m}$ from the centre are included, analogously to the experimental scheme discussed previously. After a holding time of $t_{\mathrm{hold}}=1000\,\mathrm{ms}$, the initial dimples are moved to $|\Delta y|=60\,\mu\mathrm{m}$ in $t_{\mathrm{move}}=100\,\mathrm{ms}$ using 48 of the available 96 individual potential masks stored on the DMD. This equates to steps of $0.83\,\mu\mathrm{m}$ per potential mask which is well below the optical resolution of the system. Again, using the dynamic feature of the DMD the remaining 48 potential masks are used to increase the potential depth of the two additional dimples, located at $y=\pm20\,\mu\mathrm{m}$ to $|U|_{\mathrm{dimp}}$ in $100\,\mathrm{ms}$. Finally, a holding time t_{hold} is added again to ensure the formation of an ensemble in the secondary dimple traps. Prior to any detection the purging method is deployed to reduce the density of thermal atoms in the reservoir. The complete experimental cycle is schematically visualised in Fig. 5.7.

To inspect the experimental cycle, the dynamic process is stopped after each individual step in the dynamic process, only cycling to the i-th potential mask with $i \in [1,96]$, and detection is performed in situ without TOF. This results in atomic density distributions representing each discrete potential step of the dynamic process. In Fig. 5.8 (top), the line densities, obtained by summing along the x-axis of the column density distributions, for each step are shown as a time series, visualising the displacement of the initial dimples and the growth of the atomic ensemble in the second dimples. The four bottom rows of Fig. 5.8 show the atom number, obtained by summing over the line density of each dimple¹. At the final potential configuration, each of the four dimples contains 900(150) atoms.

¹From the absorption images obtained at the experiment, the two-dimensional column density is calculated with unit atoms/m². Integrating i.e. summing these along one axis results in a line density with unit atoms/m. Summing over the second axis gives the total atom number detected in the initial column density.

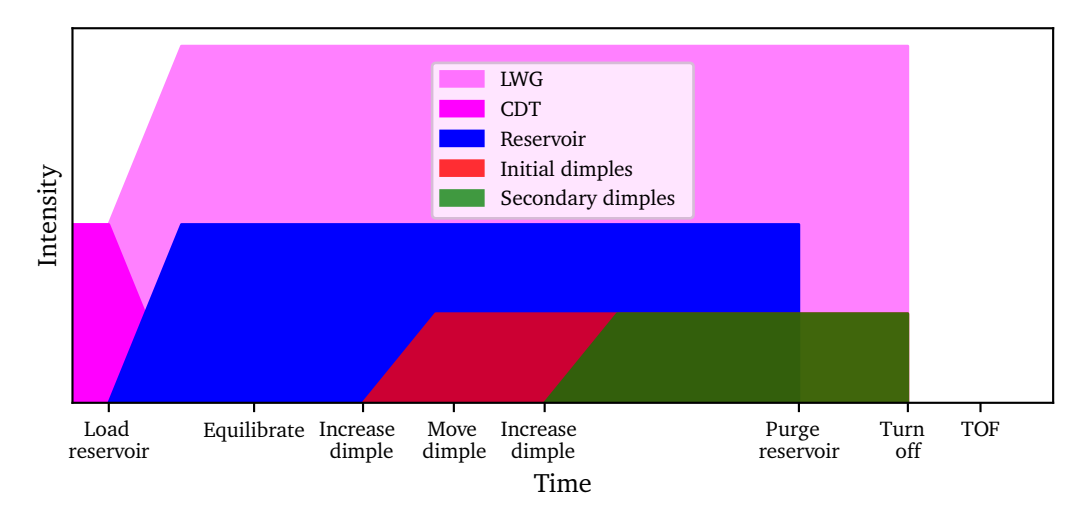


Fig. 5.7.: Schematic visualisation of the experimental cycle including the dynamic displacement of the initial two dimple traps and successive implementation of two secondary dimples. Prior to the displacement of the initial dimples and after the secondary dimple potentials have reached the final depth, a holding time is implemented to ensure the formation of an equilibrated ensemble in the dimple potentials. Again, the purging of the thermal reservoir prior to detection has to be implemented in order to evaluate the atomic ensembles formed in the dimple potentials.

Hence, this cycle can be used to produce a set of initial ensembles, dynamically move them within the thermal reservoir close to the boundary and introduce a second set of dimple potentials again producing an ensemble each. To investigate the expansion dynamics of this system of four ensembles, the complete dynamical cycle as described above is used with a holding time of $t_{\rm hold}=1000\,\rm ms$ prior to the dynamics as well as afterwards. The reservoir is purged with $t_{\rm purge}=150\,\rm ms$ in advance of the TOF. Similarly to the single- and double-dimple experiments described in the sections above, a TOF of 0 ms to 10 ms is used. In Fig. 5.9 (top) the normalised line density for each TOF is visualised for $|U|_{\rm dimp}=1\,\rm E_{rec}$ (left) and $|U|_{\rm dimp}=2\,\rm E_{rec}$ (right). Here, a remarkable effect can be observed as the ensembles released from the four dimple potentials and the density distributions start to expand and overlap. For $|U|_{\rm dimp}=1\,\rm E_{rec}$ and a TOF of 10 ms, three maxima become visible, located at the positions initially between the dimple potentials. In Fig. 5.9 (bottom left), the normalised line densities for 2 ms and 10 ms are depicted, clearly showing the three maxima at the location of initially minimal density at 10 ms.

As expected from the faster expansion along the y-axis for $|U|_{\rm dimp}=2\,\rm E_{rec}$ [see Section 5.2.1], this effect emerges for a shorter TOF of 7 ms as depicted in Fig. 5.9 (bottom right). Assuming the ensembles in the dimple potentials to be BECs and an interference effect as cause, the expected fringe spacing would be on the order of thermal de-Broglie wavelength associated with the relative velocity of the two clouds

$$\lambda_{\rm dB} = \frac{2\pi\hbar t}{md} \tag{5.1}$$

with the time t and initial distance d [71]. Evaluating this for a TOF of $10\,\mathrm{ms}$ and initial separation $d=40\,\mathrm{\mu m}$ gives a fringe period of $\lambda_\mathrm{dB}=1.15\,\mathrm{\mu m}$ which is well below the optical resolution of the experiment. Hence, this cannot be described as interference by of individual coherent wave packets but must be a density-density effect.

Taking Eq. (2.28) and integrating over one of the coordinates results in the line densities of

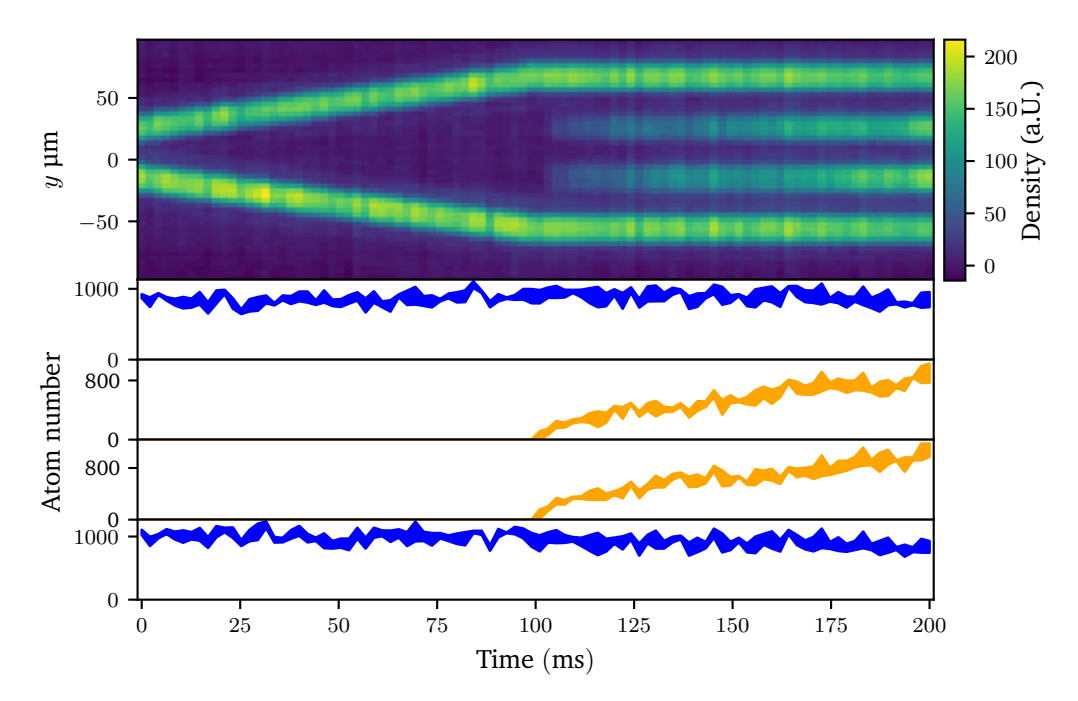


Fig. 5.8.: (top) Line densities for each potential as it changes with time via the dynamic capabilities of the DMD. The initial dimples are moved from $y=\pm 20\,\mu\mathrm{m}$ to $y=\pm 60\,\mu\mathrm{m}$ in the first $100\,\mathrm{ms}$ of the dynamical process and remain stationary afterwards. In the second $100\,\mathrm{ms}$, the potential depth of the secondary dimples ($y=\pm 20\,\mu\mathrm{m}$) is linearly increased to the same depths as the initial dimples. The formation of an localised atom ensemble can be observed with the atom number depending on the potential depth. In the bottom rows, the atom number in the dimples is shown with the rows corresponding to the vertical position of the dimple potentials.

the thermal and BEC fractions given by

$$\bar{n}_{\text{BEC}}(y) \simeq \bar{n}_{\text{BEC}}(0) \max \left[1 - \left(\frac{y}{R_y} \right)^2, 0 \right]^2$$
 (5.2a)

$$\bar{n}_{\text{therm}}(y) \simeq \bar{n}_{\text{therm}}(0)g_{5/2} \left[z \exp\left(-\frac{y^2}{2\sigma_y^2}\right) \right].$$
 (5.2b)

Given the properties of the dimple potential and of the ensemble discussed above for the single dimple case, the expansion of a purely thermal ensemble and a pure BEC can be computed. For the thermal expansion, $\sigma_y(0)$ for a TOF of 0 ms and T_y are used to compute $\sigma_y(t)$ based on Eq. (2.27) and the chemical potential μ_{therm} is set to the potential depth of the dimple to evaluate the fugacity $z = \exp(-|U_{\text{dimp}}|/k_{\text{B}}T)$ [68, Sec. 10.7]. Similarly, for the pure BEC, $R_y = \sigma_y(0)$ and Eq. (2.22) are used to model the expansion.

In Fig. 5.10 a comparison of a pure BEC expansion (left) and a fully thermal ensemble (right) is shown. Analogously to Fig. 5.9, the top panels show the expansion based on the line density as a false-colour plot. Here the different expansion behaviours become obvious with the pure BEC showing a similar effect as the ensembles measured [see Fig. 5.9 (top)]. In contrast, the thermal ensemble shows no signs of an appearing local minimum at the initial dimple locations. Hence, the observations made in the expansion of the experimental ensembles can not be explained by a non-interacting thermal ensemble described by a line density similar to Eq. (5.2b). Moreover, even when employing a line Gaussian density distribution, derived by integrating Eq. (2.26) along one axis, the results cannot be replicated.

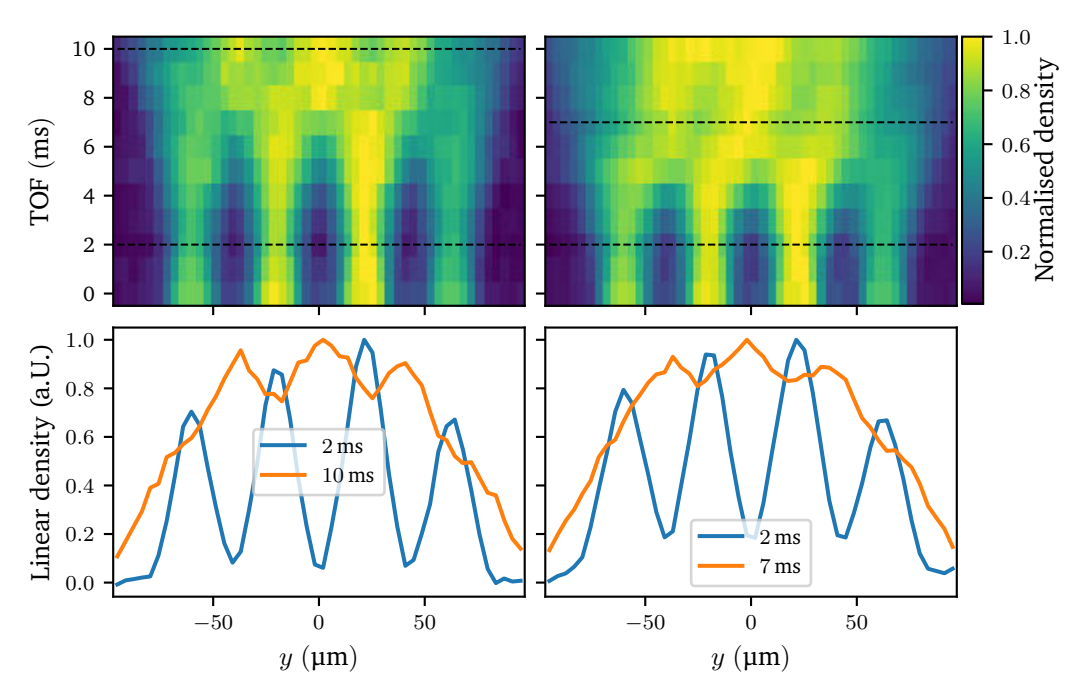


Fig. 5.9.: (top) False colour representation of the normalised line density during the TOF for $|U|_{\text{dimp}}=1\,\mathrm{E}_{\mathrm{rec}}$ (left) and $|U|_{\mathrm{dimp}}=2\,\mathrm{E}_{\mathrm{rec}}$ (right). An unexpected behaviour emerges when the density of the individual dimples start to overlap, leading to local maxima located at positions of initially low density. This effect depends on the dimple depth since the expansion rate for the tighter confinement in the deeper dimple is faster. (bottom) Corresponding line density for $2\,\mathrm{ms}$ (blue) and $10\,\mathrm{ms}$ for $|U|_{\mathrm{dimp}}=1\,\mathrm{E}_{\mathrm{rec}}$, as well as $2\,\mathrm{ms}$ (blue) and $7\,\mathrm{ms}$ for $|U|_{\mathrm{dimp}}=2\,\mathrm{E}_{\mathrm{rec}}$ (orange), visualising the initial location of the dimple potentials. At $10\,\mathrm{ms}$ for $|U|_{\mathrm{dimp}}=1\,\mathrm{E}_{\mathrm{rec}}$ and $7\,\mathrm{ms}$ for $|U|_{\mathrm{dimp}}=2\,\mathrm{E}_{\mathrm{rec}}$ local maxima emerge located between the dimple positions. Dashed lines in the top row images show the selected line densities.

The variation in emergence times of this effect arises from differences in the Thomas–Fermi radius expansion rate, which is directly linked to the trapping frequency [see Eq. (2.22)]. Since the exact optical power and optical resolution i. e. the exact potential in the atom plane is unknown, a difference in the calculated and real trapping frequency has to be expected, leading to a quantitatively varying results. Nevertheless, qualitatively a similar expansion behaviour is expected.

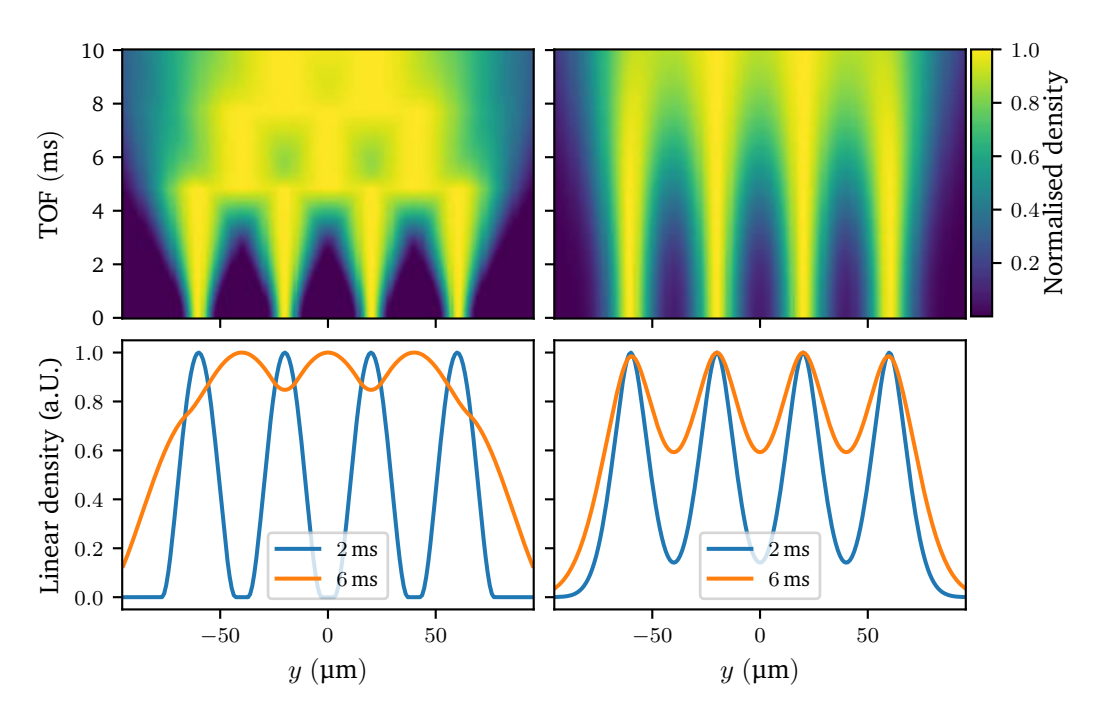


Fig. 5.10.: (top) Corresponding line density calculated for the experimental parameters determined for the single dimple ($|U|_{\rm dimp}=1\,\rm E_{rec}$) [see Section 5.2.1]. Expansion for a pure BEC (left) and thermal ensemble (right) calculated using Eq. (5.2). The pure BEC shows a similar effect as observed in the experimental data [see Fig. 5.9]. (bottom) Corresponding line density shown for $2\,\rm ms$ (blue) and $6\,\rm ms$ (orange). The selection of different times for the presentation can be justified by the uncertainties of the assumed potentials. A thermal ensemble, as described by Eq. (5.2b), will not reproduce the observed effect.

5.3. Summary

In this chapter, a new optical setup based on two DMDs was introduced. This system can be used to generate arbitrary two-dimensional potentials by directly reimaging the surface of the DMDs. Using two Ti:Sa lasers further expands the flexibility of this system by providing sufficient optical power over a wide range of wavelengths from 750 nm to 850 nm, hence any combination of red- and blue-detuned potentials can be realised. In the future, this optical setup can be used to extent the atom-interferometric measurements to versatile guiding potentials e. g. ring-shaped potentials or atomtronic circuits. Currently, corrugations on the necessary light sheet potential make experiments in combined potential of light sheet and DMD potential infeasible. These corrugations have been detected for multiple iterations of the light sheet laser and optical system and are very likely produced by interference effects of reflections of the laser beam on the window of the vacuum chamber. Several techniques to mitigate or compensate the corrugations have been investigated with limited success, including using the DMD to introduce additional correction potentials. Additional steps to improve the situation are changing the vacuum chamber window for one with an improved anti-reflective coating and building a light sheet at 1070 nm.

Combining a LWG generated by one of the CDT beams with the potentials generated by the DMD setup has been used to implement an adiabatic generation of ultracold ensembles in dynamic dimple potentials. Atom ensembles with properties diverging from a non-interacting thermal cloud were generated in single-, double- and dynamic quadruple-dimple potentials. The expansion behaviour of these ensembles was investigated leading to temperatures well below the critical temperature for various depths of the dimple. Furthermore, the aspect ratio of these ensembles defined by the ratio of their Gaussian widths σ_x/σ_y has been investigated with the ensembles expanding asymmetrically to an asymptotic aspect ratio greater then one. Using different dimple depths, the dependency of the asymptotic aspect ratio was investigated, showing the expected behaviour. Releasing four ensembles, generated by a dynamic process involving the displacement of the two initial dimples and the successive implementation of two secondary dimple potentials resulted in a density-density effect that cannot be interpreted by the incoherent sum of non-interacting thermal ensembles.

To conclude, the extension of the ATOMICS experiment by an optical setup based around two individual DMDs and realisation of the adiabatic generation of ultracold ensembles paves the way for future experiments involving multiple BECs in external guiding potentials. Possible applications are the stochastic generation of vortex states as well as guided atom interferometer.

6. Discussion and future perspectives

This thesis has significantly advanced the experimental capabilities of the ATOMICS platform, enabling large-momentum-transfer atom interferometry in external guiding potentials. Through the integration of advanced experimental control software, the development of new laser systems, and the design of optical setups for higher-order Bragg diffraction and arbitrary external potentials using digital micromirror devices, the groundwork for next-generation quantum sensing and manipulation has been established. A suite of evaluation methods for Mach–Zehnder interferometer signals was discussed, including techniques that extract differential phases from correlated interferometers without relying on state-selective measurements. These methods broaden the scope of data analysis extending the capabilities of experiments.

Implementing the *labscript suite* experimental control environment has fundamentally changed the capabilities of the ATOMICS experiment. In combination with drastic improvements in general laboratory environmental stability, this has enabled automated measurement campaigns running for more than 12 hours, allowing for large parameter scans, increased statistics or a combination of both. Many of the results presented here would have been impossible to the extent discussed in this work without this improvements. Including additional devices such as cameras and other data acquisition devices into the existing implementation will further expand the experiments capabilities by allowing automated data evaluation using the *lyse* environment. This may also be used to add auto-calibration schemes, reducing the maintenance required at the experiment.

The thesis also presents the first three-dimensional trapping of ultracold atoms using a blue-detuned bottle beam generated via conical refraction. By focusing a circularly polarised laser beam through a biaxial crystal, ring-shaped light fields with variable intensity distributions can be realised. For the optimal ring regime, a central dark focus surrounded by steep intensity gradients was achieved, providing a robust trapping potential. Numerical simulations of these light fields were validated by experimental measurements, demonstrating excellent agreement in spatial extent, trapping frequencies, and potential depths.

The experimental realisation of the dark focus using a $KGd(WO_4)_2$ crystal in combination with a Ti:Sa laser system, followed by reimaging into the vacuum chamber with achromatic lenses, enabled the implementation of a blue-detuned optical dipole trap for ^{87}Rb ensembles. The successful transfer of BECs from a crossed dipole trap into the bottle-beam potential confirms the feasibility of three-dimensional trapping in a single blue-detuned potential generated by conical refraction without additional potentials. Measurements of trapping frequencies and the spatial extent further substantiate the effectiveness of this approach, marking the first such realisation for ultracold atomic ensembles [120].

The combination of microlens arrays with conical refraction was explored numerically, revealing the Talbot effect in combination with conical refraction and enabling the theoretical design of bottle-beam arrays. These arrays hold promise for neutral atom quantum computing and quantum sensing, as they can facilitate the storage and manipulation of multiple BECs or single atoms, including highly excited Rydberg states.

Utilising a purpose-built laser system, higher-order Bragg diffraction has been experimentally demonstrated up to the fifth-order, transferring $5\hbar k_{\rm eff}$ to an atomic ensemble. Combining a series of pulses, atomic MZIs have been investigated in first- and third-order Bragg diffraction, revealing an apparent loss and revival of visibility at longer interferometer times, linked to the mixture of $m_{\rm F}$ sub-states. To evaluate the signals for longer interferometer times, a statistical approach was chosen, reasoned in the phase-unstable operation mode of the experiment, making a direct fit to the interference fringe impossible. A statistical model was introduced to describe this effect with the assumption that a state-dependent external phase is imprinted onto the individual $m_{\rm F}$ sub-states. Further experimental investigations lead to the discovery of a magnetic field gradient of 1.0(1) mT/m present in the vacuum chamber of the ATOMICS experiment. Introducing a state-selective measurement scheme based on the Stern-Gerlach method and additional evaluation techniques such as ellipse fitting for correlated interferometers allowed for an in-depth discussion of the observed effect. Moreover, an evaluation technique for cases where no state-selective measurement can be performed was introduced, making use of the phase-stable summation of the individual interferometer signals leading to the loss of visibility. Interferometer measurements using third-order Bragg diffraction were conducted, confirming the linear scaling of this effect with the Bragg order and in excellent agreement with the simple model introduced to describe the effect. Notably, the coherence time for interferometers up to third-order in free space was found to be at least 6 ms, with no loss of visibility for individual interferometers within this window.

To further increase the performance and sensitivity of large-momentum-transfer atom interferometers, a new technique for the generation of mirror pulses was experimentally implemented. Following a theoretical proposal, the length and amplitude of the mirror pulses were adjusted to generate pulses that selectively reflect only the desired diffraction order. This approach ensures transparency for parasitic paths, which are inherent to higher-order Bragg diffraction [169, 170]. Hence, mirror pulses showing a dichroic behaviour have been successfully implemented for the first time. Extensive experimental investigations in third order, accompanied by numerical studies in collaboration with the research group of Prof. E. Giese were conducted to showcase the capabilities of this new technique. Additional measurements in fifth order were used to confirm the scalability of the technique [171].

The techniques presented pave the way for the experimental implementation of higher-order MZIs at the ATOMICS experiment. To further investigate the experimental capabilities, the step towards guided interferometers is unavoidable either in a linear waveguide (LWG) or arbitrary guiding structures provided by additional optical setups. Changing the layout of the Bragg system from counter-propagating to a retro-reflective or hybrid setup will likely reduce phase noise, enabling phase-stable operation over longer interferometer times and improving signal evaluation.

Furthermore, the simplicity of the selected methods ensures they can be easily integrated into existing experimental setups that utilise Bragg diffraction for atomic interferometry. Expanding the technique to double-Bragg diffraction will further improve the robustness of quantum sensors built around atomic interferometers.

Finally, a new optical setup based on two digital micromirror devices (DMDs) has been introduced, capable of producing arbitrary two-dimensional optical dipole potentials by direct reimaging of the DMDs surfaces. Using two Ti:Sa laser systems allows both identical optical setups to be utilised in red- or blue-detuned configurations, offering a high degree of flexibility for external guiding and manipulation of ultracold ensembles such as BECs. The dynamic capabilities of the DMD modules allow for time-dependent potentials to be used, implement-

ing control over spatial and potential depth properties. Combining these external potentials with a light sheet system can be used to manipulate atomic ensembles in fully customisable two-dimensional potential landscapes. However, the appearance of corrugations in the light sheet system presents a challenge for fully implementing these potentials, and ongoing work is focused on mitigation strategies and improved optical setups.

The combination of DMD systems with a linear waveguide (LWG) generated by one of the crossed dipole trap (CDT) beams enabled the adiabatic formation of ultracold ensembles in dipole potentials. Starting with a purely thermal ensemble above the critical temperature for condensation in a reservoir potential of the attractive LWG in combination with a blue-detuned barrier generated by a DMD, narrow red-detuned dimples were introduced generated by the a DMD. Implementing purging techniques to lower the atomic density of the thermal reservoir upon detection and using time of flight methods, the expansion behaviour of single, double and quadruple dimple setups were investigated. The ensembles generated show temperatures well below the critical temperature and asymptomatically expand to aspect ratios differencing from unity, showcasing clear signs of ensembles with increased phase-space density. Implementing time-dependent dimple potentials was used to generate two initial dimple ensembles and move them from the centre of the reservoir close to the edge. This allowed for the generation of a secondary pair of ensembles, totalling to four ensembles generated from the same thermal reservoir in a dynamic process. The incoherent sum of the expanding ensembles lead to the discovery of an intriguing pattern, showing an inversion of the location of maximum and minimum intensity depending on the expansion time. Comparing the observed expansion behaviour to numerical results for purely thermal atoms and BECs in the Thomas-Fermi regime was conducted. This led to the conclusion, that the observed effect cannot be explained by thermal expansion of a non-interacting ensemble. The experimental results obtained in this project are in good agreement with similar experiments conducted in other groups at earlier times [232].

In summary, the techniques and results presented in this thesis establish a versatile platform for advanced quantum control and precision measurement with ultracold atoms. The innovations in trapping, interferometry, and potential engineering not only address key challenges in the field, but also open new avenues for scalable quantum technologies.

Future work will focus on three main directions. First, integrating automated data analysis and refining optical potentials will further optimise experimental performance. Second, the realisation of guided interferometry and multi-site quantum devices will expand the capabilities of the platform, with particular emphasis on interferometric measurements in linear waveguides using higher-order Bragg diffraction and the estimation of BEC coherence times. Third, combining compensation techniques with a new optical setup to overcome corrugations in the light sheet system will enable the use of a wider variety of external guiding potentials. Additionally, extending the promising results of adiabatic generation of ultracold ensembles and increasing the number of atoms will allow for interferometric measurements analogous to those performed with a BEC from the CDT, providing a direct means to verify the coherence properties of these ensembles.

Overall, the methods developed in this work are broadly applicable and have the potential to accelerate progress in quantum sensing, computation, and fundamental research.

119

A. ATOMICS setup supplementary material

In addition to the brief description of the ATOMICS laser systems given in Section 2.4, here some additional information is presented for documentation purposes. In Fig. A1, the hyperfine structure is schematically visualised as taken from [67]. Coloured solid arrows depict the optical transitions used for cooling ($|5^2S_{1/2},F=2\rangle \rightarrow |5^2P_{3/2},F'=3\rangle$) and repumping ($|5^2S_{1/2},F=1\rangle \rightarrow |5^2P_{3/2},F'=2\rangle$) in the MOT stage of the experiment. Additionally, the transition used for the optical pumping is shown ($|5^2S_{1/2},F=1\rangle \rightarrow |5^2P_{3/2},F'=1\rangle$).

A second set of coloured arrows shows the actual stabilised laser frequencies including their respective offset relative to the transition on 87 Rb. The spectroscopy master and repumping laser are stabilised to a fixed offset of $\Delta = +2\pi \times 200\,\mathrm{MHz}$ relative to the respective transition, while the offset of the cooling laser is shifted for the optical molasses shown by a dashed red line, visualising the maximum frequency shift. AOMs with fixed frequencies, visualised by blue downwards pointing arrows, are utilised to shift the light back into resonance. The light necessary for the optical pumping is generated by compensating the offset via an AOM in double-pass configuration (doubled blue arrows) such that the light is shifted by twice the AOM frequency.

Shaded areas depict the frequency range over which the chirp-cooling and chirp-repumping laser are continuously chirped to compensate for the changing Doppler detuning.

121

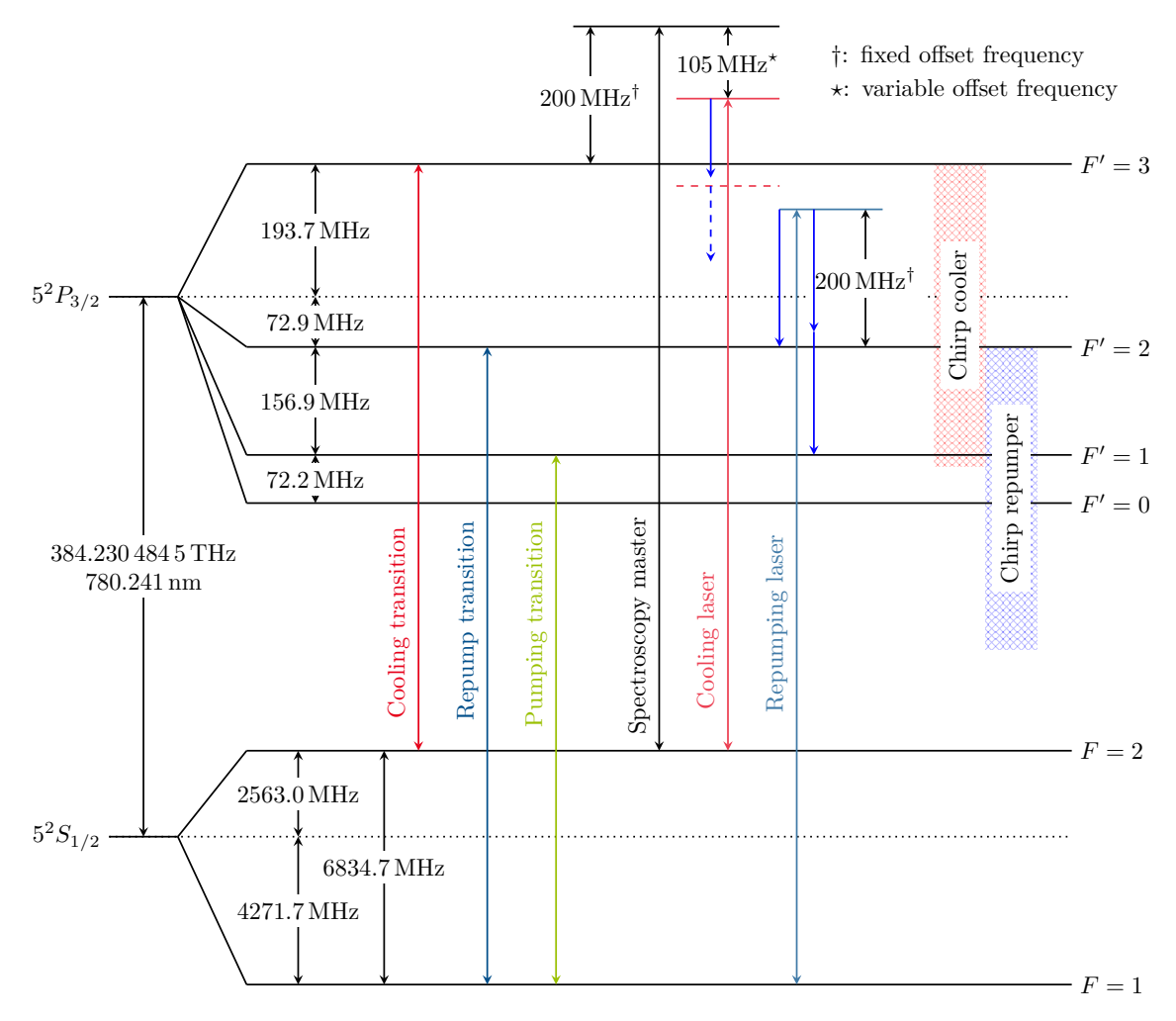


Fig. A1.: Hyperfine structure of the D2-line of 87 Rb [67]. Solid red, blue, and green arrows depict the import optical transitions for the MOT i.e. the cooling and repump transition. Furthermore the transition used for optically pumping atoms in a dedicated $m_{\rm F}$ sub-state is shown. Additional arrows depict the stabilised operating frequency for the spectroscopy master, cooling and repumping laser. The offset frequency of the cooling laser is variable and can be changed to realise the optical molasses (red dashed line below F'=3). Shaded areas show the frequency chirping range for the chirp-cooler and chirp-repump laser. Solid downwards pointing arrows depict the frequency shifts applied by AOMs. This schematic was initially made by P. Mittenbühler for his bachelor thesis and adapted for this work [101].

B. Conical refraction supplementary material

Similar to the derivation of the trapping frequencies in radial and axial direction discussed in [44, 105, 120], here the normalised coordinates are used to derive the prefactors for a harmonic approximation of the light field. The derivation presented here is a reproduction of the references mentioned, using the normalised coordinate system.

Assuming a radially symmetric Gaussian input beam, the Belskii–Khapalyuk–Berry (BKB) integrals are given by Eqs. (3.7a) and (3.7b). Using the identity of the i-th order Bessel function of the first kind J_i given by

$$J_{\alpha}(x) = \sum_{m=0}^{\infty} \frac{(-1)^m}{m!\Gamma(m+\alpha+1)} \left(\frac{x}{2}\right)^{2m+\alpha}$$
(B.1)

the BKB integrals can be solved analytically [193, Sec. 3.3.1.3.4]. This results in

$$B_0(\rho, Z) = E_0(Z) \sum_{m=0}^{\infty} \frac{(-1)^m \rho^{2m}}{m! (1 + iZ)^{m+1}} \times_1 F_1\left(m + 1, \frac{1}{2}, \frac{-\rho_0^2}{1 + iZ}\right)$$
(B.2a)

$$B_1(\rho, Z) = 2\rho_0 E_0(Z) \sum_{m=0}^{\infty} \frac{(-1)^m \rho^{2m+1}}{m! (1+\mathrm{i} Z)^{m+2}} \times_1 F_1\left(m+2, \frac{3}{2}, \frac{-\rho_0^2}{(1+\mathrm{i} Z)^2}\right) \tag{B.2b}$$

with the E_0 the initial amplitude of the Gaussian input field and ${}_1F_1$ the Kummer confluent hyper-geometric function [129, 193, Sec. 3.3.1.3.4]. Keeping only the m=0 terms, which is sufficient to describe the intensity distribution for $\rho \lesssim 1$ [44] results in

$$B_0(\rho, Z) = E_0(Z) \frac{1}{1 + iZ} \times_1 F_1\left(1, \frac{1}{2}, \frac{-\rho_0^2}{1 + iZ}\right)$$
(B.3)

$$B_1(\rho, Z) = 2\rho_0 E_0(Z) \frac{1}{(1+iZ)^2} \times_1 F_1\left(2, \frac{3}{2}, \frac{-\rho_0^2}{(1+iZ)^2}\right).$$
 (B.4)

Therefore, the intensity distribution for circularly polarised light given by

$$I(\rho \lesssim 1, Z) = |B_0(\rho, Z)|^2 + |B_1(\rho, Z)|^2$$
 (B.5)

$$= E_0(Z)^2 \times \left(\left| \frac{{}_{1}F_1\left(1, \frac{1}{2}, \frac{-\rho_0^2}{1+iZ}\right)}{1+iZ} \right|^2 + 4\rho_0^2 \rho^2 \left| \frac{{}_{1}F_1\left(2, \frac{3}{2}, \frac{-\rho_0^2}{1+iZ}\right)}{(1+iZ)^2} \right|^2 \right).$$
 (B.6)

The first term represents an offset that is equal to 0 for the dark-focus regime and Z=0 which increases for $Z \neq 0$. Dividing by the maximal intensity $I_0(Z) = |E_0(Z)|^2$ removes the dependency on specific properties of the input Gaussian beam resulting in

$$\frac{I(\rho \approx 0, Z = 0)}{I(0, 0)} \approx 4\rho_0^2 \left| {}_{1}F_{1}\left(2, \frac{3}{2}, -\rho_0^2\right) \right|^2 \rho^2 = \chi_\rho \rho^2$$
(B.7)

for the focal plane at Z=0. For planes outside of the focal plane, the parameter χ_{ρ} becomes Z-dependent

$$\chi_{\rho}(Z) = 4\rho_0^2 \left| \frac{{}_{1}F_{1}\left(2, \frac{3}{2}, \frac{-\rho_0^2}{1+\mathrm{i}Z}\right)}{(1+\mathrm{i}Z)^2} \right|^2$$
(B.8)

For the harmonic approximation along the Z-axis only $B_0(0,Z)$ has to be considered, since $B_1(0,Z) = 0$. In this case, the integral in $B_0(0,Z)$ can be solved analytically, resulting in

$$I(0,Z) = |B_0(0,Z)|^2 = \frac{E_0^2}{4} \frac{1}{|1 + iZ|} \left| 1 + \frac{2\rho_0 D\left(\frac{\rho_0}{\sqrt{1 + iZ}}\right)}{\sqrt{1 + iZ}} \right|^2$$
(B.9)

with the Dawson function D(x) [44, 105, 120, 234]. Again, dividing by $I(0,0) = E_0^2$ to remove experimental dependencies and taking the Taylor series, leads to

$$\frac{I(0,Z)}{I(0,0)} \approx \frac{1}{4}Z^2 = \chi_Z Z^2.$$
 (B.10)

Conical refraction with microlens arrays

Fig. B1 shows the minimum intensity reached in the central bottle-beam trap as a function of the ratio of pitch $a_{\rm MLA}$ of an microlens array (MLA) to the waist w0. The intensity value is shown for the optimal ring regime ρ_0 [see Fig. 3.22] for each ratio $\rho_a = a_{\rm MLA}/w_0$, normalised to the respective I_0 on a linear (blue) and logarithmic (red) scale.

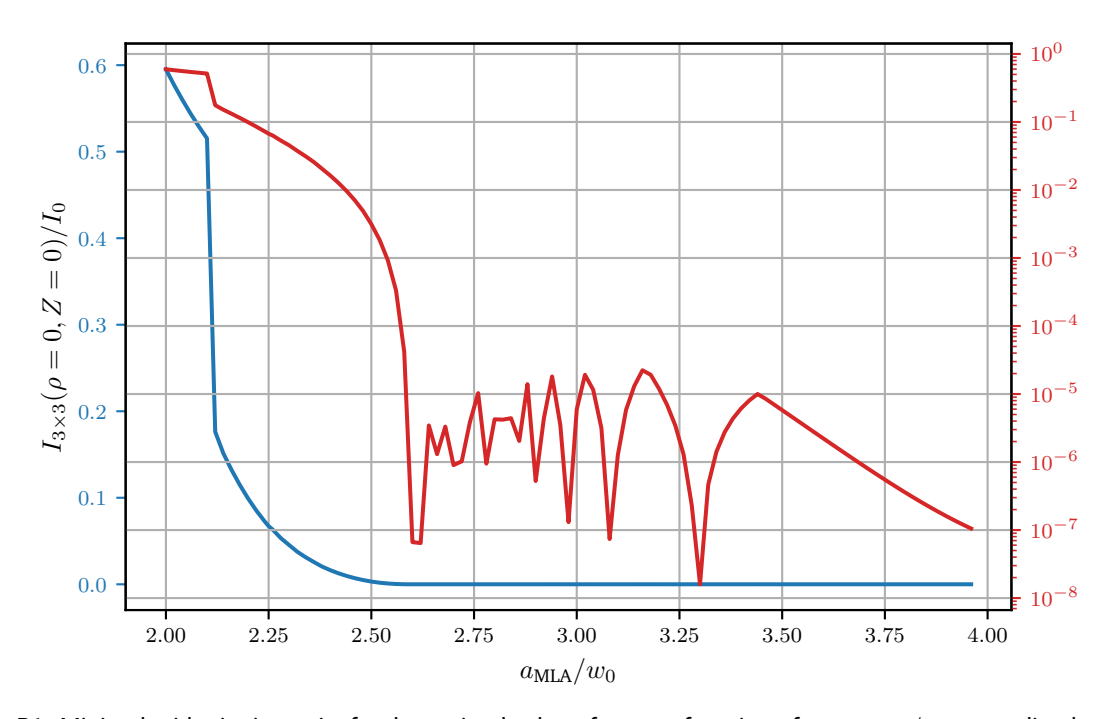


Fig. B1.: Minimal midpoint intensity for the optimal value of ρ_0 as a function of $\rho_a=a_{\rm MLA}/w_0$ normalised to the respective I_0 on a linear (blue) and logarithmic (red) scale. For $\rho_a\geq 2.54(2)$ the midpoint intensity is less then $1\times 10^{-3}\times I_0$. For values $\rho_a\geq 3.46(2)$, the optimal ring regime is $\rho_0^{\rm DF}=0.924$ and the midpoint intensity decreases as expected. The discontinuous behaviour in the centre if the logarithmic plot is likely reasoned in numerical precision of the grid chosen.

C. Bragg diffraction supplementary material

To estimate the width of a pulse width 100 μs length, the time-bandwidth product (TBP) of a Gaussian pulse is used, given by the product of the FWHM in time and frequency domain [235]:

$$TBP_{\text{Gauss}} = \text{FWHM}_t \times \text{FWHM}_{\nu} \approx 0.44$$
 (B.1)

Using the Doppler shift term of Eq. (4.2) and the FWHM of the Gaussian pulse in time domain ${\rm FWHM}_t=40.5\,\mu{\rm s}$, the resulting FWHM in momentum space is given by

$$FWHM_p = \frac{TBP_{Gauss}}{FWHM_t} \frac{m}{k_{eff}} = 0.06\hbar k_{eff}$$
 (B.2)

for 87Rb.

Statistic analysis

In Fig. C1, two histograms of the total interferometer signal $S_{\rm tot}=S_++S_-$ of a first order MZI for $T=1.6\,{\rm ms}$ (blue) and $T=2.5\,{\rm ms}$ (orange) are shown. Additionally, the PDF is plotted for the average fit parameters obtained by the bootstrapping method. For $T=1.6\,{\rm ms}$, the average visibility $\mathcal{V}(1.6\,{\rm ms})=0.18(1)$ is close to the minimum, reached for $T\approx1.75\,{\rm ms}$. At $T=2.5\,{\rm ms}$, the revival of the visibility can be observed, reaching $\mathcal{V}(2.5\,{\rm ms})=0.75(2)$ close to the initial maximum visibility $\mathcal{V}_0=0.77(1)$ [see Section 4.3].

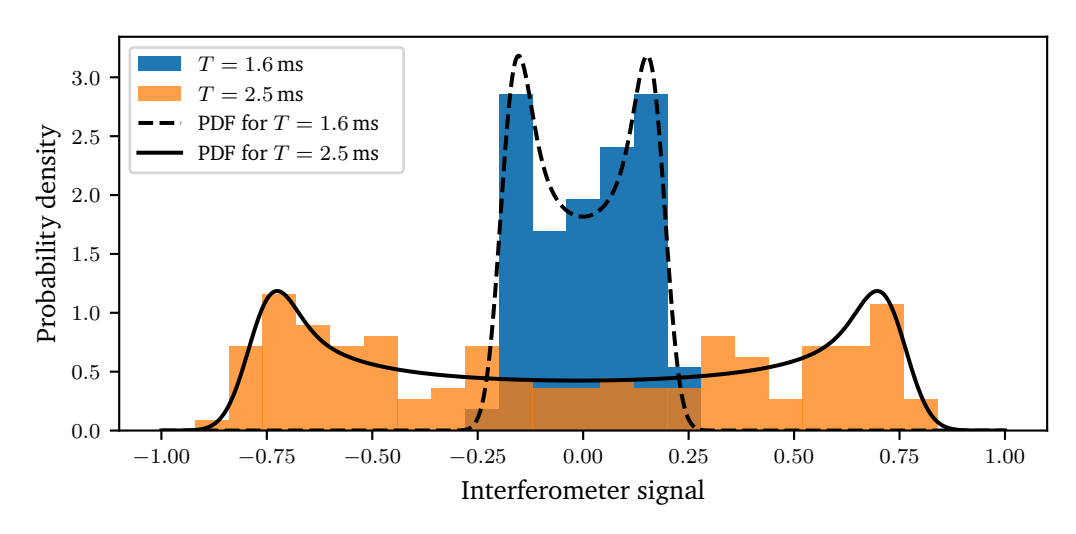


Fig. C1.: Histograms of the total interferometer signal $S_{\rm tot}=S_++S_-$ of a first order MZI for $T=1.6\,{\rm ms}$ (blue) and $T=2.5\,{\rm ms}$ (orange). A dashed line shows the PDF given by Eq. (4.18) plotted for the averaged fit parameters for $T=1.5\,{\rm ms}$ obtained by the bootstrapping method [see Section 4.3]. The solid line shows the respective PDF for $T=2.5\,{\rm ms}$ with the average visibilities given by $\mathcal{V}(1.6\,{\rm ms})=0.18(1)$ and $\mathcal{V}(2.5\,{\rm ms})=0.75(2)$.

Phase-stable summation of interferometers

Fig. C2 shows the same signals as Fig. 4.8 with reduced phase noise, revealing the interference fringes of the individual interferometers. This serves to highlight the effect of how the phase-shifted summation of two signals can lead to the total loss of visibility for $\theta_{\rm B}=\pi/2$. The visibility is set to $\mathcal{V}=0.75$ with the phase-noise generated from an uniformly distribution $[-\pi/50,\pi/50]$. The baseline noise is given by a normal distribution Eq. (4.17b) with $\sigma_b=0.025$ and $\bar{b}=0$.

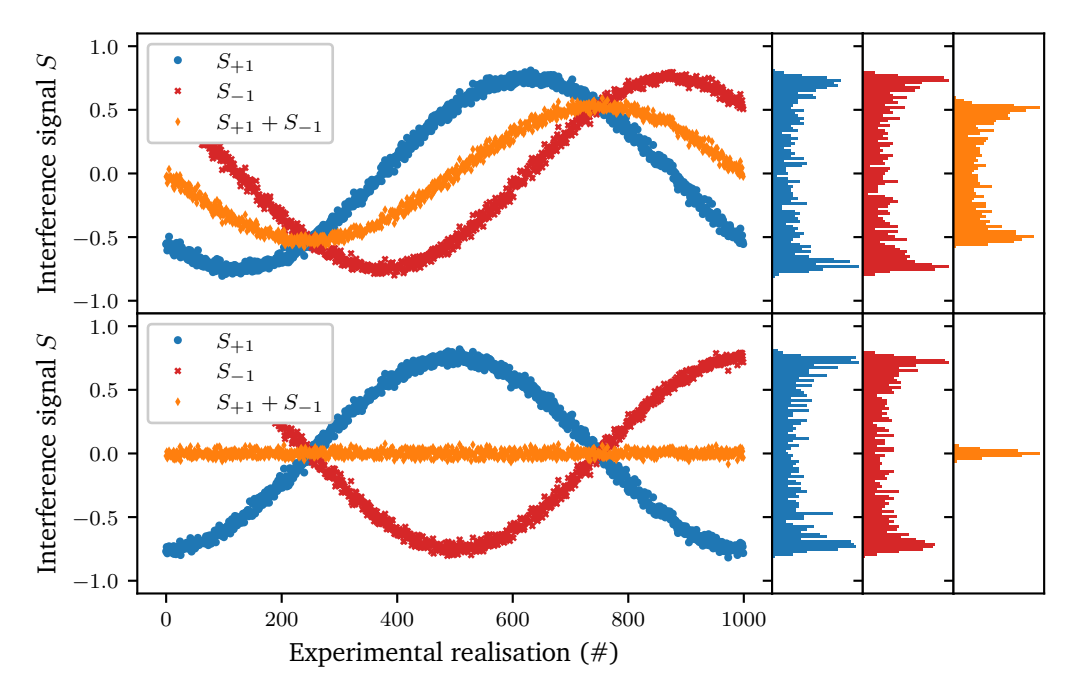
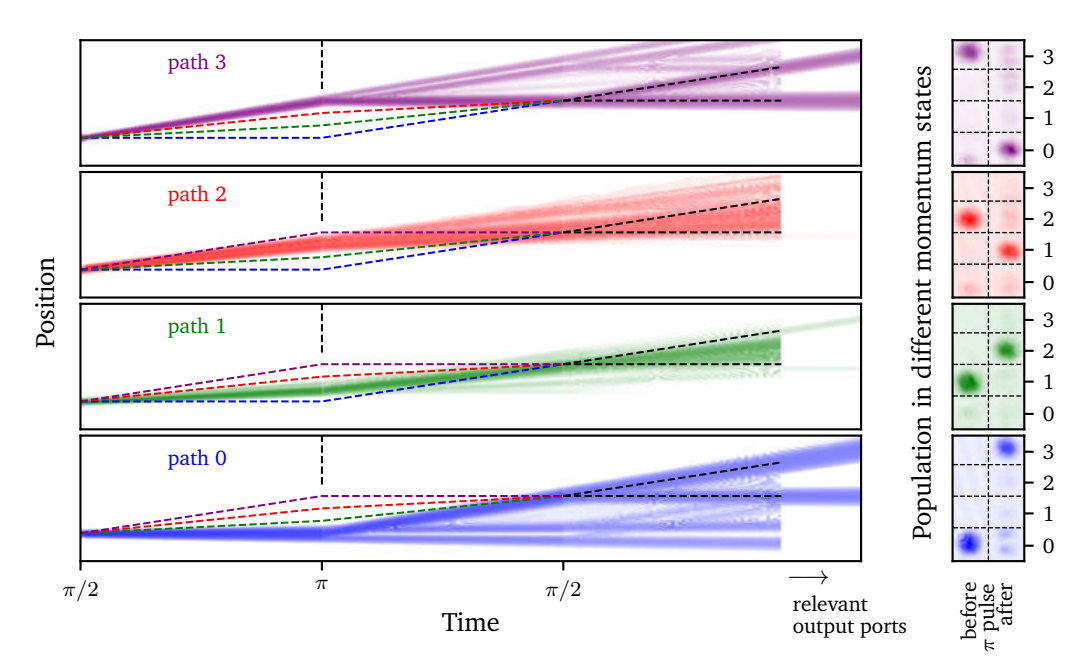


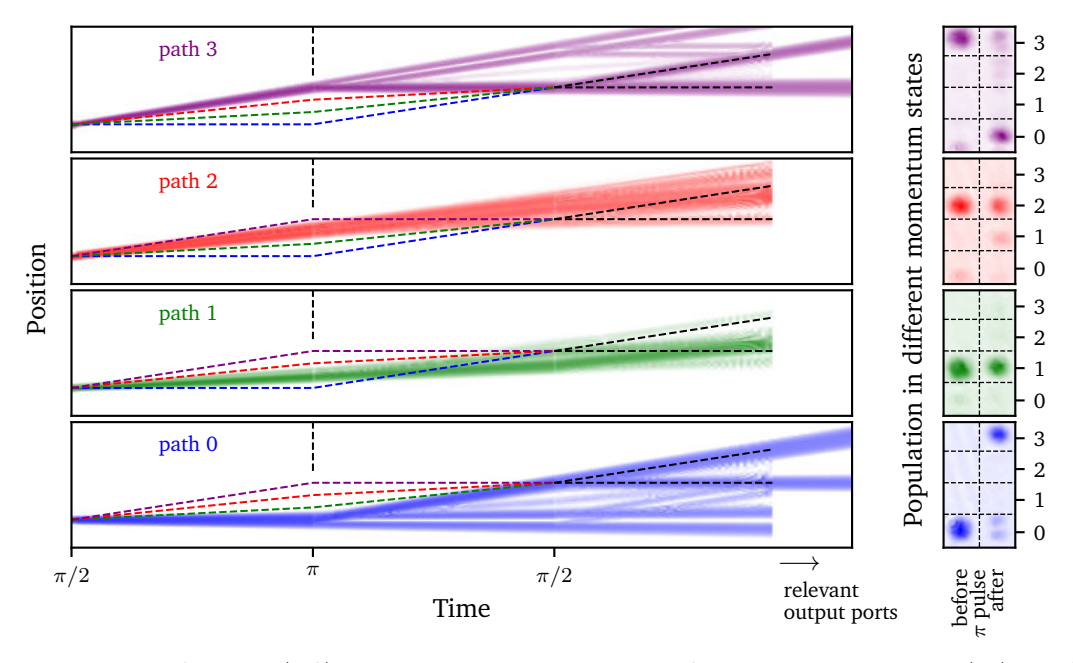
Fig. C2.: Schematic visualisation of the beating of correlated MZIs for $\theta_{\rm B}=\pi/4$ (top) and $\theta_{\rm B}=\pi/2$ (bottom). Red crosses and blue dots show the individual MZI signals $S_{\pm 1}$ with orange diamonds showing their sum. On the right side the histograms of the positive, negative and sum signals are shown in corresponding colours, showcasing a reduces apparent visibility for $\theta_{\rm B}=\pi/4$ and a complete loss for $\theta_{\rm B}=\pi/2$.

Dichroic mirror pulses

To experimentally verify the efficiency of an DMP in a MZI, interferometer times greater than 4 ms are needed to properly discard the parasitic paths which is currently not possible at the ATOMICS experiment. Therefore, only the reflectivity of the DMP was measured experimentally and the full MZI sequence was investigated numerically by P. Schach and M. Dietrich from the group of Prof. E. Giese. For a conventional mirror Fig. C3a and the optimised DMP Fig. C3b presented here to complement the experimental findings. A detailed discussion can be found in [169, 171].



(a) Initial configuration without optimised DMP. (left) Numerical simulation shows both resonant (0,3) and parasitic (1,2) paths being reflected into output ports (black dashed lines). (right) Experimental absorption images confirm parasitic orders (red/green) are reflected alongside resonant orders (blue/purple) [see Fig. 4.20].



(b) Optimised DMP configuration. (Left) Simulation demonstrates selective reflection - only resonant paths (0,3) are reflected while parasitic paths (1,2) transmit through. (Right) Experimental images show parasitic orders remain in input momentum class after mirror pulse.

Fig. C3.: Comparison of Bragg mirror pulse performance (a) without and (b) with optimised dichroic mirror pulse (DMP). Numerical simulations (left columns) and experimental absorption images (right columns) demonstrate the DMPs ability to suppress parasitic diffraction orders while maintaining high efficiency for resonant paths. Numerical data courtesy of M. Dietrich and P. Schach (group of Prof. E. Giese). The atom density is displayed on logarithmic scale with the input to every path normalised to unity. Dashed coloured lines indicate the paths of non-displayed orders and dashed black lines the output ports of the MZI associated with p_0 and p_3 . The final section of the time evolution hides the atoms not detected in these ports to augment the contribution of each path to the signal.

D. DMD potentials supplementary material

In addition to the measurements presented in Section 5.2.1, a similar measurement has been conducted with increased waist sizes $w_y=15\,\mu\mathrm{m}$ to evaluate if a different expansion behaviour can be observed. The experiment was carried out for the same parameters as discussed in the main section. In Fig. D1 the normalised line densities are shown analogously to Fig. 5.9 with the same expansion behaviour visible. For a dimple depth of $|U|_{\mathrm{dimp}}=2\,\mathrm{E}_{\mathrm{rec}}$ [Fig. D1 (top right)], the emerging pattern is qualitatively very similar to the numerically calculated expansion pattern in Fig. 5.10 (top left). This again indicates a non-thermal nature of the ensembles produced as it is described by Eq. (5.2b).

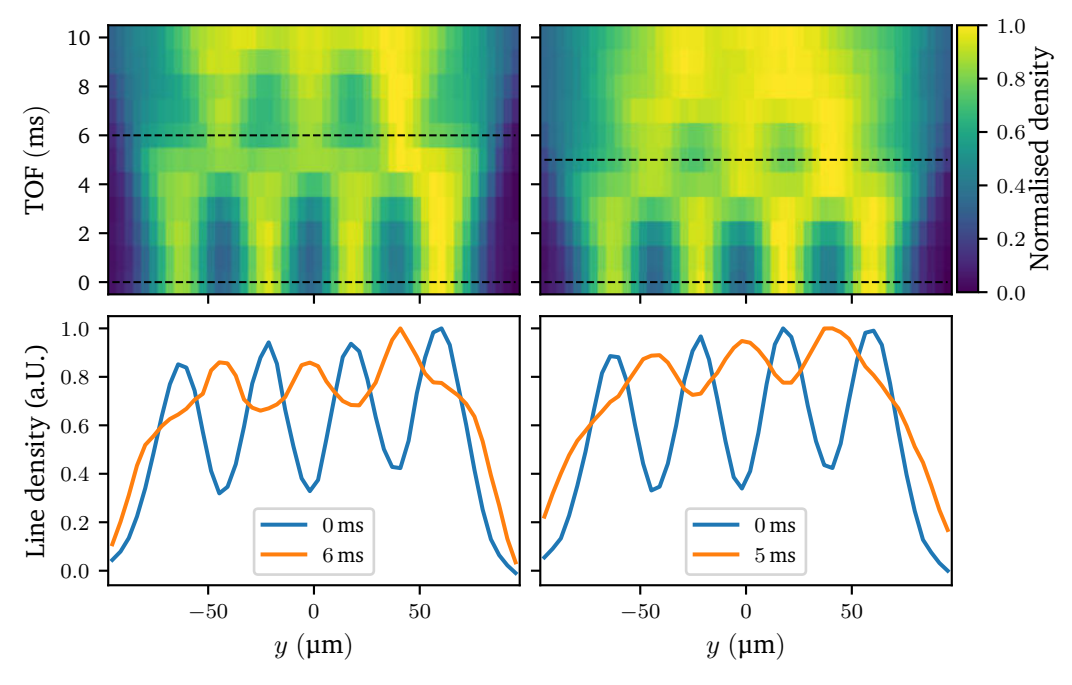


Fig. D1.: Analogue visualisation of the expansion behaviour of for dynamically generated ensembles in dimple potentials of increased waist $w_y=15\,\mu\mathrm{m}$. (top) False colour representation of the normalised one-dimensional density for the expansion during the TOF for $|U|_{\mathrm{dimp}}=1\,\mathrm{E}_{\mathrm{rec}}$ (left) and $|U|_{\mathrm{dimp}}=2\,\mathrm{E}_{\mathrm{rec}}$ (right). (bottom) Corresponding one-dimensional density for $0\,\mathrm{ms}$ (blue) and $6\,\mathrm{ms}$ for $|U|_{\mathrm{dimp}}=0\,\mathrm{E}_{\mathrm{rec}}$ and $0\,\mathrm{ms}$ for $|U|_{\mathrm{dimp}}=2\,\mathrm{E}_{\mathrm{rec}}$ (orange), visualising the initial location of the dimple potentials. Dashed lines in the top row images show the selected line densities.

E. Python environment

To run the evaluation an plotting *Python* scripts Python 3.12.3 64bit was used. Furthermore, necessary packages including their version are summarised in Tab. F1. Additionally, the complete environment has been archived.

Tab. F1.: Python environment and packages required to compile the evaluation scripts for this thesis.

Component	Version / Value
Spyder	6.0.7 (conda)
Python	3.12.3 64-bit
Qt	5.15.2
PyQt5	5.15.10
Operating System	Windows-11-10.0.26100-SP0
matplotlib	3.9.2
numba	0.60.0
numpy	1.26.4
scipy	1.13.1

F. List of publications

D. Pfeiffer, L. Lind, J. Küber, F. Schmaltz, A. Turpin, V. Ahufinger, J. Mompart, and G. Birkl, *Trapping of Bose-Einstein condensates in a three-dimensional dark focus generated by conical refraction*, Physical Review A **108**, 053320 (2023)¹

D. Pfeiffer, M. Dietrich, P. Schach, E. Giese, and G. Birkl, *mirror pulses for optimized higher-order atomic Bragg diffraction*, Physical Review Research 7, L012028 (2025)²

N. Bazhan, A. Svetlichnyi, D. Pfeiffer, D. Derr, G. Birkl, and A. Yakimenko, *Generation of Josephson vortices in stacked toroidal Bose-Einstein condensates*, Physical Review A **106**, 043305 (2022)

Y. Borysenko, N. Bazhan, O. Prykhodko, D. Pfeiffer, L. Lind, G. Birkl, and A. Yakimenko, *Acceleration-driven dynamics of Josephson vortices in coplanar superfluid rings*, Physical Review A 111, 043308 (2025)

L. Lind, D. Pfeiffer, S. Reißig, and G. Birkl, *Optimized three-dimensional bottle-beam arrays generated by conical refraction*, (in preparation)

¹My contributions to this work include the collection, evaluation, and presentation of experimental data in close collaboration with L. Lind. Furthermore, the generation, evaluation, and presentation of all numerical data has been done by me.

²My contributions to this work include the collection, evaluation, and presentation of all experimental data as well as the presentation of all numerical data generated by M. Dietrich and P. Schach.

G. Supervised theses

Bachelor theses

Pascal Mittenbühler

Neuartige Laserstabilisierung für Chirplaser zum Atomstrahlbremsen February 2022

Maximilian Damm

Aufbau und Charakterisierung eines Tapered Amplifiers bei 798 nm für die Erzeugung optischer Potentiale July 2022

Master theses

Ludwig Lind

Zeitlich veränderliche Dipolpotentiale für Bose-Einstein-Kondensate mittels digital steuerbarer Mikrospiegeleinheit

October 2021

Daniel Derr

Erweiterung des ATOMICS-Experimentes für Bose-Einstein-Kondensate in DMD-basierten Potentialen

June 2022

References

- [1] A. A. Michelson and E. W. Morley, *On the relative motion of the Earth and the luminiferous ether*, *Am. J. Sci.* **3**, 333–345 (1887).
- [2] T. L. S. Collaboration, J. Aasi, B. P. Abbott, R. Abbott, T. Abbott, M. R. Abernathy, K. Ackley, C. Adams, T. Adams, P. Addesso, et al., *Advanced LIGO*, *Classical and Quantum Gravity* **32**, 074001 (2015).
- [3] B. Caron, A. Dominjon, C. Drezen, R. Flaminio, X. Grave, F. Marion, L. Massonnet, C. Mehmel, R. Morand, B. Mours, et al., *The Virgo interferometer*, *Classical and Quantum Gravity* 14, 1461 (1997).
- [4] B. Culshaw, *The optical fibre Sagnac interferometer: an overview of its principles and applications, Meas. Sci. Technol.* 17, R1 (2005).
- [5] L. De Broglie, *Recherches sur la théorie des quanta*, PhD thesis, Migration-université en cours d'affectation (1924).
- [6] C. Davisson and L. H. Germer, *The Scattering of Electrons by a Single Crystal of Nickel, Nature* **119**, 558–560 (1927).
- [7] M. Arndt, O. Nairz, J. Petschinka, and A. Zeilinger, *High contrast interference with C60 and C70*, *C. R. Acad. Sci., Ser. IV:Phys.* **2**, 581–585 (2001).
- [8] O. Nairz, M. Arndt, and A. Zeilinger, *Quantum interference experiments with large molecules*, *Am. J. Phys.* **71**, 319–325 (2003).
- [9] Y. Y. Fein, P. Geyer, P. Zwick, F. Kiałka, S. Pedalino, M. Mayor, S. Gerlich, and M. Arndt, *Quantum superposition of molecules beyond 25 kDa*, *Nat. Phys.* **15**, 1242–1245 (2019).
- [10] A. Einstein, Quantentheorie des einatomigen idealen Gases. Zweite Abhandlung, in: Albert Einstein: Akademie-Vorträge, John Wiley & Sons, Ltd (2005), 245–257.
- [11] J. V. Prodan, W. D. Phillips, and H. Metcalf, *Laser Production of a Very Slow Monoenergetic Atomic Beam*, *Phys. Rev. Lett.* **49**, 1149–1153 (1982).
- [12] W. D. Phillips, Nobel Lecture: Laser cooling and trapping of neutral atoms, Rev. Mod. Phys. 70, 721–741 (1998).
- [13] S. Chu, Nobel Lecture: The manipulation of neutral particles, Rev. Mod. Phys. **70**, 685–706 (1998).
- [14] S. Chu, L. Hollberg, J. E. Bjorkholm, A. Cable, and A. Ashkin, *Three-dimensional viscous confinement and cooling of atoms by resonance radiation pressure*, *Phys. Rev. Lett.* **55**, 48–51 (1985).
- [15] E. L. Raab, M. Prentiss, A. Cable, S. Chu, and D. E. Pritchard, *Trapping of Neutral Sodium Atoms with Radiation Pressure*, *Phys. Rev. Lett.* **59**, 2631–2634 (1987).
- [16] E. A. Cornell and C. E. Wieman, *Nobel Lecture: Bose-Einstein condensation in a dilute gas, the first 70 years and some recent experiments, Rev. Mod. Phys.* **74**, 875–893 (2002).

- [17] W. Ketterle, Nobel lecture: When atoms behave as waves: Bose-Einstein condensation and the atom laser, Rev. Mod. Phys. 74, 1131–1151 (2002).
- [18] E. A. Cornell, W. Ketterle, and C. E. Wieman, *The Nobel Prize in Physics 2001*, Online; accessed 08.06.2025 (2001).
- [19] C. S. Adams, H. J. Lee, N. Davidson, M. Kasevich, and S. Chu, *Evaporative Cooling in a Crossed Dipole Trap, Phys. Rev. Lett.* **74**, 3577–3580 (1995).
- [20] R. Grimm, M. Weidemüller, and Y. B. Ovchinnikov, *Optical Dipole Traps for Neutral Atoms*, in: edited by B. Bederson and H. Walther, **42**, Advances In Atomic, Molecular, and Optical Physics, Academic Press (2000), 95–170.
- [21] M. Kasevich and S. Chu, *Atomic interferometry using stimulated Raman transitions*, *Phys. Rev. Lett.* **67**, 181–184 (1991).
- [22] M. M. Beydler, E. R. Moan, Z. Luo, Z. Chu, and C. A. Sackett, *Guided-wave Sagnac atom interferometer with large area and multiple orbits*, *AVS Quantum Sci.* **6**, 014401 (2024).
- [23] M. Kasevich and S. Chu, Measurement of the gravitational acceleration of an atom with a light-pulse atom interferometer, Appl. Phys. B 54, 321–332 (1992).
- [24] A. D. Cronin, J. Schmiedmayer, and D. E. Pritchard, *Optics and interferometry with atoms and molecules*, *Rev. Mod. Phys.* **81**, 1051–1129 (2009).
- [25] S. Gupta, K. Dieckmann, Z. Hadzibabic, and D. E. Pritchard, *Contrast Interferometry using Bose-Einstein Condensates to Measure* h/m *and* α , *Phys. Rev. Lett.* **89**, 140401 (2002).
- [26] R. H. Parker, C. Yu, W. Zhong, B. Estey, and H. Müller, *Measurement of the fine-structure constant as a test of the Standard Model, Science* **360**, 191–195 (2018).
- [27] P. Asenbaum, C. Overstreet, M. Kim, J. Curti, and M. A. Kasevich, *Atom-Interferometric Test of the Equivalence Principle at the* 10^{-12} *Level, Phys. Rev. Lett.* **125**, 191101 (2020).
- [28] M. H. et al., *Interferometry with Bose-Einstein Condensates in Microgravity*, *Phys. Rev. Lett.* **110**, 093602 (2013).
- [29] B. Barrett, L. Antoni-Micollier, L. Chichet, B. Battelier, T. Lévèque, A. Landragin, and P. Bouyer, *Dual matter-wave inertial sensors in weightlessness*, *Nat. Commun.* 7, 13786 (2016).
- [30] M. D. Lachmann, H. Ahlers, D. Becker, A. N. Dinkelaker, J. Grosse, O. Hellmig, H. Müntinga, V. Schkolnik, S. T. Seidel, T. Wendrich, et al., *Ultracold atom interferometry in space*, *Nat. Commun.* 12, 1317 (2021).
- [31] J. R. Williams, C. A. Sackett, H. Ahlers, D. C. Aveline, P. Boegel, S. Botsi, E. Charron, E. R. Elliott, N. Gaaloul, E. Giese, et al., *Pathfinder experiments with atom interferometry in the Cold Atom Lab onboard the International Space Station*, *Nat. Commun.* **15**, 6414 (2024).
- [32] M. He, X. Chen, J. Fang, Q. Chen, H. Sun, Y. Wang, J. Zhong, L. Zhou, C. He, J. Li, et al., The space cold atom interferometer for testing the equivalence principle in the China Space Station, npj Microgravity 9, 58 (2023).
- [33] S. Abend, B. Allard, I. Alonso, J. Antoniadis, H. Araújo, G. Arduini, A. S. Arnold, T. Asano, N. Augst, L. Badurina, et al., *Terrestrial very-long-baseline atom interferometry: Workshop summary*, *AVS Quantum Sci.* **6**, 024701 (2024).

- [34] A. Abdalla, M. Abe, S. Abend, M. Abidi, M. Aidelsburger, A. Alibabaei, B. Allard, J. Antoniadis, G. Arduini, N. Augst, et al., *Terrestrial Very-Long-Baseline Atom Interferometry:* summary of the second workshop, *EPJ Quantum Technol.* 12, 42 (2025).
- [35] S.-w. Chiow, T. Kovachy, H.-C. Chien, and M. A. Kasevich, $102\hbar k$ Large Area Atom Interferometers, *Phys. Rev. Lett.* **107**, 130403 (2011).
- [36] L. Morel, Z. Yao, P. Cladé, and S. Guellati-Khélifa, *Determination of the fine-structure constant with an accuracy of 81 parts per trillion*, *Nature* **588**, 61–65 (2020).
- [37] M. Gebbe, J.-N. Siemß, M. Gersemann, H. Müntinga, S. Herrmann, C. Lämmerzahl, H. Ahlers, N. Gaaloul, C. Schubert, K. Hammerer, S. Abend, and E. M. Rasel, *Twin-lattice atom interferometry*, *Nat. Commun.* **12**, 2544 (2021).
- [38] S. Abend, M. Gebbe, M. Gersemann, H. Ahlers, H. Müntinga, E. Giese, N. Gaaloul, C. Schubert, C. Lämmerzahl, W. Ertmer, W. P. Schleich, and E. M. Rasel, *Atom-Chip Fountain Gravimeter*, *Phys. Rev. Lett.* **117**, 203003 (2016).
- [39] D. Schlippert, *The Hannover very long baseline atom interferometry facility*, in: Quantum *Sensing, Imaging, and Precision Metrology III*, SPIE (2025), PC1339208.
- [40] L. Amico, M. Boshier, G. Birkl, A. Minguzzi, C. Miniatura, L.-C. Kwek, D. Aghamalyan, V. Ahufinger, D. Anderson, N. Andrei, et al., *Roadmap on Atomtronics: State of the art and perspective, AVS Quantum Sci.* 3, 039201 (2021).
- [41] W. R. Hamilton, Third supplement to an essay on the theory of systems of rays, The *Transactions of the Royal Irish Academy* (1831).
- [42] H. Lloyd, On the phenomena presented by light in its passage along the axes of biaxal crystals, The Transactions of the Royal Irish Academy, 145–157 (1831).
- [43] A. Turpin, J. Polo, Y. V. Loiko, J. Küber, F. Schmaltz, T. K. Kalkandjiev, V. Ahufinger, G. Birkl, and J. Mompart, *Blue-detuned optical ring trap for Bose-Einstein condensates based on conical refraction, Opt. Express* **23**, 1638–1650 (2015).
- [44] A. Turpin Avilés, *Conical refraction: fundamentals and applications*, PhD thesis, Universitat Autònoma de Barcelona (2015).
- [45] J. Küber, *Dynamics of Bose-Einstein condensates in novel optical potentials*, Dissertation, Technische Universität Darmstadt (2014).
- [46] F. Schmaltz, Bose-Einstein-Kondensate in dynamischen Dipolpotentialen aus konischer Refraktion, Dissertation, Technische Universität Darmstadt (2019).
- [47] G. Gauthier, I. Lenton, N. M. Parry, M. Baker, M. J. Davis, H. Rubinsztein-Dunlop, and T. W. Neely, *Direct imaging of a digital-micromirror device for configurable microscopic optical potentials*, *Optica* 3, 1136–1143 (2016).
- [48] G. Del Pace, K. Xhani, A. Muzi Falconi, M. Fedrizzi, N. Grani, D. Hernandez Rajkov, M. Inguscio, F. Scazza, W. J. Kwon, and G. Roati, *Imprinting Persistent Currents in Tunable Fermionic Rings*, *Phys. Rev. X* **12**, 041037 (2022).
- [49] D. Cassettari, G. Mussardo, and A. Trombettoni, *Holographic realization of the prime number quantum potential*, *PNAS Nexus* **2**, pgac279 (2022).
- [50] K. Henderson, C. Ryu, C. MacCormick, and M. G. Boshier, *Experimental demonstration of painting arbitrary and dynamic potentials for Bose–Einstein condensates*, *New J. Phys.* 11, 043030 (2009).

- [51] L. Amico and M. G. Boshier, Atomtronics, arxiv:1511.07215 (2015).
- [52] R. Dumke, Z. Lu, J. Close, N. Robins, A. Weis, M. Mukherjee, G. Birkl, C. Hufnagel, L. Amico, M. G. Boshier, K. Dieckmann, W. Li, and T. C. Killian, *Roadmap on quantum optical systems*, *J. Opt* **18**, 093001 (2016).
- [53] C. Ryu, E. C. Samson, and M. G. Boshier, Quantum interference of currents in an atomtronic SQUID, Nat. Commun. 11, 3338 (2020).
- [54] Y. Borysenko, N. Bazhan, O. Prykhodko, D. Pfeiffer, L. Lind, G. Birkl, and A. Yakimenko, *Acceleration-driven dynamics of Josephson vortices in coplanar superfluid rings, Phys. Rev.* A 111, 043308 (2025).
- [55] C. W. Woffinden, A. J. Groszek, G. Gauthier, B. J. Mommers, M. W. J. Bromley, S. A. Haine, H. Rubinsztein-Dunlop, M. J. Davis, T. W. Neely, and M. Baker, *Viability of rotation sensing using phonon interferometry in Bose-Einstein condensates*, *SciPost Phys.* 15, 128 (2023).
- [56] O. Wille, *Manipulation von Bose-Einstein-Kondensaten in optischen Dipolpotentialen*, Dissertation, Technische Universität Darmstadt (2010).
- [57] T. Lauber, *Kohärente Dynamik von Bose-Einstein-Kondensaten in Dipolpotentialen*, Dissertation, Technische Universität Darmstadt (2012).
- [58] R. C. Jones, A New Calculus for the Treatment of Optical SystemsI. Description and Discussion of the Calculus, J. Opt. Soc. Am. 31, 488–493 (1941).
- [59] D. Meschede, Gerthsen Physik, 24. Auflage, Springer-Verlag, Berlin, Heidelberg (2010).
- [60] J. Wen, Y. Zhang, and M. Xiao, *The Talbot effect: recent advances in classical optics, nonlinear optics, and quantum optics, Adv. Opt. Photon.* **5**, 83–130 (2013).
- [61] M. Young, Optics and Lasers: Including Fibers and Optical Waveguides, Springer (2000).
- [62] T. Lauber, J. Küber, O. Wille, and G. Birkl, *Optimized Bose-Einstein-condensate production* in a dipole trap based on a 1070-nm multifrequency laser: Influence of enhanced two-body loss on the evaporation process, *Phys. Rev. A* 84, 043641 (2011).
- [63] L. Pause, T. Preuschoff, D. Schäffner, M. Schlosser, and G. Birkl, *Reservoir-based deterministic loading of single-atom tweezer arrays*, *Phys. Rev. Res.* **5**, L032009 (2023).
- [64] L. Pause, L. Sturm, M. Mittenbühler, S. Amann, T. Preuschoff, D. Schäffner, M. Schlosser, and G. Birkl, *Supercharged two-dimensional tweezer array with more than 1000 atomic qubits*, *Optica* 11, 222–226 (2024).
- [65] A. Ashkin, G. Mourou, and D. Strickland, *The Nobel Prize in Physics 2018*, Online; accessed 21.04.2025 (2018).
- [66] H. J. Metcalf and P. Van der Straten, *Laser cooling and trapping*, Springer Science & Business Media, New York (1999).
- [67] D. A. Steck, *Rubidium 87 D Line Data*, revision 2.2.3 (2024).
- [68] L. P. Pitaevskii and S. Stringari, *Bose-Einstein Condensation*, Oxford University Press, Oxford (2003).
- [69] A. J. Leggett, Superfluidity, Rev. Mod. Phys. 71, S318–S323 (1999).
- [70] M. R. Matthews, B. P. Anderson, P. C. Haljan, D. S. Hall, C. E. Wieman, and E. A. Cornell, *Vortices in a Bose-Einstein Condensate*, *Phys. Rev. Lett.* **83**, 2498–2501 (1999).

- [71] M. R. Andrews, C. G. Townsend, H.-J. Miesner, D. S. Durfee, D. M. Kurn, and W. Ketterle, *Observation of Interference Between Two Bose Condensates*, *Science* **275**, 637–641 (1997).
- [72] Y. Castin and R. Dum, Bose-Einstein Condensates in Time Dependent Traps, Phys. Rev. Lett. 77, 5315–5319 (1996).
- [73] W. Ketterle, D. S. Durfee, and D. Stamper-Kurn, *Making, probing and understanding Bose-Einstein condensates*, in: *Bose-Einstein condensation in atomic gases*, IOS Press (1999), 67–176.
- [74] J. Nes, *Cold atoms and Bose-Einstein condensates in optical dipole potentials*, Dissertation, Technische Universität Darmstadt (2008).
- [75] M. Hetzel, M. Quensen, J. S. Haase, and C. Klempt, *All-optical production of Bose-Einstein condensates with a 2-Hz repetition rate*, *Phys. Rev. A* **111**, L061301 (2025).
- [76] P. T. Starkey, C. J. Billington, S. P. Johnstone, M. Jasperse, K. Helmerson, L. D. Turner, and R. P. Anderson, *A scripted control system for autonomous hardware-timed experiments*, *Rev. Sci. Instrum.* **84**, 085111 (2013).
- [77] P. T. Starkey, *State-dependent forces in cold quantum gases*, PhD thesis, Monash University (2019).
- [78] C. J. Billington, *State-dependent forces in cold quantum gases*, PhD thesis, Monash University (2018).
- [79] L. Pause, A New Setup for Scaling Up Microlens-Based Individual-Atom Quantum Processors, Dissertation, Technische Universität Darmstadt (2023).
- [80] D. Derr, Erweiterung des ATOMICS-Experiments für Bose-Einstein-Kondensate in DMD-basierten Potentialen, Master Thesis, Technische Universität Darmstadt (2022).
- [81] P. S. Foundation, *Python Language Reference, version 3.12*, Online; accessed 06.06.2025, Python Software Foundation (2025).
- [82] C. R. Harris, K. J. Millman, S. J. van der Walt, R. Gommers, P. Virtanen, D. Cournapeau, E. Wieser, J. Taylor, S. Berg, N. J. Smith, et al., *Array programming with NumPy*, *Nature* **585**, 357–362 (2020).
- [83] P. Virtanen, R. Gommers, T. E. Oliphant, M. Haberland, T. Reddy, D. Cournapeau, E. Burovski, P. Peterson, W. Weckesser, J. Bright, et al., *SciPy 1.0: Fundamental Algorithms for Scientific Computing in Python*, *Nat. Methods* 17, 261–272 (2020).
- [84] J. D. Hunter, Matplotlib: A 2D graphics environment, Comput. Sci. Eng. 9, 90–95 (2007).
- [85] labscript suite, the labscript suite, (Online; accessed 30.05.2025) (2025).
- [86] labscript suite, the labscript suite GitHub, (Online; accessed 30.05.2025) (2025).
- [87] M. Egorov, B. Opanchuk, P. Drummond, B. V. Hall, P. Hannaford, and A. I. Sidorov, *Measurement of s-wave scattering lengths in a two-component Bose-Einstein condensate*, *Phys. Rev. A* **87**, 053614 (2013).
- [88] C. Monroe, W. Swann, H. Robinson, and C. Wieman, *Very cold trapped atoms in a vapor cell, Phys. Rev. Lett.* **65**, 1571–1574 (1990).
- [89] S. Pollock, *Integration of Magneto Optical Traps in Atom Chips*, PhD thesis, Imperial College London (2010).
- [90] J. Dalibard and C. Cohen-Tannoudji, *Laser cooling below the Doppler limit by polarization gradients: simple theoretical models*, *J. Opt. Soc. Am. B* **6**, 2023–2045 (1989).

- [91] D. J. Gardiner, *Introduction to Raman Scattering*, in: *Practical Raman Spectroscopy*, edited by D. J. Gardiner and P. R. Graves, Springer Berlin Heidelberg, Berlin, Heidelberg (1989), 1–12.
- [92] T. Müther, *Evaporative Kühlung in optischen Dipolpotentialen*, Dissertation, Universität Hannover (2005).
- [93] S. Reißig, Optisches Pumpen von Rubidiumatomen im ATOMICS-Experiment, Master Thesis (2025).
- [94] W. Gerlach and O. Stern, *Der experimentelle Nachweis der Richtungsquantelung im Magnetfeld*, in: *Walther Gerlach (1889–1979): Eine Auswahl aus seinen Schriften und Briefen*, edited by H.-R. Bachmann and H. Rechenberg, Springer Berlin Heidelberg, Berlin, Heidelberg (1989), 26–29.
- [95] M. Bauer, The Stern-Gerlach Experiment, Translation of: "Der experimentelle Nachweis der Richtungsquantelung im Magnetfeld" (2023).
- [96] P. Baus, Current Drivers and Control Electronics for the Laser Spectroscopy of Highly Charged Ions, Dissertation, Technische Universität Darmstadt (2024).
- [97] T. Preuschoff, Laser Technologies for Applications in Quantum Information Science, Dissertation, PhD thesis, Technische Universität Darmstadt (2023).
- [98] X. Baillard, A. Gauguet, S. Bize, P. Lemonde, P. Laurent, A. Clairon, and P. Rosenbusch, *Interference-filter-stabilized external-cavity diode lasers*, *Opt. Commun.* **266**, 609–613 (2006).
- [99] T. Preuschoff, M. Schlosser, and G. Birkl, *Optimization strategies for modulation transfer spectroscopy applied to laser stabilization*, *Opt. Express* **26**, 24010–24019 (2018).
- [100] T. Preuschoff, M. Schlosser, and G. Birkl, Digital laser frequency and intensity stabilization based on the STEMlab platform (originally Red Pitaya), Rev. Sci. Instrum. 91, 083001 (2020).
- [101] P. Mittenbühler, Neuartige Laserstabilisierung für Chirplaser zum Atomstrahlbremsen, Bachelor Thesis, Technische Universität Darmstadt (2022).
- [102] D. Pfeiffer, *Optimierung der experimentellen Erzeugung von Bose-Einstein Kondensaten*, German, Master Thesis (2020).
- [103] Q. Hu, J. Yang, Y. Luo, A. Jia, C. Wei, and Z. Li, A theoretical analysis and determination of the technical requirements for a Bragg diffraction-based cold atom interferometry gravimeter, Optik 131, 632–639 (2017).
- [104] M. Acker, *Entwicklung eines AOM-DDS-Treibers zur Phasenmodulation von Bragg-Pulsen*, Bachelor Thesis, Technische Universität Darmstadt (2017).
- [105] A. Turpin, Y. V. Loiko, T. K. Kalkandjiev, and J. Mompart, *Conical refraction: fundamentals and applications, Laser Photonics Rev.* **10**, 750–771 (2016).
- [106] A. L. Gaunt, T. F. Schmidutz, I. Gotlibovych, R. P. Smith, and Z. Hadzibabic, *Bose-Einstein Condensation of Atoms in a Uniform Potential*, *Phys. Rev. Lett.* **110**, 200406 (2013).
- [107] S. Zhang, F. Robicheaux, and M. Saffman, *Magic-wavelength optical traps for Rydberg atoms*, *Phys. Rev. A* **84**, 043408 (2011).

- [108] M. J. Piotrowicz, M. Lichtman, K. Maller, G. Li, S. Zhang, L. Isenhower, and M. Saffman, Two-dimensional lattice of blue-detuned atom traps using a projected Gaussian beam array, Phys. Rev. A 88, 013420 (2013).
- [109] D. Barredo, V. Lienhard, P. Scholl, S. de Léséleuc, T. Boulier, A. Browaeys, and T. Lahaye, Three-Dimensional Trapping of Individual Rydberg Atoms in Ponderomotive Bottle Beam Traps, Phys. Rev. Lett. 124, 023201 (2020).
- [110] P. Xu, X. He, J. Wang, and M. Zhan, *Trapping a single atom in a blue detuned optical bottle beam trap*, *Opt. Lett.* **35**, 2164–2166 (2010).
- [111] R. Ozeri, L. Khaykovich, and N. Davidson, *Long spin relaxation times in a single-beam blue-detuned optical trap, Phys. Rev. A* **59**, R1750–R1753 (1999).
- [112] P. Rudy, R. Ejnisman, A. Rahman, S. Lee, and N. P. Bigelow, *An all optical dynamical dark trap for neutral atoms*, *Opt. Express* **8**, 159–165 (2001).
- [113] L. Cacciapuoti, M. de Angelis, G. Pierattini, and G. M. Tino, *Single-beam optical bottle for cold atoms using a conical lens*, *Eur. Phys. J. D* **14**, 373–376 (2001).
- [114] L. Isenhower, W. Williams, A. Dally, and M. Saffman, *Atom trapping in an interferometrically generated bottle beam trap*, *Opt. Lett.* **34**, 1159–1161 (2009).
- [115] G. Li, S. Zhang, L. Isenhower, K. Maller, and M. Saffman, *Crossed vortex bottle beam trap for single-atom qubits*, *Opt. Lett.* **37**, 851–853 (2012).
- [116] T. Puppe, I. Schuster, A. Grothe, A. Kubanek, K. Murr, P. W. H. Pinkse, and G. Rempe, Trapping and Observing Single Atoms in a Blue-Detuned Intracavity Dipole Trap, Phys. Rev. Lett. 99, 013002 (2007).
- [117] V. G. Shvedov, C. Hnatovsky, N. Shostka, and W. Krolikowski, *Generation of vector bottle beams with a uniaxial crystal*, *J. Opt. Soc. Am. B* **30**, 1–6 (2013).
- [118] Y. V. Loiko, A. Turpin, T. K. Kalkandjiev, E. U. Rafailov, and J. Mompart, *Generating a three-dimensional dark focus from a single conically refracted light beam*, *Opt. Lett.* **38**, 4648–4651 (2013).
- [119] M. Esseling, C. Alpmann, J. Schnelle, R. Meissner, and C. Denz, *Conical Refraction Bottle Beams for Entrapment of Absorbing Droplets*, *Sci. Rep.* **8**, 5029 (2018).
- [120] D. Pfeiffer, L. Lind, J. Küber, F. Schmaltz, A. Turpin, V. Ahufinger, J. Mompart, and G. Birkl, *Trapping of Bose-Einstein condensates in a three-dimensional dark focus generated by conical refraction*, *Phys. Rev. A* **108**, 053320 (2023).
- [121] Y. V. Loiko, A. Turpin, T. K. Kalkandjiev, and J. Mompart, *Conical refraction multiplexing for free-space optical communications*, in: *Free-Space Laser Communication Technologies XXIV*, edited by H. Hemmati and D. M. Boroson, **8246**, International Society for Optics and Photonics, SPIE (2012), 82460T.
- [122] A. Turpin, Y. Loiko, T. K. Kalkandjiev, and J. Mompart, *Free-space optical polarization demultiplexing and multiplexing by means of conical refraction*, *Opt. Lett.* **37**, 4197–4199 (2012).
- [123] M. V. Berry and M. R. Jeffrey, *Conical diffraction: Hamilton's diabolical point at the heart of crystal optics*, *Prog. Opt.* **50**, 13–50 (2007).
- [124] A. Turpin, Y. V. Loiko, T. K. Kalkandjiev, and J. Mompart, *Light propagation in biaxial crystals*, *J. Opt.* **17**, 065603 (2015).

- [125] A. M. Belskii and A. P. Khapalyuk, *Internal conical refraction of bounded light beams in biaxial crystals*, *Opt. Spectrosc.* **44**, 436–439 (1978).
- [126] M. V. Berry, Conical diffraction asymptotics: fine structure of Poggendorff rings and axial spike, J. Opt. A:Pure Appl. Opt. 6, 289 (2004).
- [127] E. Hecht, *Optik*, De Gruyter, Berlin, Boston (2018).
- [128] F. Weigand, *Charakterisierung von Bose-Einstein-Kondensaten in Dipolpotentialen*, Master Thesis, Technische Universität Darmstadt (2018).
- [129] W. N. M. Jr, M. A. Esrick, Z. Teoh, and J. K. Freericks, *A physicist's guide to the solution of Kummer's equation and confluent hypergeometric functions*, *arXiv:2111.04852* (2021).
- [130] R. Darcy, D. McCloskey, K. Ballantine, B. Jennings, J. Lunney, P. Eastham, and J. Donegan, *White light conical diffraction*, *Opt. Express* **21**, 20394–20403 (2013).
- [131] D. A. Steck, *Cesium D Line Data*, revision 2.2.3 (2024).
- [132] D. A. Steck, Rubidium 85 D Line Data, revision 2.2.3 (2024).
- [133] D. A. Steck, *Sodium D Line Data*, revision 2.2.3 (2024).
- [134] M. e. Gehm, *Properties of* ⁶*Li*, revision 1.1 (2003).
- [135] T. Tiecke, *Properties of potassium*, *University of Amsterdam*, *The Netherlands, Thesis*, 12–14 (2010).
- [136] M. S. Fischer, *Properties of Lithium-7* (2023).
- [137] M. C. Pujol, M. Rico, C. Zaldo, R. Solé, V. Nikolov, et al., *Crystalline structure and optical spectroscopy of Er3+-doped KGd(WO4)2 single crystals, Applied Physics B: Lasers and Optics* **68**, 187–197 (1999).
- [138] A. M. Kaufman and K.-K. Ni, *Quantum science with optical tweezer arrays of ultracold atoms and molecules*, *Nat. Phys.* **17**, 1324–1333 (2021).
- [139] M. Schlosser, D. Ohl de Mello, D. Schäffner, T. Preuschoff, L. Kohfahl, and G. Birkl, *Assembled arrays of Rydberg-interacting atoms*, *J. Phys. B:At., Mol. Opt. Phys.* **53**, 144001 (2020).
- [140] H. J. Manetsch, G. Nomura, E. Bataille, K. H. Leung, X. Lv, and M. Endres, *A tweezer array with 6100 highly coherent atomic qubits*, *arxiv:2403.12021* (2024).
- [141] R. Lin, H.-S. Zhong, Y. Li, Z.-R. Zhao, L.-T. Zheng, T.-R. Hu, H.-M. Wu, Z. Wu, W.-J. Ma, Y. Gao, et al., AI-Enabled Rapid Assembly of Thousands of Defect-Free Neutral Atom Arrays with Constant-time-overhead, arxiv:2412.14647 (2024).
- [142] I. H. Deutsch, G. K. Brennen, and P. S. Jessen, *Quantum Computing with Neutral Atoms in an Optical Lattice*, *Fortschr. Phys.* **48**, 925–943 (2000).
- [143] Y. T. Chew, M. Poitrinal, T. Tomita, S. Kitade, J. Mauricio, K. Ohmori, and S. de Léséleuc, *Ultraprecise holographic optical tweezer array*, *Phys. Rev. A* **110**, 053518 (2024).
- [144] D. Schäffner, T. Schreiber, F. Lenz, M. Schlosser, and G. Birkl, *Quantum Sensing in Tweezer Arrays: Optical Magnetometry on an Individual-Atom Sensor Grid*, *PRX Quantum* 5, 010311 (2024).
- [145] M. Schlosser, S. Tichelmann, D. Schäffner, D. O. de Mello, M. Hambach, J. Schütz, and G. Birkl, *Scalable Multilayer Architecture of Assembled Single-Atom Qubit Arrays in a Three-Dimensional Talbot Tweezer Lattice*, *Phys. Rev. Lett.* **130**, 180601 (2023).

- [146] M. Born and E. Wolf, *Principles of optics: electromagnetic theory of propagation, interference and diffraction of light*, Elsevier (2013).
- [147] Y. Li and E. Wolf, Focal shifts in diffracted converging spherical waves, Opt. Commun. 39, 211–215 (1981).
- [148] J. T. Winthrop and C. R. Worthington, *Theory of Fresnel Images. I. Plane Periodic Objects in Monochromatic Light**, *J. Opt. Soc. Am.* **55**, 373–381 (1965).
- [149] L. R. and, XXV. On copying diffraction-gratings, and on some phenomena connected therewith, The London, Edinburgh, and Dublin Philosophical Magazine and Journal of Science 11, 196–205 (1881).
- [150] S. Reißig, Erzeugung einer dreidimensionalen Fallenkonfiguration durch Kombination von Mikrolinsenregistern mit konischer Refraktion, Master Proposal, Technische Universität Darmstadt (2024).
- [151] T. Kovachy, P. Asenbaum, C. Overstreet, C. A. Donnelly, S. M. Dickerson, A. Sugarbaker, J. M. Hogan, and M. A. Kasevich, *Quantum superposition at the half-metre scale*, *Nature* **528**, 530–533 (2015).
- [152] M. Abe, P. Adamson, M. Borcean, D. Bortoletto, K. Bridges, S. P. Carman, S. Chattopadhyay, J. Coleman, N. M. Curfman, K. DeRose, et al., *Matter-wave Atomic Gradiometer Interferometric Sensor (MAGIS-100)*, *Quantum Sci. Technol.* **6**, 044003 (2021).
- [153] S. Hartmann, J. Jenewein, E. Giese, S. Abend, A. Roura, et al., *Regimes of atomic diffraction: Raman versus Bragg diffraction in retroreflective geometries*, *Phys. Rev. A* **101**, 053610 (2020).
- [154] S. Hartmann, J. Jenewein, S. Abend, A. Roura, and E. Giese, *Atomic Raman scattering: Third-order diffraction in a double geometry*, *Phys. Rev. A* **102**, 063326 (2020).
- [155] H. Müller, S.-w. Chiow, Q. Long, S. Herrmann, and S. Chu, *Atom Interferometry with up to 24-Photon-Momentum-Transfer Beam Splitters*, *Phys. Rev. Lett.* **100**, 180405 (2008).
- [156] P. Cladé, S. Guellati-Khélifa, F. Nez, and F. Biraben, *Large Momentum Beam Splitter Using Bloch Oscillations*, *Phys. Rev. Lett.* **102**, 240402 (2009).
- [157] G. D. McDonald, C. C. N. Kuhn, S. Bennetts, J. E. Debs, K. S. Hardman, M. Johnsson, J. D. Close, and N. P. Robins, $80\hbar k$ momentum separation with Bloch oscillations in an optically guided atom interferometer, *Phys. Rev. A* **88**, 053620 (2013).
- [158] Z. Pagel, W. Zhong, R. H. Parker, C. T. Olund, N. Y. Yao, et al., *Symmetric Bloch oscillations of matter waves*, *Phys. Rev. A* **102**, 053312 (2020).
- [159] T. Rahman, A. Wirth-Singh, A. Ivanov, D. Gochnauer, E. Hough, et al., *Bloch oscillation phases investigated by multipath Stückelberg atom interferometry*, *Phys. Rev. Res.* **6**, L022012 (2024).
- [160] F. Fitzek, J.-N. Kirsten-Siemß, E. M. Rasel, N. Gaaloul, and K. Hammerer, *Accurate and efficient Bloch-oscillation-enhanced atom interferometry*, *Phys. Rev. Res.* **6**, L032028 (2024).
- [161] J. Rudolph, T. Wilkason, M. Nantel, H. Swan, C. M. Holland, et al., *Large Momentum Transfer Clock Atom Interferometry on the 689 nm Intercombination Line of Strontium*, *Phys. Rev. Lett.* **124**, 083604 (2020).
- [162] P. Berg, S. Abend, G. Tackmann, C. Schubert, E. Giese, et al., *Composite-Light-Pulse Technique for High-Precision Atom Interferometry*, *Phys. Rev. Lett.* **114**, 063002 (2015).

- [163] J. M. McGuirk, M. J. Snadden, and M. A. Kasevich, *Large Area Light-Pulse Atom Inter- ferometry*, *Phys. Rev. Lett.* **85**, 4498–4501 (2000).
- [164] H. Ahlers, H. Müntinga, A. Wenzlawski, M. Krutzik, G. Tackmann, S. Abend, N. Gaaloul, E. Giese, A. Roura, R. Kuhl, et al., *Double Bragg Interferometry*, *Phys. Rev. Lett.* **116**, 173601 (2016).
- [165] H. Müller, S.-w. Chiow, S. Herrmann, and S. Chu, *Atom Interferometers with Scalable Enclosed Area*, *Phys. Rev. Lett.* **102**, 240403 (2009).
- [166] B. Canuel, S. Abend, P. Amaro-Seoane, F. Badaracco, Q. Beaufils, A. Bertoldi, K. Bongs, P. Bouyer, C. Braxmaier, W. Chaibi, et al., *ELGAR—a European Laboratory for Gravitation and Atom-interferometric Research*, *Classical Quantum Gravity* 37, 225017 (2020).
- [167] M.-S. Zhan, J. Wang, W.-T. Ni, D.-F. Gao, G. Wang, L.-X. He, R.-B. Li, L. Zhou, X. Chen, J.-Q. Zhong, et al., *ZAIGA*: *Zhaoshan long-baseline atom interferometer gravitation antenna*, *Int. J. Mod. Phys. D* **29**, 1940005 (2020).
- [168] J. Küber, F. Schmaltz, and G. Birkl, Experimental realization of double Bragg diffraction: robust beamsplitters, mirrors, and interferometers for Bose-Einstein condensates, arxiv:1603.08826 (2016).
- [169] J.-N. Kirsten-Siemß, F. Fitzek, C. Schubert, E. M. Rasel, N. Gaaloul, and K. Hammerer, Large-Momentum-Transfer Atom Interferometers with μrad-Accuracy Using Bragg Diffraction, Phys. Rev. Lett. 131, 033602 (2023).
- [170] J.-N. Kirsten-Siemß, Theory of Large-Momentum-Transfer Atom Interferometry in the Quasi-Bragg Regime, PhD thesis, Leibniz University Hannover (2023).
- [171] D. Pfeiffer, M. Dietrich, P. Schach, G. Birkl, and E. Giese, *Dichroic mirror pulses for optimized higher-order atomic Bragg diffraction*, *Phys. Rev. Res.* **7**, L012028 (2025).
- [172] E. Giese, Mechanisms of matter-wave diffraction and their application to interferometers, Fortschr. Phys. 63, 337–410 (2015).
- [173] W. L. Bragg, *The Diffraction of X-rays by Crystals*, *Zeitschrift für Physikalische Chemie* **228**, 957–968 (2014).
- [174] S. S. Szigeti, J. E. Debs, J. J. Hope, N. P. Robins, and J. D. Close, *Why momentum width matters for atom interferometry with Bragg pulses*, *New J. Phys.* **14**, 023009 (2012).
- [175] B. Gadway, D. Pertot, R. Reimann, M. G. Cohen, and D. Schneble, *Analysis of Kapitza-Dirac diffraction patterns beyond the Raman-Nath regime*, *Opt. Express* 17, 19173–19180 (2009).
- [176] H. Müller, S.-w. Chiow, and S. Chu, Atom-wave diffraction between the Raman-Nath and the Bragg regime: Effective Rabi frequency, losses, and phase shifts, Phys. Rev. A 77, 023609 (2008).
- [177] W. P. Schleich, Quantum Optics in Phase Space, Wiley-VCH, Berlin (2001).
- [178] E. Giese, A. Roura, G. Tackmann, E. M. Rasel, and W. P. Schleich, *Double Bragg diffraction: A tool for atom optics*, *Phys. Rev. A* **88**, 053608 (2013).
- [179] A. Béguin, T. Rodzinka, J. Vigué, B. Allard, and A. Gauguet, *Characterization of an atom interferometer in the quasi-Bragg regime*, *Phys. Rev. A* **105**, 033302 (2022).
- [180] J.-N. Siemß, F. Fitzek, S. Abend, E. M. Rasel, N. Gaaloul, et al., *Analytic theory for Bragg atom interferometry based on the adiabatic theorem*, *Phys. Rev. A* **102**, 033709 (2020).

- [181] B. Plotkin-Swing, D. Gochnauer, K. E. McAlpine, E. S. Cooper, A. O. Jamison, et al., *Three-Path Atom Interferometry with Large Momentum Separation*, *Phys. Rev. Lett.* **121**, 133201 (2018).
- [182] R. H. Parker, C. Yu, B. Estey, W. Zhong, E. Huang, and H. Müller, *Controlling the multiport nature of Bragg diffraction in atom interferometry*, *Phys. Rev. A* **94**, 053618 (2016).
- [183] A. Bott, F. Di Pumpo, and E. Giese, *Atomic diffraction from single-photon transitions in gravity and Standard-Model extensions*, *AVS Quantum Sci.* **5**, 044402 (2023).
- [184] D. A. Steck, Quantum and Atom Optics, revision 0.16.1 (2024).
- [185] K. P. Zetie, S. F. Adams, and R. M. Tocknell, *How does a Mach-Zehnder interferometer work?*, *Physics Education* **35**, 46 (2000).
- [186] W. P. Schleich, D. M. Greenberger, and E. M. Rasel, A representation-free description of the Kasevich–Chu interferometer: a resolution of the redshift controversy, New J. Phys. 15, 013007 (2013).
- [187] R. Chattamvelli and R. Shanmugam, *Arcsine Distribution*, in: *Continuous Distributions in Engineering and the Applied Sciences-Part I*, Springer (2021), 57–68.
- [188] T. Berrada, S. van Frank, R. Bücker, T. Schumm, J.-F. Schaff, and J. Schmiedmayer, Integrated Mach–Zehnder interferometer for Bose–Einstein condensates, Nat. Commun. 4, 2077 (2013).
- [189] C. Pelluet, R. Arguel, M. Rabault, V. Jarlaud, C. Metayer, B. Barrett, P. Bouyer, and B. Battelier, *Atom interferometry in an Einstein Elevator*, *arxiv*:2407.07183 (2024).
- [190] B. Barrett, L. Antoni-Micollier, L. Chichet, B. Battelier, P.-A. Gominet, A. Bertoldi, P. Bouyer, and A. Landragin, *Correlative methods for dual-species quantum tests of the weak equivalence principle*, *New J. Phys* 17, 085010 (2015).
- [191] J. K. Stockton, X. Wu, and M. A. Kasevich, *Bayesian estimation of differential interferometer phase*, *Phys. Rev. A* **76**, 033613 (2007).
- [192] K. S. Hardman, P. J. Everitt, G. D. McDonald, P. Manju, P. B. Wigley, M. A. Sooriyabandara, C. C. N. Kuhn, J. E. Debs, J. D. Close, and N. P. Robins, *Simultaneous Precision Gravimetry and Magnetic Gradiometry with a Bose-Einstein Condensate: A High Precision, Quantum Sensor*, *Phys. Rev. Lett.* **117**, 138501 (2016).
- [193] I. N. Bronstein and K. A. Semendjajew, *Taschenbuch der Mathematik*, B.G. Teubner Verlagsgesellschaft, Leipzig, Germany (1987).
- [194] M. Zych, F. Costa, I. Pikovski, and Č. Brukner, *Quantum interferometric visibility as a witness of general relativistic proper time*, *Nat. Commun.* **2**, 505 (2011).
- [195] M. Meister, G. Müller, P. Boegel, A. Roura, A. Pichery, D. B. Reinhardt, T. Estrampes, J. Ströhle, E. Giese, H. Ahlers, et al., *Space magnetometry with a differential atom interferometer*, *arxiv*:2505.23532 (2025).
- [196] G. T. Foster, J. B. Fixler, J. M. McGuirk, and M. A. Kasevich, *Method of phase extraction between coupled atom interferometers using ellipse-specific fitting*, *Opt. Lett.* **27**, 951–953 (2002).
- [197] C. Farrell and M. Player, *Phase step measurement and variable step algorithms in phase-shifting interferometry*, *Meas. Sci. Technol.* **3**, 953 (1992).

- [198] K. Ridley and A. Rodgers, *An investigation of errors in ellipse-fitting for cold-atom interferometers*, *EPJ Quantum Technol.* 11, 79 (2024).
- [199] S.-w. Chiow, J. Williams, and N. Yu, *Noise reduction in differential phase extraction of dual atom interferometers using an active servo loop*, *Phys. Rev. A* **93**, 013602 (2016).
- [200] R. Halır and J. Flusser, Numerically stable direct least squares fitting of ellipses, in: Proc. 6th International Conference in Central Europe on Computer Graphics and Visualization. WSCG, 98, Citeseer (1998), 125–132.
- [201] A. Fitzgibbon, M. Pilu, and R. Fisher, *Direct Least Square Fitting of Ellipses*, *IEEE Transactions on Pattern Analysis and Machine Intelligence* **21** (2000).
- [202] C. Hill, Ellipse Fitting Algorithm, Accessed: 24.04.2025.
- [203] K. H. Knuth, *Optimal data-based binning for histograms and histogram-based probability density models*, *Digit. Signal Process.* **95**, 102581 (2019).
- [204] B. Efron, The Bootstrap and Modern Statistics, J. Am. Stat. Assoc. 95, 1293–1296 (2000).
- [205] Z. Zhou, S. C. Carrasco, C. Sanner, V. S. Malinovsky, and R. Folman, *Geometric phase amplification in a clock interferometer for enhanced metrology*, *Sci. Adv.* **11**, eadr6893 (2025).
- [206] W. Auzinger, H. Hofstätter, D. Ketcheson, and O. Koch, *Practical splitting methods for the adaptive integration of nonlinear evolution equations. Part I: Construction of optimized schemes and pairs of schemes*, *BIT Numer. Math.* **57**, 55–74 (2017).
- [207] J. W. Z. Lau, K. S. Gan, R. Dumke, L. Amico, L.-C. Kwek, and T. Haug, *Atomtronic multiterminal Aharonov-Bohm interferometer*, *Phys. Rev. A* **107**, L051303 (2023).
- [208] C. Ryu and M. G. Boshier, *Integrated coherent matter wave circuits*, *New J. Phys.* 17, 092002 (2015).
- [209] T. A. Bell, J. A. P. Glidden, L. Humbert, M. W. J. Bromley, S. A. Haine, M. J. Davis, T. W. Neely, M. A. Baker, and H. Rubinsztein-Dunlop, *Bose–Einstein condensation in large time-averaged optical ring potentials*, *New J. Phys.* **18**, 035003 (2016).
- [210] K. S. Gan, *An atomtronic experimental setup for engineering quantised circulations*, PhD thesis, Nanyang Technological University (2021).
- [211] S. Simjanovski, G. Gauthier, M. J. Davis, H. Rubinsztein-Dunlop, and T. W. Neely, *Optimizing persistent currents in a ring-shaped Bose-Einstein condensate using machine learning, Phys. Rev. A* **108**, 063306 (2023).
- [212] G. Gauthier, T. A. Bell, A. B. Stilgoe, M. Baker, H. Rubinsztein-Dunlop, and T. W. Neely, *Chapter One Dynamic high-resolution optical trapping of ultracold atoms*, in: edited by L. F. Dimauro, H. Perrin, and S. F. Yelin, **70**, Advances In Atomic, Molecular, and Optical Physics, Academic Press (2021), 1–101.
- [213] G. Gauthier, M. T. Reeves, X. Yu, A. S. Bradley, M. A. Baker, T. A. Bell, H. Rubinsztein-Dunlop, M. J. Davis, and T. W. Neely, *Giant vortex clusters in a two-dimensional quantum fluid*, *Science* **364**, 1264–1267 (2019).
- [214] G. Gauthier, S. S. Szigeti, M. T. Reeves, M. Baker, T. A. Bell, H. Rubinsztein-Dunlop, M. J. Davis, and T. W. Neely, *Quantitative Acoustic Models for Superfluid Circuits*, *Phys. Rev. Lett.* 123, 260402 (2019).

- [215] L. Pezzè, K. Xhani, C. Daix, N. Grani, B. Donelli, F. Scazza, D. Hernandez-Rajkov, W. J. Kwon, G. Del Pace, and G. Roati, *Stabilizing persistent currents in an atomtronic Josephson junction necklace*, *Nat. Commun.* **15**, 4831 (2024).
- [216] K. Xhani, G. Del Pace, F. Scazza, and G. Roati, *Decay of Persistent Currents in Annular Atomic Superfluids*, *Atoms* 11 (2023).
- [217] D. Hernández-Rajkov, N. Grani, F. Scazza, G. Del Pace, W. J. Kwon, M. Inguscio, K. Xhani, C. Fort, M. Modugno, F. Marino, and G. Roati, *Connecting shear flow and vortex array instabilities in annular atomic superfluids*, *Nat. Phys.* **20**, 939–944 (2024).
- [218] L. Lind, Zeitlich veränderliche Dipolpotentiale für Bose-Einstein-Kondensate mittels digital steuerbarer Mikrospiegeleinheit, Master Thesis, Technische Universität Darmstadt (2021).
- [219] N. Bazhan, A. Svetlichnyi, D. Pfeiffer, D. Derr, G. Birkl, and A. Yakimenko, *Generation of Josephson vortices in stacked toroidal Bose-Einstein condensates*, *Phys. Rev. A* **106**, 043305 (2022).
- [220] M. Mignardi, *The pioneering work that led to the DMD*, (Online; acessed 13.05.2025) (2016).
- [221] DLP® LightCrafter™ Evaluation Module (EVM) User's Guide, Texas Instruments (2014).
- [222] B. E. Bayer, An optimum method for two-level rendition of continuous-tone pictures, in: *Ineternl. Conf. on Comm.* **50** (1976), 69–77.
- [223] D. Schäffner, Interacting Neutral Atoms in a Scalable Platform of Optical Tweezers for Quantum Computation and Sensing, Dissertation, Technische Universität Darmstadt (2022).
- [224] A. Tononi, L. Salasnich, and A. Yakimenko, *Quantum vortices in curved geometries*, *AVS Quantum Sci.* **6**, 030502 (2024).
- [225] T. Bland, I. V. Yatsuta, M. Edwards, Y. O. Nikolaieva, A. O. Oliinyk, A. I. Yakimenko, and N. P. Proukakis, *Persistent current oscillations in a double-ring quantum gas*, *Phys. Rev. Res.* 4, 043171 (2022).
- [226] Y. Nikolaieva, L. Salasnich, and A. Yakimenko, Engineering phase and density of Bose–Einstein condensates in curved waveguides with toroidal topology, New J. Phys. 25, 103003 (2023).
- [227] J. Teske, Technical Matter Wave Optics: Imaging devices for Bose condensed matter waves an aberration analysis in space and time, Dissertation, Technische Universität Darmstadt (2023).
- [228] J. Henning, Strategies for compensating corrugations in a light sheet for trapping Bose-Einstein condensates, Master Proposal, Technische Universität Darmstadt (2025).
- [229] H.-J. Miesner, D. M. Stamper-Kurn, M. R. Andrews, D. S. Durfee, S. Inouye, and W. Ketterle, *Bosonic Stimulation in the Formation of a Bose-Einstein Condensate*, *Science* **279**, 1005–1007 (1998).
- [230] D. M. Stamper-Kurn, H.-J. Miesner, A. P. Chikkatur, S. Inouye, J. Stenger, and W. Ketterle, *Reversible Formation of a Bose-Einstein Condensate*, *Phys. Rev. Lett.* **81**, 2194–2197 (1998).
- [231] C.-C. Chen, R. González Escudero, J. Minář, B. Pasquiou, S. Bennetts, and F. Schreck, *Continuous Bose–Einstein condensation*, *Nature* **606**, 683–687 (2022).

- [232] M. C. Garrett, A. Ratnapala, E. D. van Ooijen, C. J. Vale, K. Weegink, S. K. Schnelle, O. Vainio, N. R. Heckenberg, H. Rubinsztein-Dunlop, and M. J. Davis, *Growth dynamics of a Bose-Einstein condensate in a dimple trap without cooling*, *Phys. Rev. A* **83**, 013630 (2011).
- [233] S. Dutta and E. J. Mueller, *Kinetics of Bose-Einstein condensation in a dimple potential*, *Phys. Rev. A* **91**, 013601 (2015).
- [234] J. McCabe, A continued fraction expansion, with a truncation error estimate, for Dawson's integral, Mathematics of Computation 28, 811–816 (1974).
- [235] C. Chen and H. Chen, *Coherence time-bandwidth product for chirped Gaussian pulses*, *Optik* **124**, 5199–5201 (2013).

Danksagung

"If I have seen further, it is by standing on the shoulders of giants."

- Sir Isaac Newton

Last but not least – abschließend ist es Zeit, einige Worte des Dankes auszusprechen, denn ganz ohne Unterstützung kann ein Projekt wie dieses nicht umgesetzt werden! Ich werde mit Sicherheit den einen oder anderen übersehen, doch nicht aus bösem Willen, sondern eher meiner zunehmenden Vergesslichkeit geschuldet. Bitte seht es mir nach.

Zuerst sei an dieser Stelle Herrn Prof. Birkl gedankt, der mir nicht nur die Möglichkeit gab, an einem fantastischen Experiment zu arbeiten, sondern es ebenso vermochte, in unzähligen fachlichen Diskussionen meine Begeisterung für das Neue, Unbekannte und insbesondere scheinbar Unmögliche stets zu steigern. Bereits zur Zeit der Masterarbeit vertrauten Sie mir das ATOMICS-Experiment an, eine Zeit, in der ich unfassbar viel Neues lernen konnte, auf das ich bis heute zurückgreifen kann. Neben dem Fachlichen habe ich mich ebenfalls an einigen Diskussionen über Allerweltliches erfreut, für die neben dem Laboralltag dennoch genügend Zeit blieb.

Weiterhin möchte ich mich ausdrücklich bei Herrn Prof. Giese bedanken, nicht nur für die unkomplizierte Übernahme des zweiten Gutachtens, sondern insbesondere für die Einblicke in den Bereich der Atominterferometrie, die maßgeblich zum Erfolg dieser Arbeit beigetragen haben. Von morgendlichen Diskussionen zwischen Tür und Angel über ausgedehnte Meetings bis zu den gelegentlichen Unterhaltungen an dem einen oder anderen Wochenende war es mir immer eine große Freude, mit Ihnen zu arbeiten. Auch die reibungslose Zusammenarbeit in mehreren Projekten wird mir in positiver Erinnerung bleiben.

Herrn Prof. Walther und Herrn Prof. Schneck möchte ich ebenso meinen Dank für die bereitwillige Teilnahme am Prüfungskomitee aussprechen.

Im Folgenden sei vielen meiner ehemaligen und aktuellen Kolleginnen und Kollegen sowie Freundinnen und Freunden gedankt, die mich teils gänzlich oder abschnittsweise auf dieser Reise begleitet haben. Beginnend beim Team des ATOMICS-Experiments und meinem direkten Vorgänger Felix, der mich schon zur Bachelorarbeit betreute und mich in die Geheimnisse der konischen Refraktion einweihte. Daniel und Ludwig haben mich nicht nur schon als Masterstudent tatkräftig im Labor unterstützt und durch ihre Projekte das Experiment vorangetrieben, wofür ihnen mein Dank gebührt, sondern sind bereits zu Studienzeiten zu guten Freunden und mittlerweile Kollegen geworden. Ihr habt maßgeblich zur guten Stimmung in Labor, Büro und drumherum beigetragen, insbesondere wenn mal das eine oder andere Tief zu überwinden war – danke!

Auch bei meinen weiteren aktuellen und ehemaligen Kolleginnen und Kollegen aus der Arbeitsgruppe möchte ich mich herzlich für die gute Zusammenarbeit und die familiäre Umgebung über die letzten Jahre bedanken. Dominik und Tobias vom Experiment eine Tür weiter, stets für einen netten Plausch am Ti:Sa zu haben, sowie Lars, Tilman, Lukas und Marcel vom ehemaligen und aktuellen Team des QUIPS-C Experiments, die ebenfalls jederzeit für fachliche und allerweltliche Gespräche zu haben waren. Weiterhin sei Patrick erwähnt, der nicht nur allerlei Messelektronik inklusive fachlicher Kompetenz zur Verfügung stellte, sondern auch für jede

Koboldjagd im Labor zu haben war, ungeachtet der Tageszeit oder des Wochentages. Ebenso Arya vom GSI-Teil unserer AG, der Austausch über Technisches hat mich stets gefreut. Malte hat mir insbesondere im letzten Abschnitt dieser Arbeit durch seine konstanten kulinarischen Bemühungen einen Fixpunkt in der Woche gegeben, ohne den die Wochentage sicher mehr ineinander verschwommen wären. Danke euch allen! Jede und jeder Einzelne, inklusive vieler ungenannter Bachelor- und Masterstudierender sowie HiWis, hat meine Zeit in der Arbeitsgruppe bereichert!

Nicht vergessen möchte ich die AG Giese mit Patrik, Daniel, Christo und Christian sowie den vielen Studierenden, die ich im Laufe der Zeit kennenlernen durfte. Jedes Gespräch, egal ob fachlich oder nicht, beim Mittagessen oder auf dem Gang (selbst an Wochenenden), sowie die fantastische Zusammenarbeit bei Projekten und allgemeinem Wissensaustausch, ist für mich der Inbegriff dessen, wie Forschung sein sollte!

Jan und Oleksandr dürfen selbstverständlich nicht unerwähnt bleiben, eine Freundschaft, begründet an einem zugefrorenen See hoch in den spanischen Pyrenäen im Rahmen einer bis heute unübertroffenen ATOMTRONICS-Konferenz. Die vielen Diskussionen und Gespräche, kleine, von schierer Neugier getriebene Nebenprojekte und jeden Abend in Darmstadts Kneipen habe ich sehr genossen! - iA caballo!

Furthermore, I would like to thank Prof. Yakymenko and his group for the fantastic collaboration over the past years. I really enjoyed the fruitful discussions, whether in online meetings, in person at conferences, or in Darmstadt.

Weiterhin sei der Feinmechanikwerkstatt rund um Herrn Weick ein großes Dankeschön gewidmet, die es vermochten, meine nicht vorhandenen CAD-Fähigkeiten mit Geduld und Mühe vorzüglich zu kompensieren. Jedes noch so abstruse Projekt wurde in Windeseile optimiert und fertiggestellt – eine Möglichkeit, die ich nicht hätte missen mögen.

Auch den erweiterten Kolleginnen und Kollegen der AG Walther, AG Halfmann und AG Walser sei gedankt für viele nette Gespräche und die gute kollegiale Atmosphäre auf unserem Stockwerk und in unserem Institut.

Abseits der Arbeit im Labor konnte ich mich immer auf Luca, Leon und Maxym sowie die gesamte DSW-Laufgruppe verlassen, die mich, um die geistige Beanspruchung auszugleichen, sportlich auf Trab gehalten haben. Ob 1000 m-Intervalle im Stadion, Longruns am Sonntag oder Training im Studio, danke für eure Unterstützung.

Abschließend möchte ich mich bei meiner Familie bedanken. Allen voran meinen Eltern, Claudia und Andreas, die mir in vielerlei Hinsicht dieses Studium ermöglicht haben. Danke für eure Unterstützung nicht nur finanzieller Art, die mir den Freiraum gibt, das zu tun was ich möchte. Auch Pascale, meiner Schwester, und ihrer Familie möchte ich danken, die mich stets in meinem Weg bestärkt haben. Weiter möchte ich meinen Großeltern danken, Angela und Lothar, Ursula sowie Manfred und Mechthild, die mich auf vielerlei Weisen unterstützt und motiviert haben meinen Weg zu gehen. Danke euch allen, die Familie als sicheres Netz hinter sich zu wissen, hat mich gut durch die vergangenen Jahre gebracht.

Ein ganz besonderer Dank gilt natürlich Thyrza, die seit dem Masterstudium an meiner Seite steht und geduldig jede noch so stressige Phase ertragen hat. Danke für deine Geduld und die Fürsorge, die du mir entgegengebracht hast, sodass ich mich gänzlich dieser Arbeit widmen konnte. Keine Feiertage mehr im Labor, versprochen!

Curriculum Vitae

The CV is not included in the online version for reasons of data protection.

Erklärungen laut Promotionsordnung
§ 8 Abs. 1 lit. c Prom0
Ich versichere hiermit, dass die elektronische Version meiner Dissertation mit der schriftlichen Version übereinstimmt.
§ 8 Abs. 1 lit. d PromO
Ich versichere hiermit, dass zu einem vorherigen Zeitpunkt noch keine Promotion versucht wurde. In diesem Fall sind nähere Angaben über Zeitpunkt, Hochschule, Dissertationsthema und Ergebnis dieses Versuchs mitzuteilen.
§ 9 Abs. 1 PromO
Ich versichere hiermit, dass die vorliegende Dissertation – abgesehen von den in ihr ausdrücklich genannten Hilfen – selbstständig verfasst wurde und dass die "Grundsätze zur Sicherung guter wissenschaftlicher Praxis an der Technischen Universität Darmstadt" und die "Leitlinien zum Umgang mit digitalen Forschungsdaten an der TU Darmstadt" in den jeweils aktuellen Versionen bei der Verfassung der Dissertation beachtet wurden.
§ 9 Abs. 2 PromO
Die Arbeit hat bisher noch nicht zu Prüfungszwecken gedient.
Darmstadt, 24.06.2025 Dominik Pfeiffer